LA-13686-C
Conference

Issued: January 2000

Workshop on the Origin of the Heavy Elements: Astrophysical Models and Experimental Challenges Santa Fe, New Mexico

September 3-4, 1999

Edited by
Robert C. Haight
John L. Ullmann
Daniel D. Strottman
*Paul E. Koehler**
*Franz Kaeppeler***

* *Laboratory Affiliate at Los Alamos. Physics Division, Oak Ridge National Laboratory, Bldg. 6010, MS 6354, Oak Ridge, TN 37831-6354*
** *Laboratory Affiliate at Los Alamos. Forschungszentrum Karlsruhe, IK Bau 425, D-76021, Postfach 3640, Karlsruhe, Germany*

Los Alamos
NATIONAL LABORATORY
Los Alamos, New Mexico 87545

DISCLAIMER

Workshop on the Origin of the Heavy Elements: Astrophysical Models and Experimental Challenges

Edited by

R. C. Haight, J. L. Ullmann, D. D. Strottman
Los Alamos National Laboratory

P. E. Koehler
Oak Ridge National Laboratory

and

F. Kaeppeler
Forschungszentrum Karlsruhe

ABSTRACT

This Workshop was held on September 3-4, 1999, following the 10th International Symposium on Capture Gamma-Ray Spectroscopy. Presentations were made by 14 speakers, 6 from the US and 8 from other countries on topics relevant to s-, r- and rp-process nucleosynthesis. Laboratory experiments, both present and planned, and astrophysical observations were represented as were astrophysical models. Approximately 50 scientists participated in this Workshop. These Proceedings consist of copies of vu-graphs presented at the Workshop. For further information, the interested readers are referred to the authors.

Workshop on the Origin of the Heavy Elements: Astrophysical Models and Experimental Challenges

Schedule

Friday, September 3

1:50 - 2:00	Welcome	

r-process Nucleosynthesis

2:00 - 2:30	Peter Möller	Nuclear Mass Models: Past Achievements, Current Status, and Future Challenges
2:30 - 3:00	Stephen A. Becker	Approximating the r-process on Earth with Thermonuclear Explosions
3:00- 3:30	Stephane Goriely	Uncertainties in the Th Cosmochronology
3:30- 4:00	Discussion on the r-process with refreshments	
4:00 - 4:30	Paolo Mutti	Neutron Capture Cross Sections of Kr-84 and Kr-86 and Their Impact on Stellar Nucleosynthesis

Proton-rich Nuclides

4:30- 5:00	Paul Kienle	Half-lives of rp-process Waitingpoint Nuclei
5:00 - 5:30	H. H. Pitz	Photoactivation of 180mTa and Implications for the Nucleosynthesis of Nature's Rarest Stable Isotope
5:30- 7:00	Discussion of proton-rich nuclei with refreshments	

Continued (next page)

Workshop Schedule (continued)

Saturday, September 4

Astronomical Observations and Models

8:30 - 9:00	A. Mengoni	Structure and EM Dissociation of 9Be
9:00 - 9:30	Joyce Ann Guzik	Sensitivity of Solar Oscillation Frequencies to Element Abundances and Composition Gradients
9:30 - 10:00	Corinne Neuforge	Linking Field Metal-Poor Stars and Globular Clusters
10:00 - 10:30	Hideo Harada	Thermal Neutron Capture Cross Sections and Resonance Integrals of Fission Products
10:30 - 11:00	Break and Discussion	

New Capabilities and Plans

11:00 - 11:30	O. Shcherbakov	Neutron Time-of-flight Sepctrometer GNEIS at the 1-GeV Proton Synchrotron of PNPI
11:30 - 12:00	Rene Reifarth	The Use of 4pi Detectors at Spallation Neutron Sources
12:00 - 12:30	Paul Koehler	Plans for Measurements at Oak Ridge
12:30 - 1:00	Working Lunch --	
1:00 - 1:30	Robert Rundberg	Plans for Measurements at Los Alamos

Nuclear Mass Models: Past Achievments, Current Status and Future Challenges

Peter Möller
Theoretical Division, Los Alamos National Laboratory, Los Alamos, NM 87545

The history of mass models is briefly discussed. Features of some commonly used mass models, such as those developed by Liran-Zeldes, von Groote-Hilf, Pearson-Tondeur, Myers-Swiatecki, and Möller-Nix are compared and discussed.

We particularly discuss how the models behave when applied to masses outside the region to which parameters were adjusted, that is how reliably the models behave in regions close to the drip lines and in the superheavy-element region.

We discuss the deviations that remain between model results and experimental data, and what physical effects need be more realistically described to remove such deviations so that greater model accuracies may be obtained.

Our latest manuscripts and mass tables are available from URL:

http://t2.lanl.gov

and various links from this URL.

For data related to the Möller-Nix mass model the URL is:

http://t2.lanl.gov/data/astro/molnix96/molnix.html

A nuclear mass model should be able to:

- predict the energy of any minimum and saddle
- predict the next magic numbers beyond Pb
- provide additional nuclear-structure insight

VERY!
IMPORTANT

Our approach to nuclear structure models:

Microscopic content	Wave functions Real insight
Few parameters	
Unified	Same model for many phenomena
Consistent	Same parameters in different calculations
Experimental connection	Comparisons – Predictions

Macroscopic-microscopic model:

- Macroscopic models: Liquid-drop, droplet, finite-range liquid-drop and finite-range droplet models.
- Microscopic models: Nilsson modified oscillator, two-center oscillator, Woods-Saxon and folded-Yukawa single-particle potentials.
- For each model several parameter sets.

For progress it is necessary to proceed in a consistent manner with a clear strategy of model development.

Important developments leading to current FRDM model:

- Folded-Yukawa single-particle potential (1969–1972)
- New single-particle parameters (Nilsson 1973)
- Finite-range surface-energy effects (1973, 1979)
- Mass calculation (1979–1981)

The improvements in the mass calculation relative to earlier work led to a revision of the understanding of the stability of the superheavy elements and to the discovery of octupole effects on nuclear masses (1979–1984)

Important developments leading to current FRDM model, continued:

- Finite-range droplet model (1984)
- New pairing models, parameters, (1986–1990)
- Calculation of octupole and P_6 effects on nuclear masses (1990-1991)
- Mass calculation to drip lines, 8979 masses (1991)

The new calculation led to the discovery of Coulomb redistribution effects on nuclear masses and to much lower errors in the calculated masses for nuclei with $N > 65$.

SIGNIFICANT ACHIEVMENTS:

First mass-asymmetric saddle	(1970)
First non-divergent mass model	(1981)
First demo of octupole effects on masses	(1981)
First study of deformation and β strength	(1984)
First multi-valley fission half-life calculation	(1987)
First consistent $T_{1/2}$ and P_{n} calculation	(late 80's)
First interpretable r-process calculation	(late 80's)

1980- 1981 MÖLLER - NIX

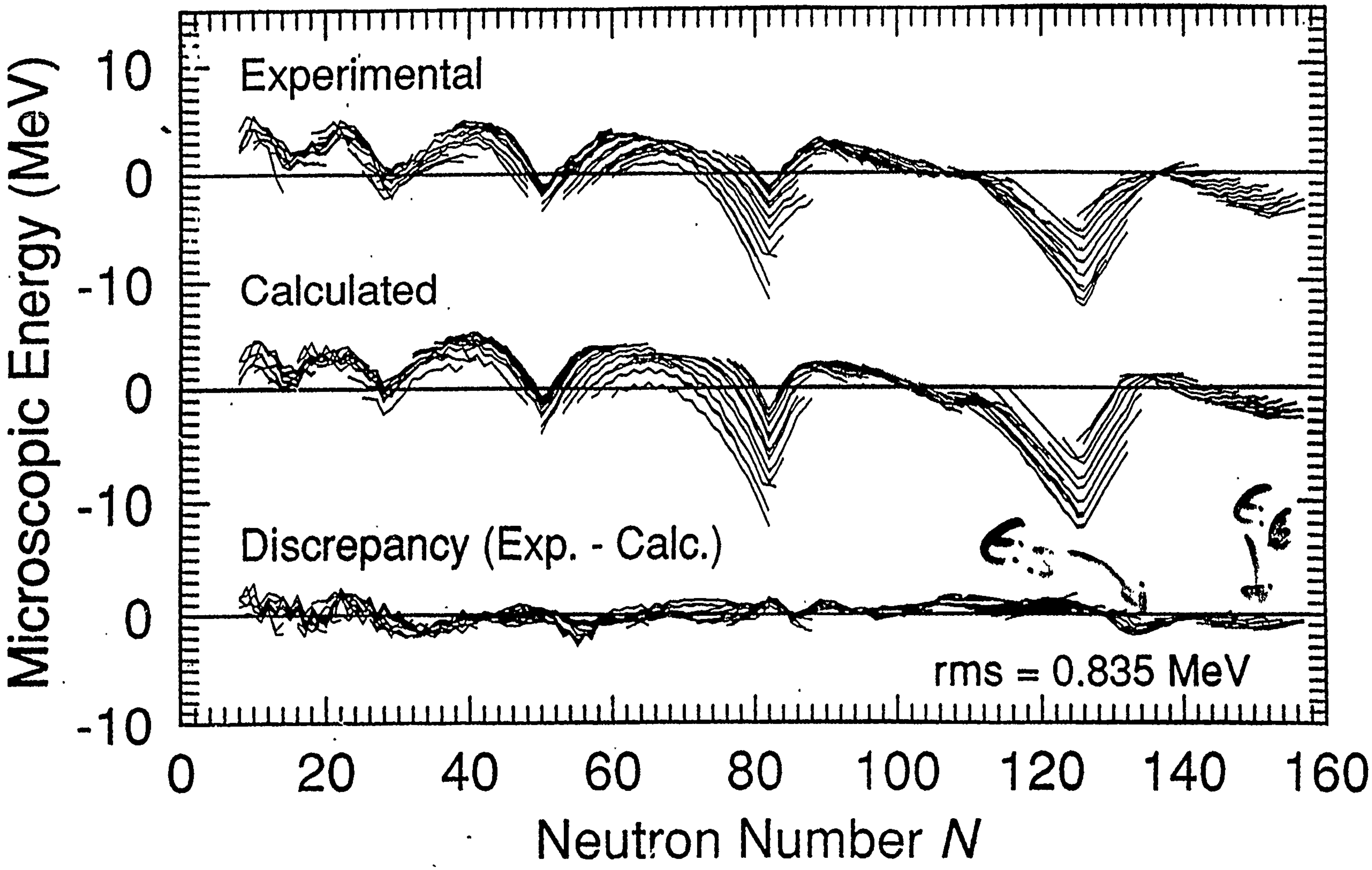

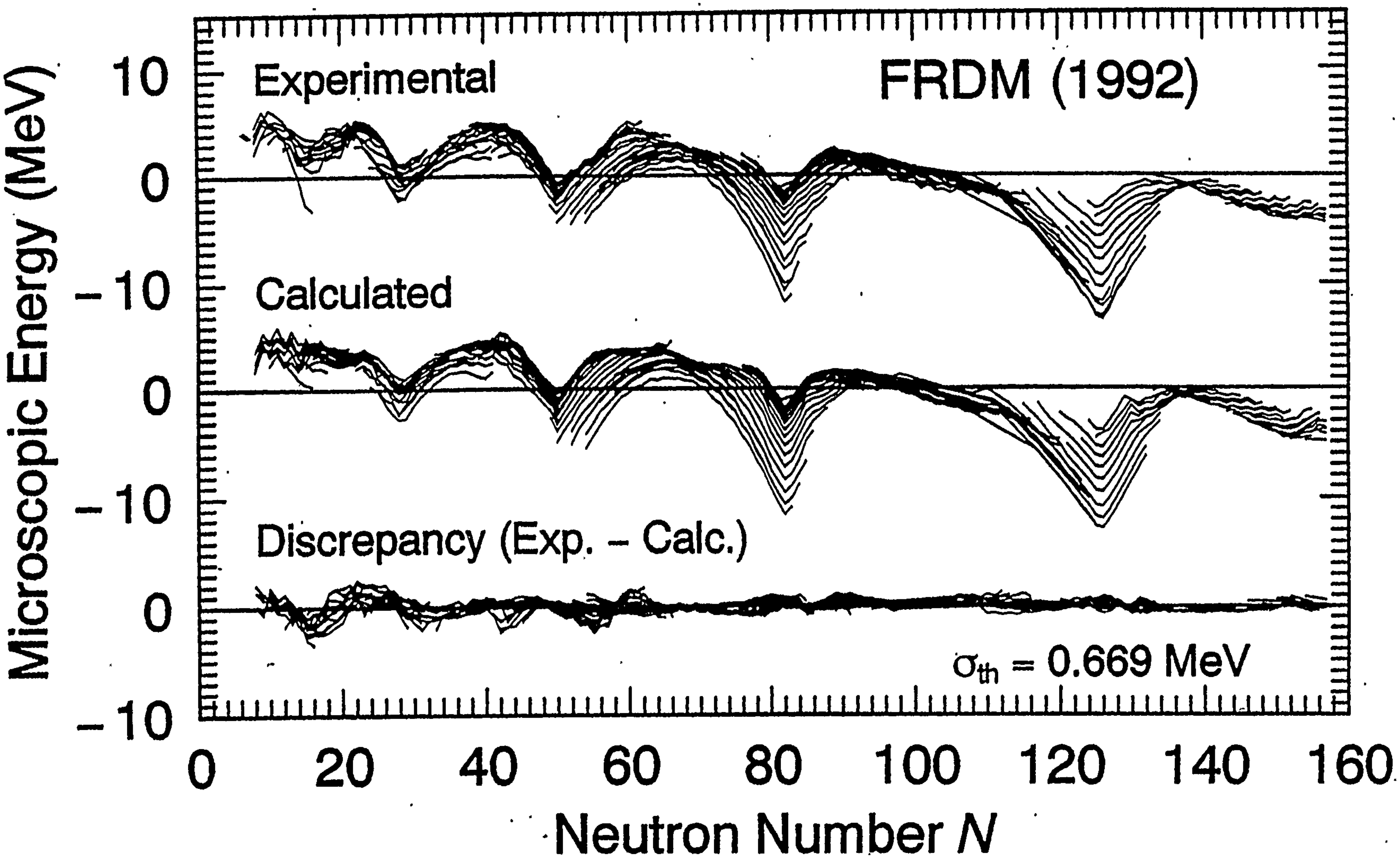
Experimental
FRDM (1992)
Calculated
Discrepancy (Exp. – Calc.)
σ_{th} = 0.669 MeV
Microscopic Energy (MeV)
10
0
–10
0
–10
0
–10
0
20
40
60
80
100
120
140
160
Neutron Number N

Limited-region adjustments lead to divergences
when model is applied outside region of adjustment

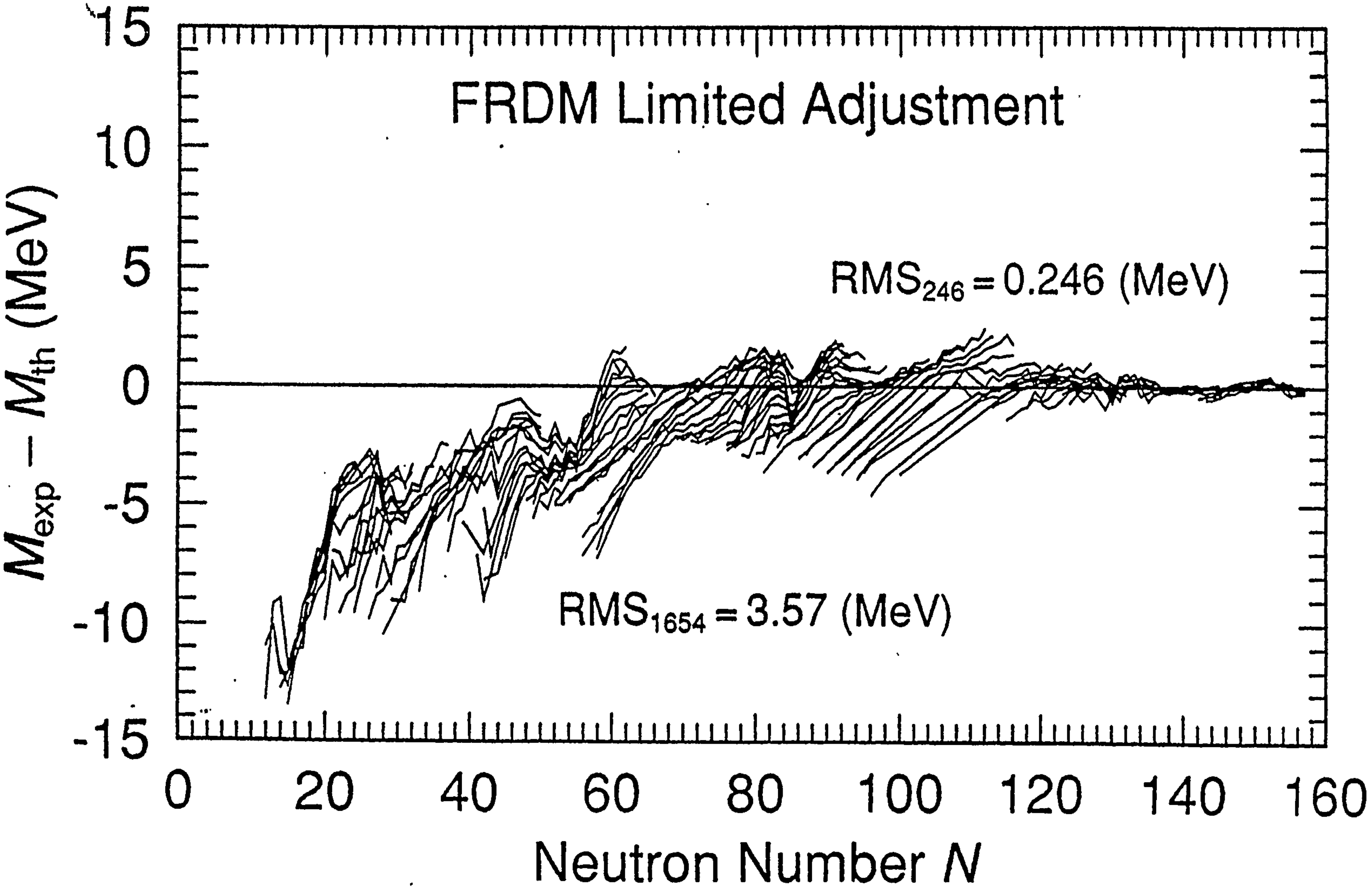

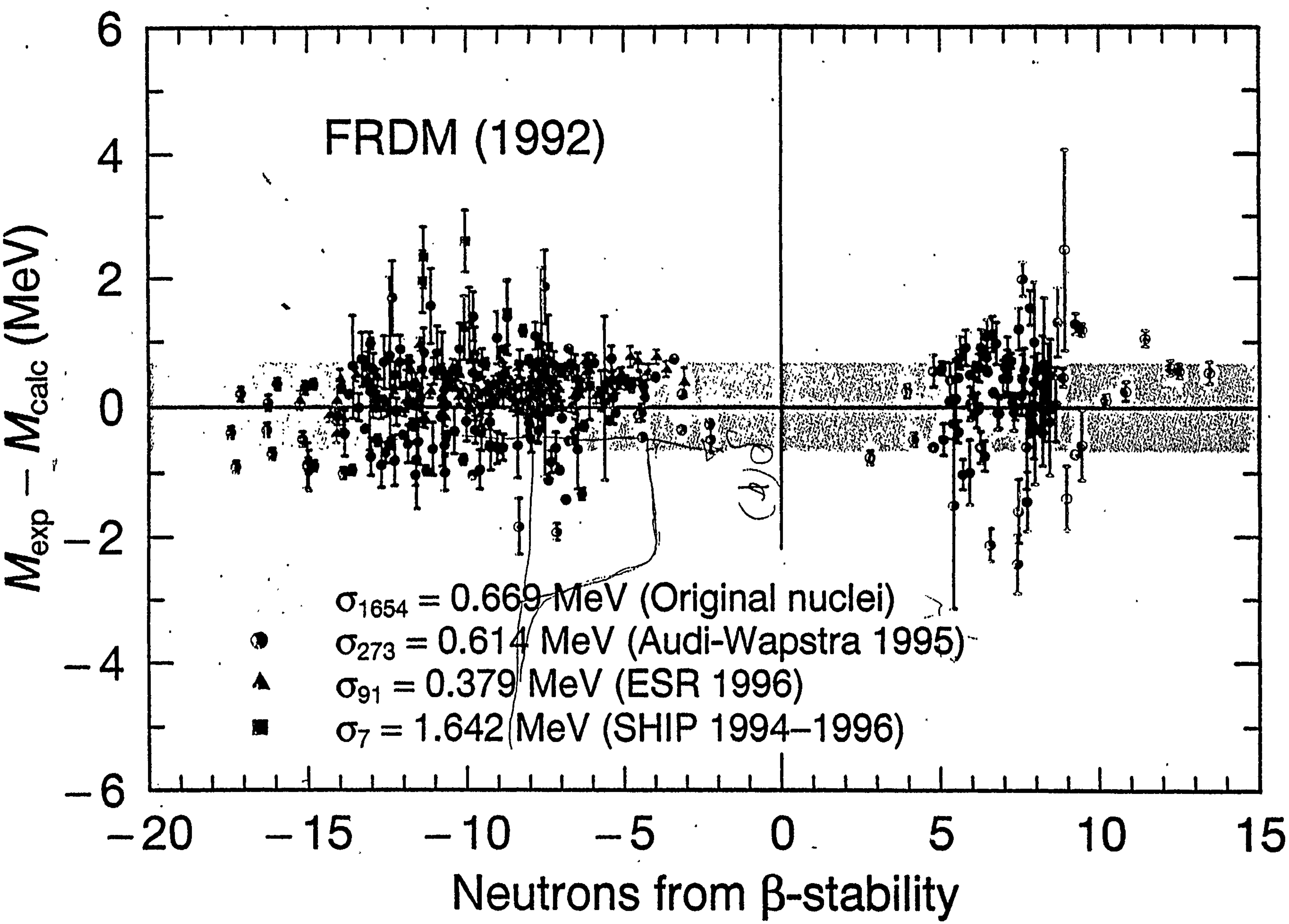
FRDM (1992)
$M_{exp} - M_{calc}$ (MeV)
6
4
2
0
−2
−4
−6
−20
−15
−10
−5
0
5
10
15
Neutrons from β-stability
σ_{1654} = 0.669 MeV (Original nuclei)
● σ_{273} = 0.614 MeV (Audi-Wapstra 1995)
▲ σ_{91} = 0.379 MeV (ESR 1996)
■ σ_7 = 1.642 MeV (SHIP 1994–1996)
p(r)

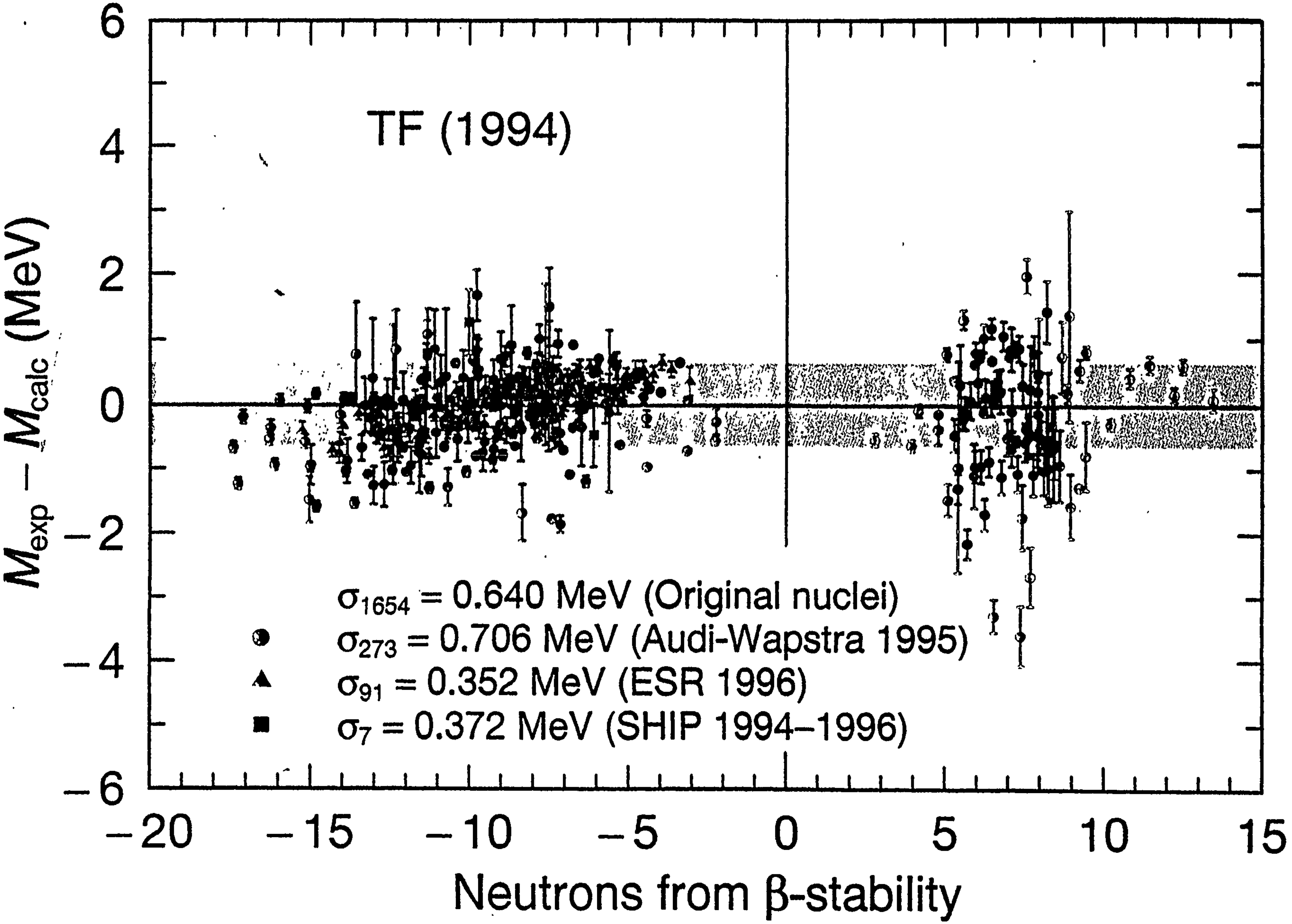
TF (1994)
$M_{exp} - M_{calc}$ (MeV)
6
4
2
0
−2
−4
−6
−20
−15
−10
−5
0
5
10
15
Neutrons from β-stability
$\sigma_{1654} = 0.640$ MeV (Original nuclei)
● $\sigma_{273} = 0.706$ MeV (Audi-Wapstra 1995)
▲ $\sigma_{91} = 0.352$ MeV (ESR 1996)
■ $\sigma_{7} = 0.372$ MeV (SHIP 1994–1996)

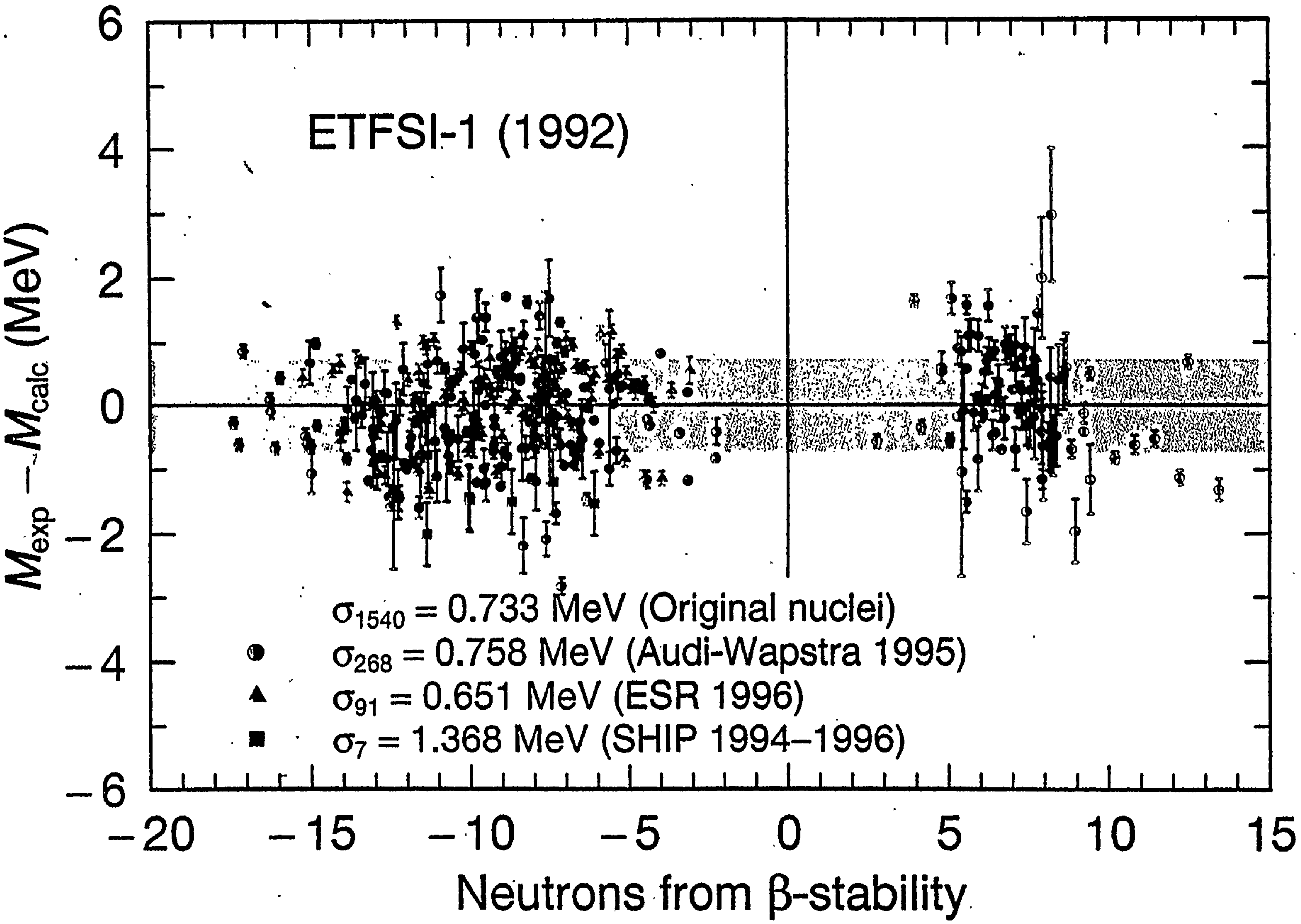
ETFSI-1 (1992)
$M_{exp} - M_{calc}$ (MeV)
6
4
2
0
−2
−4
−6
−20
−15
−10
−5
0
5
10
15
Neutrons from β-stability
● σ_{1540} = 0.733 MeV (Original nuclei)
● σ_{268} = 0.758 MeV (Audi-Wapstra 1995)
▲ σ_{91} = 0.651 MeV (ESR 1996)
■ σ_{7} = 1.368 MeV (SHIP 1994–1996)

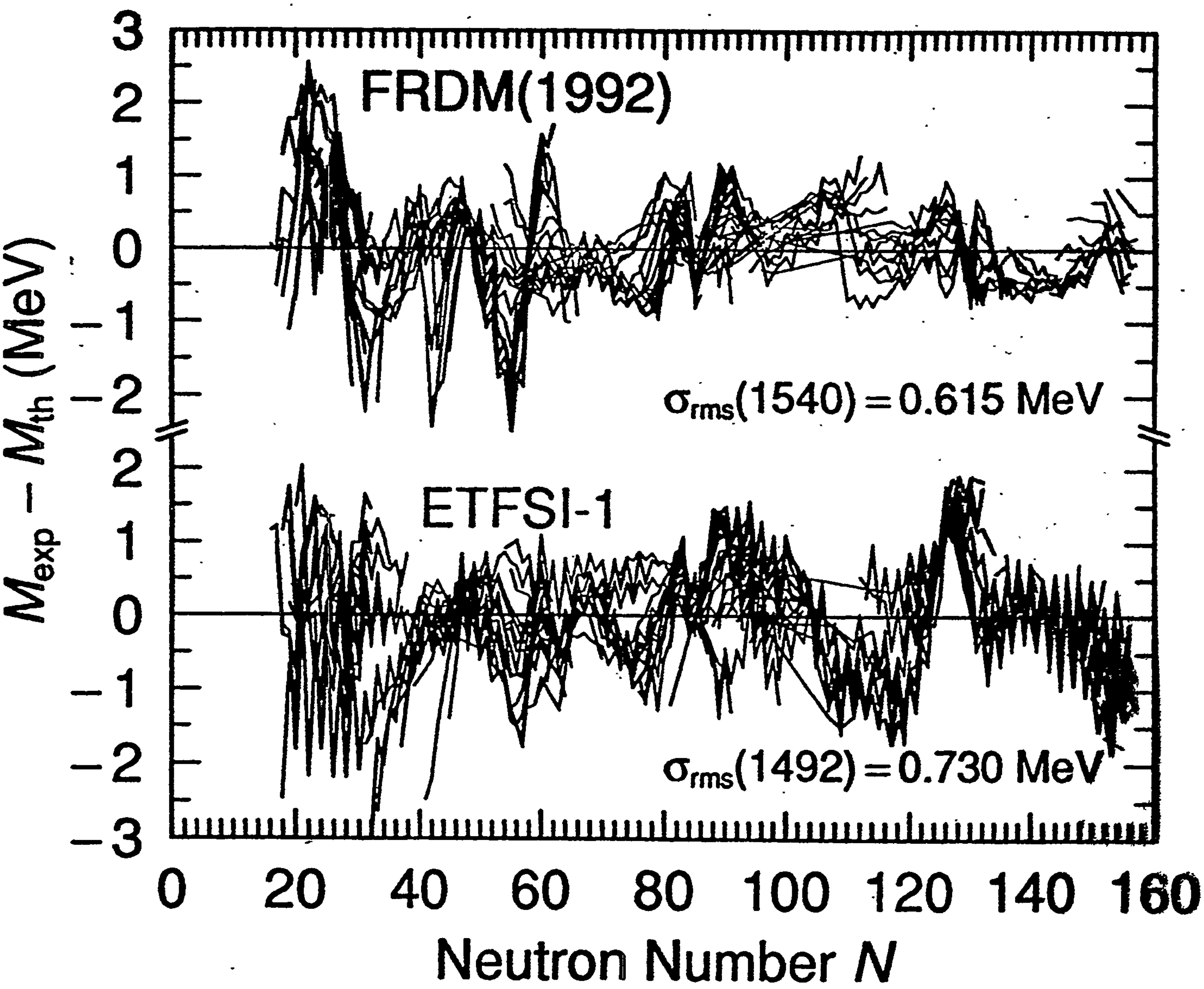
FRDM(1992)
ETFSI-1
$\sigma_{rms}(1540) = 0.615$ MeV
$\sigma_{rms}(1492) = 0.730$ MeV
$M_{exp} - M_{th}$ (MeV)
Neutron Number N
3
2
1
0
−1
−2
2
1
0
−1
−2
−3
0
20
40
60
80
100
120
140
160

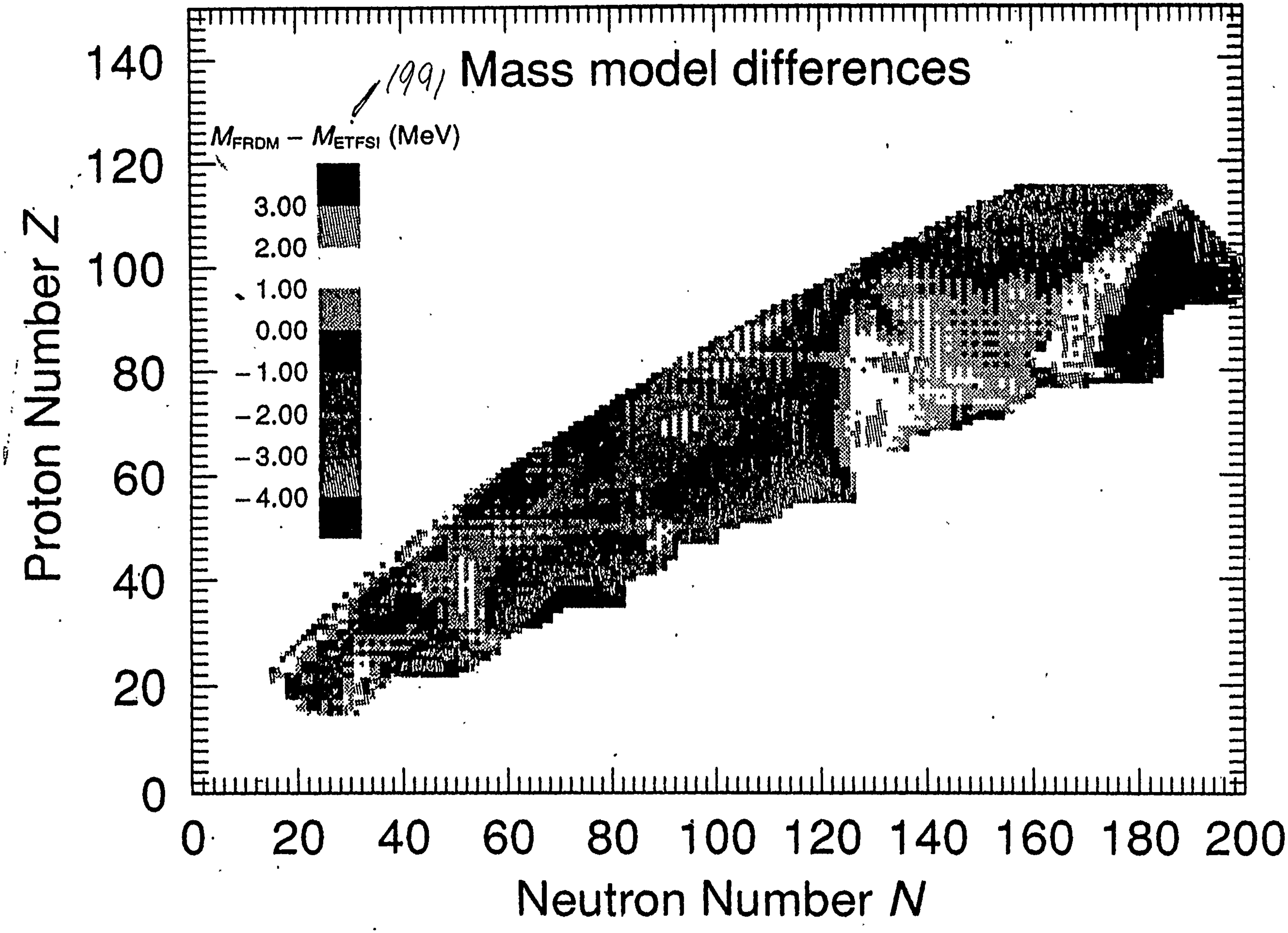
1991
Mass model differences
$M_{FRDM} - M_{ETFSI}$ (MeV)
3.00
2.00
1.00
0.00
−1.00
−2.00
−3.00
−4.00
Proton Number Z
140
120
100
80
60
40
20
0
Neutron Number N
0
20
40
60
80
100
120
140
160
180
200

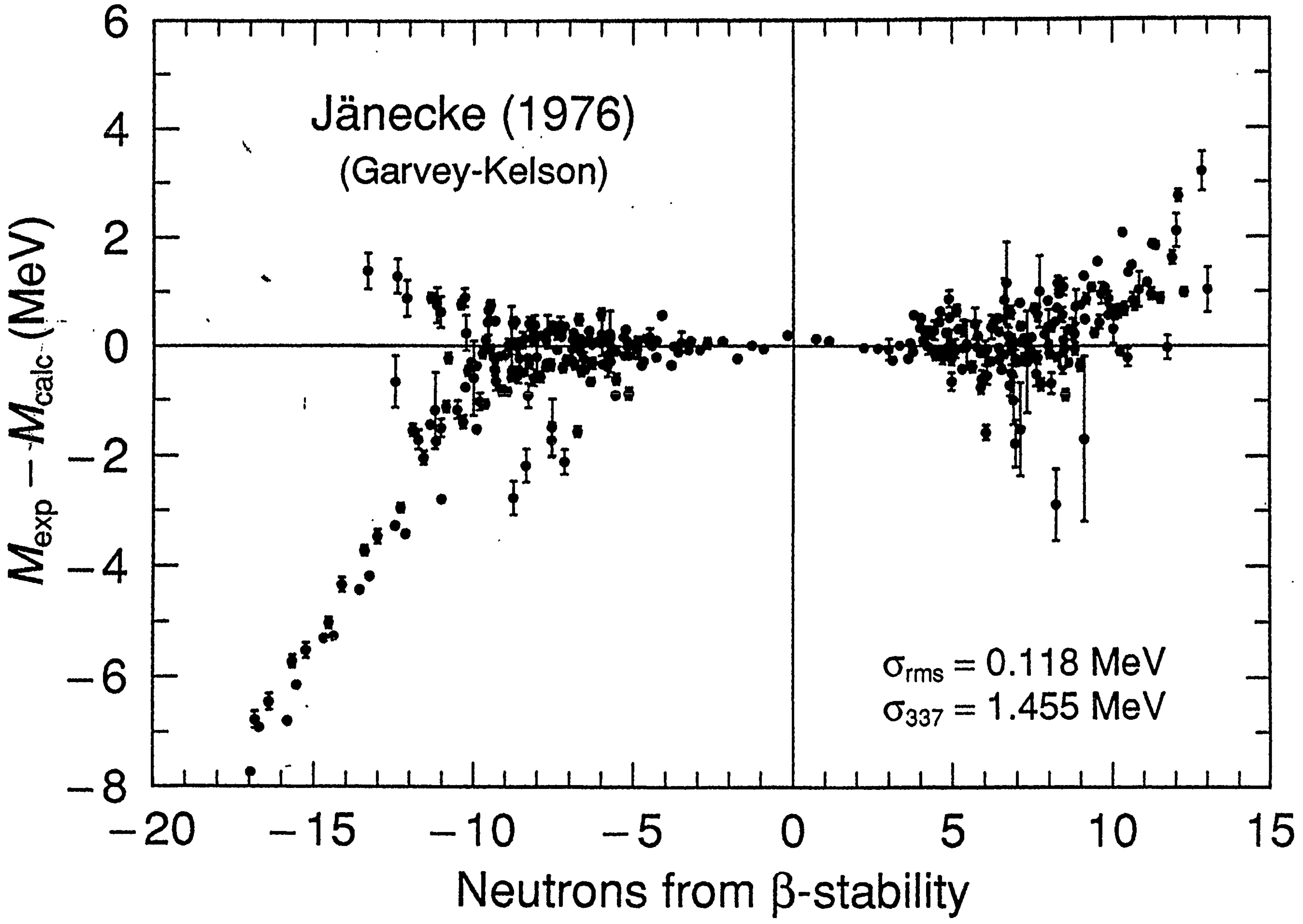
Jänecke (1976)
(Garvey-Kelson)
σ_{rms} = 0.118 MeV
σ_{337} = 1.455 MeV
$M_{exp} - M_{calc}$ (MeV)
6
4
2
0
−2
−4
−6
−8
−20
−15
−10
−5
0
5
10
15
Neutrons from β-stability

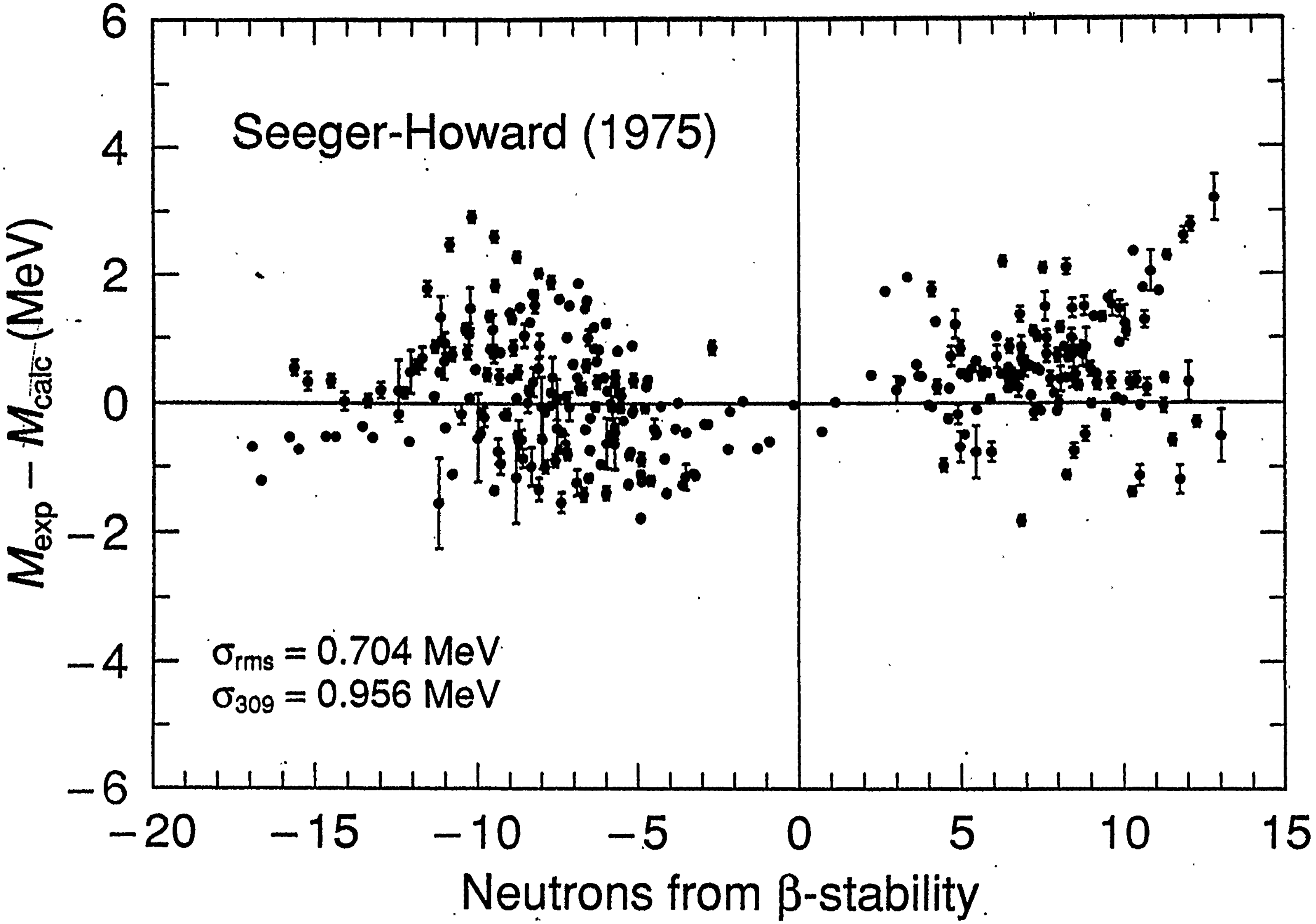
Seeger-Howard (1975)
$\sigma_{rms} = 0.704$ MeV
$\sigma_{309} = 0.956$ MeV
$M_{exp} - M_{calc}$ (MeV)
6
4
2
0
−2
−4
−6
−20
−15
−10
−5
0
5
10
15
Neutrons from β-stability

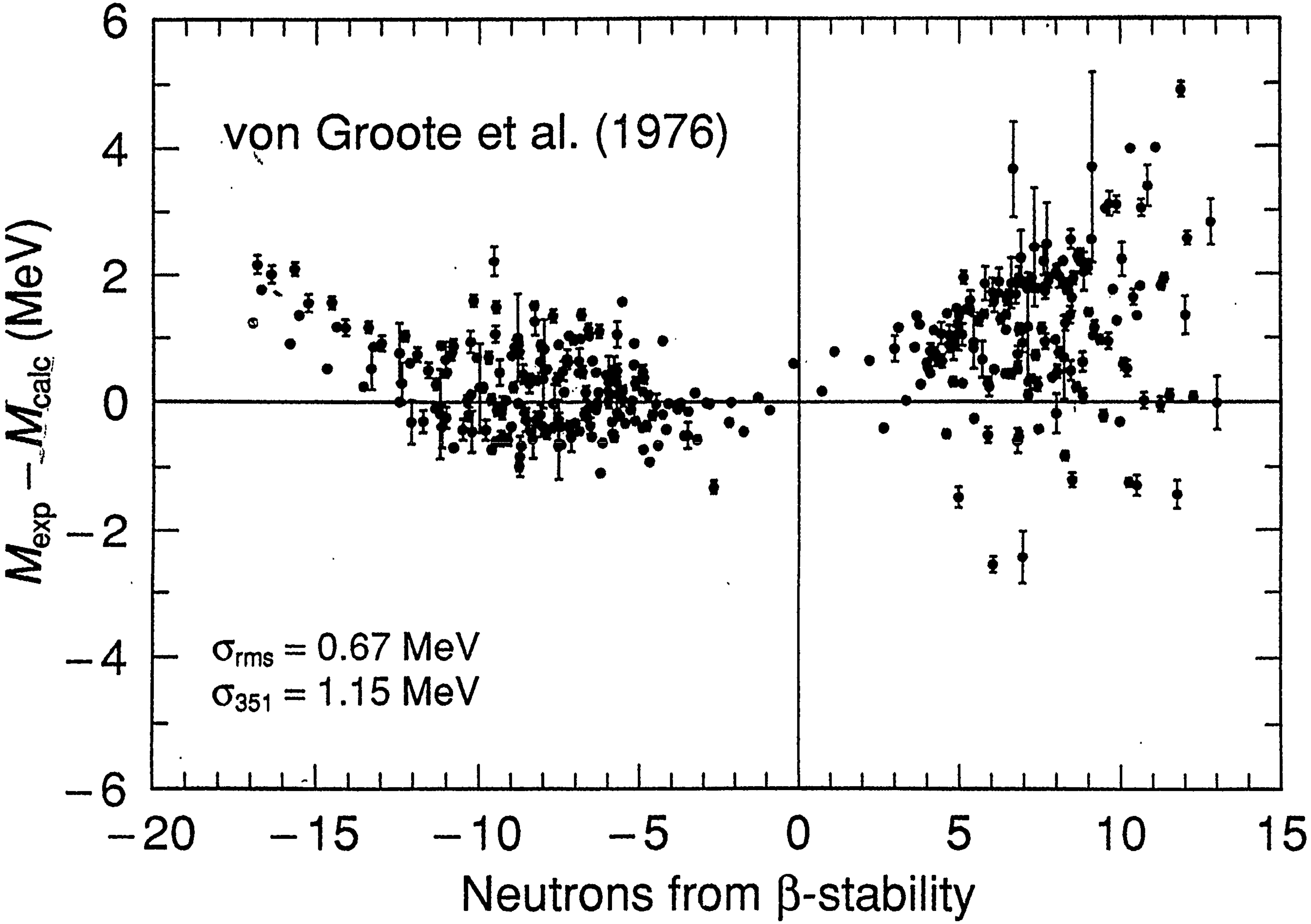von Groote et al. (1976)
$\sigma_{rms} = 0.67$ MeV
$\sigma_{351} = 1.15$ MeV
$M_{exp} - M_{calc}$ (MeV)
6
4
2
0
−2
−4
−6
−20
−15
−10
−5
0
5
10
15
Neutrons from β-stability

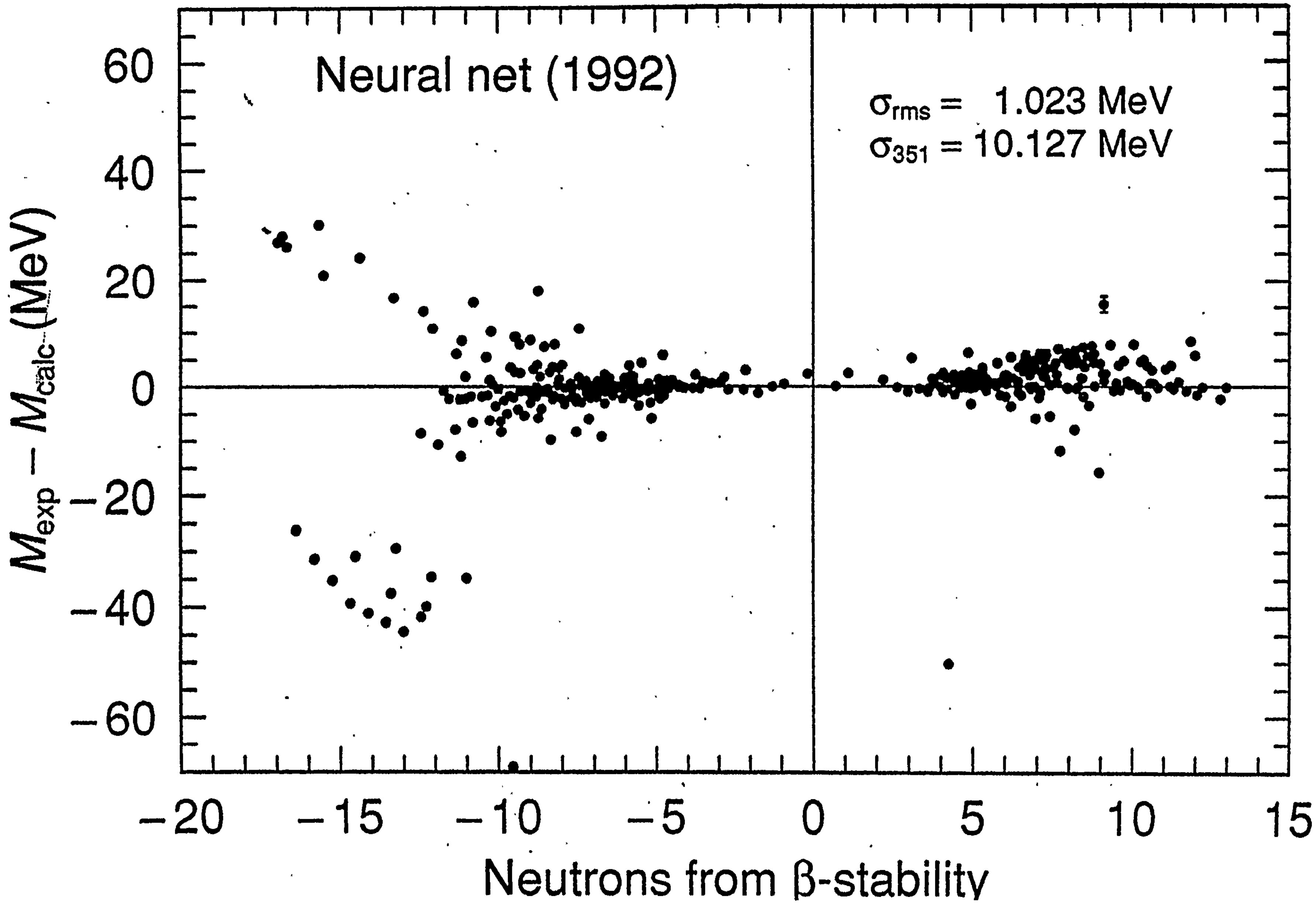
Neural net (1992)
σ_{rms} = 1.023 MeV
σ_{351} = 10.127 MeV
$M_{exp} - M_{calc}$ (MeV)
60
40
20
0
−20
−40
−60
−20
−15
−10
−5
0
5
10
15
Neutrons from β-stability

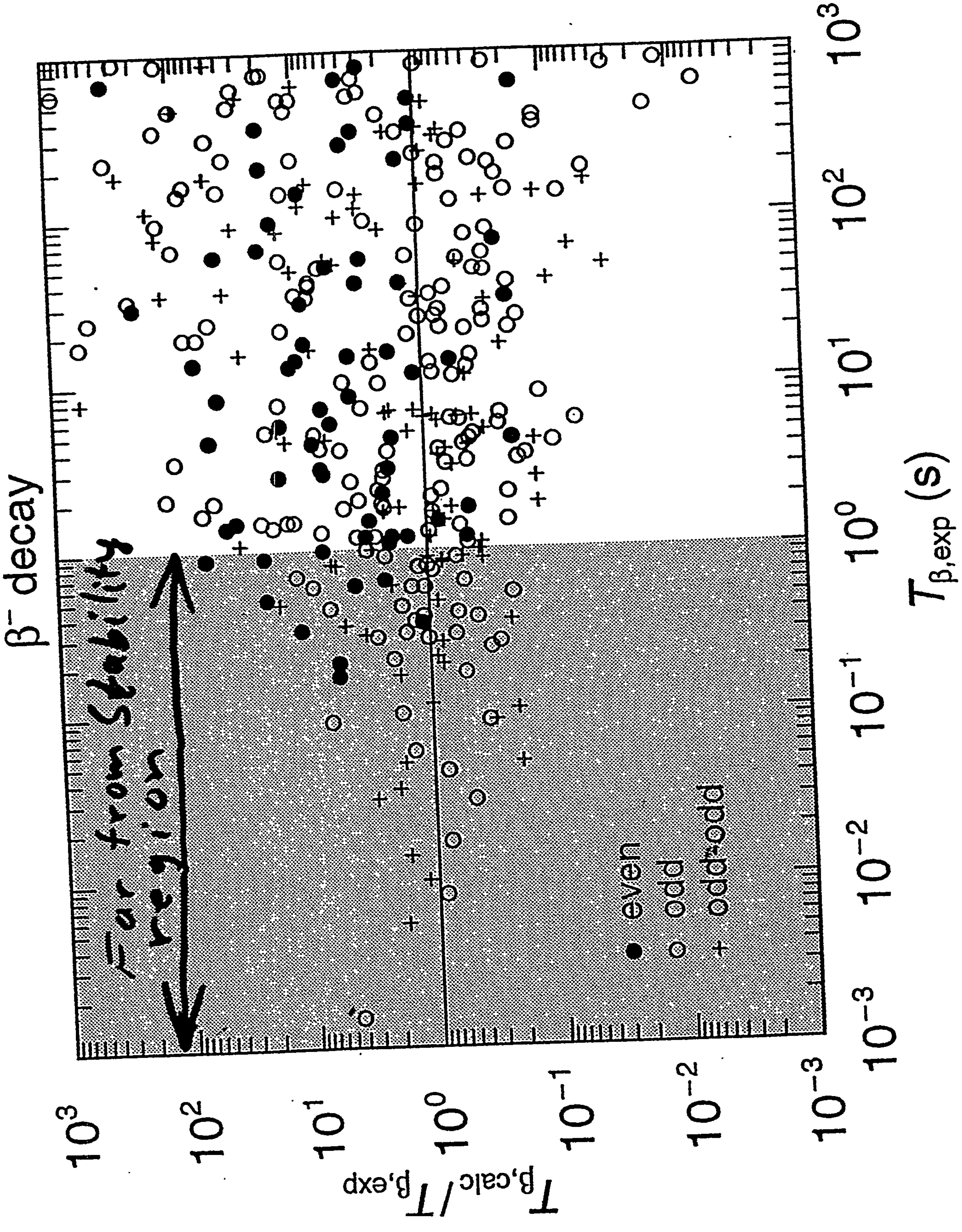
β⁻ decay
Far from Stability region
$T_{\beta,\mathrm{calc}}/T_{\beta,\mathrm{exp}}$
10^3
10^2
10^1
10^0
10^{-1}
10^{-2}
10^{-3}
$T_{\beta,\mathrm{exp}}$ (s)
10^{-3}
10^{-2}
10^{-1}
10^0
10^1
10^2
10^3
● even
○ odd
+ odd-odd

Figure 22

TABLE 4

Analysis of the discrepancy between calculated and measured deformed β^--decay half-lives.

	n	M_{r_l}	$M_{r_l}^{10}$	σ_{r_l}	$\sigma_{r_l}^{10}$	$t_{\mathrm{exp}}^{\mathrm{max}}$ (s)
o-o	29	0.10	1.27	0.46	2.87	1
o-e	35	0.09	1.23	0.41	2.59	1
e-e	11	0.94	8.70	0.54	3.43	1
o-o	58	0.11	1.28	0.63	4.26	10
o-e	85	0.20	1.59	0.69	4.87	10
e-e	35	0.75	5.63	0.66	4.57	10
o-o	79	0.18	1.50	0.77	5.88	100
o-e	130	0.26	1.82	0.82	6.55	100
e-e	54	0.74	5.51	0.69	4.92	100

Ener	Beta Strength	IP	IN	SIG	OMP	OMN	DV	Int. (%)	log(ft)
0.00	0.2269178E-02	22	25	2	7/2+	9/2+	2	0.6881	6.2602
0.15	0.5407312E-02	22	23	1	7/2+	7/2+	2	1.4688	5.8831
0.16	0.5596421E-03	22	21	2	7/2+	5/2+	2	0.1500	6.8681
0.17	0.5889094E-03	21	23	2	5/2+	7/2+	2	0.1573	6.8460
0.18	0.1063045E-01	21	22	2	5/2+	3/2+	2	2.8182	5.5895
0.20	0.4127658E-02	21	21	1	5/2+	5/2+	2	1.0778	6.0004
0.23	0.3279001E-02	22	28	2	7/2+	5/2+	2	0.8317	6.1003
0.26	0.1705452E-02	21	28	1	5/2+	5/2+	2	0.4226	6.3842
0.96	0.1103525E-02	29	28	1	5/2+	5/2+	2	0.1540	6.5733
1.04	0.9086635E-03	22	30	2	7/2+	5/2+	2	0.1174	6.6577
1.10	0.4314473E-03	21	29	2	5/2+	3/2+	2	0.0528	6.9811
1.15	0.1169358E-02	26	27	2	3/2+	1/2+	2	0.1368	6.5481
1.16	0.7843665E-02	21	30	1	5/2+	5/2+	2	0.9153	5.7215
1.16	0.1546999E-01	26	26	1	3/2+	3/2+	2	1.7972	5.4266
1.19	0.6622375E-02	27	26	2	1/2+	3/2+	2	0.7480	5.7950
1.21	0.8096625E-03	27	27	2	1/2+	1/2+	2	0.0902	6.7078
1.21	0.6674730E-03	24	24	2	1/2+	1/2+	2	0.0740	6.7916
1.22	0.2101538E-02	28	26	2	5/2+	3/2+	2	0.2317	6.2935
1.26	0.3317328E-02	24	22	2	1/2+	3/2+	2	0.3509	6.0953
1.27	0.3760729E-02	23	24	2	3/2+	1/2+	2	0.3971	6.0408
1.28	0.8104613E-02	28	23	2	5/2+	7/2+	2	0.8416	5.7073
1.34	0.5236775E-02	22	32	1	7/2+	7/2+	2	0.5137	5.8970
1.43	0.3602986E+00	23	21	2	3/2+	5/2+	2	32.4981	4.0594
1.45	0.1181799E+00	28	21	1	5/2+	5/2+	2	10.4804	4.5435
2.12	0.1341998E-02	32	30	2	7/2+	5/2+	2	0.0602	6.4883
2.14	0.7119387E-03	24	29	2	1/2+	3/2+	2	0.0312	6.7636
2.17	0.7732958E-03	28	29	2	5/2+	3/2+	2	0.0326	6.7277
2.20	0.6653872E-03	24	31	2	1/2+	1/2+	2	0.0272	6.7930
2.62	0.3542069E-02	24	31	1	1/2+	1/2+	2	0.0889	6.0668
2.64	0.7646189E-02	33	26	2	1/2+	3/2+	2	0.1880	5.7326
2.94	0.3474520E-02	33	27	1	1/2+	1/2+	2	0.0582	6.0752
2.94	0.3342398E-02	40	26	2	1/2+	3/2+	2	0.0559	6.0920
3.01	0.2722210E-02	40	27	2	1/2+	1/2+	2	0.0415	6.1811
3.07	0.9626113E-03	20	20	2	1/2-	1/2-	2	0.0135	6.6326
3.34	0.1518484E-01	20	20	1	1/2-	1/2-	2	0.1475	5.4346
3.40	0.2246724E-02	41	27	2	3/2+	1/2+	2	0.0201	6.2645
3.42	0.5216458E-01	41	28	2	3/2+	5/2+	2	0.4550	4.8987
3.46	0.2717932E-01	41	26	1	3/2+	3/2+	2	0.2235	5.1818
3.46	0.1808200E-01	26	33	2	3/2+	1/2+	2	0.1484	5.3588
3.74	0.1987367E+01	27	33	1	1/2+	1/2+	2	10.7678	3.3178
3.74	0.4106316E+01	27	33	2	1/2+	1/2+	2	22.1748	3.0026
3.96	0.5368497E-03	41	30	2	3/2+	5/2+	2	0.0021	6.8862
4.10	0.9467234E-01	26	39	2	3/2+	1/2+	2	0.2939	4.6398

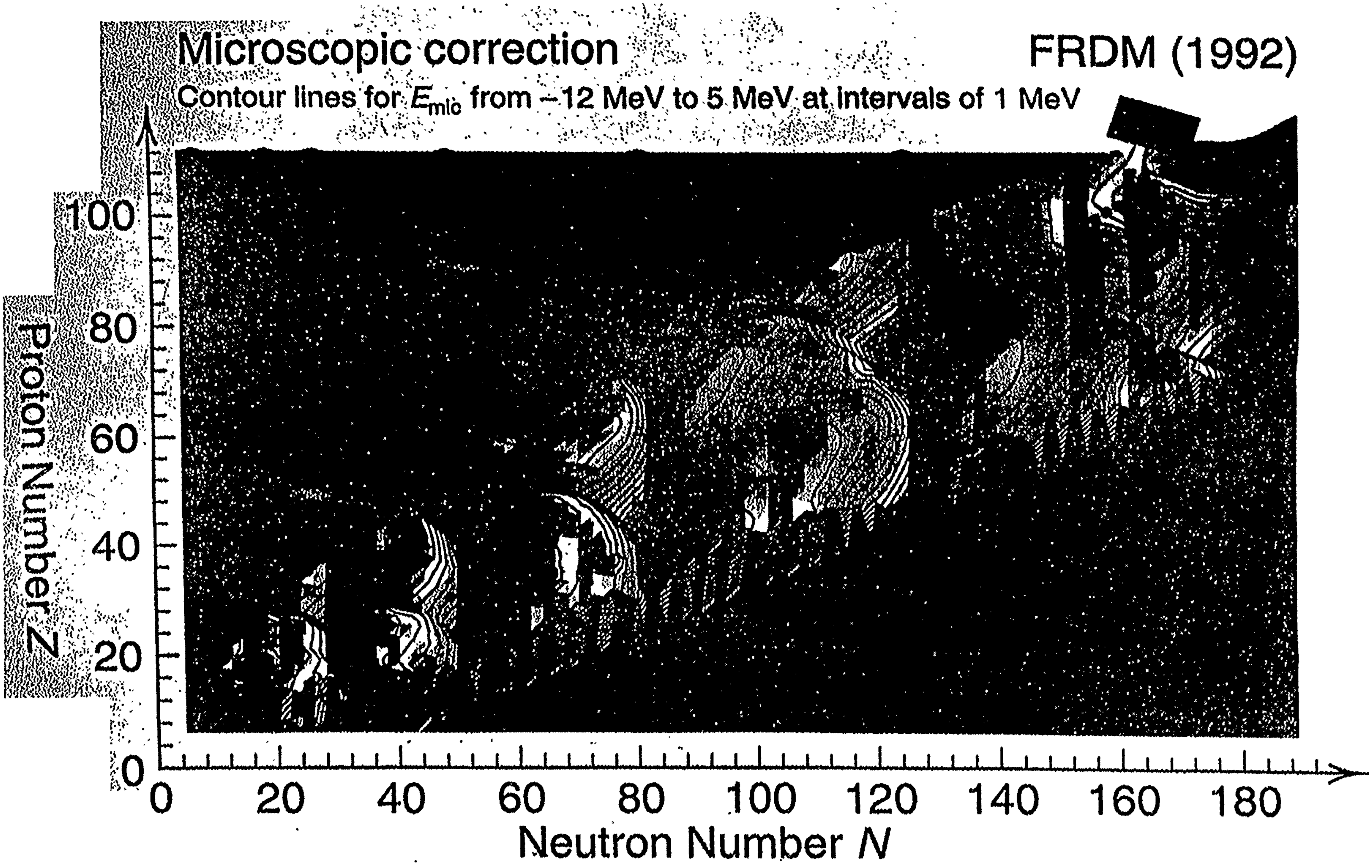
Microscopic correction
Contour lines for $E_{\rm mic}$ from −12 MeV to 5 MeV at intervals of 1 MeV
FRDM (1992)
Proton Number Z
0
20
40
60
80
100
Neutron Number N
0
20
40
60
80
100
120
140
160
180

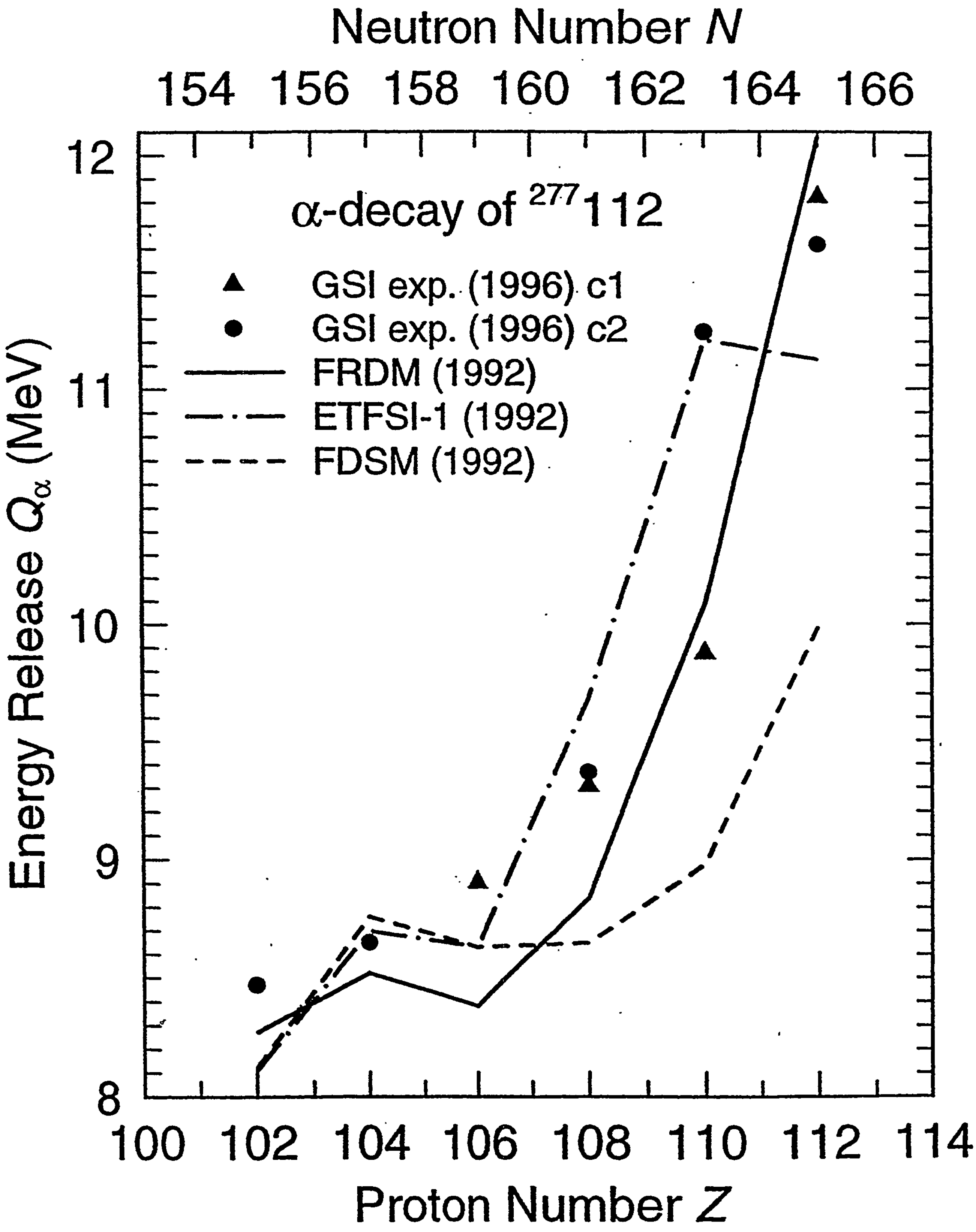
Neutron Number N
154
156
158
160
162
164
166
12
11
10
9
8
α-decay of $^{277}112$
▲ GSI exp. (1996) c1
● GSI exp. (1996) c2
FRDM (1992)
ETFSI-1 (1992)
FDSM (1992)
Energy Release Q_α (MeV)
100
102
104
106
108
110
112
114
Proton Number Z

Figure 34

Calculated ground-state spin compared to experiment

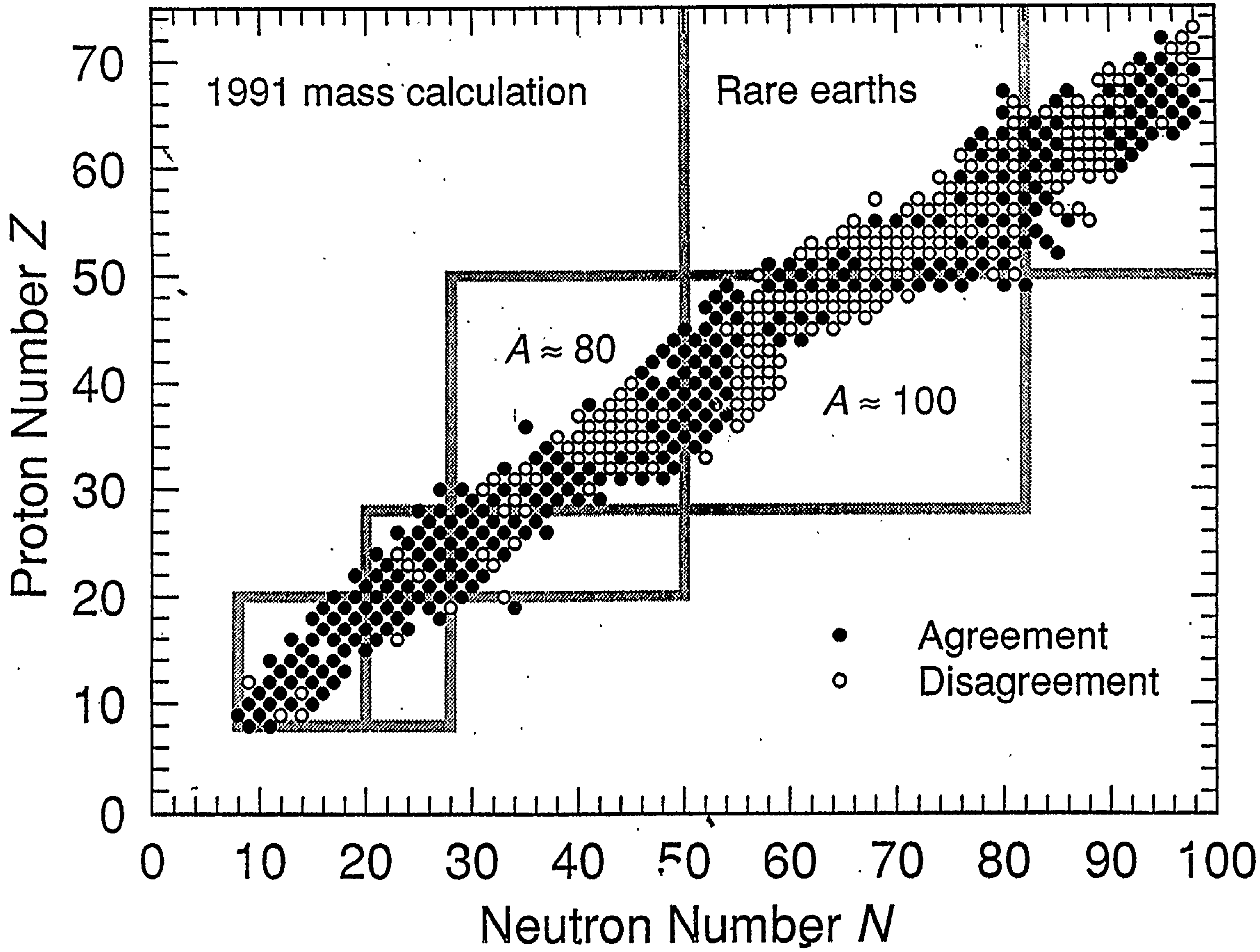

Calculated ground-state spin compared to experimen

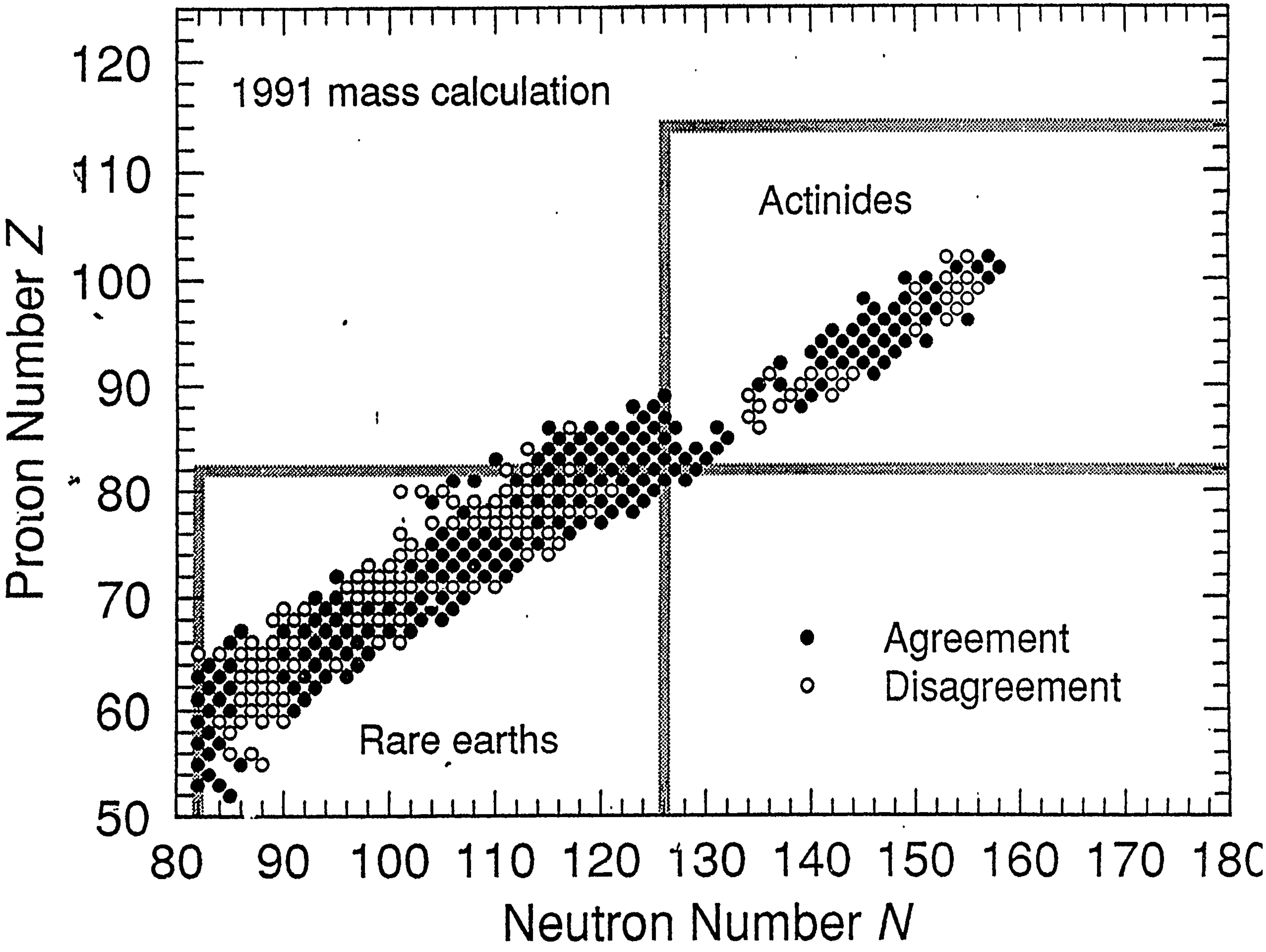

SPIN–PARITY

	Agreement	Disagreement	% Agreement
No ϵ_3, ϵ_6	428	285	60.0
With ϵ_3, ϵ_6	446	267	62.5

SUMMARY

MANY NUCLEAR-STRUCTURE PROPERTIES NOW UNDERSTOOD IN TERMS OF GLOBAL, UNIFIED MODEL

REMAINING DEVIATIONS GIVE IMPORTANT CLUES TO UNDERLYING PHYSICS

LARGE-SCALE COMPUTING EFFORTS ARE REQUIRED IN SOME AREAS FOR FURTHER PROGRESS

Approximating the r-process on Earth with Thermonuclear Explosions

Stephen A. Becker
Los Alamos National Laboratory

Abstract

The astrophysical r-process can be approximately simulated in certain types of thermonuclear explosions. Between 1952 and 1969 23 nuclear tests were fielded by the United States which had as one of their objectives the production of heavy transuranic elements. Of these tests 15 were at least partially successful. Some of these shots were conducted under project Plowshare Peaceful Nuclear Explosion Program as scientific research experiments. A review of the program, target nuclei used, and heavy element yields achieved will be presented as well as a discussion where the program might have gone if it was allowed to continue.

92-1783

TITLE: "APPROXIMATING THE r-PROCESS ON EARTH WITH THERMONUCLEAR EXPLOSIONS"

AUTHOR(S): Stephen A. Becker
University of California
Los Alamos National Laboratory
P. O. Box 1663
Los Alamos, NM 87544

SUBMITTED TO: Origin & Evolution of the Elements
Paris, FRANCE

Los Alamos
Los Alamos National Laboratory
Los Alamos, New Mexico 87545

APPROXIMATING THE r–PROCESS ON EARTH WITH THERMONUCLEAR EXPLOSIONS

S. A. BECKER
Los Alamos National Laboratory

☒ UNCLASSIFIED
☐ CONFIDENTIAL
☐ SECRET ☐ RD
☐ FRD
☐ NSI
5-29-9
Date
EmL
OS-6

ABSTRACT

The astrophysical r–process can be approximately simulated in certain types of thermonuclear explosions. Between 1952 and 1969 twenty–three nuclear tests were fielded by the United States which had as one of their objectives the production of heavy transuranic elements. Of these tests, fifteen were at least partially successful. Some of these shots were conducted under the project Plowshare Peaceful Nuclear Explosion Program as scientific research experiments. A review of the program, target nuclei used, and heavy element yields achieved, will be presented as well as discussion of plans for a new experiment in a future nuclear test.

1 OVERVIEW

Nuclear explosions have been used in a number of scientific investigations and applications.[1] One such study was the Heavy Element Program which had as its objectives the production of heavy transuranic elements and the investigation of nuclear properties of very neutron–rich isotopes.[2,3] For such an experiment an intense flux of neutrons is produced primarily by the D(T,n)^{4}He reaction. These neutrons which begin with a 14.1 Mev energy are thermalized and are then used to induce multiple captures in a target such as ^{238}U. The intense flux of thermal neutrons is only present for ten to twenty nanoseconds which means that the target nuclei undergo multiple neutron captures at constant Z because there is no time for beta decay. The rapid multiple captures of neutrons by a target in a thermonuclear explosion has been given the name "prompt capture."[4] Once the "prompt capture" process is over, the neutron–rich nuclei transform into longer lived nuclei primarily through a series of beta decays back to the line of beta stability. The term "decay back" is used to refer to the series of beta decays to the line of beta stability experienced by a neutron–rich nucleus.[5]

Table 1 compares the environments for four different neutron capture processes. For neutron capture in the High Flux Isotopic Reactor (HFIR) at the Oak Ridge National Laboratory and during the s–process, the time scale for beta decay is much less than the time scale for successive neutron captures which results in production of nuclei close to the line of beta stability. In contrast, both the r–process and the "prompt capture" process undergo neutron capture so rapidly that multiple captures can occur before the onset of beta decay, thus producing nuclei far from the line of beta stability. The r–process differs from the "prompt capture" process in that it takes place on a longer time scale and at hotter temperatures. The net effect of these differences is that the neutron capture cross sections are smaller for the r–process than for the "prompt capture" process and the longer time scale allows some beta decays to occur during the r–process at the same time that neutrons captures are occurring. The similarities between the r–process and "prompt capture" process are, however, such that the data from a number of nuclear tests have been used to calibrate the nuclear physics used in r–process nucleosynthesis codes.[6]

TABLE 1

NEUTRON EXPOSURE ENVIRONMENTS

Type of Exposure	Flux $(n\bar{v})$	Duration (δt)	Fluence $(n\bar{v}\delta t)$	Temperature
HFIR	$5 \times 10^{15}/\mathrm{cm}^2\text{–s}$	≈ 0.5yr	$\approx 10^{23}/\mathrm{cm}^2$	2.5×10^{-5} keV
s–process	$\approx 10^{16}/\mathrm{cm}^2\text{–s}$	$\approx 10^3$yr	$\approx 10^{26}/\mathrm{cm}^2$	10 to 30 keV
r–process	$> 10^{27}/\mathrm{cm}^2\text{–s}$	1 to 100 s	$> 10^{27}/\mathrm{cm}^2$	$\approx$ 100 keV
"prompt capture"	$> 10^{32}/\mathrm{cm}^2\text{–s}$	$< 10^{-7}$s	$\approx 10^{25}/\mathrm{cm}^2$	10 to 20keV

2 Historical Review

The fact the heavy transuranic isotopes could be produced in a thermonuclear device was discovered serendipitously through the analysis of the Mike test (fired 31/10/52) debris. All told 15 new isotopes[4] and 2 new elements[7], einsteinium and fermium, were discovered. A maximum of 17 neutron captures happened on some of the ^{238}U target nuclei which became ^{255}U and later underwent 8 beta decays to become ^{255}Fm. The estimated thermal neutron flux on the target was 2 to 3 moles of neutrons/cm^2. The discoveries from the Mike test lead to the development of the Heavy Element Program as a result of which 23 nuclear tests were conducted which had as one of their objectives the production of heavy transuranic elements. Of these tests 15 were at least partially successful, but only the milestone events will be discussed here. Some of these shots were performed under the project Plowshare Peaceful Nuclear Explosion Program. The results of the Mike test were later approximately duplicated at a much lower device yield in the Anacostia test (fired 27/11/62).[2,8] New discoveries were made with the Par (fired 9/10/64) and Barbel (16/10/64) tests which achieved an estimated thermal neutron flux of 11 moles of neutrons/cm^2. The very neutron–rich isotope ^{250}Cm was discovered and 19 neutron captures were achieved by some target ^{238}U nuclei to produce ^{257}Fm.[2,9] Higher thermal neutron fluxes of approximately 18 moles of neutrons/cm^2 and 35 moles of neutrons/cm^2 were respectively achieved in the Cyclamen[10] (fired 5/5/66) and Hutch (fired 16/7/69) tests.[11] These higher neutron fluxes produced a greater yield of heavy transuranic isotopes, but disappointingly no new isotopes or elements were discovered. Figure 1 illustrates the heavy element production as a function of atomic number for the Cyclamen and Hutch devices.[11] The inability to produce new isotopes heavier than ^{257}Fm eventually lead to a loss of interest in the Heavy Element Program.

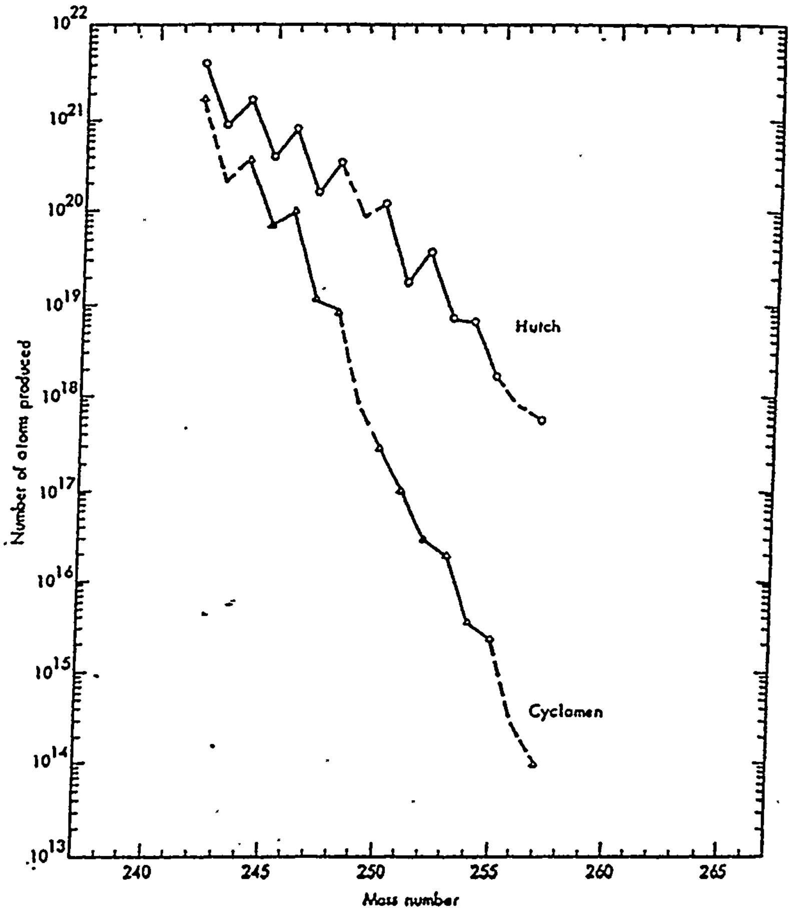

Fig. 1. Heavy element yields from the Hutch and Cyclamen experiments.

In the end, the Heavy Element Program was responsible for the discovery of 2 new elements and 16 new transuranic isotopes. The "prompt capture" process proved to be an efficient method of production for very neutron–rich isotopes like ^{250}Cm, ^{251}Cf, ^{254}Cf, ^{255}Es, and ^{257}Fm. Detailed studies were done to learn the nuclear properties of isotopes recovered from these tests. Sufficient quantities of ^{250}Cm and ^{257}Fm were extracted to use them as targets in accelerators to produce even heavier isotopes.

Besides ^{238}U, which produced the best results, target nuclei of ^{232}Th, ^{237}Np, ^{240}Pu, ^{242}Pu, and ^{243}Am were also fielded. Of these, positive results were obtained from ^{232}Th and ^{242}Pu where up to 13 neutron captures were observed. The other targets were destroyed by fission induced from the high energy neutrons.

Work in the Heavy Element Program came to an end with a number of questions remaining unanswered. One such question is, for example: "Is the saw tooth abundance pattern shown in Figure 1 produced as a result of secondary capture chain on an odd Z nucleus resulting from the (n,p) reaction on the target nuclei, or is it the result of beta–delayed fission during the "decay back" to the line of beta stability?"[12]

3 Future Prospects

At present the only experimental test of theoretical predictions of beta–delayed fission and fission barrier heights for neutron–rich unstable nuclei come from the analysis of the products produced in heavy element nuclear tests.[12] As discussed in reference six, the data from nuclear tests for the uranium capture chain has been used to modify the input physics based on theoretical calculations for one r–process nucleosynthesis code. For example, nuclear test data have shown that some calculated theoretical fission barriers are too low for neutron–rich nuclei.

It now appears likely in an upcoming nuclear test that a heavy element experiment will be conducted using a ^{232}Th target. While ^{232}Th was fielded in the Hutch test, its performance was somewhat clouded by the presence of the more abundant ^{238}U target. In the upcoming nuclear test, ^{232}Th will be the only target which should provide a clear picture of the thorium capture chain and give additional experiment calibration for r–process nucleosynthesis codes. With a thorium target it may be possible to achieve more than 19 neutron captures. If this experiment is successful, an odd Z target like ^{231}Pa might be fielded in another future event.

REFERENCE

1. Dorn, B. C. (1970) Ann. Rev. Nuc. Sci. 20, 79–103.
2. Ingley, J. S. (1969) Nuc. Phys. A124, 130–144.
3. Eberle, S. H. (1972) Kerntechnik 14, 65–71.
4. Cowen, G. A. (1967) Los Alamos Scientific Laboratory Report LA–3738.
5. Wene, C. O. and Johansson (1974) Phys. Scr. 10A, 157–162.
6. Cowan, J. J. Thielemann, J. K., and Truran, J. W. (1991) Physics Reports 208, 267–394.
7. Ghiorso, A. et al (1955) Phys. Rev. 99, 1048–1049.
8. Hoff, R. W. and Dorn, D. W. (1964) Nuc. Sci. Eng. 18, 110–112.
9. Bell, G. I. (1965) Phys. Rev. 139, B1207–B1216.
10. Hoffmann, D. C. (1967) Arkiv For Fysik 36, 533–537.
11. Hoff, R. W. and Hulet, E. K. (1970) in Engineering With Nuclear Explosives, Lawrence Radiation Laboratory Report CONF 700101 p1283–1294.
12. Hoff, R. W. (1988) J. Phys. G. 14, S343–S356.

APPROXIMATING THE r-PROCESS ON EARTH WITH THERMONUCLEAR EXPLOSIONS

Stephen Allan Becker

Thermonuclear Applications, X-2
Applied Theoretical Physics Division
Los Alamos National Laboratory

THE PROMPT CAPTURE PROCESS

1) Neutron Production
   - $D + T \rightarrow {}^4He + n$ (14.1 MeV)
   - $D + D \rightarrow {}^3He + n$ (2.5 MeV)
   - ${}^9Be\ (n,2n)\ 2\ {}^4He$
   - Fission neutrons from target

2) Prompt Capture
   - ${}^{238}U(n, \gamma)\ {}^{239}U(n, \gamma)\ {}^{240}U(n, \gamma) \ldots\ldots {}^{257}U(n,\gamma) \ldots$
   - (n,f) and (γ,n) reactions compete with the above chain

3) Decay Back
   - ${}^{257}U\ (\beta^- \bar{\nu})\ {}^{257}Np(\beta^- \bar{\nu})\ {}^{257}Pu(\beta^- \bar{\nu})\ {}^{257}Am \ldots\ {}^{257}Fm$
   - Competing processes: β-delayed fission, spontaneous fission, β-delayed neutron emission

4) Secondary Reactions
   - ${}^{238}U(n,p)\ {}^{238}Pa$ for odd Z capture chain
   - Parasite neutron absorbers like ${}^3He(n,p)T$

COMPARATIVE NEUTRON EXPOSURE ENVIRONMENTS

TYPE OF EXPOSURE	FLUX ($n\bar{v}$)	DURATION (Δt)	FLUENCE ($n\bar{v}\Delta t$)	TEMPERATURE
HFIR	$5 \times 10^{15}/cm^2 - s$	~ 0.5 yr.	$\sim 10^{23}/cm^2$	2.5×10^{-5} keV
s-Process	$\sim 10^{16}/cm^2 - s$	$\sim 10^3$ yr.	$\sim 10^{26}/cm^2$	10 to 30 keV
r-Process	$> 10^{27}/cm^2 - s$	1 to 100 s	$> 10^{27}/cm^2$	~ 100 keV
Prompt Capture	$> 10^{32}/cm^2 - s$	$< 10^{-7}$s	$\sim 10^{25}/cm^2$	10 to 20 keV

The r-process and the prompt capture process are similar in behavior

TARGET NUCLEI (IDEAL $\sigma_c > \sigma_f$)

^{238}U: Best results so far, 19 confirmed neutron captures

^{232}Th: 13 confirmed neutron captures

^{242}Pu: 13 confirmed neutron cpatures

^{237}Np, ^{240}Pu, ^{243}Am: Virtually consumed by fission

Suggested Targets: ^{226}Ra, ^{231}Pa, ^{250}Cm, ^{252}Cf

HEAVY ELEMENT PROGRAM

- Objective was the production of heavy transuranic elements and the investigation of very neutron-rich isotopes.
- Many tests done as part of project Plowshare, the peaceful nuclear explosion program
- Twenty-three tests related to heavy element program were fired; fifteen were successful to some degree
- U.S. appears to be the only nuclear power to pursue this line of research

HIGHLIGHTS OF THE HEAVY ELEMENT PROGRAM

EVENT	DATE	TARGET	FLUENCE (moles/cm^2)	NOTES
Mike	10/31/52	^{238}U	2 to 3	1) Es, Fm, and 15 new isotopes discovered 2) Up to 17 neutron captures
Anacostia	10/27/62	^{238}U	2.5 to 4	Relative heavy element yield similar to Mike, but requiring much less explosive yield
Kennebec	6/25/63	^{238}U	4.6 to 6	Not as successful as Anacostia
Anchovy	11/14/63	^{238}U	2 to 3	Not as successful as Anacostia
Par	10/9/64	^{238}U	11	1) First test to outperform Mike results 2) ^{250}Cm discovered; up to 19 neutron captures

HIGHLIGHTS OF THE HEAVY ELEMENT PROGRAM (cont.)

EVENT	DATE	TARGET	FLUENCE (moles/cm^2)	NOTES
Barbel	10/16/64	^{238}U	11	Results similar to Par
Tweed	5/21/65	^{242}Pu ^{237}Np	12	Results not as good as Par, only up to 13 neutron captures
Cyclamen	5/5/66	^{238}U ^{243}Am	18	Output exceeded Par and Barbel, but no new isotopes; 17% target converted to $A \geq 242$
Kankakee	6/15/66	^{238}U	12	Results similar to Par
Vulcan	6/25/66	^{238}U	12	Repeat of Tweed with different target
Hutch	9/16/69	^{238}U ^{232}Th	35	Output exceeded Cyclamen, but no new isotopes; 19% target converted to $A \geq 242$

NEW PRODUCTS IDENTIFIED IN THE "MIKE" THERMONUCLEAR DEBRIS

Pu: 244, 245*, 246
Am: 246
Cm: 246, 247, 248
Bk: 249
Cf: 249, 252, 253, 254
Es: 253, 255
Fm: 255

* ^{245}Pu was identified in 1954

TARGET ^{238}U

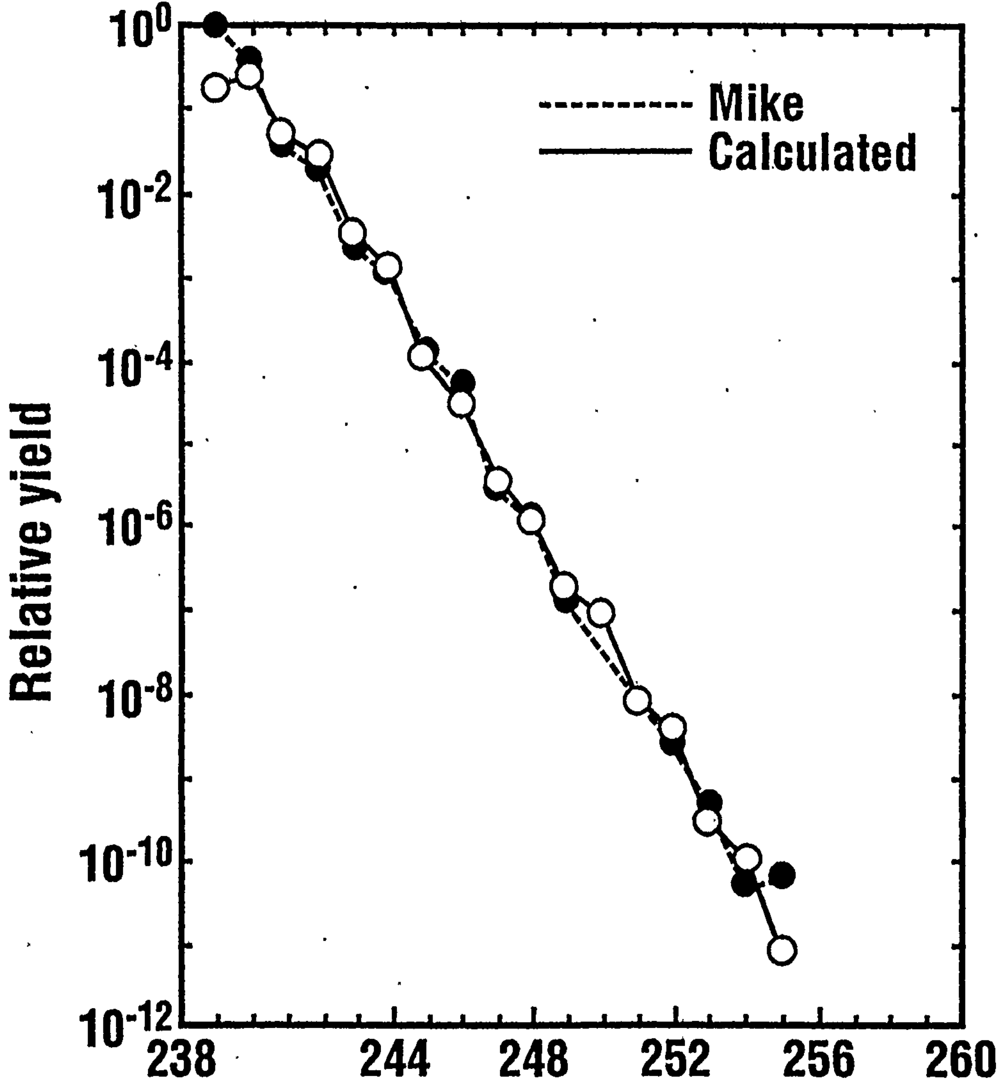
Relative yield
10^0
10^-2
10^-4
10^-6
10^-8
10^-10
10^-12
238
244
248
252
256
260
Mike
Calculated

COMPARISON OF THE ELEMENT YIELDS OF THE ANACOSTIA EXPERIMENT WITH THE MIKE EXPERIMENT

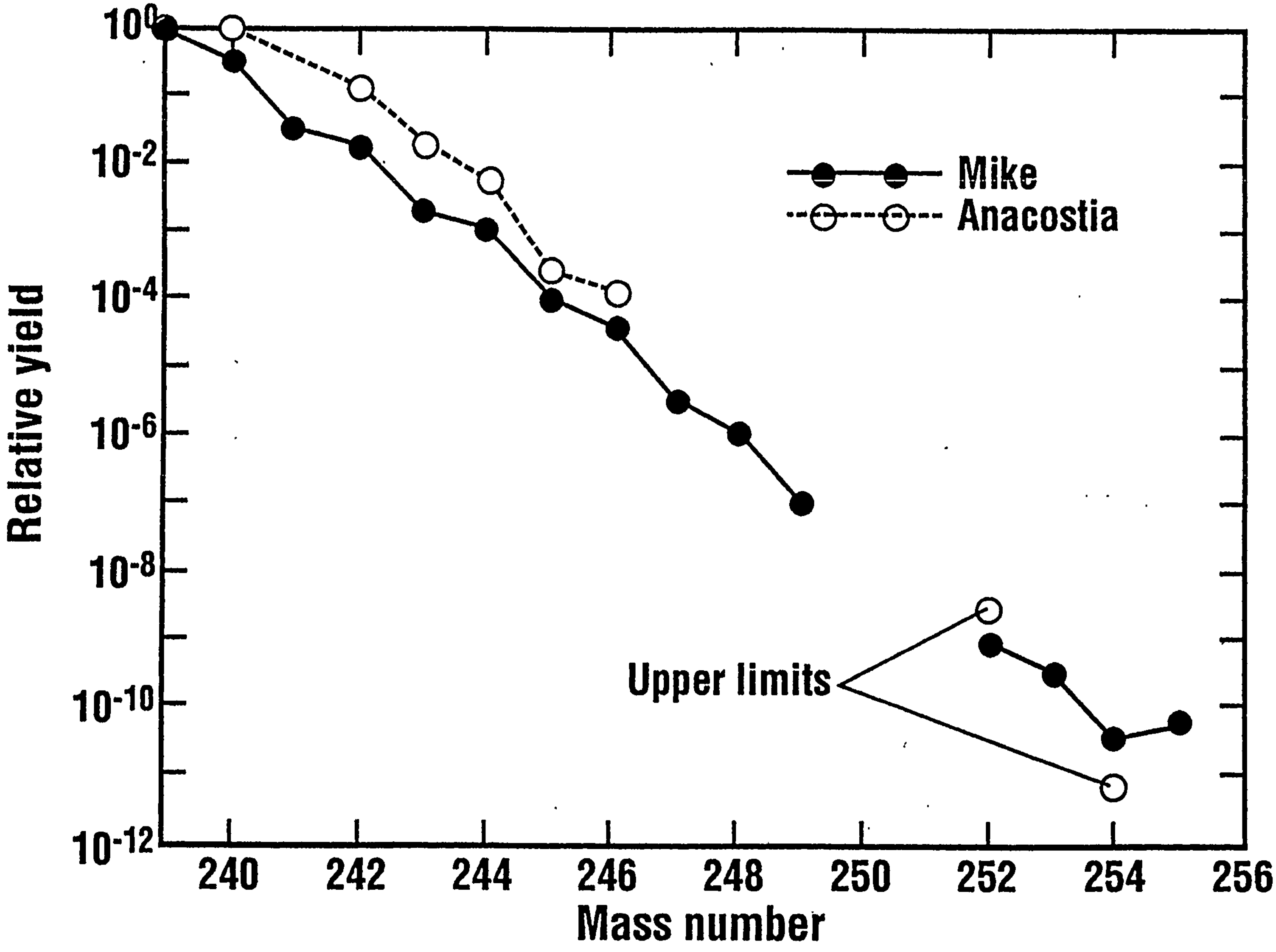

HEAVY NUCLIDE YIELD FOR A = 244-257, PLOTTED RELATIVE TO MASS 244 YIELD FOR THE PAR, BARBEL, AND MIKE EXPLOSIONS

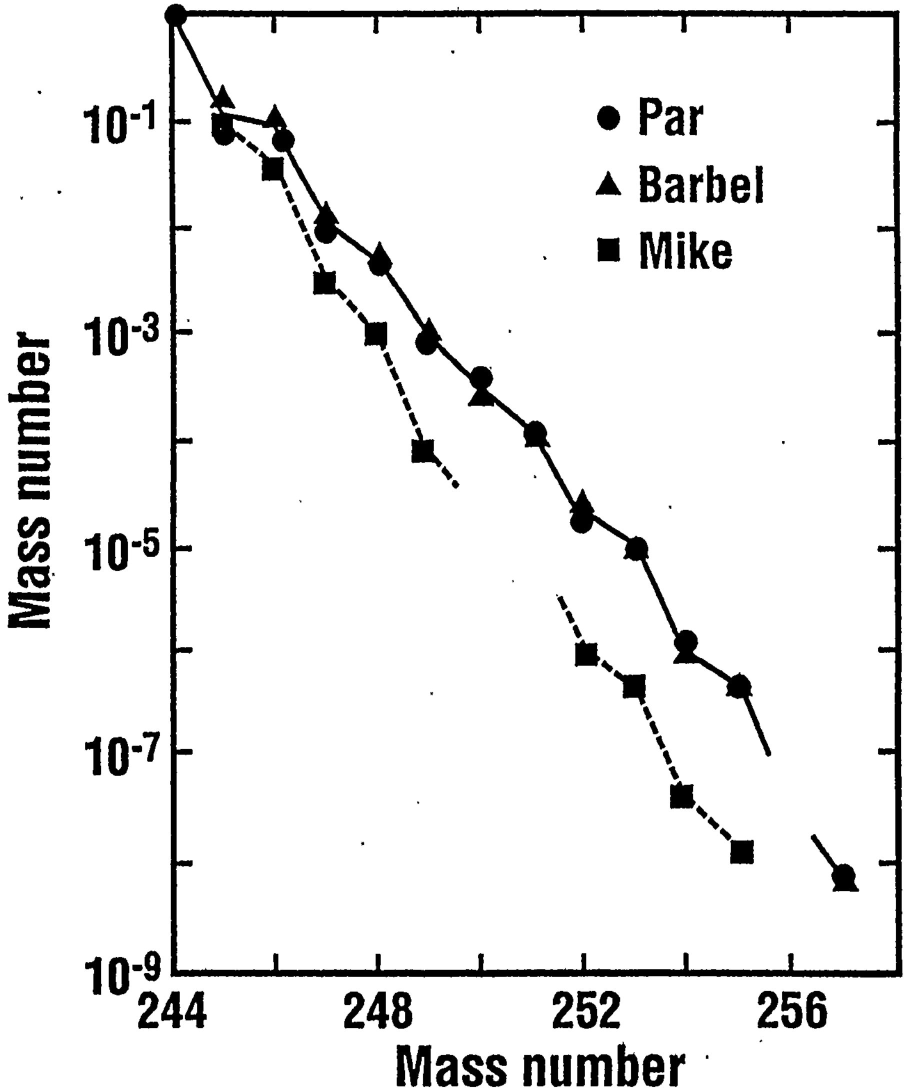

The mass-yield curve from the Barbel and Cyclamen experiments

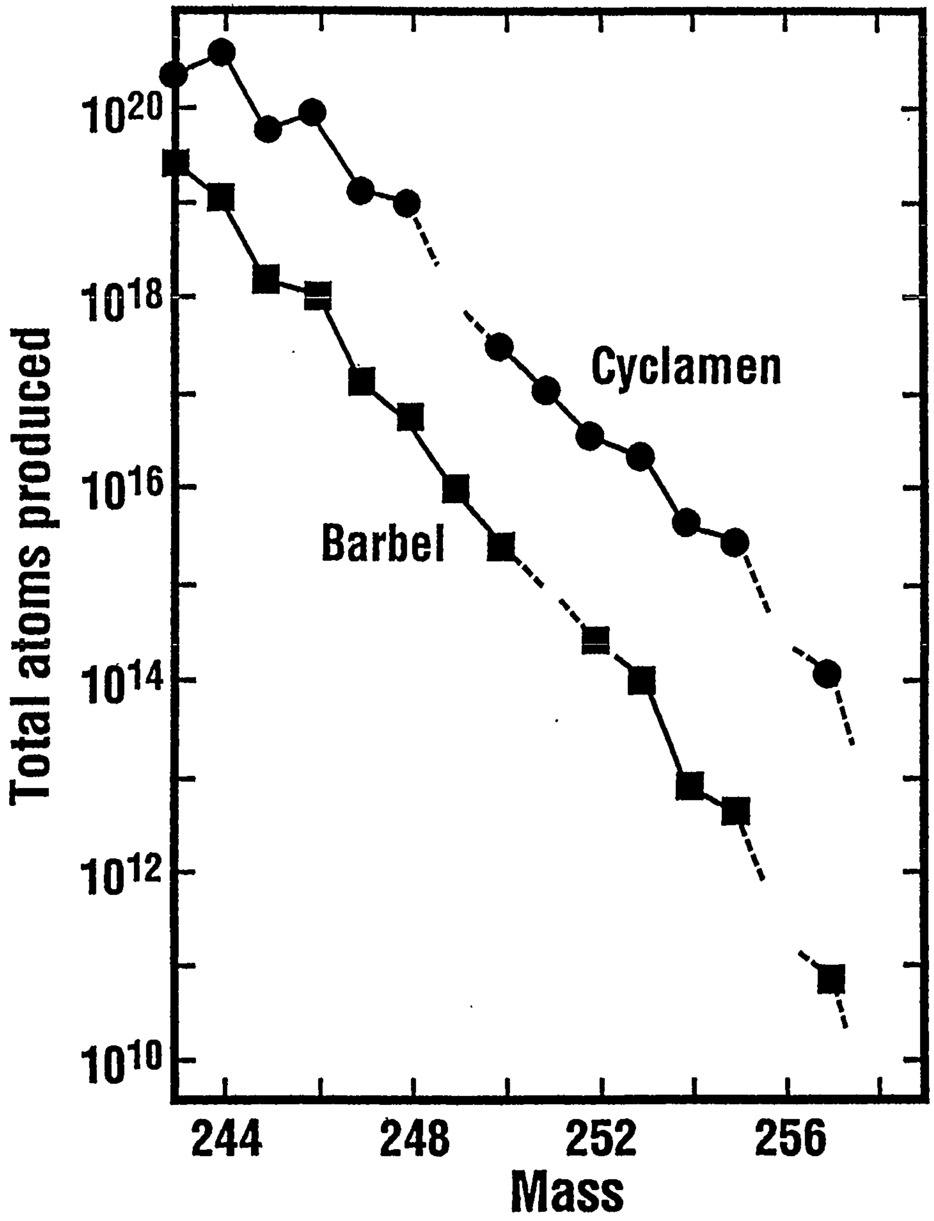

Heavy element yields from the Hutch and Cyclamen experiments

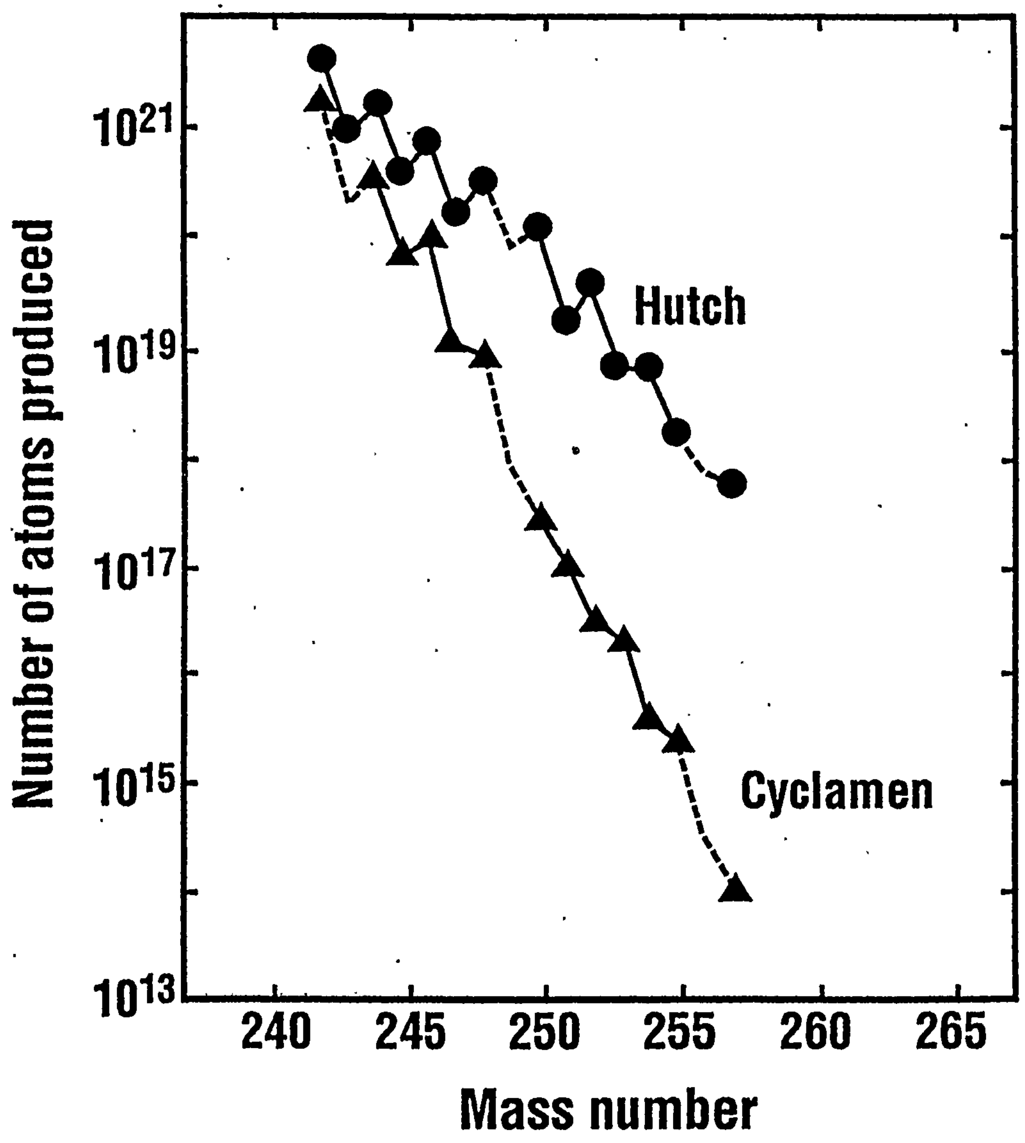

AMOUNTS OF ^{250}Cm AND ^{257}Fm MADE IN VARIOUS EXPERIMENTS AS A FUNCTION OF NEUTRON EXPOSURE

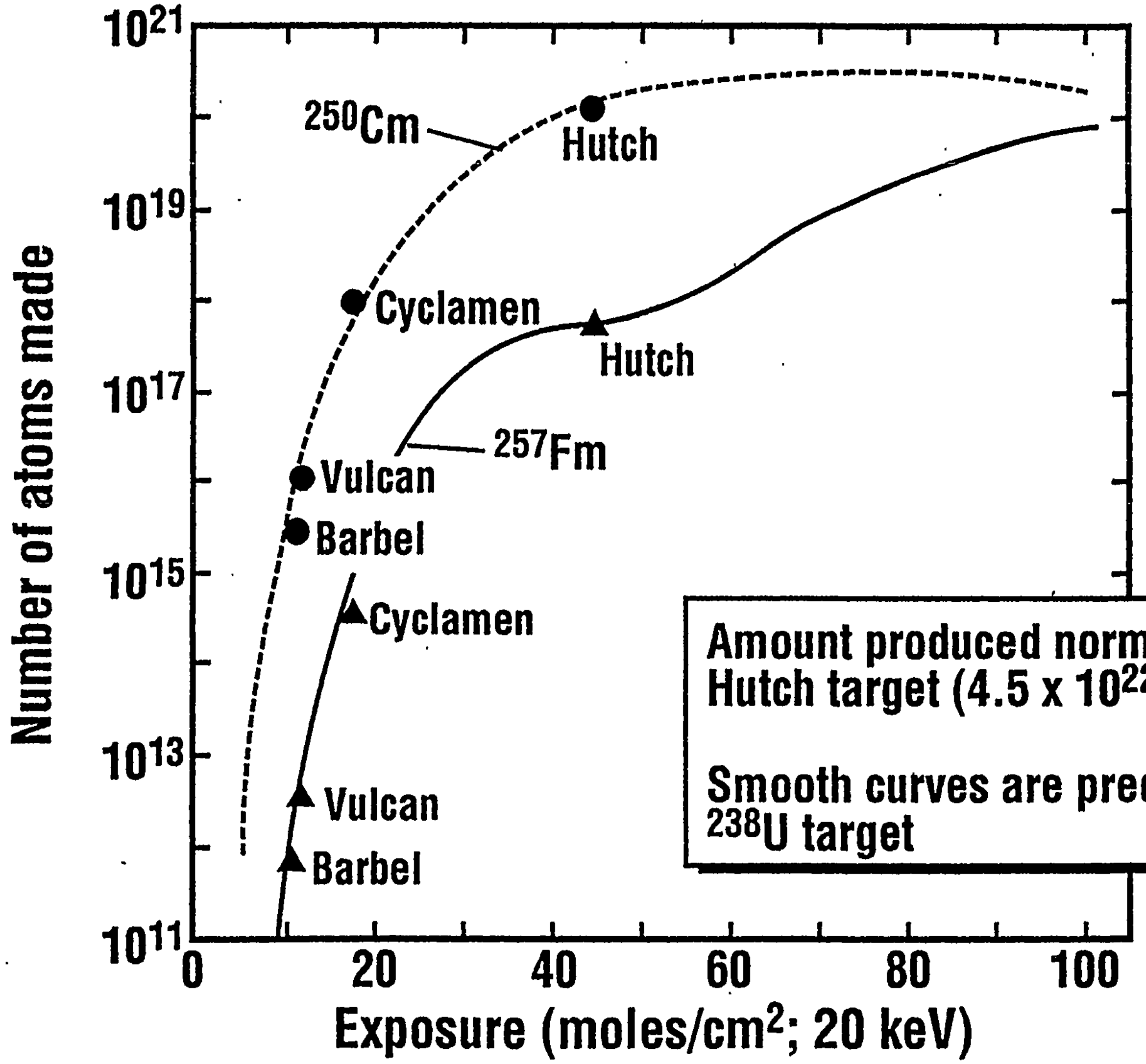

Amount produced normalized to the ^{238}U Hutch target (4.5×10^{22} atoms)

Smooth curves are preditions for a ^{238}U target

THE HUTCH SUBSIDENCE CRATER AT THE DEPARTMENT OF ENERGY'S NEVADA TEST SITE WITH RECOVERY DRILL RIG IN PLACE

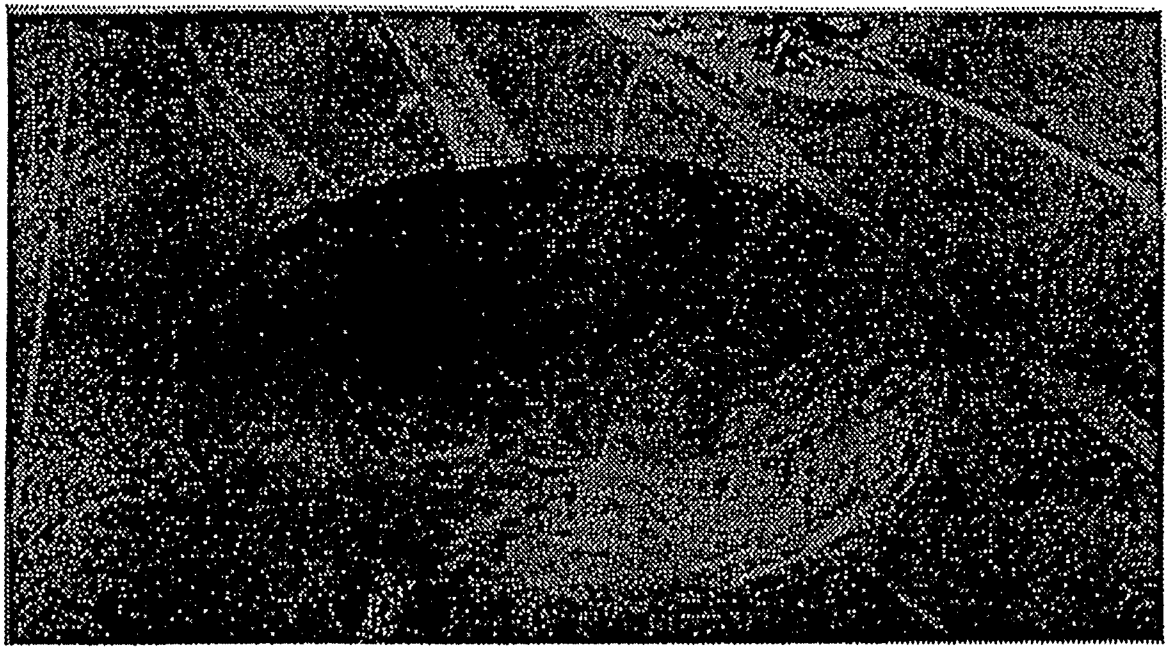

RESULTS OF THE HEAVY ELEMENTS PROGRAM

- Two new elements and sixteen isotopes of transuranic elements discovered
- Efficient method of production for neutron-rich isotopes like ^{250}Cm, ^{251}Cf, ^{254}Cf, ^{255}Es, ^{257}Fm
- Detailed studies performed on nuclear properties of isotopes extracted; some like ^{250}Cm and ^{257}Fm were used as targets in accelerators
- Nuclear properties of short-life isotopes in the prompt capture chain were deduced from relative abundances of the decay back products (neutron capture cross sections, fission to capture ratios, size of the fission barrier,...)

SOME REMAINING UNANSWERED QUESTIONS

- Is the reversal of the odd-even abundance distribution pattern due to a separate capture chain working on Pa (odd-Z hypothesis) or due to the effects of β-delayed fission during decay back?
- Is ^{257}Fm as far as we can go with the prompt capture process?
- Could this be a pathway to the superheavy elements?

THE PROMPT CAPTURE PROCESS CAN PROVIDE INPUT FOR r- PROCESS NUCLEOSYNTHESIS CALCULATIONS

- β-delayed fission and neutron-induced fission become important for nuclei with Z > 80
- Only available experimental test for theoretical predictions of β-delayed fission comes from the analysis of heavy element products from nuclear tests
- Data from thermonuclear explosions indicate that theoretical fission barriers are too low for very neutron-rich nuclei
- Absence of A=256 isotopes argues for the existence of the β-delayed fission effect
- Data from the U capture chain has been used so far

A FUTURE HEAVY ELEMENT EXPERIMENT

- In the near future there should be an opportunity to field a heavy element experiment with a ^{232}Th target.
- Why ^{232}Th?
  - ^{232}Th performance in Hutch clouded by presence of the more abundant ^{238}U target.
  - Th isotopes should be less susceptible to thermal fission.
  - See if more than 13 neutron captures can be achieved. Even if ^{257}Fm is an effective limit, the possibility of 25 neutron captures would exceed the record of 19 captures on ^{238}U achieved in Par, Barbel, Cyclamen, Kankakee, Vulcan, and Hutch.
  - Provide additional experimental calibration for r-process codes with another capture chain.
- If this experiment is successful an odd-Z target like ^{231}Pa might be fielded in a future event.

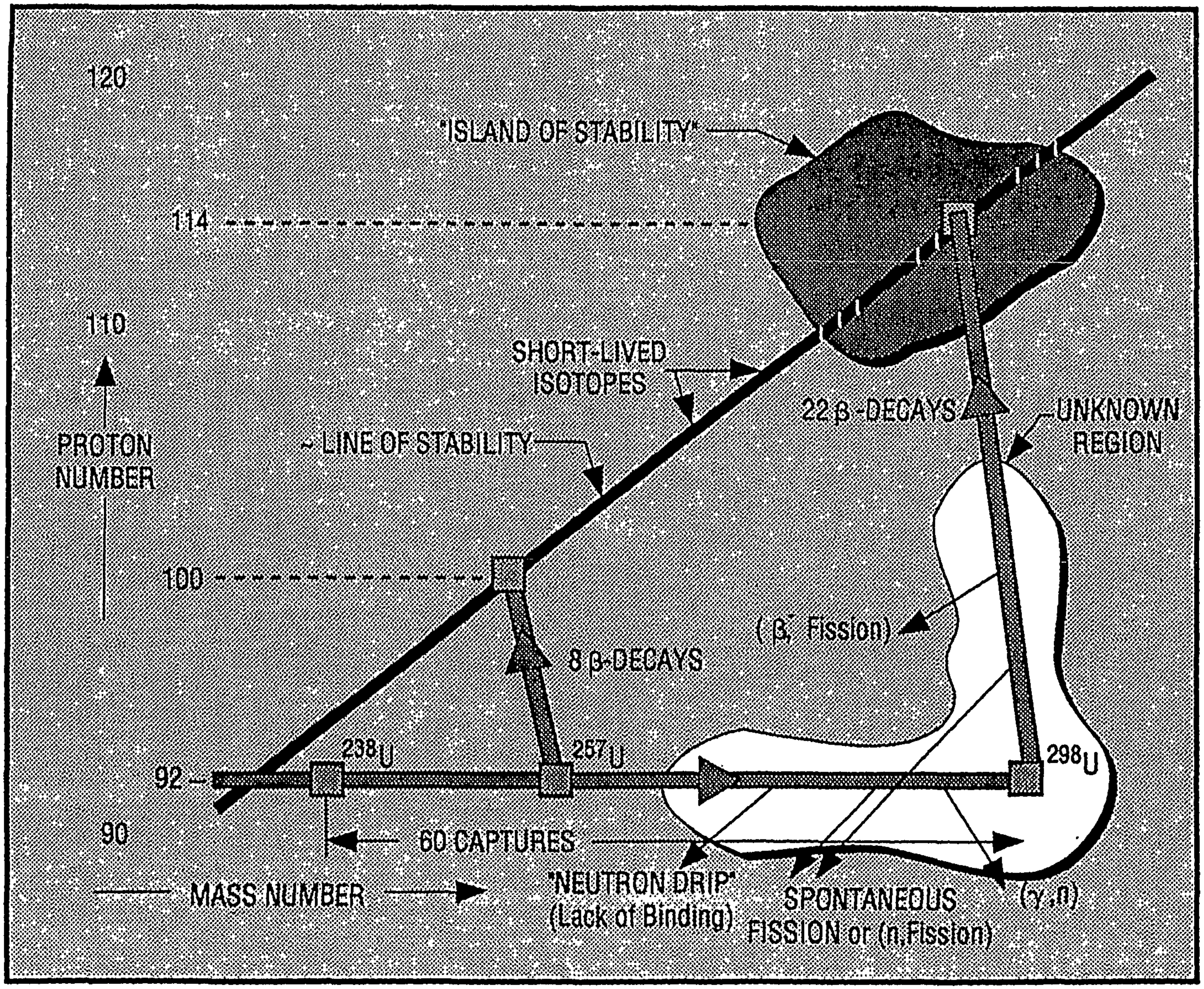
120
"ISLAND OF STABILITY"
114
110
SHORT-LIVED ISOTOPES
PROTON NUMBER
~ LINE OF STABILITY
22 β-DECAYS
UNKNOWN REGION
100
(β⁻ Fission)
8 β-DECAYS
^{238}U
^{257}U
^{298}U
92
90
60 CAPTURES
MASS NUMBER
"NEUTRON DRIP" (Lack of Binding)
SPONTANEOUS FISSION or (n,Fission)
(γ,n)

Uncertainties in the Th cosmochronometry

S. Goriely
Institut d'Astronomie et d'Astrophysique
Universite Libre de Bruxelles, CP 226
Campus de la Plaine - B-1050 Brussels, Belgium

Recent observations of r-nuclei, and in particular of Th, in ultra-metal poor stars revived the old idea that the Th cosmochronometry could provide an age estimate of the oldest stars in the Galaxy, and therefore a lower limit to the age of the Galaxy. Unfortunately, some nuclear, astrophysics and observational uncertainties still affect the theoretical r-process models required to predict the original production of Th. The impact of these uncertainties, in particular of nuclear origin, on the prediction of the age of the Galaxy is analyzed and discussed.

What can we learn from the r-element distribution of CS 22892-052 ?

CS 22892-052 is
- a ultra-metal-poor star [Fe/H] = -3.1
- abundant in r-elements [Eu/Fe] = +1.7
- a C-rich star [C/Fe] = +1 & [O/Fe] < +0.6

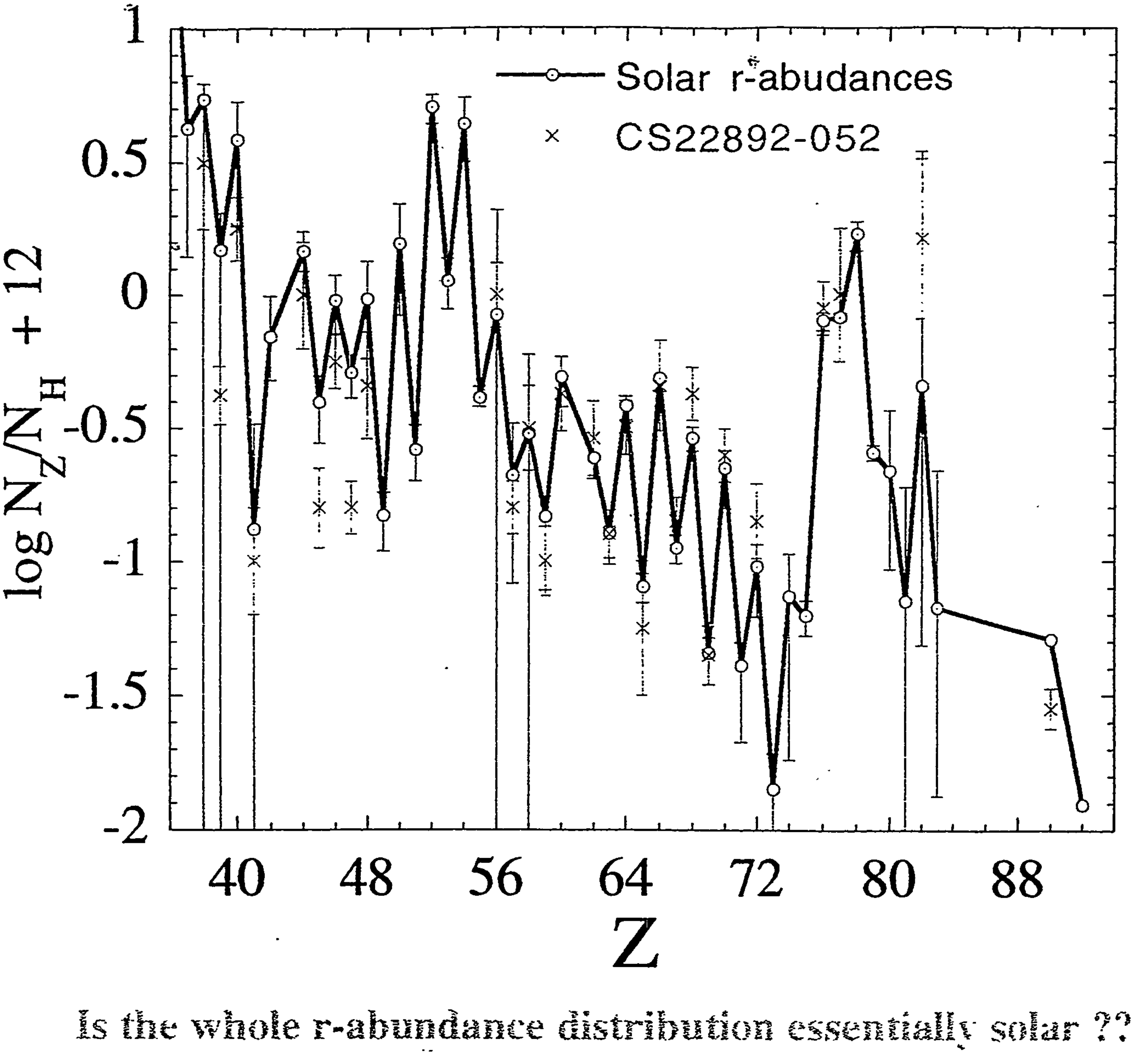

Is the whole r-abundance distribution essentially solar ??

⟹ *SS r-distribution originates from a small number of astrophysical events*
⟹ *r-process yields independent of Mass and Metallicity of the supernova*
⟹ *relative r-nuclidic abundances not influenced by galactic chemical evolution effects*
⟹ *possible Th nucleocosmochronometry*

Is the whole CS22892-052 r-distribution solar ??

Comparison: Random (unweighted) superposition of events
Best-fit (weighted) superposition of events

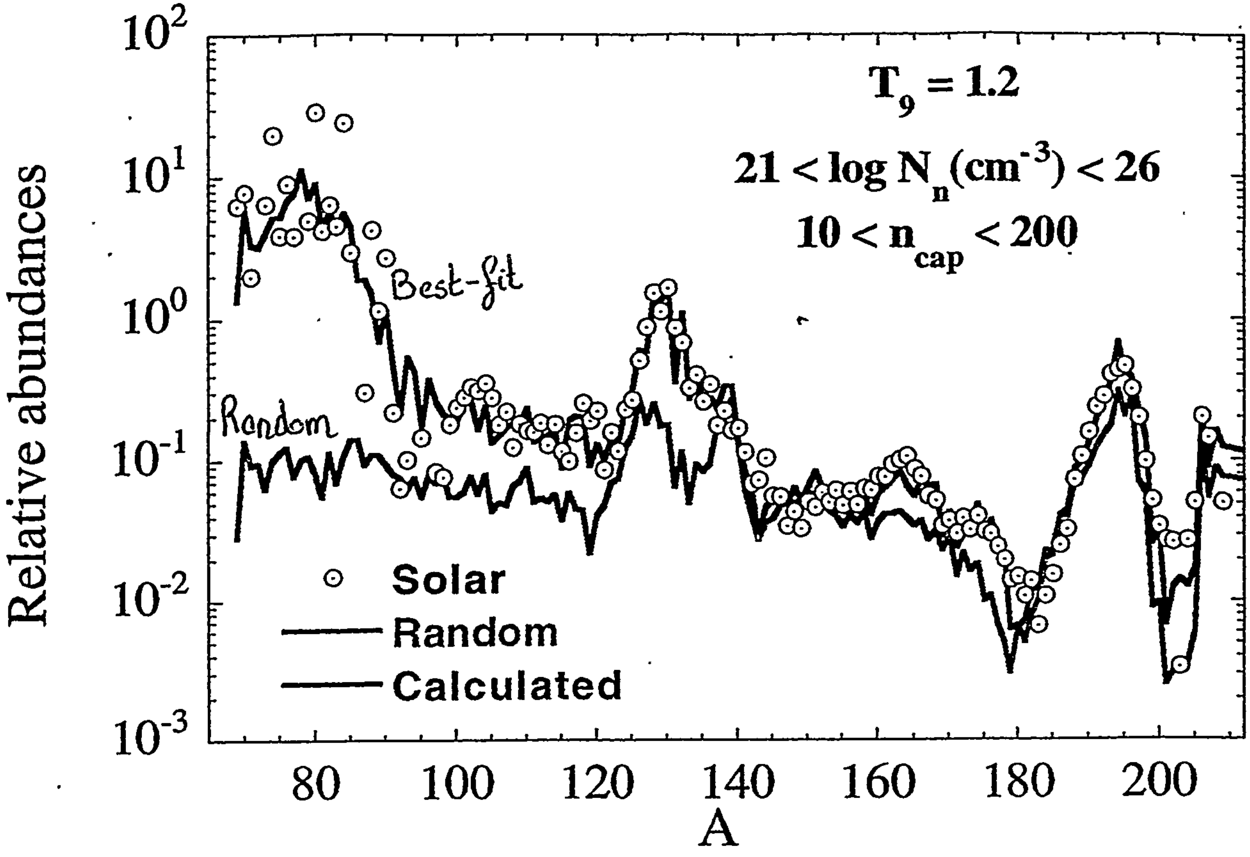

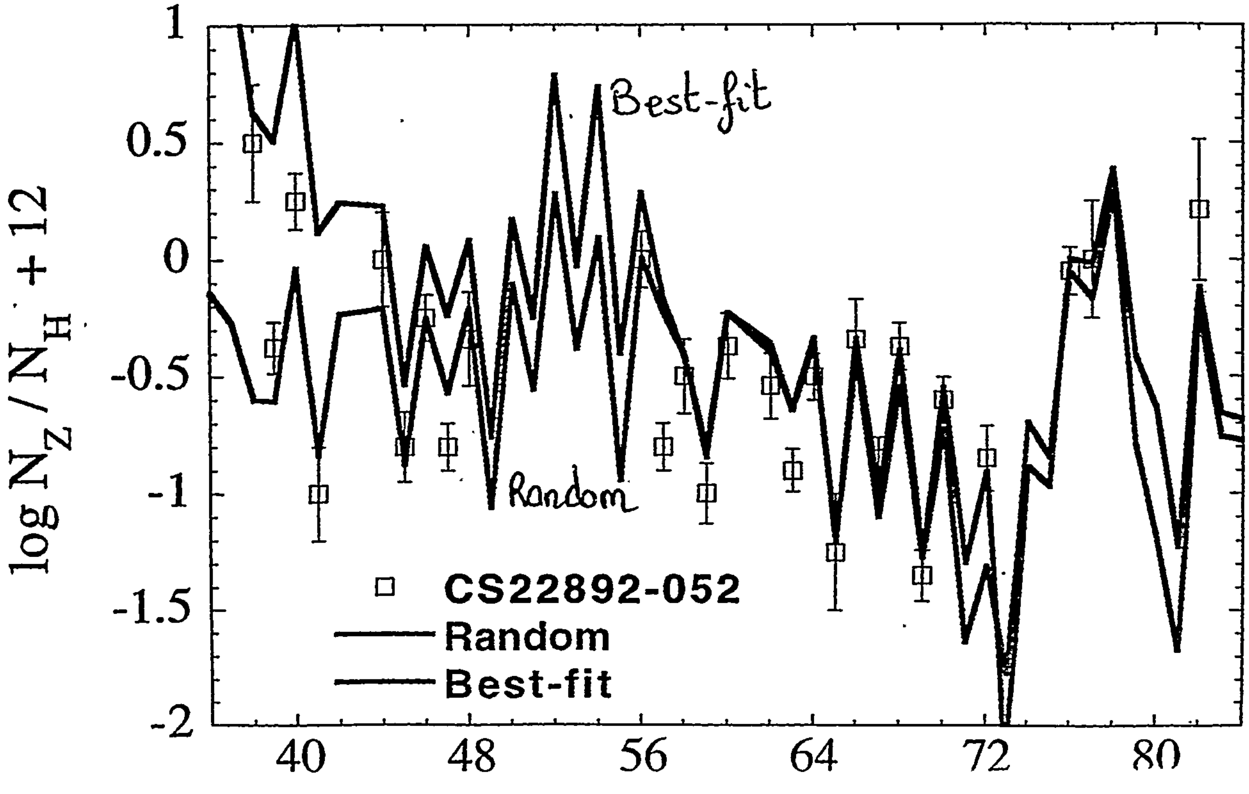

** FUNDAMENTAL ASSUMPTION: UNIQUE R-PROCESS ;

⇒ Is it possible to use the Th cosmochrometry to estimate
the age of the star ⇒ limit on the age of Ga

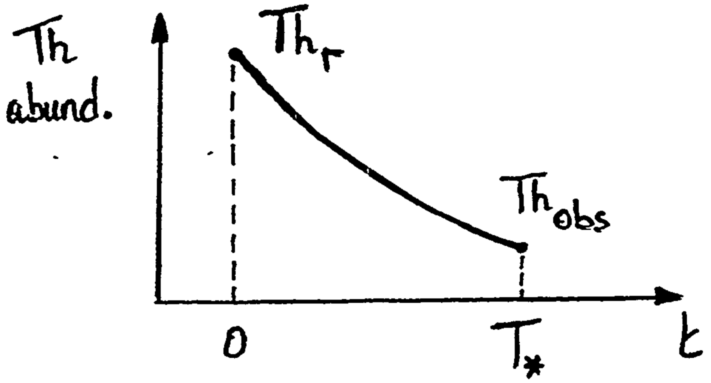

$$\left.\frac{Th}{Eu}\right|_{obs} = \left.\frac{Th}{Eu}\right|_{r} \, e^{-\frac{T^*}{\tau(Th}}$$

$\tau(Th) \simeq 20.27$ Gy

Recent observations $\left.\frac{Th}{Eu}\right|_{obs} = \begin{array}{ll} -0.6 \pm 0.08 & \text{HD115444} \\ -0.7 \pm 0.08 & \text{CS22892-} \end{array}$

⇒ Determination of the $\left.\frac{Th}{Eu}\right|_{r}$ produced by the r-process

(PARAMETRIC MODELS ONLY !)

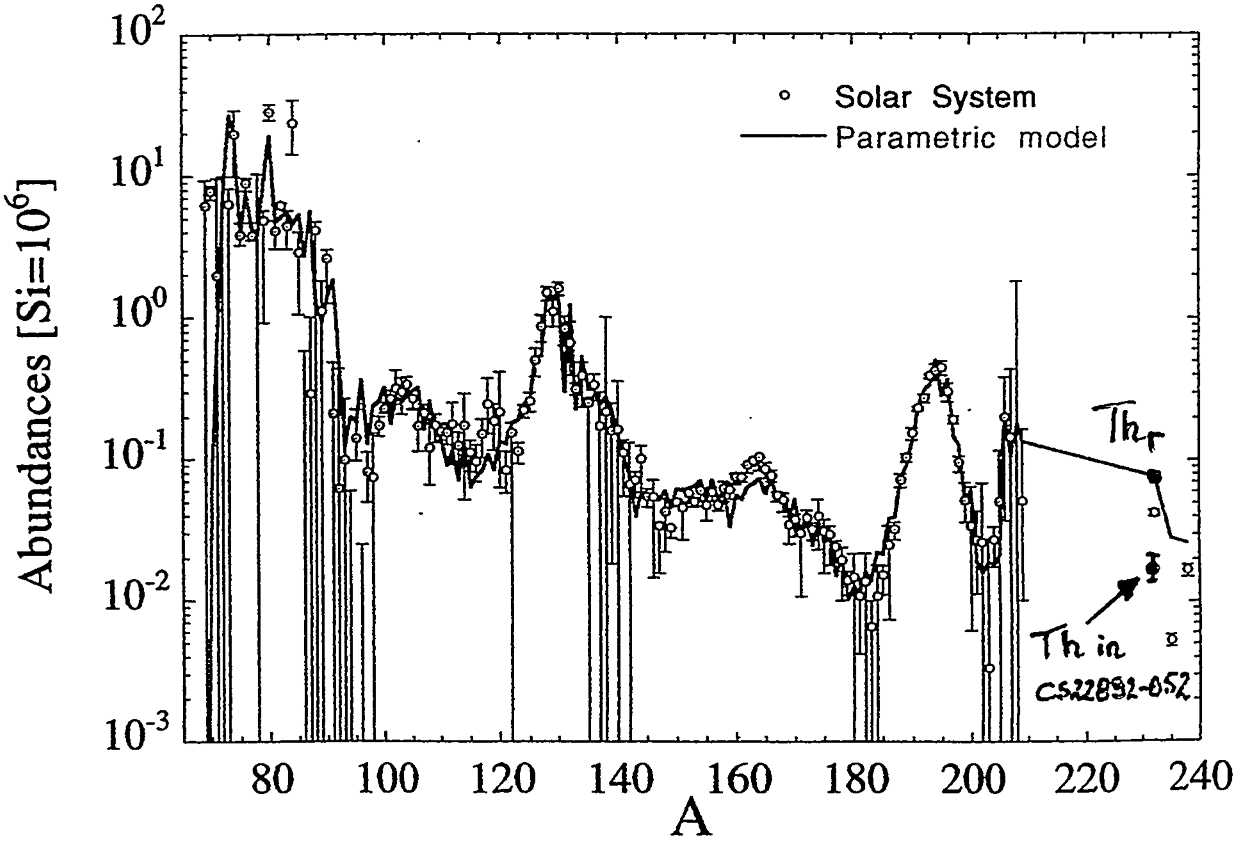

The multi-event r-process model

* Based on the canonical model (B^2FH, 1957)

- ^{56}Fe seed nuclei
- Constant T, N_n during neutron irradiation $0 \leq t_s$
- (Waiting point approximation $(n,\gamma) \rightleftharpoons (\gamma,n)$ equili

including
  - β^- & βdn processes.
  - fission processes (sf, βdf, nif)
  - α-decay processes

* Fit to the Solar System abundances with an iterative inversion

$$N^r_\odot(Z,A) \simeq N^r_{cal}(Z,A) = \sum_{T,N_n,\tau_{irr}} n(Z,A;T,N_n,\tau_{irr})\,\phi(T,N_n,\tau_{in}$$

Excellent tool for testing the model uncertainties

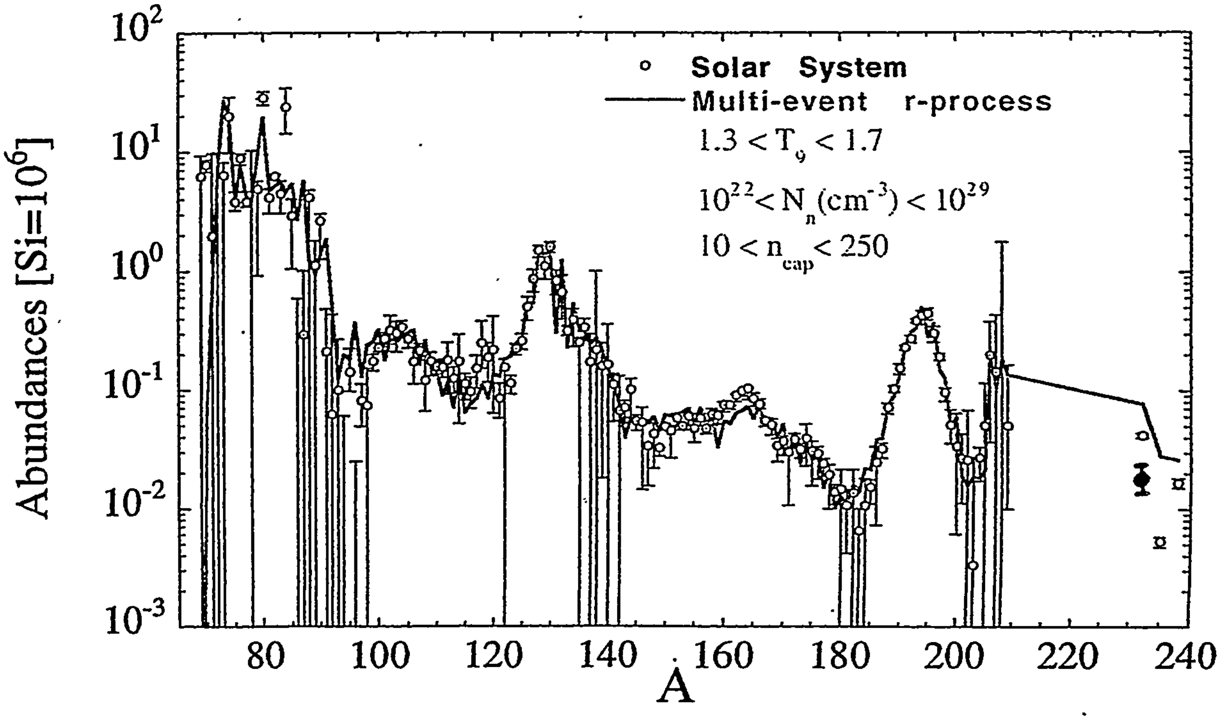

Best-fit to the Solar System Abundances and distribution of even

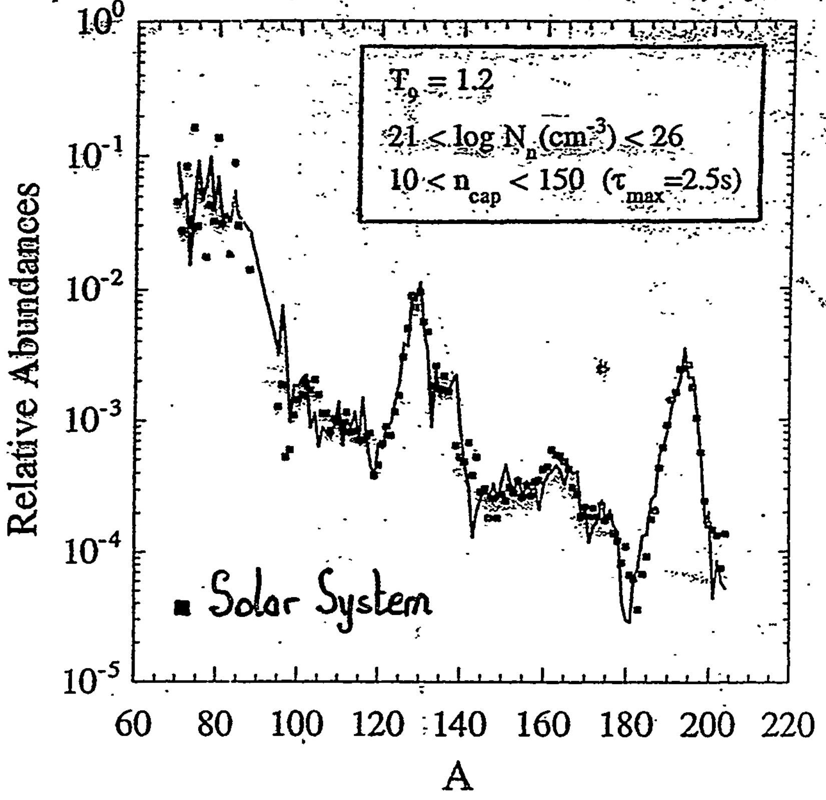

Distribution of events in the (S_a^0, n_{cap}) plane

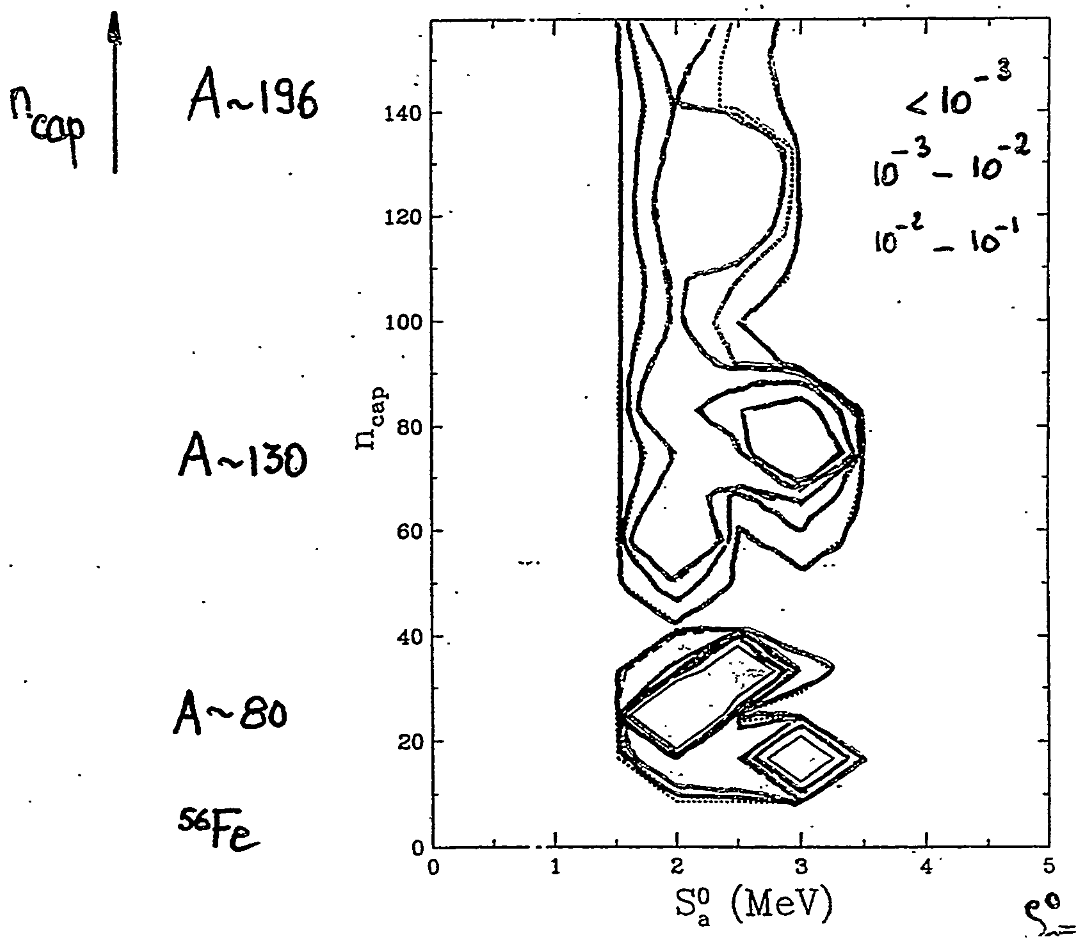

$S_a^0 = [34 - \log N_n + \frac{3}{2} \log T_9]\, T_9/$

Uncertainties in the prediction of the Th abundance

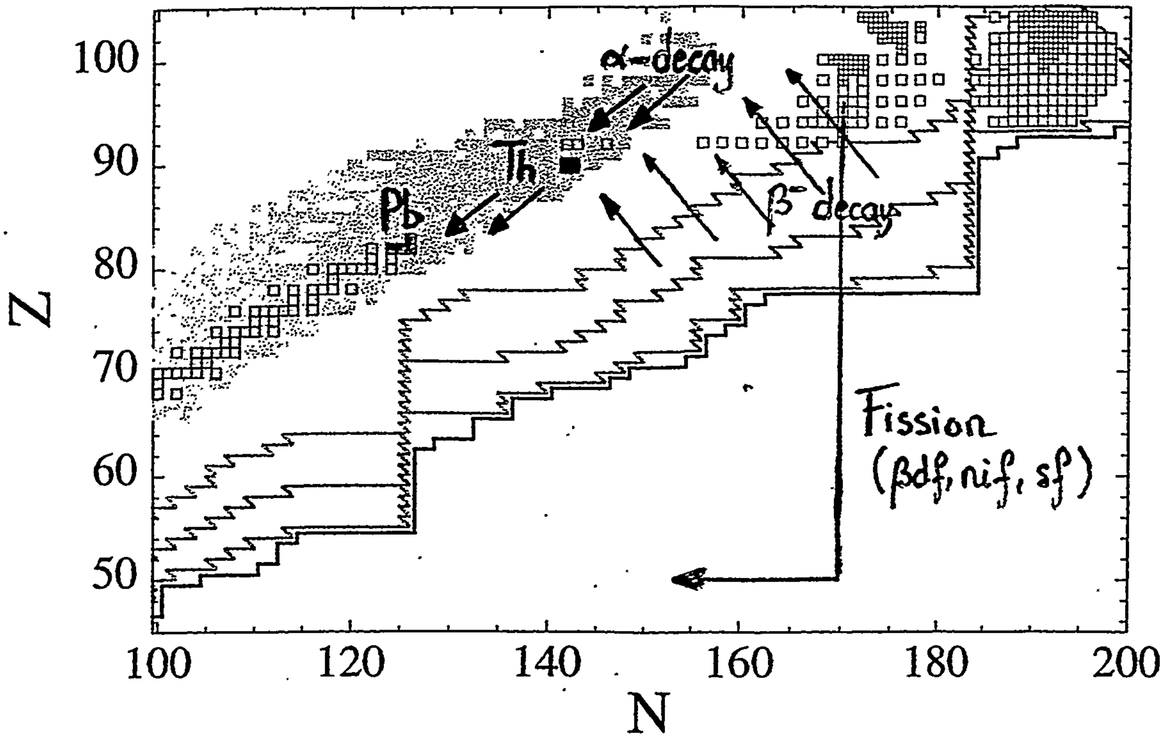

1) Uncertainties in the astrophysics modelling (T_9, N_n, n_{cap})
in particular in the strength of the r-process (n_{cap}^{max})
2) Uncertainties in the nuclear physics modelling
in particular in the masses, β^--rates & fission rates
3) Uncertainties in the Solar System r-abundance distribution
in particular in the Th-region

Influence of Nuclear Masses on Th predictions

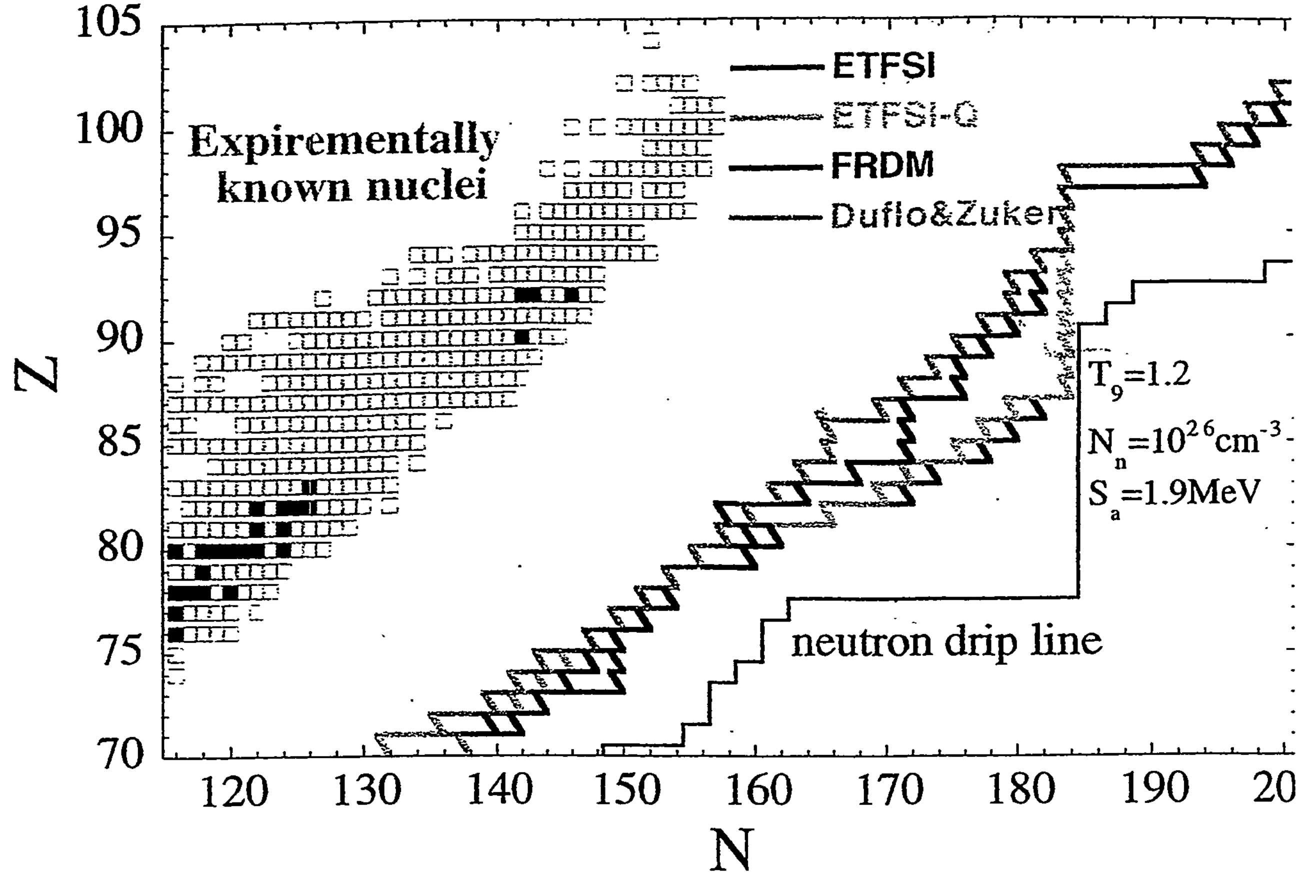

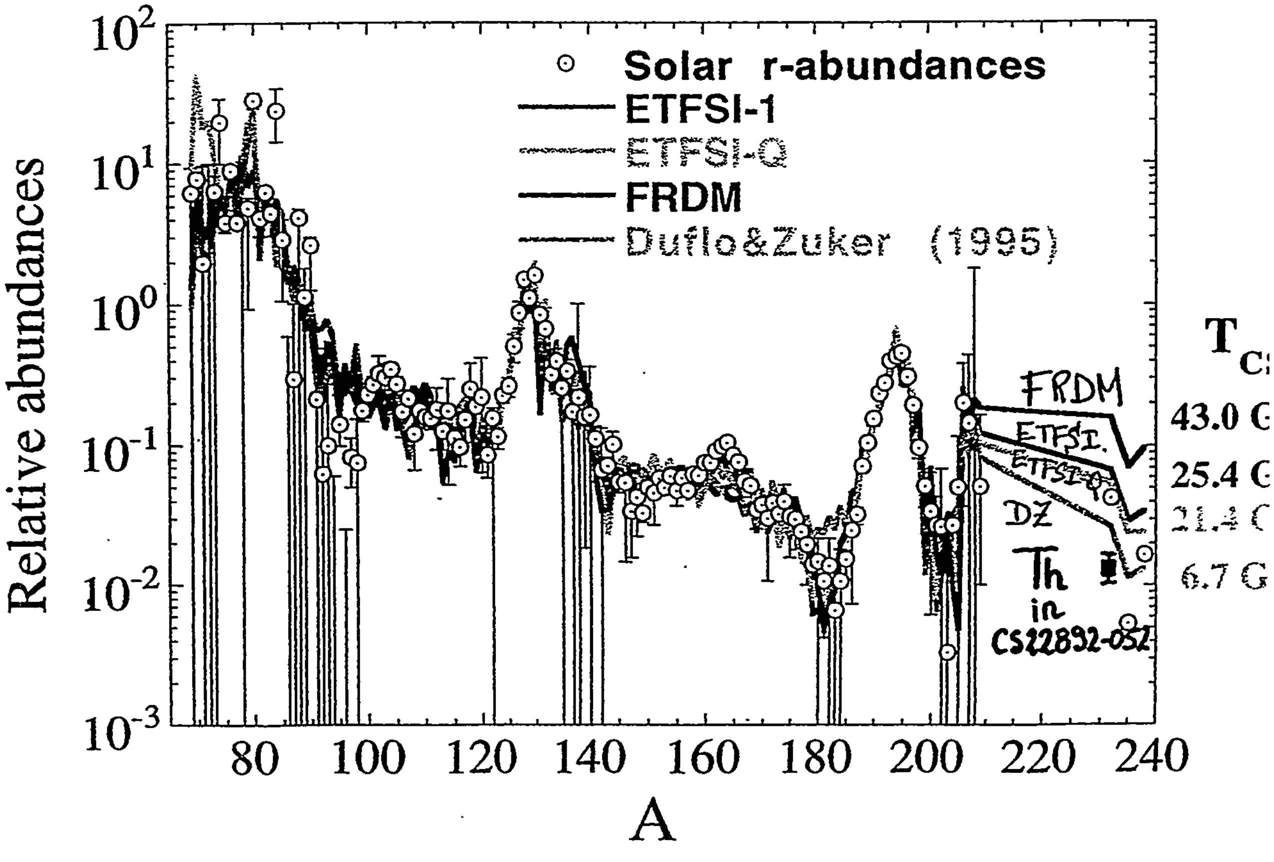

Fit : $T_9 = 1.2$, $21 < \log N_n(\text{cm}^{-3}) < 26$, $10 < n_{cap} < 200$

Influence of β-decay rates on rn predictions

Comparison of β^--decay predictions for nuclei in the $2 < S_n$ [MeV] < 2.5 range

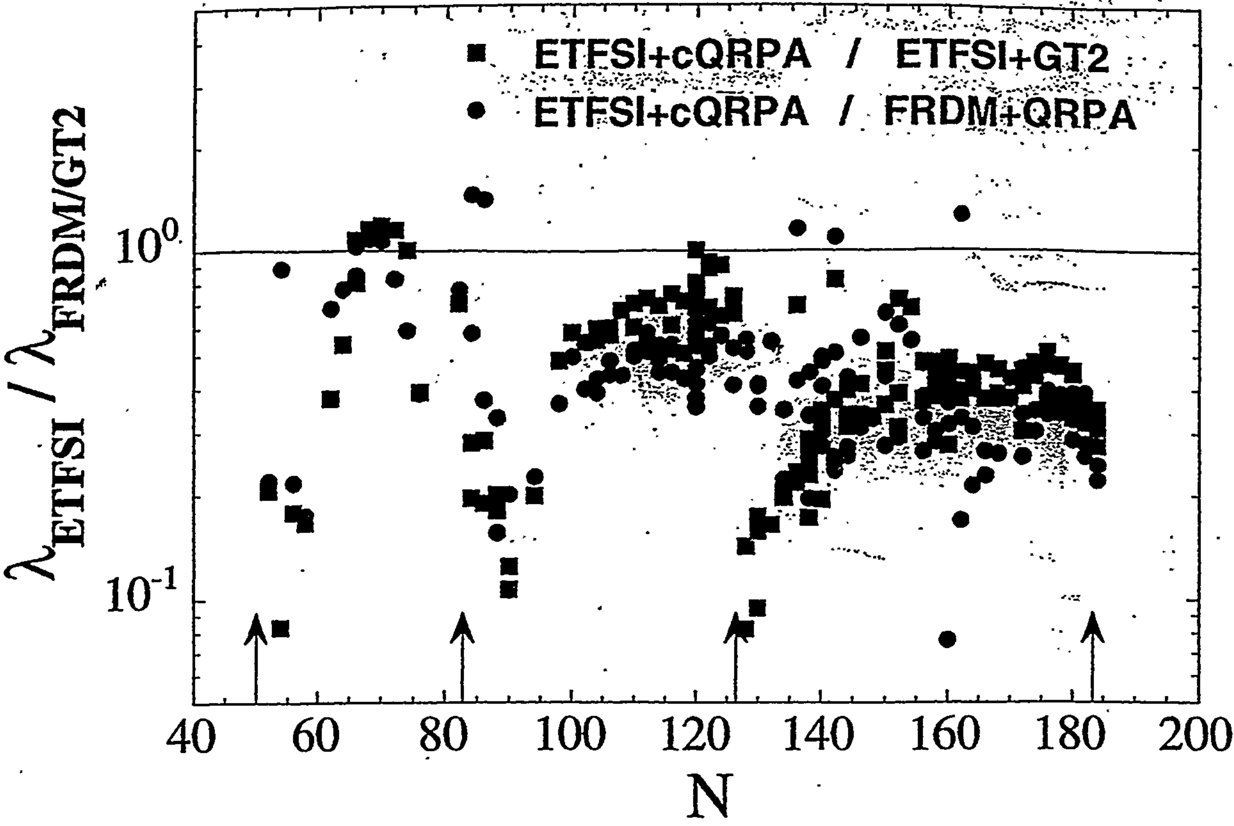

Fit : $T_9 = 1.2$, $21 < \log N_n(\mathrm{cm}^{-3}) < 26$, $10 < n_{cap} < 200$

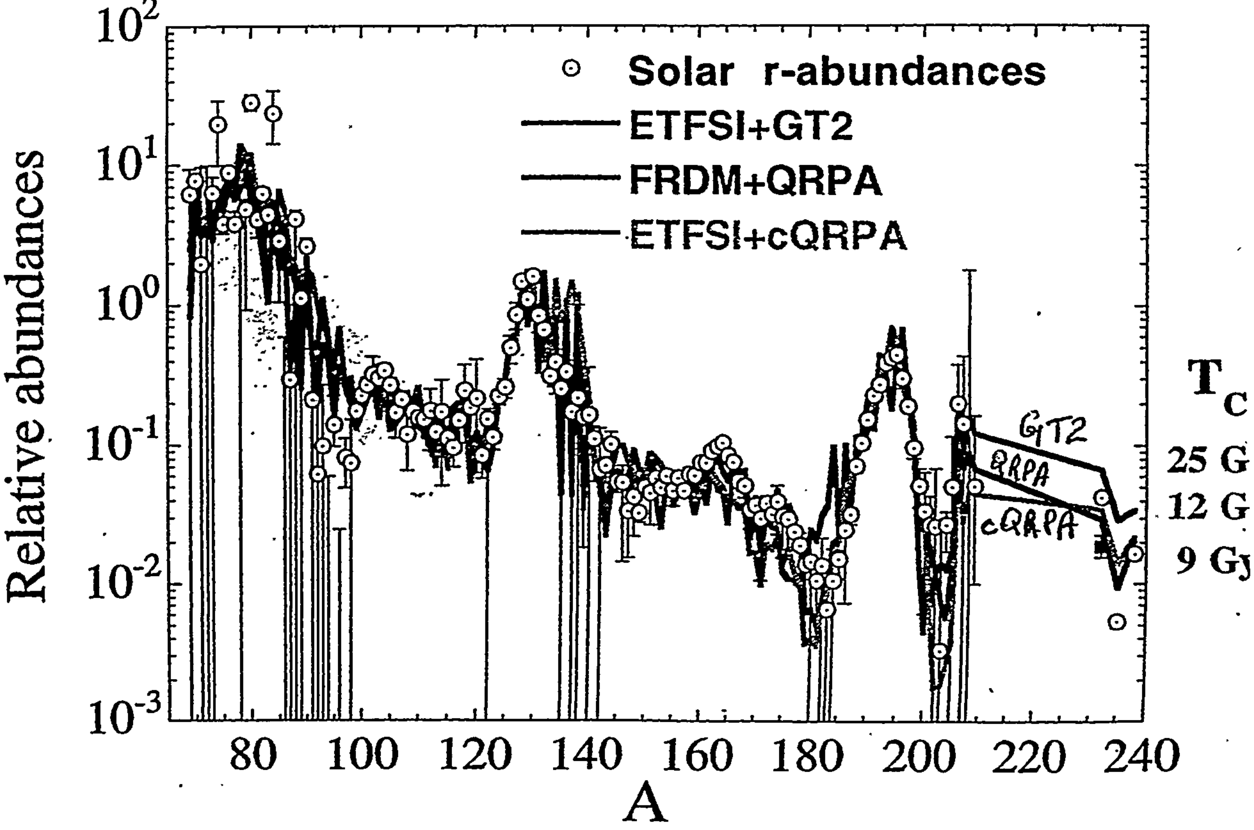

Influence of Fission on Th predictions

Fission barriers from ETFSI (Mamdouh et al. 1999)

→ spontaneous, β-delayed and neutron-induced fission

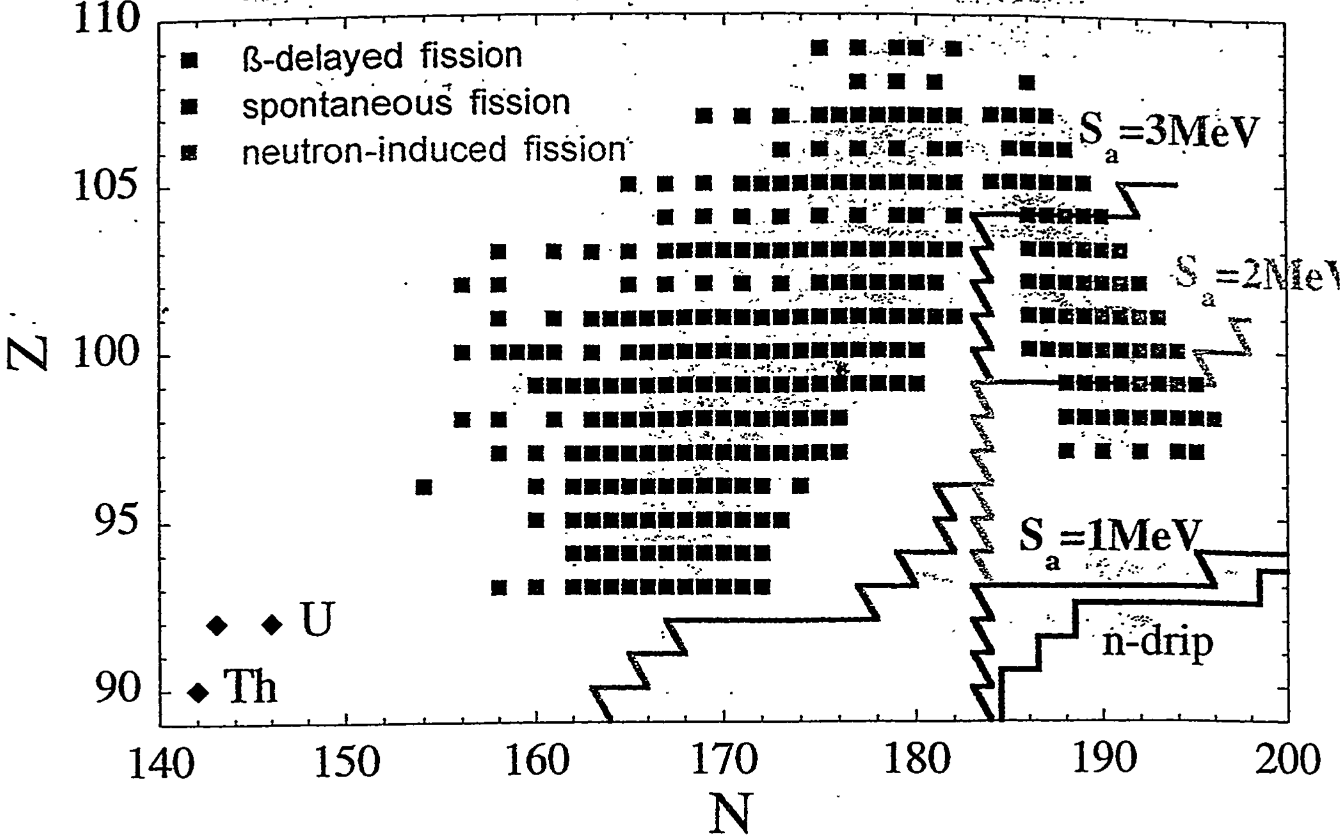

Fit : $T_9 = 1.2$, $21 < \log N_n(\mathrm{cm}^{-3}) < 26$, $10 < n_{cap} < 200$

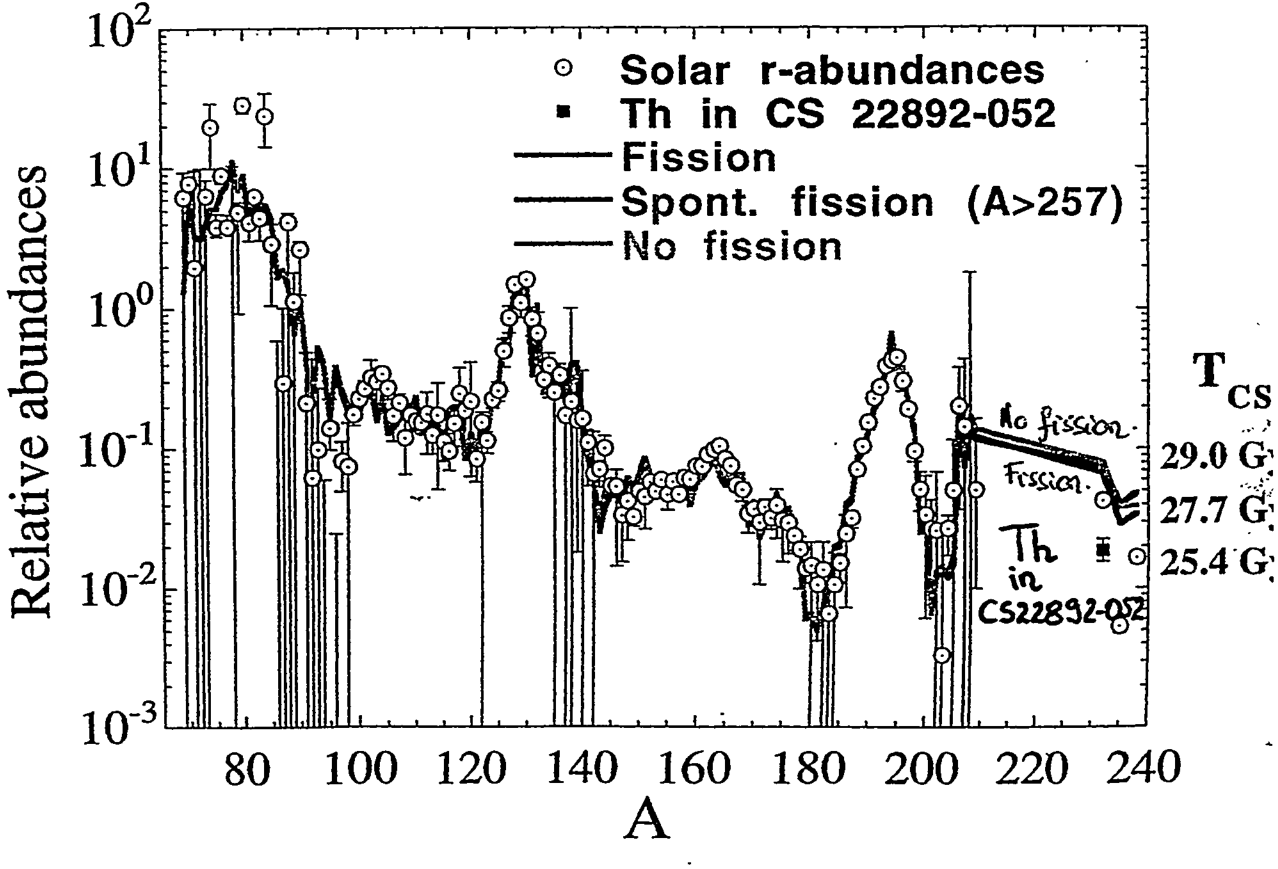

CONCLUSIONS

Nuclear Uncertainties (masses, β-decay rates, fission) affect Th cosmochronometry

$$\boxed{7 < T^* \text{ [Gyr] } < 43}$$

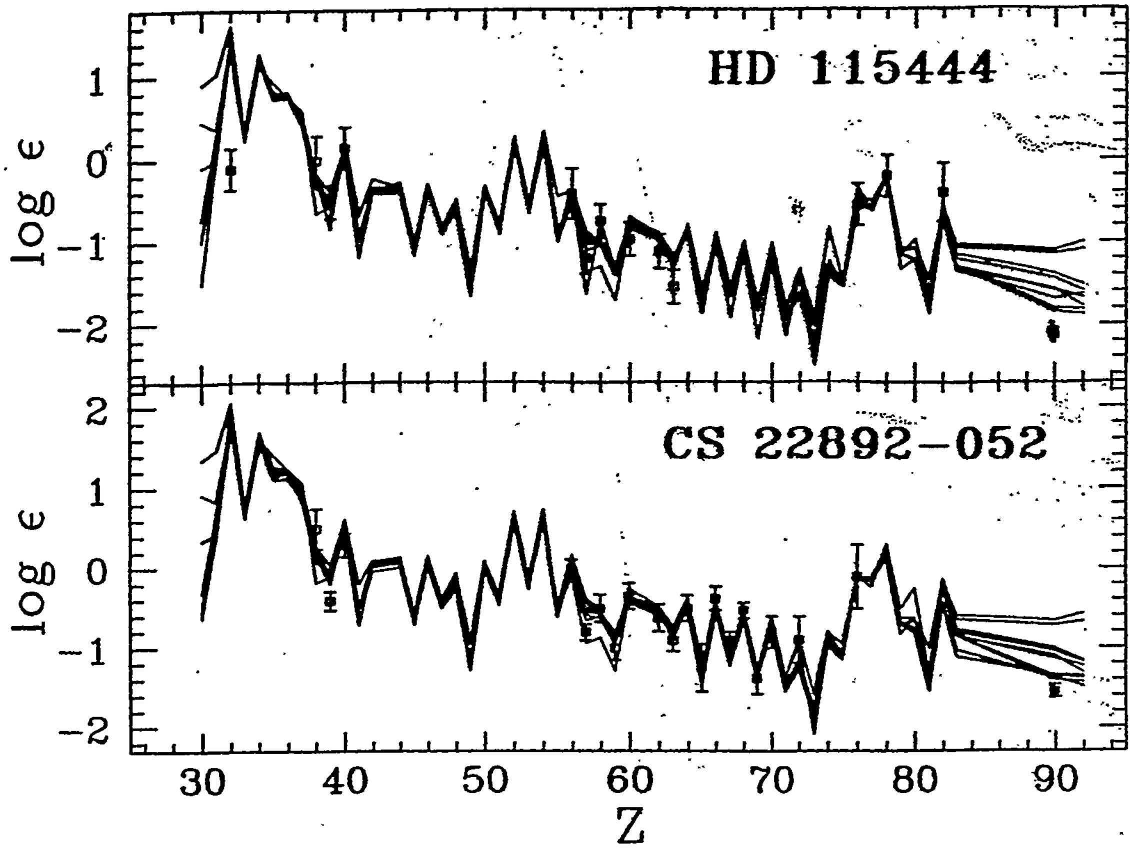

Some hope in the Th/U COSMOCHRONOMETRY

$$\log \left.\frac{\mathrm{Th}}{\mathrm{U}}\right|_{obs} = \log \left.\frac{\mathrm{Th}}{\mathrm{U}}\right|_{r} + \log \mathrm{e} \left(\frac{1}{\tau(\mathrm{U})} - \frac{1}{\tau(\mathrm{Th})}\right) T_*$$

$\tau(\mathrm{U})$=6.41Gyr

$\tau(\mathrm{Th})$=20.27Gyr

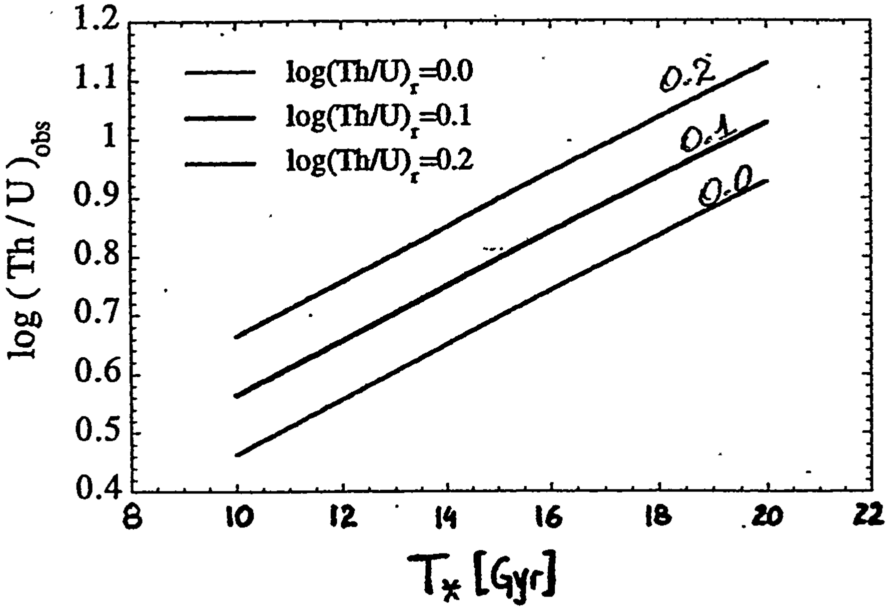

$$\Delta \log \left(\frac{\mathrm{Th}}{\mathrm{U}}\right) = \pm\, 0.$$

$$\boxed{\longrightarrow \Delta T_* = \pm 2.1\mathrm{Gy}}$$

NEUTRON CAPTURE CROSS SECTIONS OF ^{84}Kr AND ^{86}Kr AND THEIR IMPACT ON STELLAR NUCLEOSYNTHESIS

P. Mutti, F. Corvi, A. Noriega
(Institute for Reference Materials and Measurements, Retieseweg, B-2440 Geel, Belgium),

H. Beer
(Forschungszentrum Karlsruhe, Institut für Kernphysik, P.O.Box 3640,D-76021 Karlsruhe, Germany)

The Krypton isotopes lie in a most sensitive, complicated and, therefore, interesting region of s-process nucleosynthesis. This mass region, in fact, receives substantial contributions from both the weak and the main component of the s-process which correspond to different stellar sites in stars of different size. It is well known that the weak component is associated to core He burning and shell C burning in massive stars, while the main component takes place in He shell burning of low mass stars during the thermal instabilities which characterize the AGB evolutionary phase.

^{86}Kr has a magic neutron number (50) consequently its neutron capture cross section is small and therefore sensitive to the s-process neutron exposure (the local approximation N = constant does not hold). The two isotopes are also involved in one of the most important s-process branching at 85Kr which delivers important details about neutron flux. An accurate s-process analysis can give important hints on the solar (cosmic) Krypton abundance, which cannot be determined from primitive meteorites because Krypton is a noble gas. An additional reason of interest is related to the explanation of the so-called isotopic anomalies of Krypton found in circumstellar SiC grains.

With the aim to improve the knowledge of the neutron capture cross section of the Krypton isotopes and therefore to reduce the uncertainties on the s-process models related to nuclear quantities, the neutron capture cross section for ^{84}Kr and ^{86}Kr, on both resolved and unresolved resonance regions, have been measured with high resolution at the GELINA facility in Geel, and the Maxwellian-averaged capture cross section versus stellar temperature has been derived. The astrophysical implications of the new results are discussed.

EUROPEAN COMMISSION
JOINT RESEARCH CENTRE
Institute for Reference Materials and Measurements

Geel, Belgium

Neutron Capture Cross Section of ^{84}Kr and ^{86}Kr and Their Impact on Stellar Nucleosynthesis

P. Mutti[1], A. Brusegan[1], F. Corvi[1], R. Galleano[1], A. Noriega[1]
and H. Beer[2]

1 EC, JRC, Institute for Reference Materials and Measurements
2 Forschungszentrum Karlsruhe, Institut für Kernphysik

Summary

- Motivation for the Measurements
- ^{84}Kr Capture and Transmission
- ^{86}Kr Capture
- Results

^{85}Kr Branching

s-process path

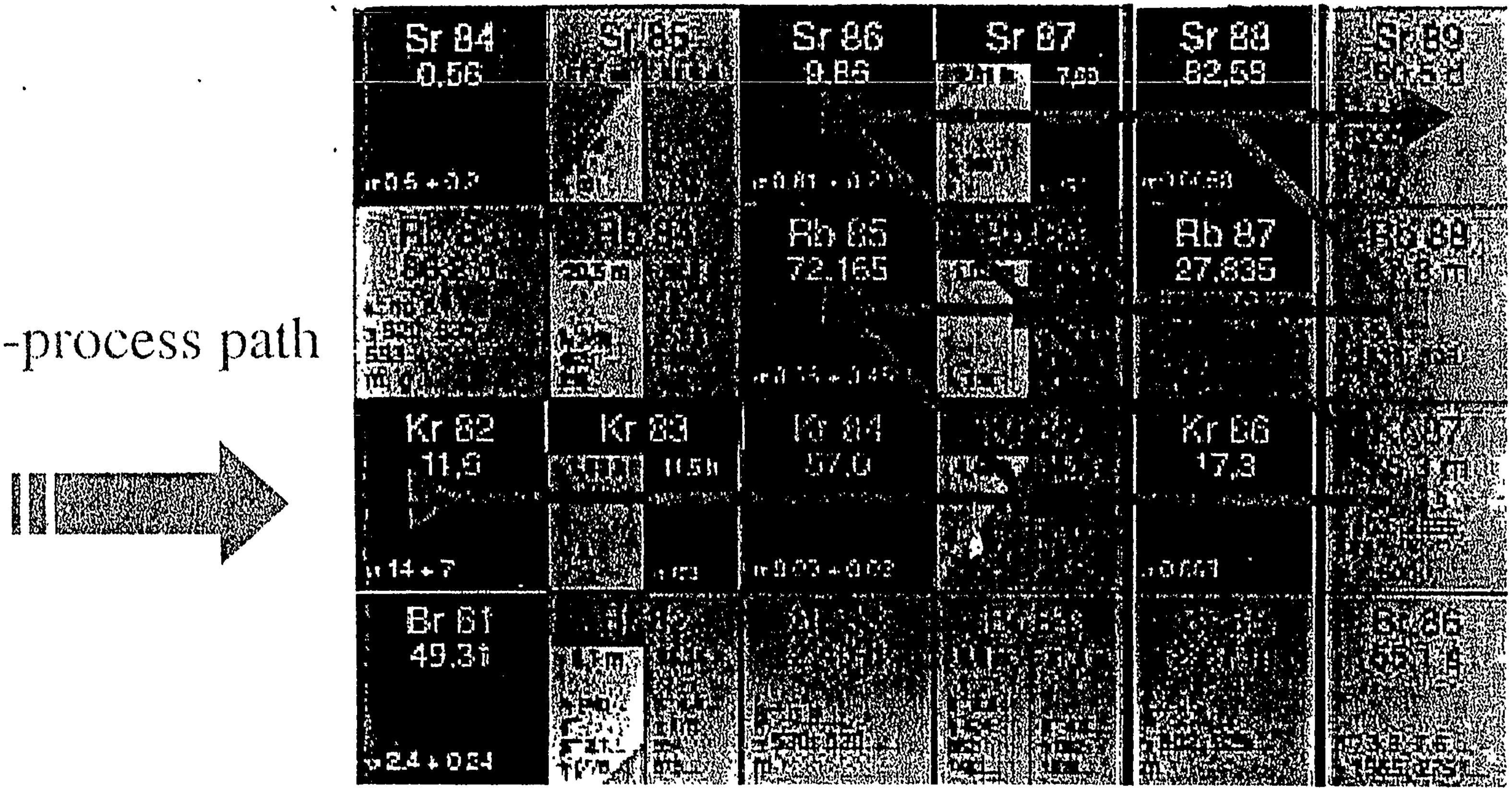

Motivations

- Determination of Kr solar abundances via *s*-process analysis.
- Stellar evolution parameters via ^{85}Kr branching.
- Isotopic anomalies in SIC.

^{84}Kr Data - Literature ...

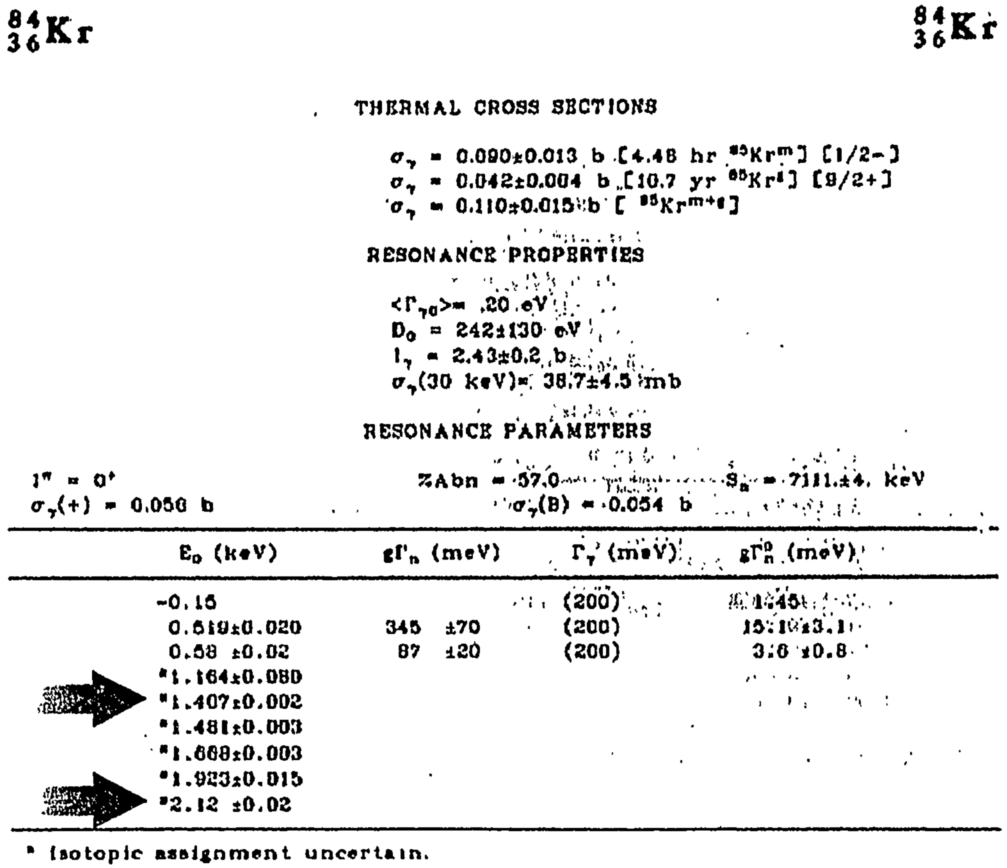

$^{84}_{36}$Kr $^{84}_{36}$Kr

THERMAL CROSS SECTIONS

σ_γ = 0.090±0.013 b [4.48 hr ^{85}Kr^m] [1/2−]
σ_γ = 0.042±0.004 b [10.7 yr ^{85}Kr^g] [9/2+]
σ_γ = 0.110±0.015 b [^{85}Kr^{m+g}]

RESONANCE PROPERTIES

$\langle\Gamma_{\gamma 0}\rangle$ = .20 eV
D_0 = 242±130 eV
I_γ = 2.43±0.2 b
σ_γ(30 keV) = 38.7±4.5 mb

RESONANCE PARAMETERS

$J^\pi = 0^+$ %Abn = 57.0 S_n = 7111.±4. keV
$\sigma_\gamma(+)$ = 0.050 b $\sigma_\gamma(B)$ = 0.054 b

E_0 (keV)	$g\Gamma_n$ (meV)	Γ_γ (meV)	$g\Gamma_n^0$ (meV)
−0.15		(200)	14.45
0.519±0.020	345 ±70	(200)	15.1±3.1
0.58 ±0.02	87 ±20	(200)	3.6 ±0.8
*1.164±0.080			
*1.407±0.002			
*1.481±0.003			
*1.668±0.003			
*1.923±0.015			
*2.12 ±0.02			

* Isotopic assignment uncertain.

Neutron Cross Sections
F. Mughabghab et al. (1981)

GELINA - White Neutron Source

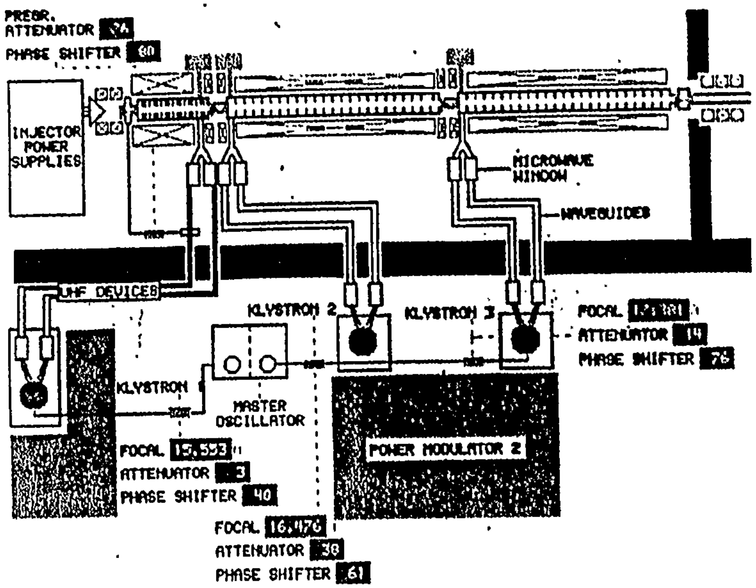

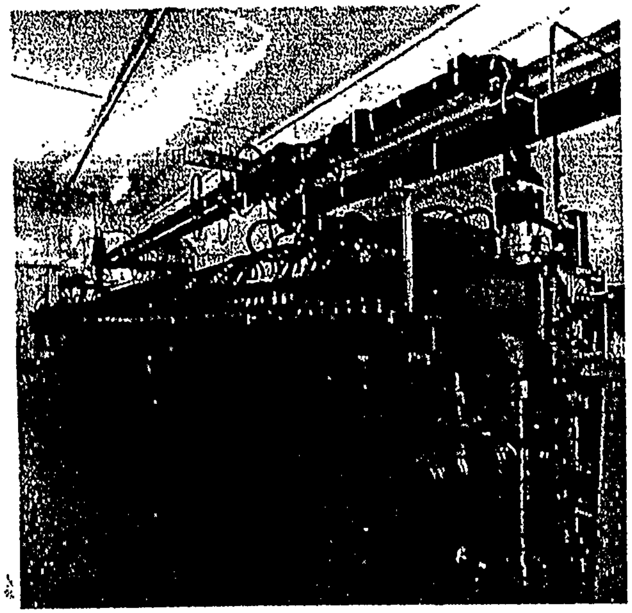

- Frequency: 800 *Hz*
- Peak Current: 80 μA
- Mean Power: 7.5 *kW*
- Average Neutron Rate: 2.5 x 10^{13} *n/s*

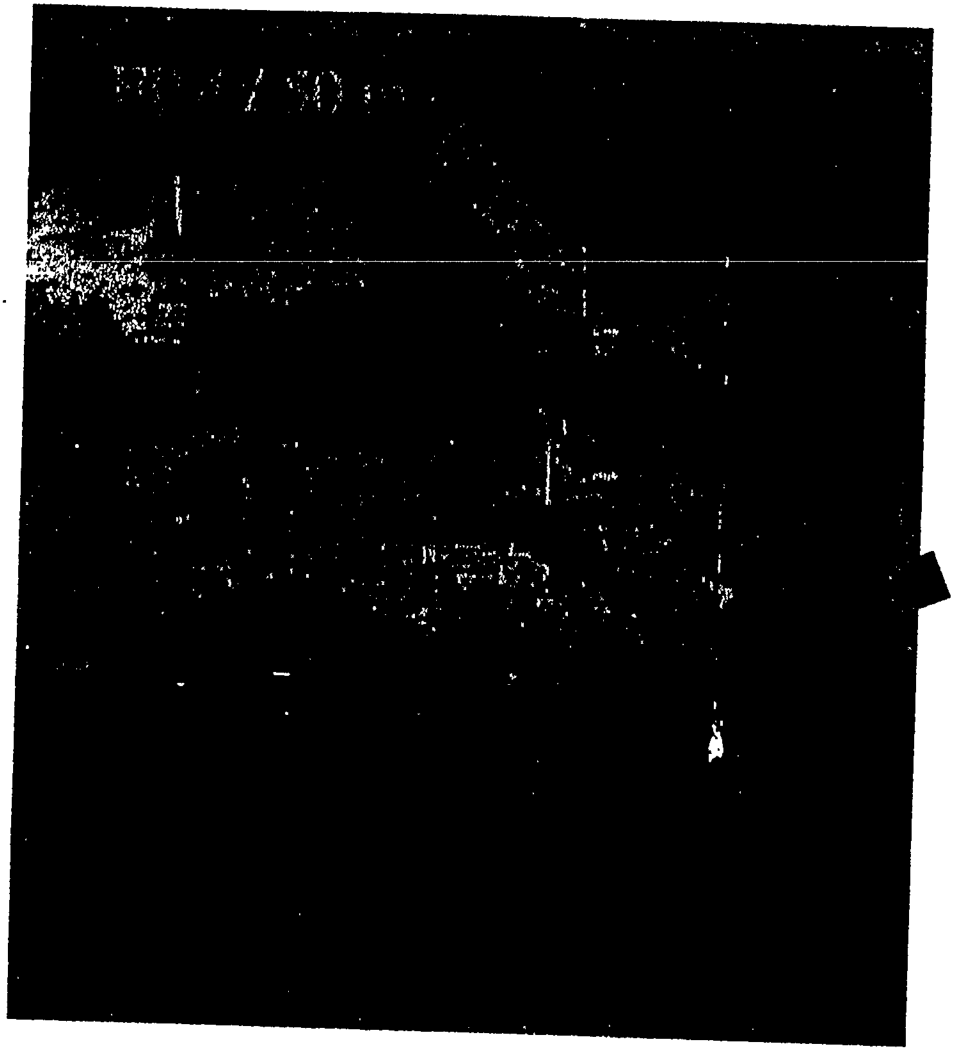

FP 14 / 60 m

Capture Measurement - Setup at FP14 - 58.40 m

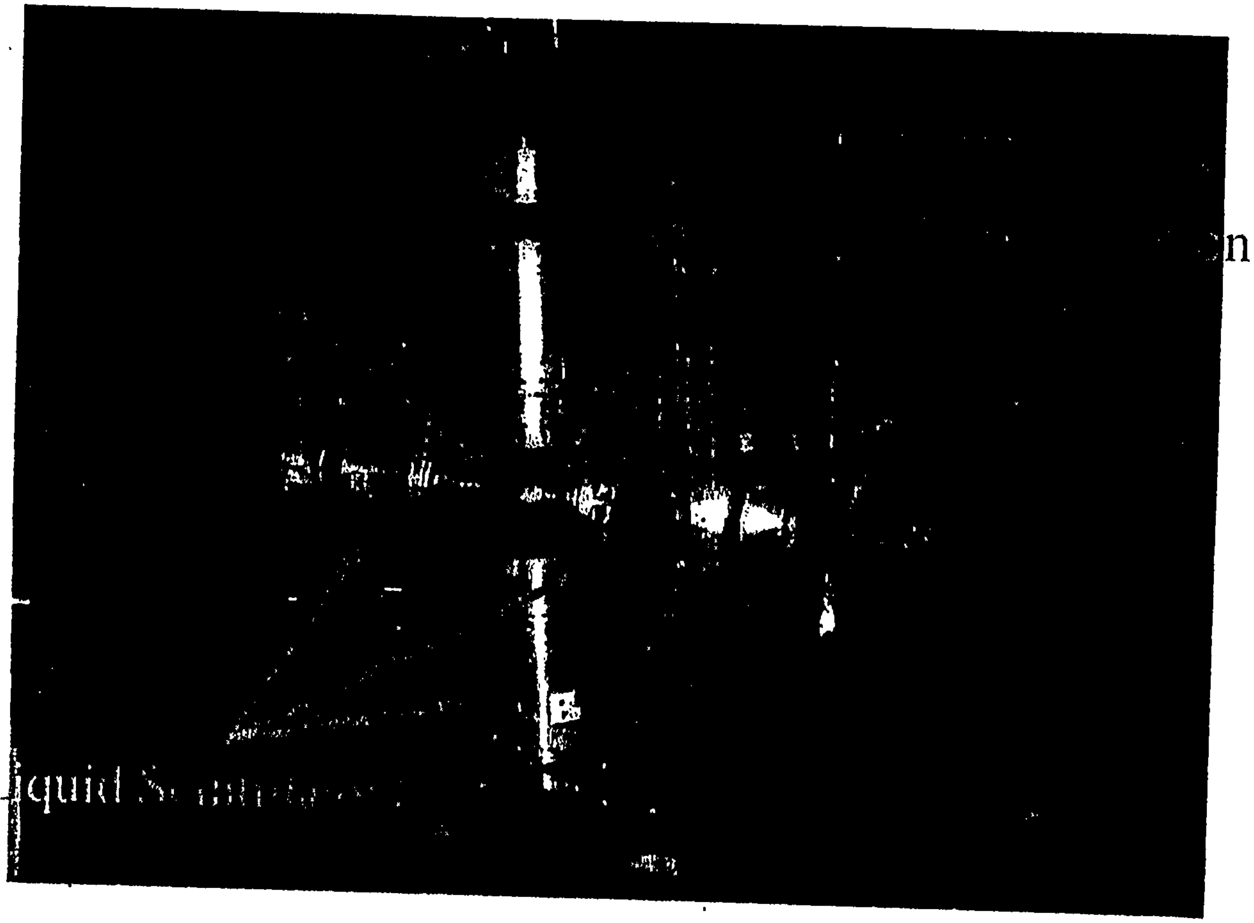

n Chamber

C_6D_6 Based Liquid S

Transmission Measurement - Setup at FP4 - 42.33 m

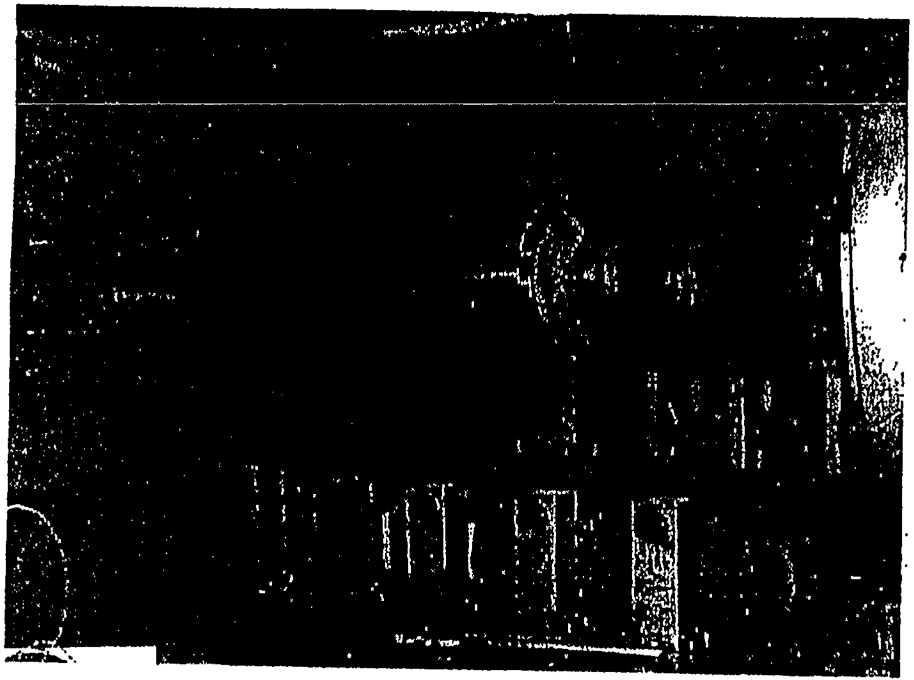

The Sample

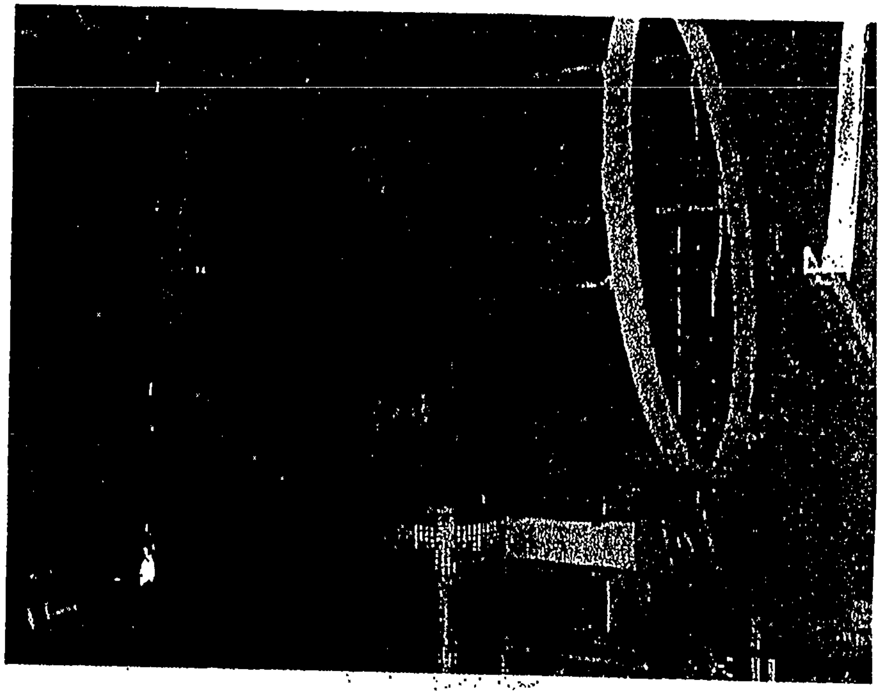

The Detector

^{84}Kr Measurements

Capture

Time of Flight method:
Flight path distance 58.41 *m* and 28.42 *m*

Capture event detectors:
4 C_6D_6 based liquid scintillators placed 90° with respect to the neutron direction.

Flux detector:
Ionization chamber with 3 back-to-back ^{10}B layers.

Sample:
$AlMg_3$ alloy spherical containers of 8 *cm* diameter and 1 *mm* wall thickness, able to hold a pressure of 20 *bar*.

Transmission

Time of Flight method:
Flight path distance 49.33 *m*.

Transmission detector:
1/4” NE912 Li glass seen with ~10% solid angle by a 5” EMI 9823-KQB PM set orthogonal to the neutron beam.

Sample:
Al cylinder, 4.6 *cm* inner diameter and 40 *cm* length holding 6.9 *bar* gas pressure placed at 23 *m* from the neutron source.

^{84}Kr Capture and Transmission Spectra

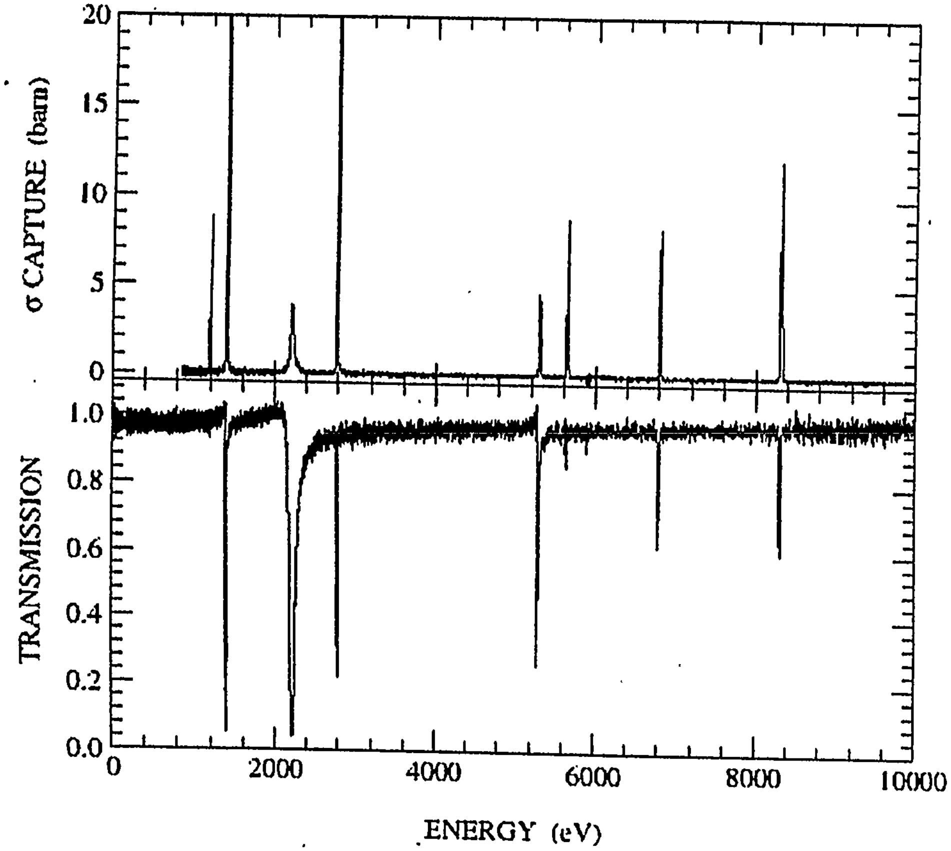

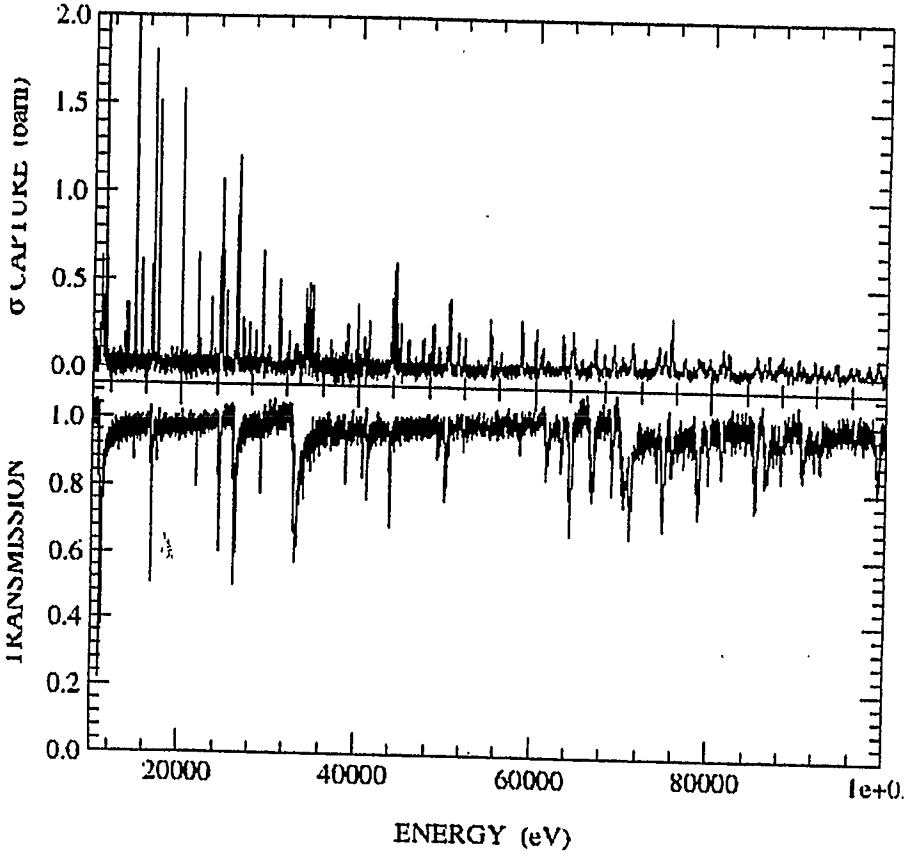

Resolution Improvement

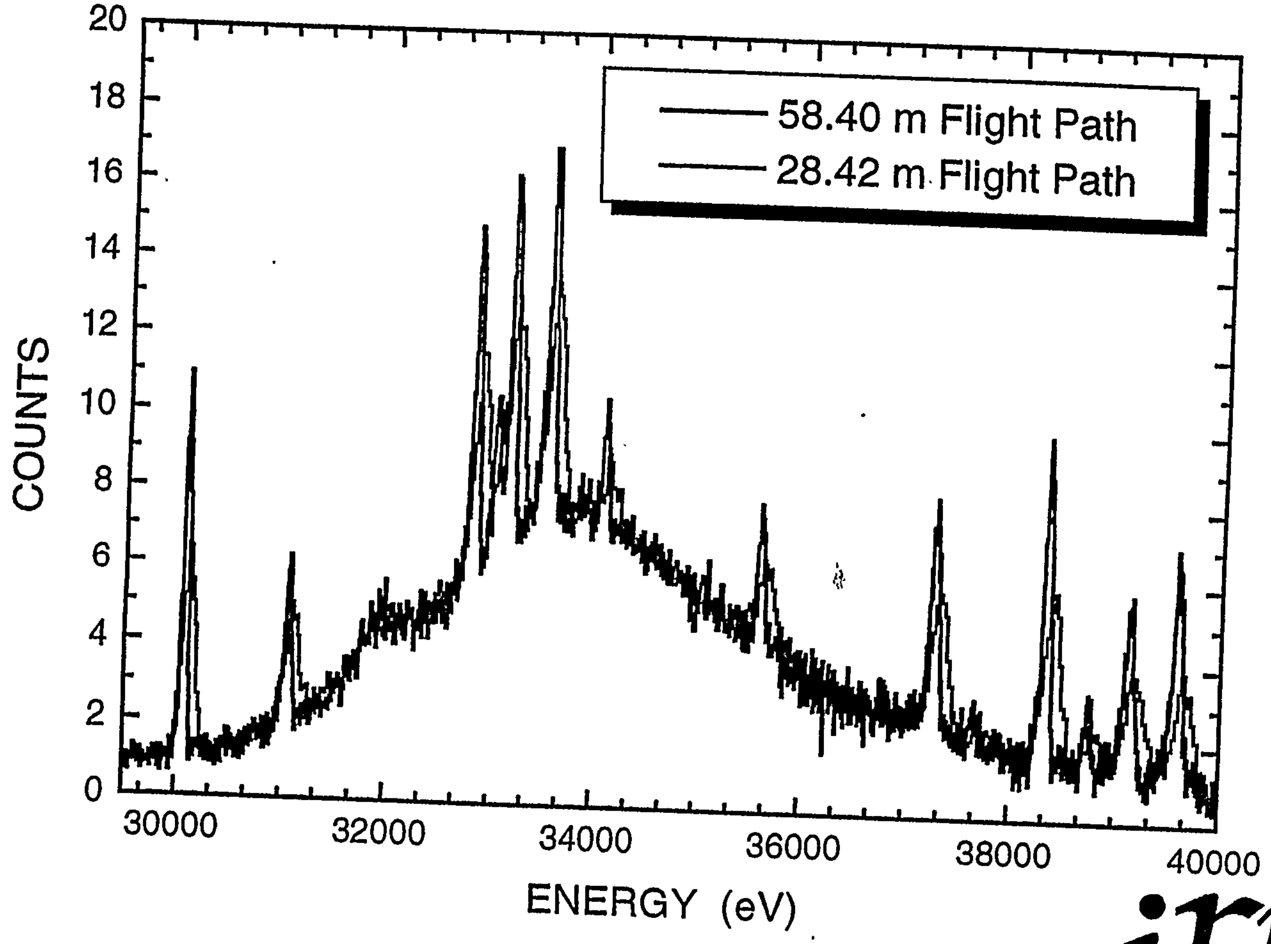

DATA ANALYSIS

- R-MATRIX FITTING CODE REFIT
- ASSUMPTIONS:
  - SAMPLE CONSIDERED CYLINDRICAL.
  - EFFECTIVE MASS OF AL DERIVED FROM THE ANALYSIS OF 5.9 KeV RESONANCE.
  - AL CONSIDERED HOMOGENEOUSLY MIXED WITH KR IN THE SAMPLE.

^{84}Kr Normalization

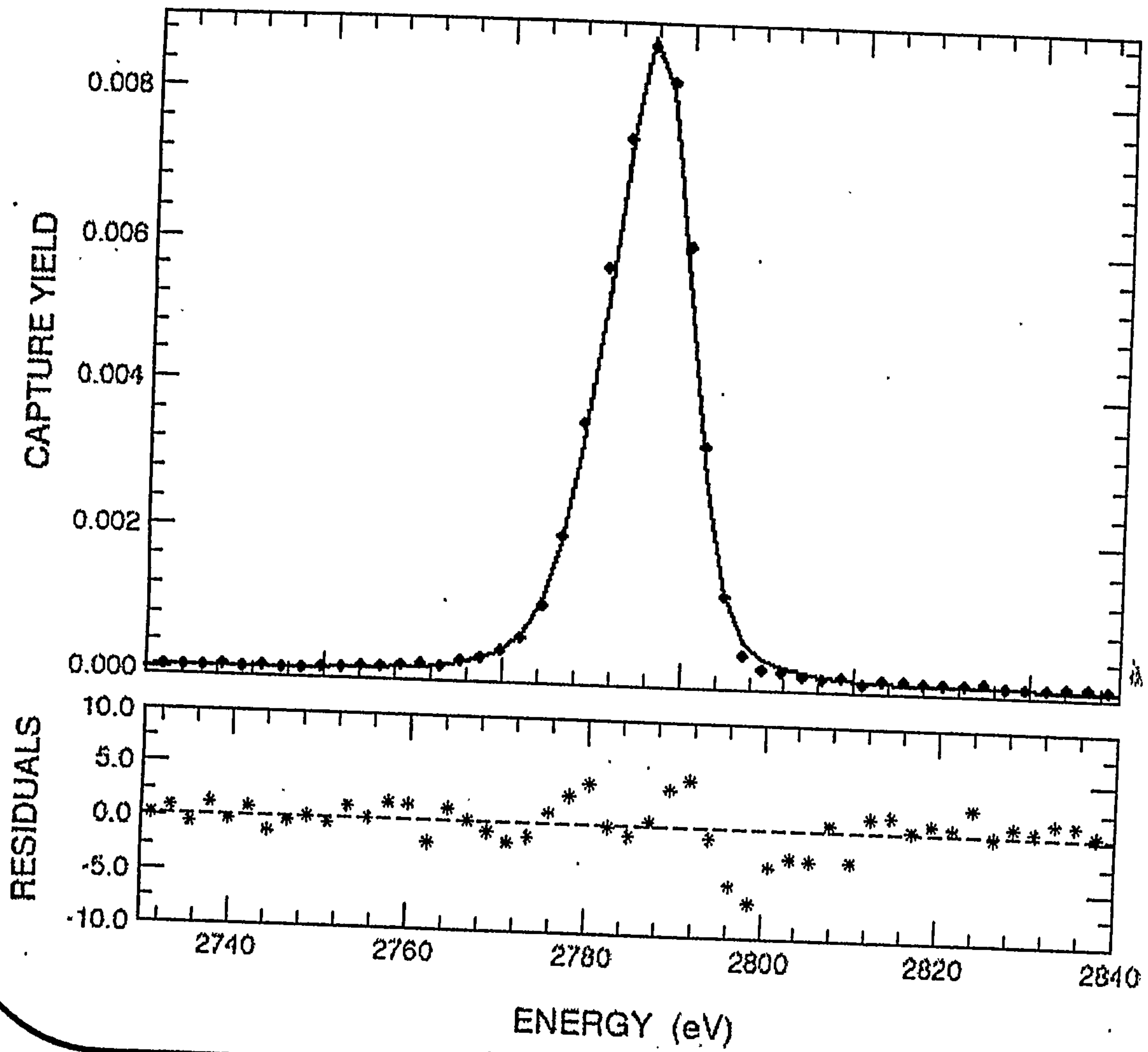

Reference Resonances:

^{131}Xe - E_n=46.0 eV

^{131}Xe - E_n=75.6 eV

^{131}Xe - E_n=114.9 eV

^{84}Kr:

$l = 0$ $J = 1/2$ $E_n = 2785$ eV

$\Gamma_n = 1.25 \pm 0.04\ eV$

1st normalisation:

$\Gamma_\gamma = 0.82 \pm 0.02\ eV$

$A_\gamma = 0.50 \pm 0.01\ eV$

2nd normalisation:

$\Gamma_\gamma = 0.88 \pm 0.02\ eV$

$A_\gamma = 0.52 \pm 0.01\ eV$

Difference:

4.2%

^{86}Kr Capture Spectrum

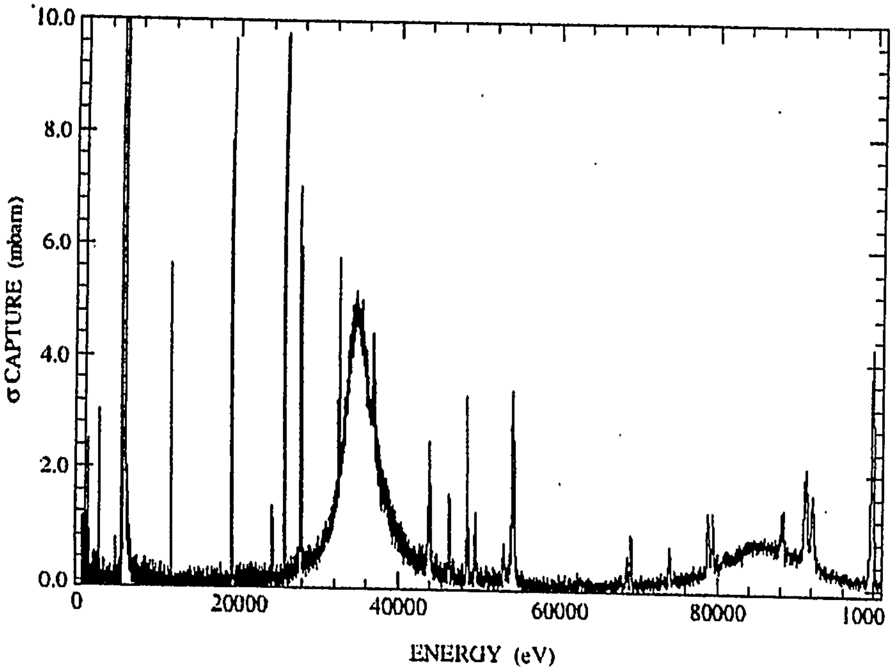

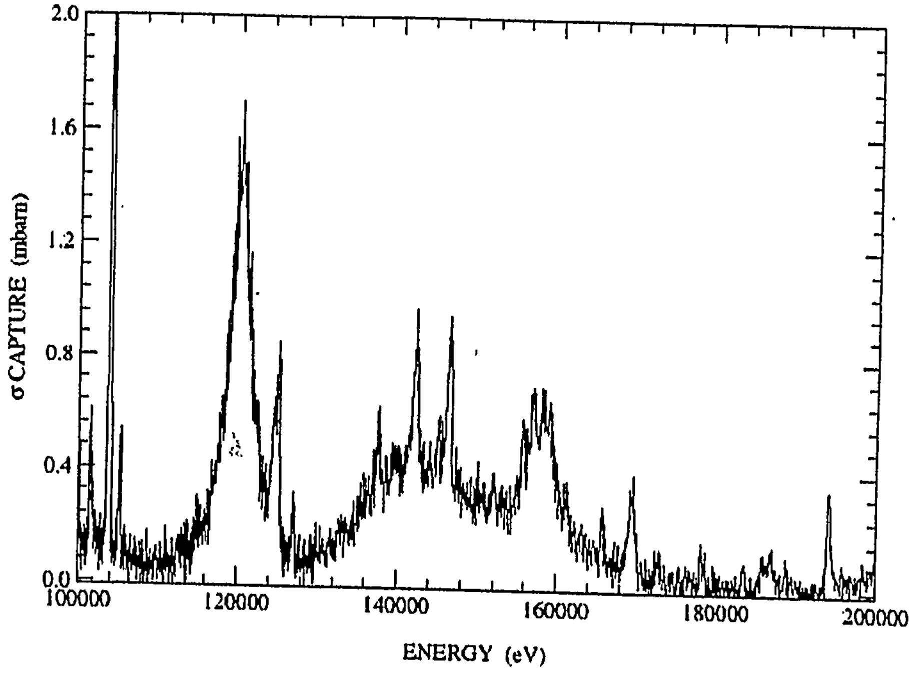

^{84}Kr MAC Cross Section

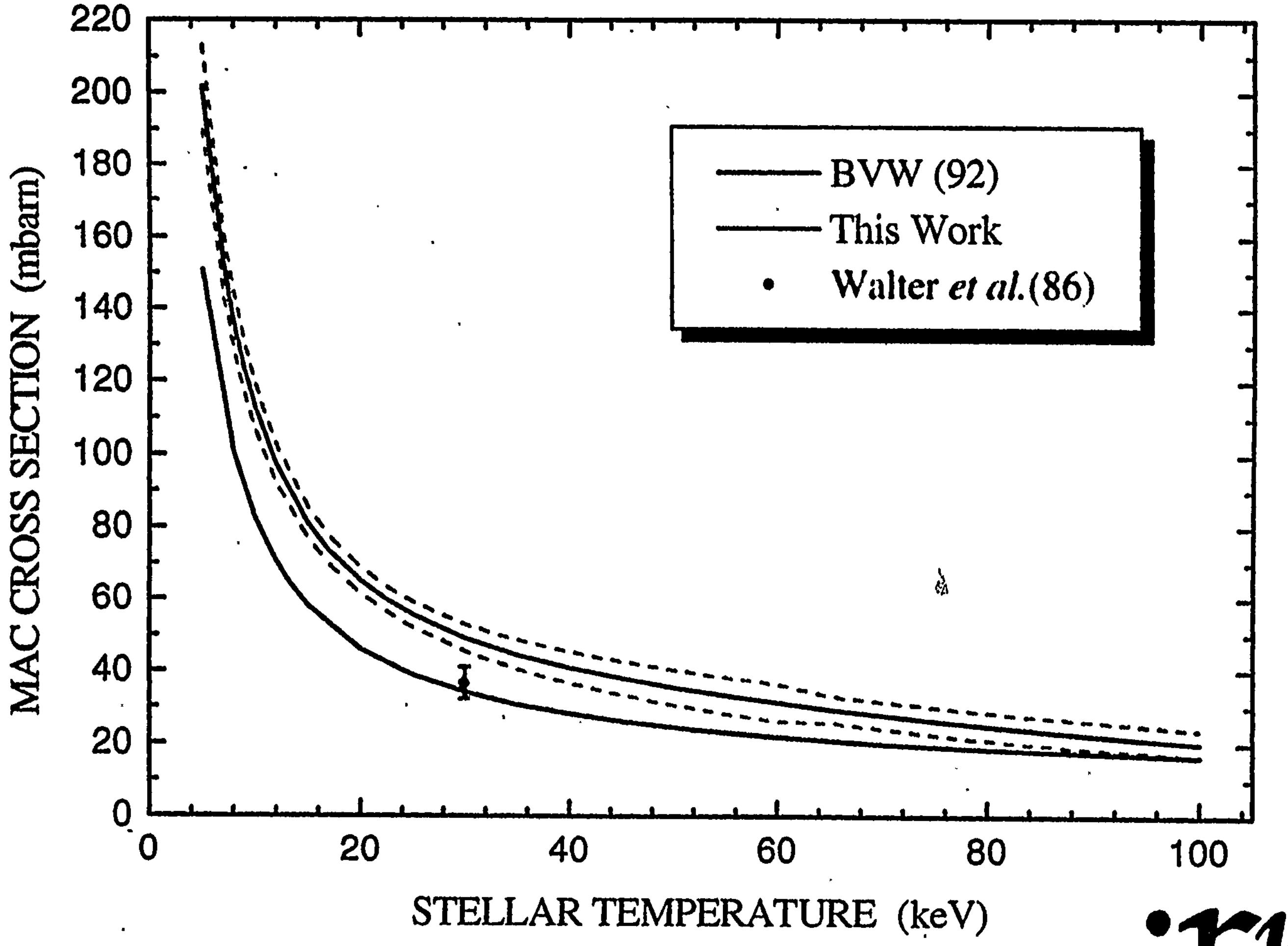

^{86}Kr MAC Cross Section

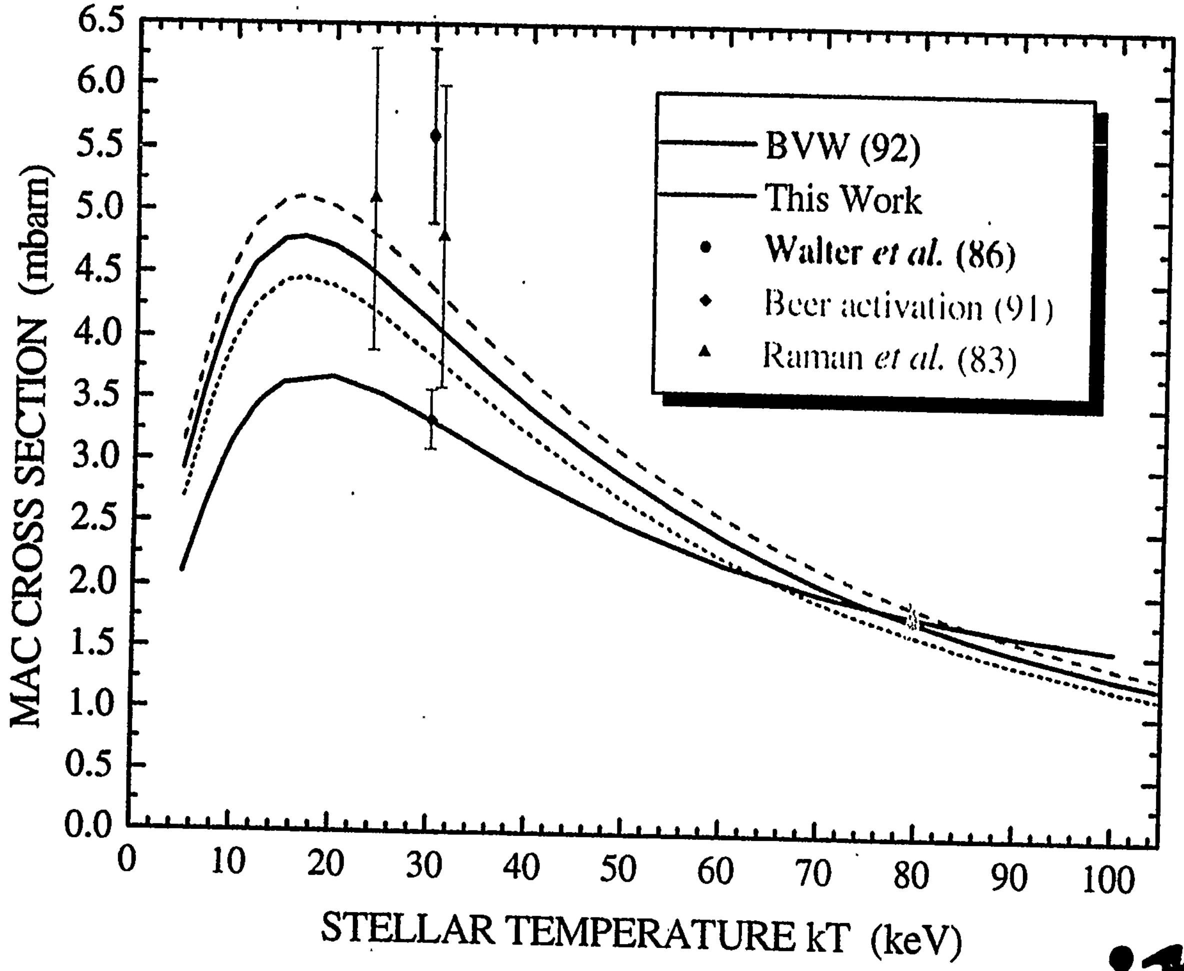

Halflives of rp-process Waitingpoint Nuclei

Paul Kienle
Technical University - Munich

A large number of nuclei near the proton drip line has been produced by fragmentation reactions of a 1 A GeV ^{112}Sn on a ^{9}Be target. The reaction products were anlyzed with respect to their nuclear charge Z and mass number by the fragment separator FRS at GSI, Darmstadt. In addition two ionization chambers identified the Z independently. The ions were stopped in the middle of a stack of Si detectors, which detected in 4π geometry succeeding decays by β (or proton) emission. Because of the segmentation of the stopping detectors, the decays could be correlated in space and time with the stopped nucleus.

Halflives of rp-Process Waiting Point Nuclei

E. Wefers[a], T. Faestermann[a], M. Münch[a], R. Schneider[a], A. Stolz[a],
K. Sümmerer[b], J. Friese[a], H. Geissel[b], M. Hellström[c], P. Kienle[a], H.-J. Körner[a],
G. Münzenberg[b], C. Schlegel[b], P. Thirolf[d], H. Weick[b], and K. Zeitelhack[a]

[a]*Technische Universität München, 85748 Garching, Germany,* [b]*Gesellschaft für Schwerionenforschung mbH, 64291 Darmstadt, Germany,* [c]*Lund University, 22100 Lund, Sweden and* [d]*Ludwig-Maximilians-Universität, 85748 Garching, Germany*

Abstract. The fragment separator at GSI, Darmstadt, has been used to produce and separate very proton rich nuclei in the ^{100}Sn region. By fragmentation of a ^{112}Sn beam at 1 A·GeV we produced nuclei along the rp-process path between ^{77}Y and ^{98}In. By implanting these ions into a silicon detector stack we were able to determine their halflives. Preliminary data are presented.

Neutron deficient nuclei near ^{100}Sn have been produced by fragmentation of a 1 A·GeV ^{112}Sn beam in a beryllium target. The fragments were separated in the 0° magnetic spectrometer FRS at GSI, Darmstadt, and identified with detector systems, tracking the ion position through the FRS and measuring the energy loss and the time of flight. The unambiguously identified ions (see fig. 1) were stopped in an implantation detector. Among others we identified two ^{76}Y and one ^{78}Zr ions.

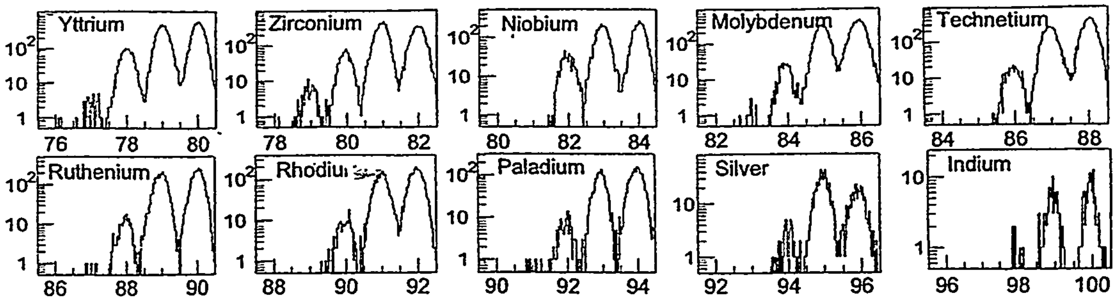

FIGURE 1. Identification plots (preliminary).

The implantation zone of our detector consists of four two-sided Si-strip detectors ($64 \times 25 \times 0.5\,\mathrm{mm}^3$) with a strip pitch of 0.5 mm on both sides (x and y direction), mounted in a compact stack. By correlating the implantation position of an identified ion with its decay position we were able to suppress the background effectively and to determine the halflives of the implanted ions. Around the implanation zone two 10 mm thick stacks of Si detectors were mounted for the β-energy measurement. For gamma spectroscopy about 25% of the solid angle was covered by a segmented Clover germanium detector.

One purpose of this experiment was to measure the Gamov-Teller-Strength and the γ spectrum in the decay of ^{100}Sn, ^{102}Sn and ^{98}Cd. During a 50 hrs run only one event could be clearly identified as ^{100}Sn, for ^{102}Sn and ^{98}Cd we observed some 1000 decays respectively. These data are still being analyzed.

The nuclei with even Z near the proton dripline below ^{100}Sn are waiting points in the rp-process and their halflives determine the flux towards heavier nuclei and the respective isotopic abundances. We measured for the first time the halflives of these nuclei from ^{80}Zr up to ^{92,93}Pd.

On the other hand the rp-process flux is determined by the proton dripline. Therefore we investigated the possibly proton-unstable nuclei ^{77}Y and ^{81}Nb. ^{77}Y ions could be identified and we observed their decay with a short halflife, consistent with a superallowed Fermi beta decay. From the non-observation of ^{81}Nb we deduce a halflife shorter than 200 ns, considering the flight time through the fragment separator.

We also investigated the six cases of odd-odd $N = Z$ nuclei between ^{78}Y and ^{98}In, which are the heaviest nuclei where one can hope to study pure Fermi beta transitions. In a very preliminary analysis of our data we are able to show that even ^{90}Rh and ^{94}Ag are Fermi beta emitters. For the three lighter members of this series ^{78}Y to ^{86}Tc a low lying T=1, 0^+ state decaying with a superallowed Fermi transition was recently detected at GANIL [1]. Our new data on these nuclei are in good agreement.

Finally we measured the halflives of so far unknown Rh and Tc isotopes near the $N = Z$-line. First (preliminary) results and their statistical errors are shown in the table below. Up to now only a part of the data is analyzed.

Isotope	^{77}Y	^{78}Y	^{80}Zr	^{82}Nb	^{84}Mo	^{85}Mo
Halflife	53^{+29}_{-14} ms	67^{+18}_{-12} ms	$5.7^{+0.9}_{-0.7}$ s	44^{+8}_{-6} ms	$3.6^{+1.0}_{-0.7}$ s	$6.3^{+1.3}_{-1.0}$ s
Isotope	^{86}Tc	^{87}Tc	^{88}Ru	^{89}Ru	^{90}Rh	^{91}Rh
Halflife	45^{+10}_{-7} ms	$1.9^{+0.2}_{-0.2}$ s	$1.1^{+0.4}_{-0.2}$ s	$1.6^{+0.3}_{-0.2}$ s	44^{+60}_{-16} ms	$1.8^{+0.3}_{-0.3}$ s
Isotope	^{92}Rh	^{93}Rh	^{92}Pd	^{93}Pd	^{94}Ag	^{98}In
Halflife	$2.9^{+1.5}_{-0.8}$ s	$5.7^{+1.3}_{-0.9}$ s	$0.7^{+0.4}_{-0.2}$ s	$9.3^{+2.5}_{-1.7}$ s	38^{+38}_{-13} ms	to be analyzed

Acknowledgments

We would like to thank J. Gerl and R. Simon for providing us the γ-detectors, and the FRS group for their help during our beamtime.

This work was supported by BMBF (06TM872 TPI) and SFB 375.

REFERENCES

1. C. Longour et al., Phys. Rev. Lett. 81 (1998) 3337

Halflifes of rp-Process Waiting Point Nuclei

E. Wefers[1], T. Faestermann[1], M. Münch[1], R. Schneider[1], A. Stolz[1], K. Sümmerer[2], J. Friese[1],
H. Geissel[2], J. Gerl[2], M. Hellström[3], P. Kienle[1], H.-J. Körner[1], G. Münzenberg[2], C. Schlegel[2],
K. Schmidt[2], R. Simon[2], P. Thirolf[4], H. Weick[2], K. Zeitelhack[1]

[1]Physik-Department E12, TU Munich [2]Gesellschaft für Schwerionenforschung, Darmstadt [3]University of Lund, Sweden
[4]Ludwig Maximilians Universität, Munich

Fragmentation Program

- Cross sections of production of nuclei far off stability (^{100}Sn ....)
- GT-strength in the ^{100}Sn-, ^{102}Sn-, ^{98}Cd-decays
- Particle-hole-states around N=Z=50
- Superallowed Fermi decays of heavy N=Z odd-odd nuclei
- Even Z-nuclei near the p-dripline, as waiting point nuclei for the rp-process
- p-decay unstable nuclei

Hendrik Schatz

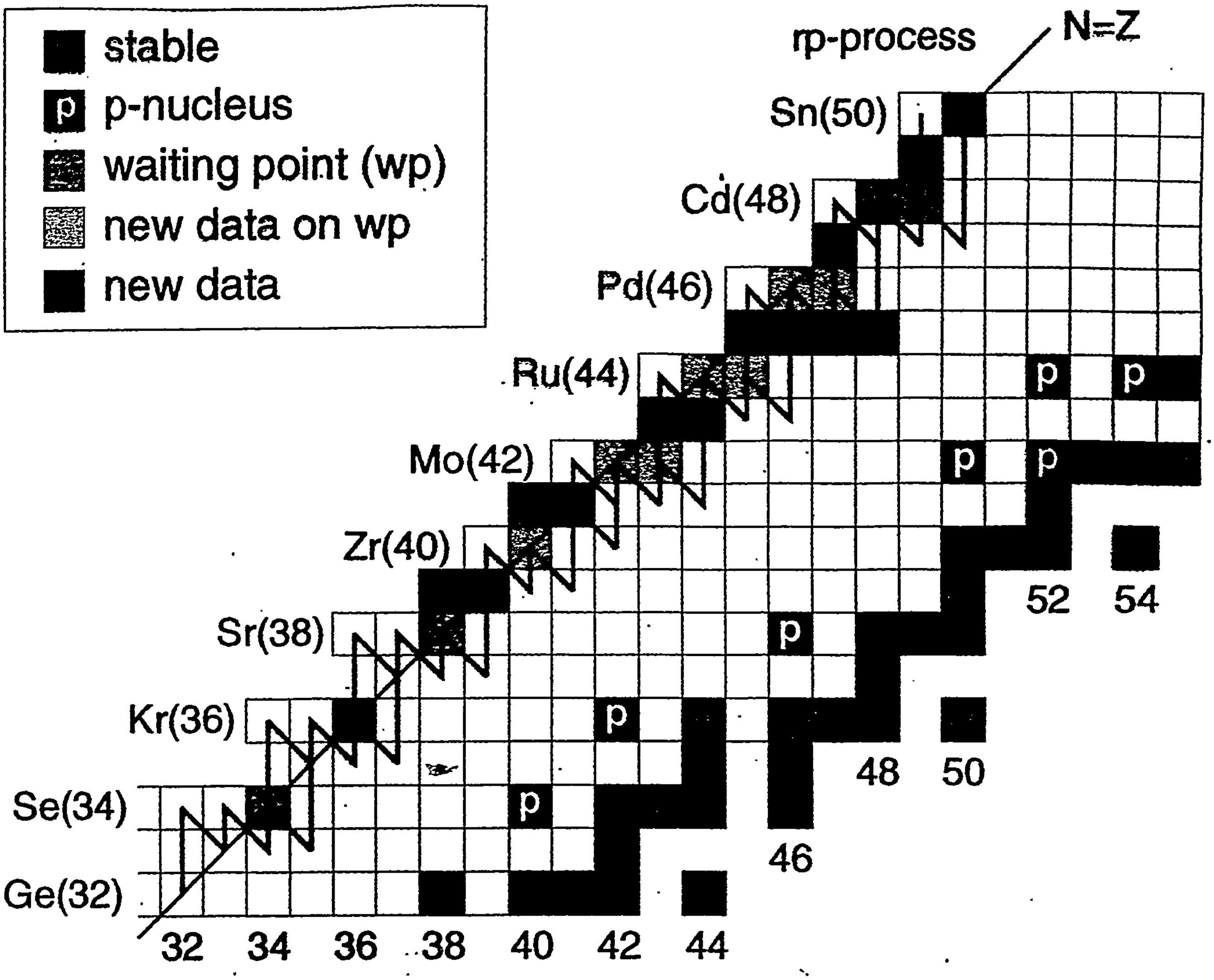

GSI Accelerator Complex

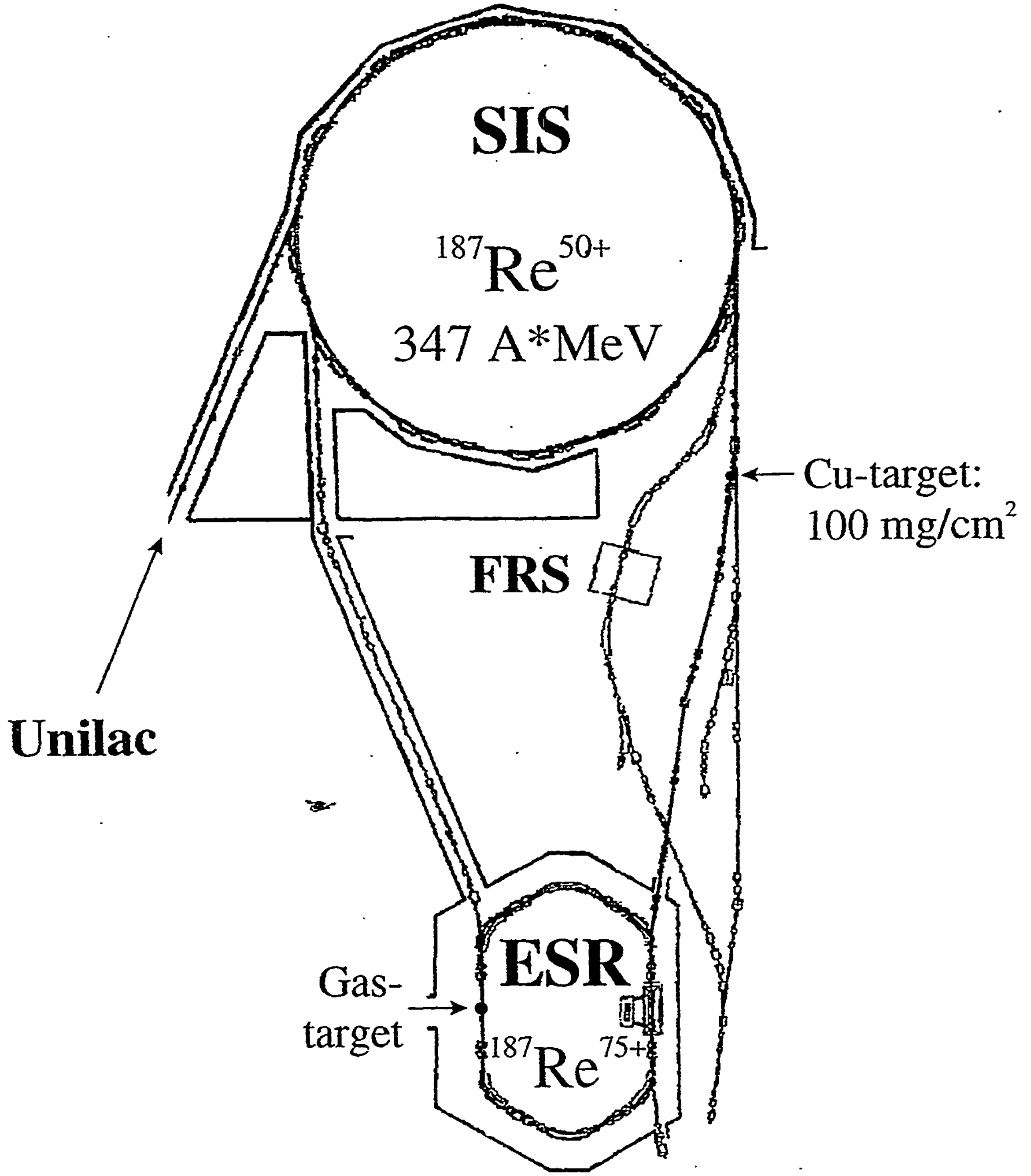

Notizen:

FRS-Setup

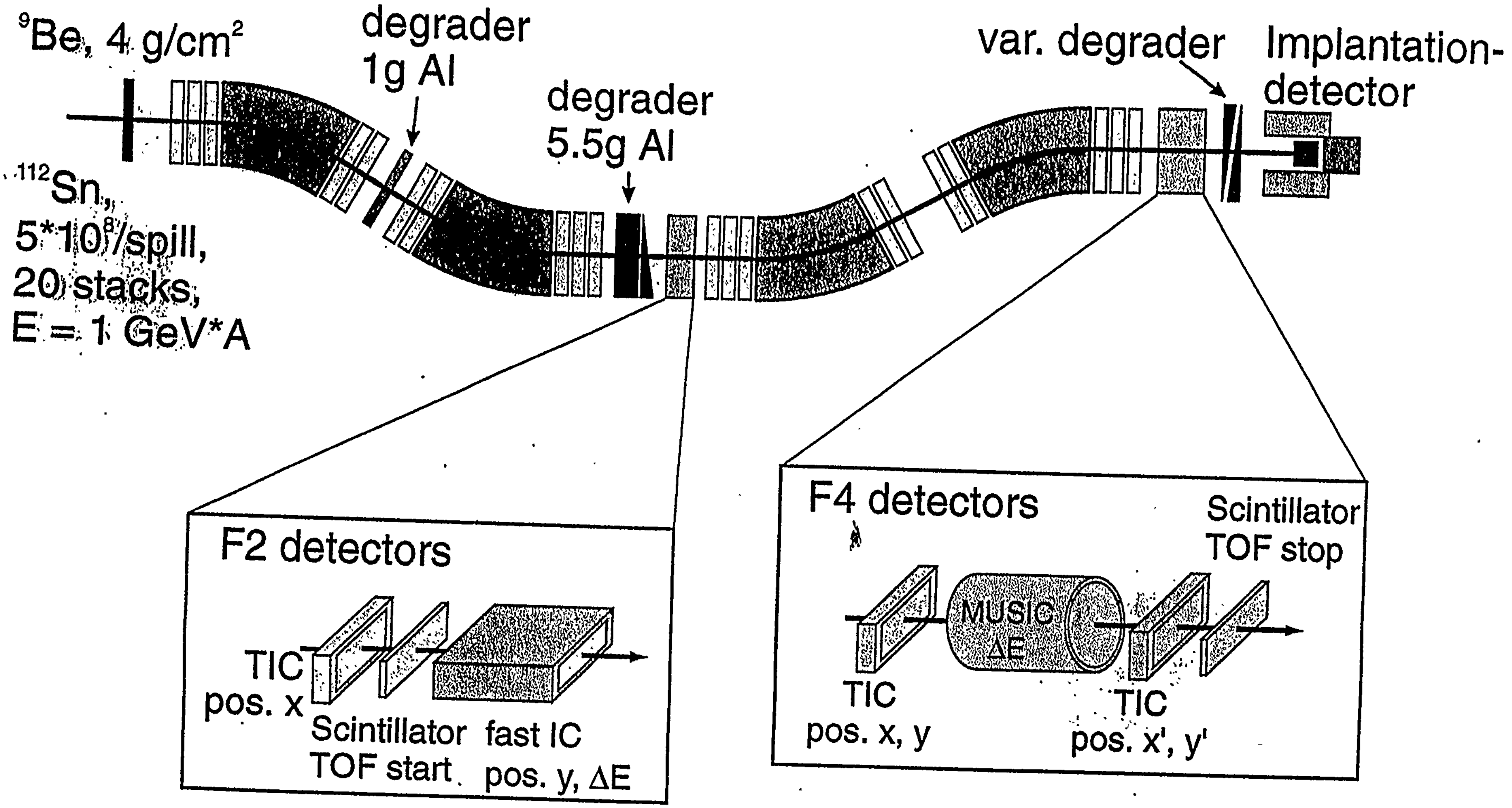
^{9}Be, 4 g/cm^{2}
^{112}Sn,
5*10^{8}/spill,
20 stacks,
E = 1 GeV*A
degrader
1g Al
degrader
5.5g Al
var. degrader
Implantation-
detector
F2 detectors
TIC
pos. x
Scintillator
TOF start
fast IC
pos. y, ΔE
F4 detectors
Scintillator
TOF stop
MUSIC
ΔE
TIC
pos. x, y
TIC
pos. x', y'

Implantationdetector

β-calorimeter
2×10 Si-PIN dectors
60×40×1 mm^3
7-fold segmented
$\Delta E < 30$ keV, $E_\beta < 10$ MeV

Silicon detectorstack:
4π-detector for
- α-decay (E_α= 10 MeV)
- β-decay (E_β= 10 MeV)
- p emission
- halflife t > 1ms

efficiency ~ 100%

<u>Implantation zone</u>
4 double sided Si-strip
detectors: 64×25 mm^2 ×
500 μm: 128 vertical ×
50 horizontal strips (0.5 mm
8192 pixels

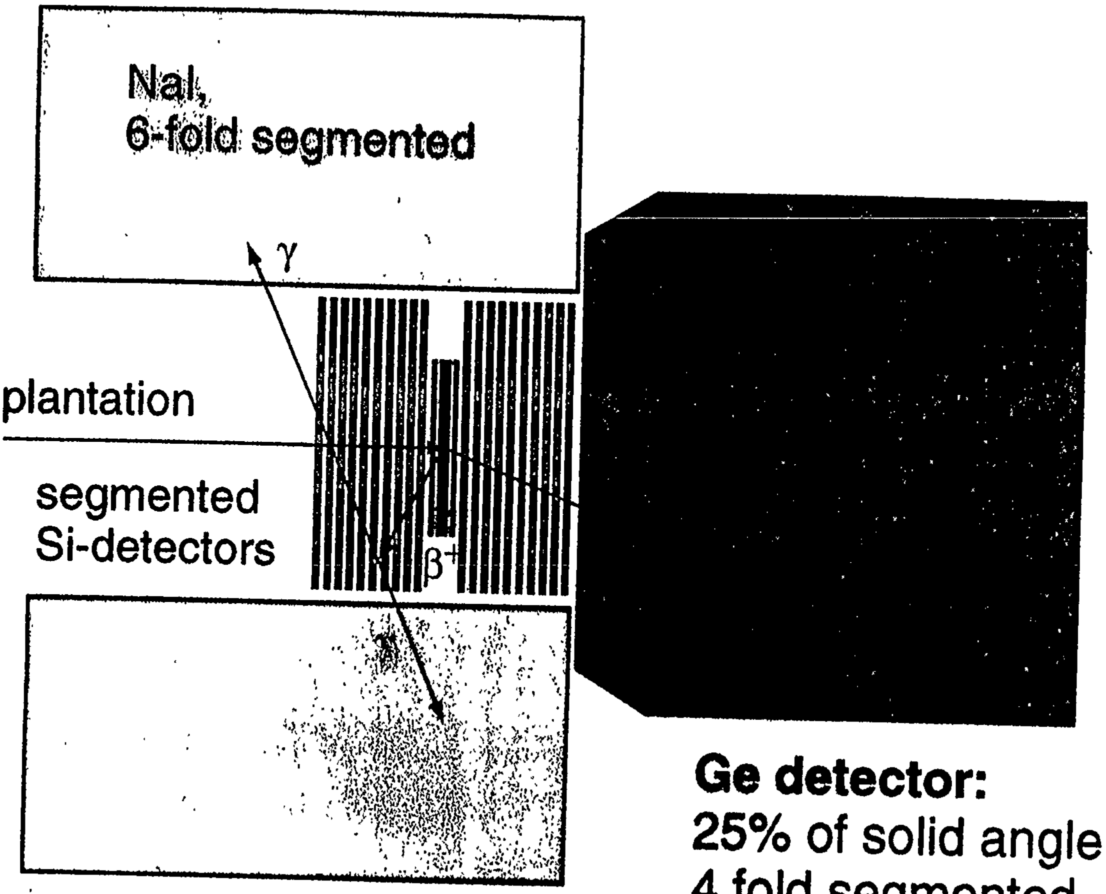

NaI,
6-fold segmented

implantation

segmented
Si-detectors

NaI-detector:
60% of solid angle
6 segments

Ge detector:
25% of solid angle
4 fold segmented
E-resolution ~ 2.5 keV

Implantationdepth

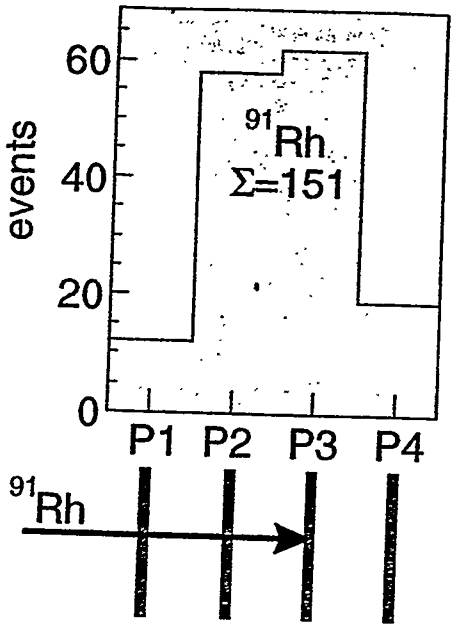

Decay of ^{77}Y and its daughter

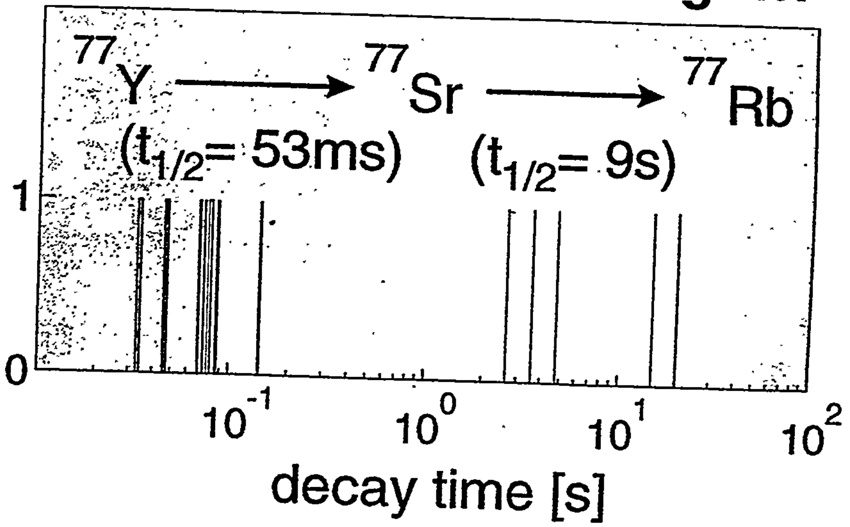

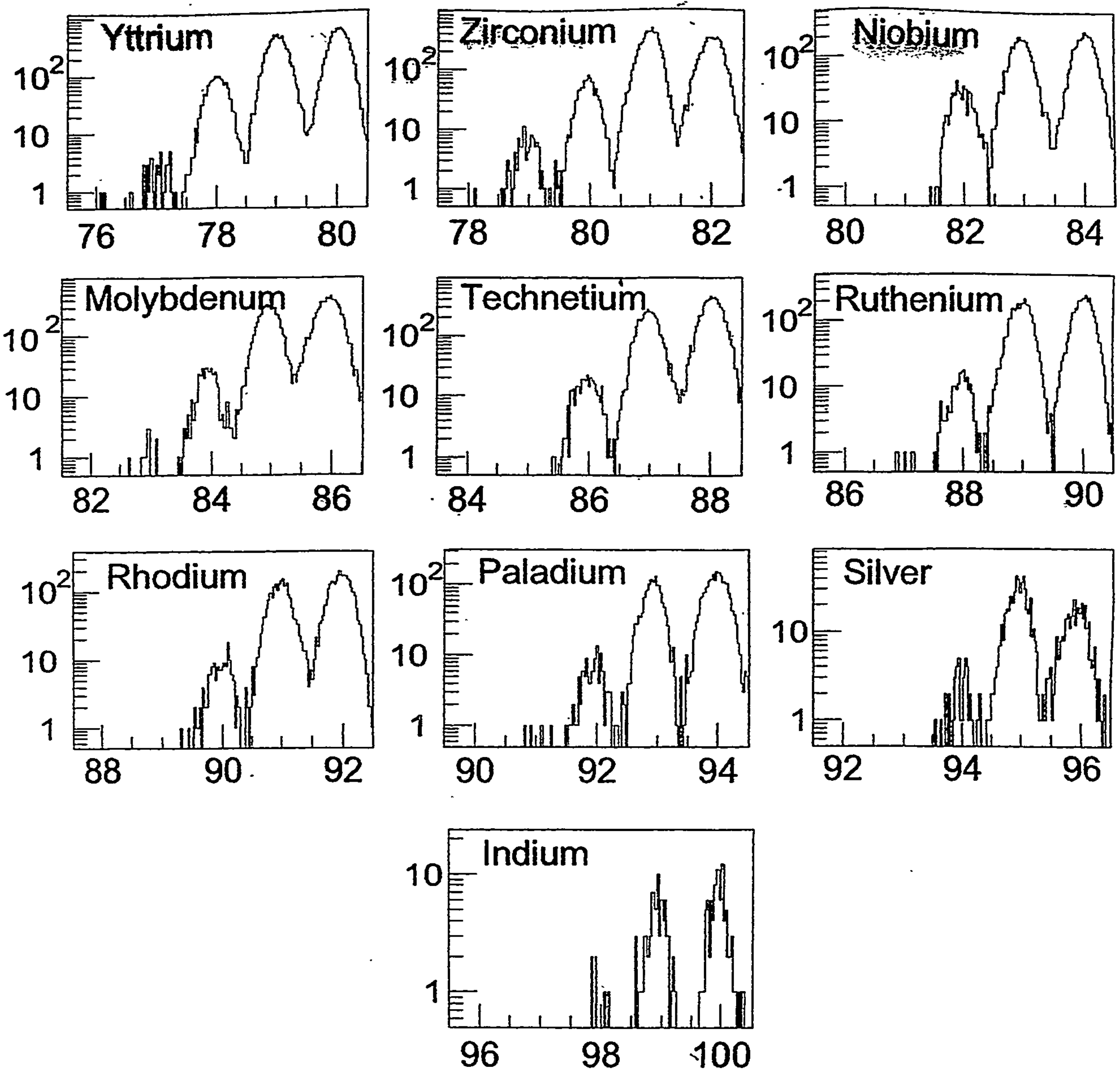
Yttrium
Zirconium
Niobium
Molybdenum
Technetium
Ruthenium
Rhodium
Paladium
Silver
Indium
10^2
10
1
76
78
80
82
84
86
88
90
92
94
96
98
100

First Results - very preliminary!

Isotope	Decays	Halflife $t_{1/2}$
^{77}Y	8	53^{+29}_{-14} ms
^{78}Y	23	67^{+18}_{-12} ms
^{80}Zr	62	$5.7^{+0.9}_{-0.7}$ s
^{82}Nb	43	44^{+8}_{-6} ms
^{84}Mo	24	$3.6^{+1.0}_{-0.7}$ s
^{86}Tc	28	45^{+10}_{-7} ms
^{87}Tc	155	$1.9^{+0.2}_{-0.2}$ s
^{88}Ru	20	$1.1^{+0.4}_{-0.3}$ s
^{89}Ru	79	$1.6^{+0.3}_{-0.2}$ s
^{90}Rh	3	44^{+60}_{-20} ms
^{91}Rh	55	$1.8^{+0.3}_{-0.3}$ s
^{92}Pd	11	$0.7^{+0.4}_{-0.2}$ s
^{92}Rh	9	$2.9^{+1.5}_{-0.7}$ s
^{94}Ag	4	38^{+38}_{-13} ms
^{98}In	<6	?

Photoactivation of ^{180m}Ta and Implications for the Nucleosynthesis of Nature's Rarest Stable Isotope

H. H. Pitz
Universität Stuttgart

The exotic odd-odd nucleus ^{180}Ta carries a dual distinction. It is nature's rarest isotope with a relative abundance of 0.02% of the rarest element tantalum and the only naturally occuring isomer with a half-life longer than 10^{15} years (while $T_{1/2} = 8.15$ h for the ground state). The nucleosynthesis of ^{180}Ta remains a puzzle [1] because it does not lie in the main path of the *s* process and it is shielded against the *r* process by the stable isobar ^{180}Hf. However, more exotic *s* process production paths have been suggested via β decay of a high-spin isomer in ^{180}Hf [2] or β decay of thermally excited levels in ^{179}Hf and subsequent neutron capture on the radioactive ^{179}Ta [3]. Recent experimental results [4] limit the former possibility to 20% of the solar abundance while for an estimate of the latter data on the ^{179}Ta capture cross section are missing. A complication of any *s*-process scenario is a possible coupling between isomer and ground state via intermediate states (IS) at higher excitation energies in the accompanying thermal photon bath. This could drastically alter the half-life under stellar conditions. Large cross sections have been observed [5,6] for such a process in irradiations with bremsstrahlung, but at IS energies too high [5] for a significant population at typical *s*-process temperatures of about $3 \bullet 10^8$ K. We report a new search [7] for astrophysically relevant IS at the DYNAMITRON accelerator in Stuttgart. By combining the high electron currents available there with an optimized off-line system for detection of the ^{180}Ta ground state decay and a target consisting of the world's resources of ^{180}Ta enriched material (150 mg Ta_2O_5 at 5.45%) we have been able to identify IS at photon energies as low as 1 MeV. This results in a drastic reduction of the effective half-life during the *s* process. Consequences for a possible *s*-process nucleosynthesis of ^{180}Ta are discussed.

[1] F. Käppeler, H. Beer, and K. Wisshak, Rep. Prog. Phys. 52, 945 (1989).
[2] H. Beer and R. A. Ward, Nature **291**, 308 (1981).
[3] K. Yokoi and K. Takahashi, Nature **305**, 198 (1983).
[4] S. E. Kellogg and E. B. Norman, Phys. Rev. C **46** , 1115 (1992).
[5] C.B. Collins *et al.*, Phys. Rev.C 42, R1813 (1990).
[6] Zs. N'emeth, F. Käppeler, and G. Reffo, Astrophys. J. 392, 277 (1992).
[7] D. Belic *et al.*, Phys. Rev. Lett. (submitted).

Work performed by : D. Belic[1], C. Arlandini[2], J. Besserer[3], J. de Boer[3], J.J. Carroll[4], J. Enders[5], T. Hartmann[5], F. Käppeler[2], H. Kaiser[5], U. Kneissl[1], M. Loewe[3], H. Maser [1], P. Mohr[5], P. von Neumann-Cosel[5], A. Nord[1], H.H. Pitz[3], A. Richter[5], M. Schumann [2], S. Volz[5], A. Zilges[5]

1. Institut für Strahlenphysik, Universität Stuttgart, D-70569 Stuttgart, Germany
2. Forschungszentrum Karlsruhe, Institut für Kernphysik, D-76021 Karlsruhe, Germany
3. Sektion Physik, Ludwig-Maximilians-Universität München, D-85748 Garching, Germany
4. Department of Physics and Astronomy, Youngstown State University, Youngstown, Ohio 44555
5. Institut für Kernphysik, Techn. Universität Darmstadt, D-64289 Darmstadt, Germany

Photoactivation of ^{180m}Ta and Implications for the Nucleosynthesis of Nature´s Rarest Stable Isotope

Darmstadt - Karlsruhe - München - Stuttgart -
Youngstown Collaboration

- **Motivation**
- **Photoactivation with bremsstrahlung**
- **Experimental setup**
- **Results**
  - Photon energy and photon flux determination (^{115}In)
  - Half-life measurement
  - Photoactivation yields
- **Astrophysical consequences**
- **Summary**

H. H. Pitz, D. Belic, C. Arlandini, J. Besserer, J. de Boer, J. J. Carroll, J. Enders,
T. Hartmann, F. Käppeler, H. Kaiser, U. Kneissl, M. Loewe, H. J. Maier,
H. Maser, P. Mohr, P. von Neumann-Cosel, A. Nord, A. Richter,
M. Schumann, S. Volz, A. Zilges

Nucleosynthesis of ^{180m}Ta

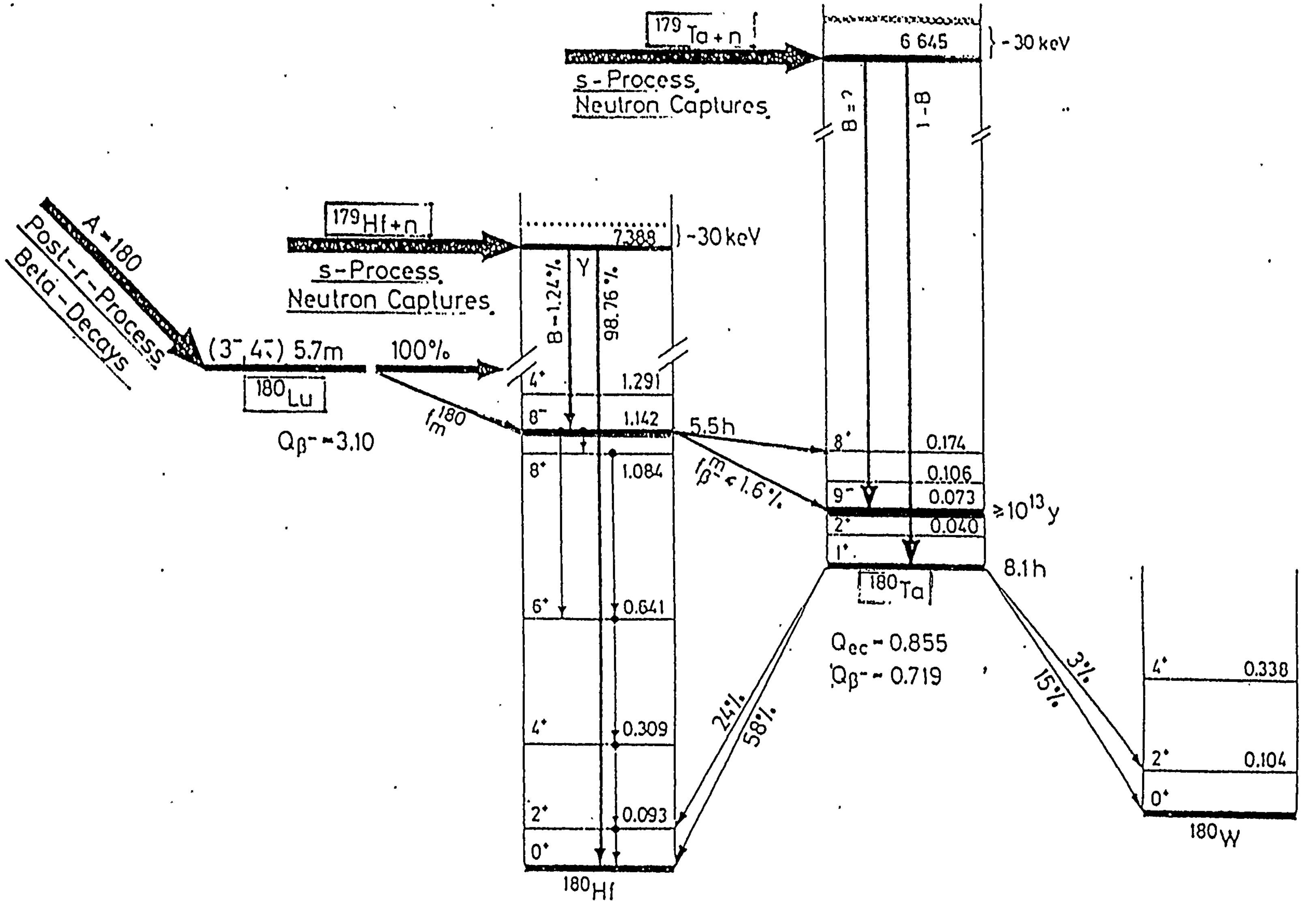

Depopulation of ^{180m}Ta by Real Photons

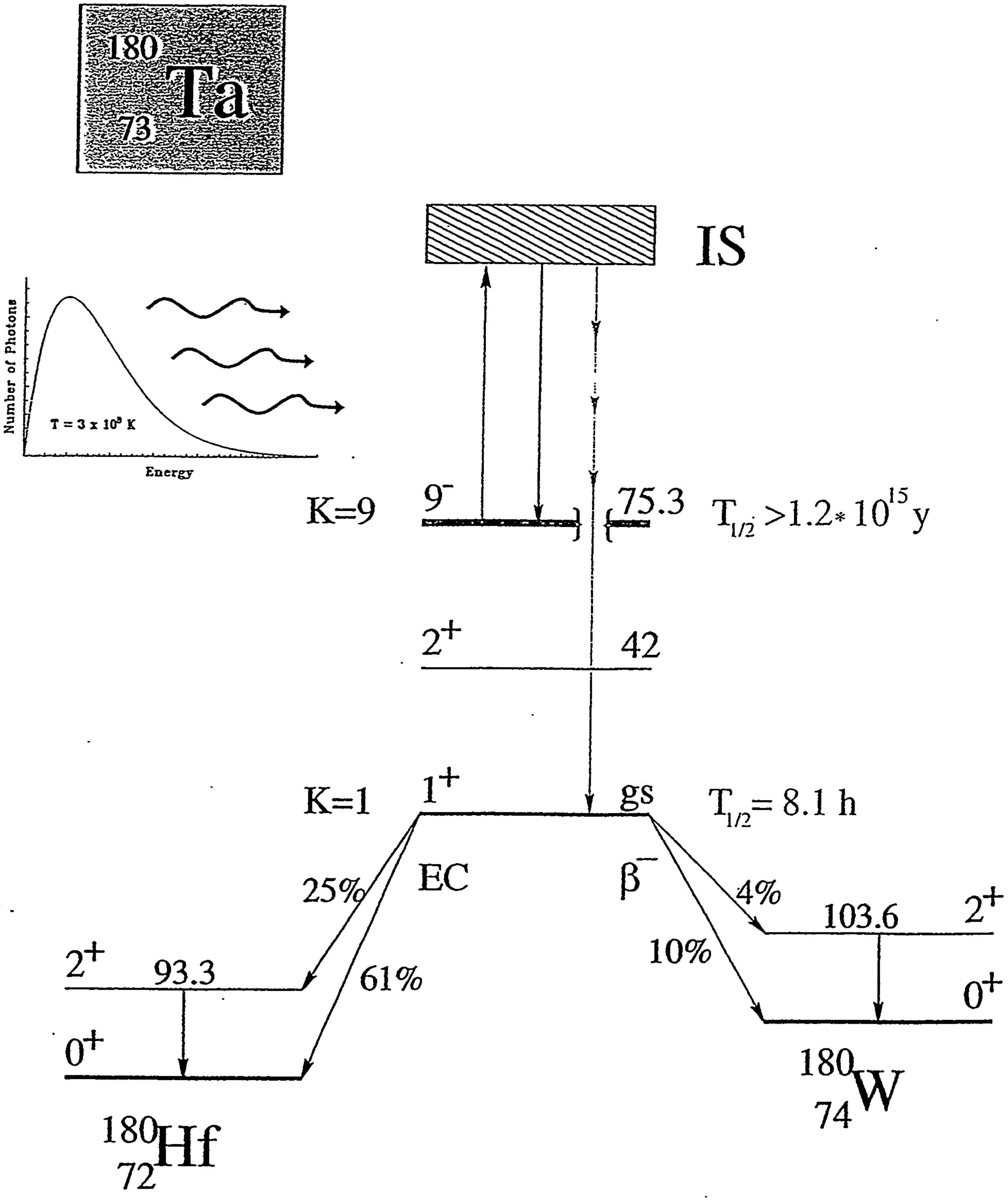

Photoactivation Using Bremsstrahlung

PRINCIPLE OF THE METHOD

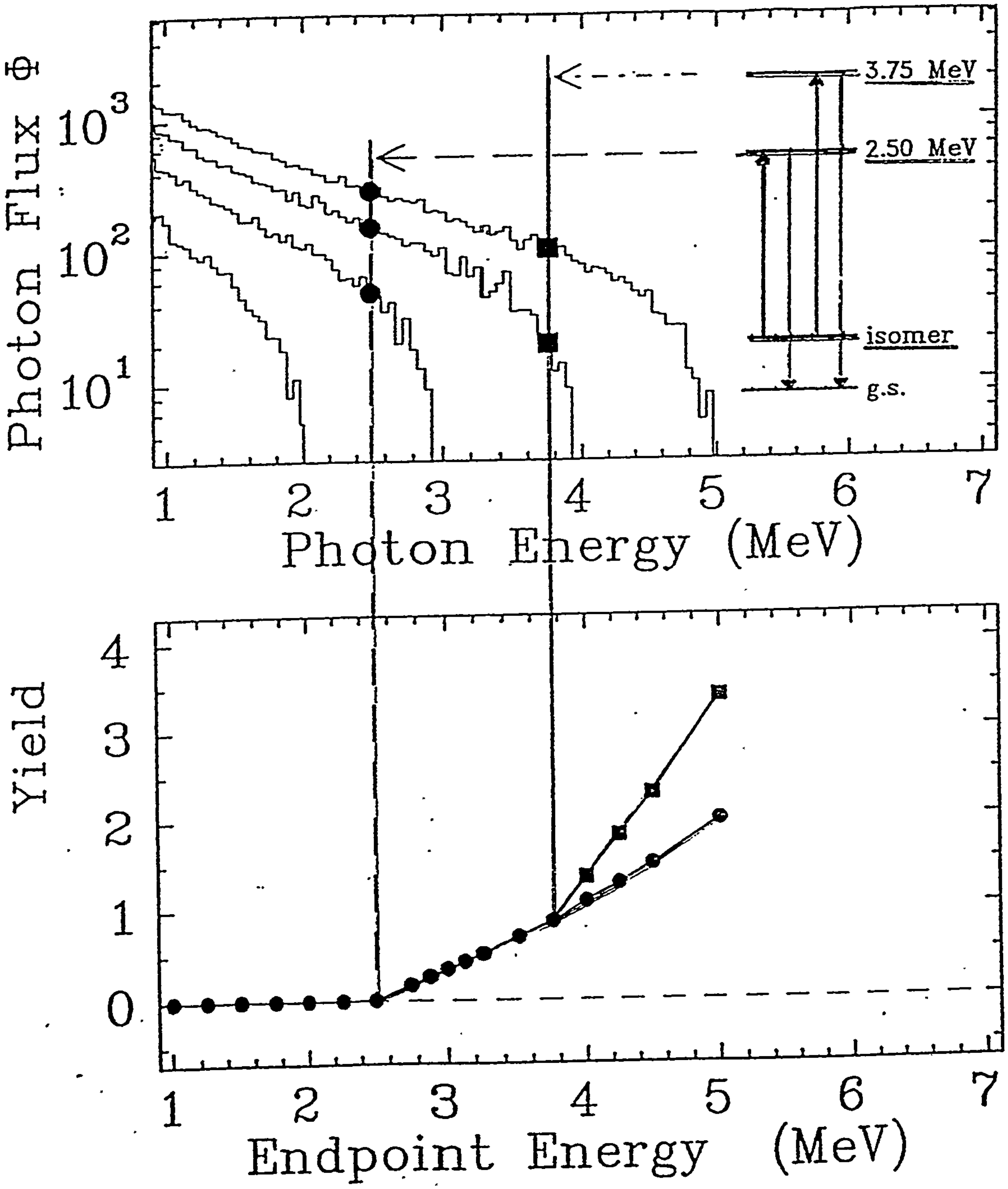

$$\boxed{Y\ (E_0) = \int_0^{E_0} \sigma_\gamma (E_\gamma) \cdot \underline{N_{BS}(E_0,\, E_\gamma)} \cdot dE_\gamma}$$

Figures from : C. Spieler, Diploma Thesis, TH Darmstadt 1993, unpublished

Experimental Setup at Stuttgart

Photoactivation of ^{180m}Ta

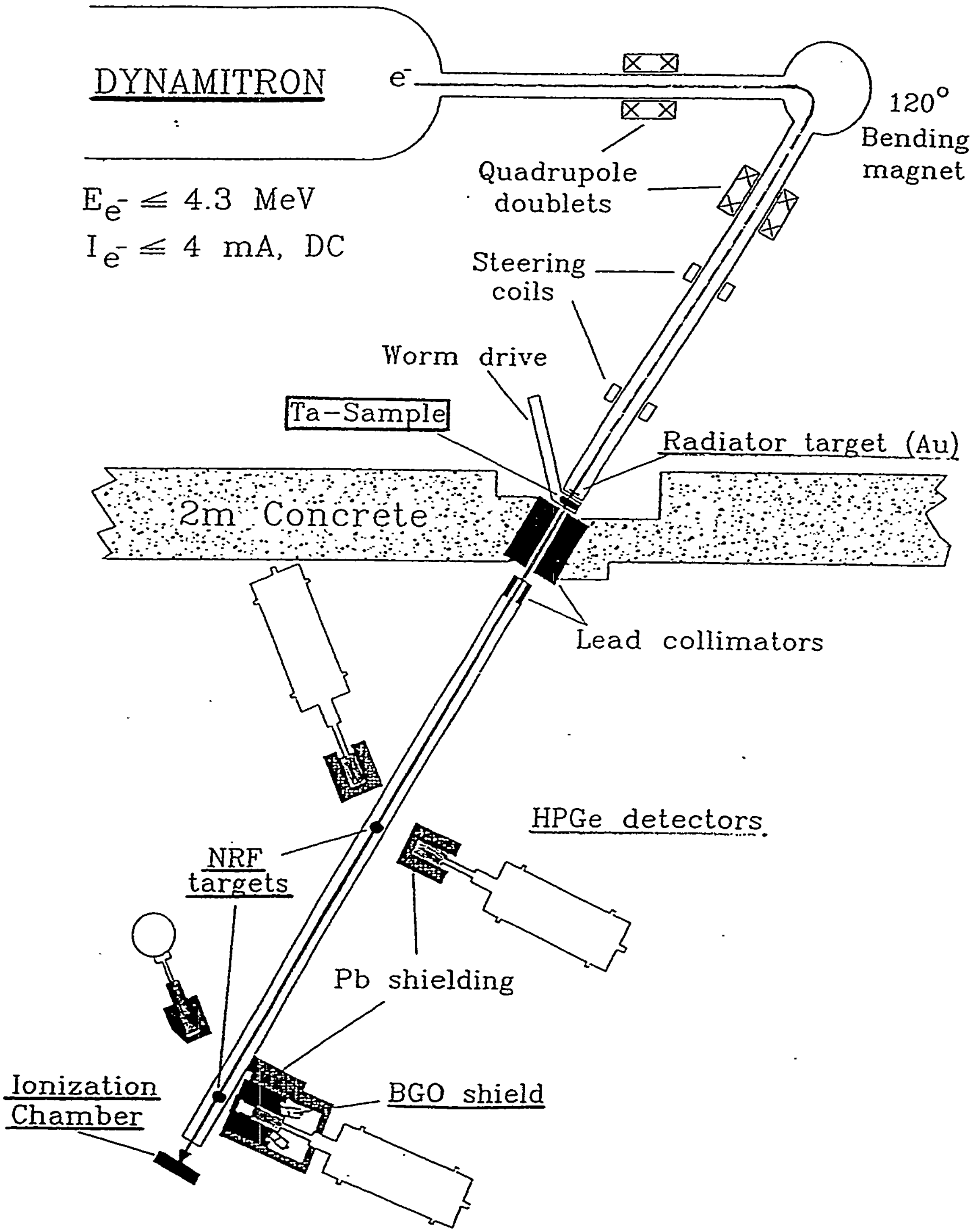

Darmstadt-Karlsruhe-München-Stuttgart – Collaboration

Bremsstrahlung Irradiation Facility

at the STUTTGART 4 MV DYNAMITRON

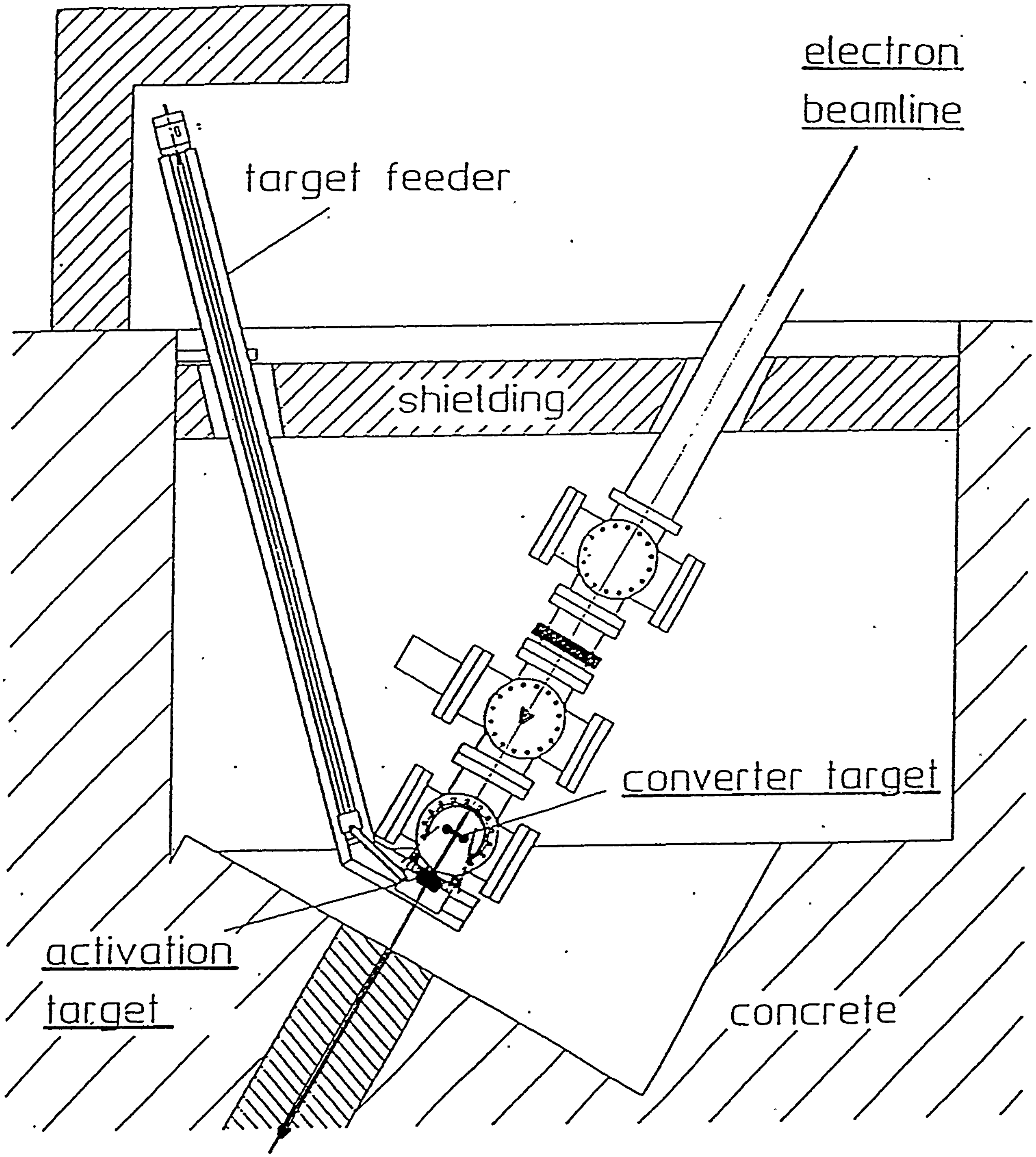

DARMSTADT-KARLSRUHE-MÜNCHEN-STUTTGART – COLLABORATION

Photon Beam Parameters

Online Flux Determination

- Integrated Flux
  - ➡ Integrated e^--current
  - ➡ Ionisation Chamber

- Spectral Photon Distribution
  - ➡ NRF with Mixed Target (LiF/Cu/Al)

- At Target Position
  - ➡ $\boxed{{}^{115}\mathrm{In}\,(\gamma,\gamma')\,{}^{115m}\mathrm{In}}$

Offline Flux Determination

- MC-Simulations with GEANT and EGS

Energy Calibration

- Rotating Voltmeter
- NRF on Pb
- NRF with ${}^{27}\mathrm{Al}/{}^{13}\mathrm{C}$-Target

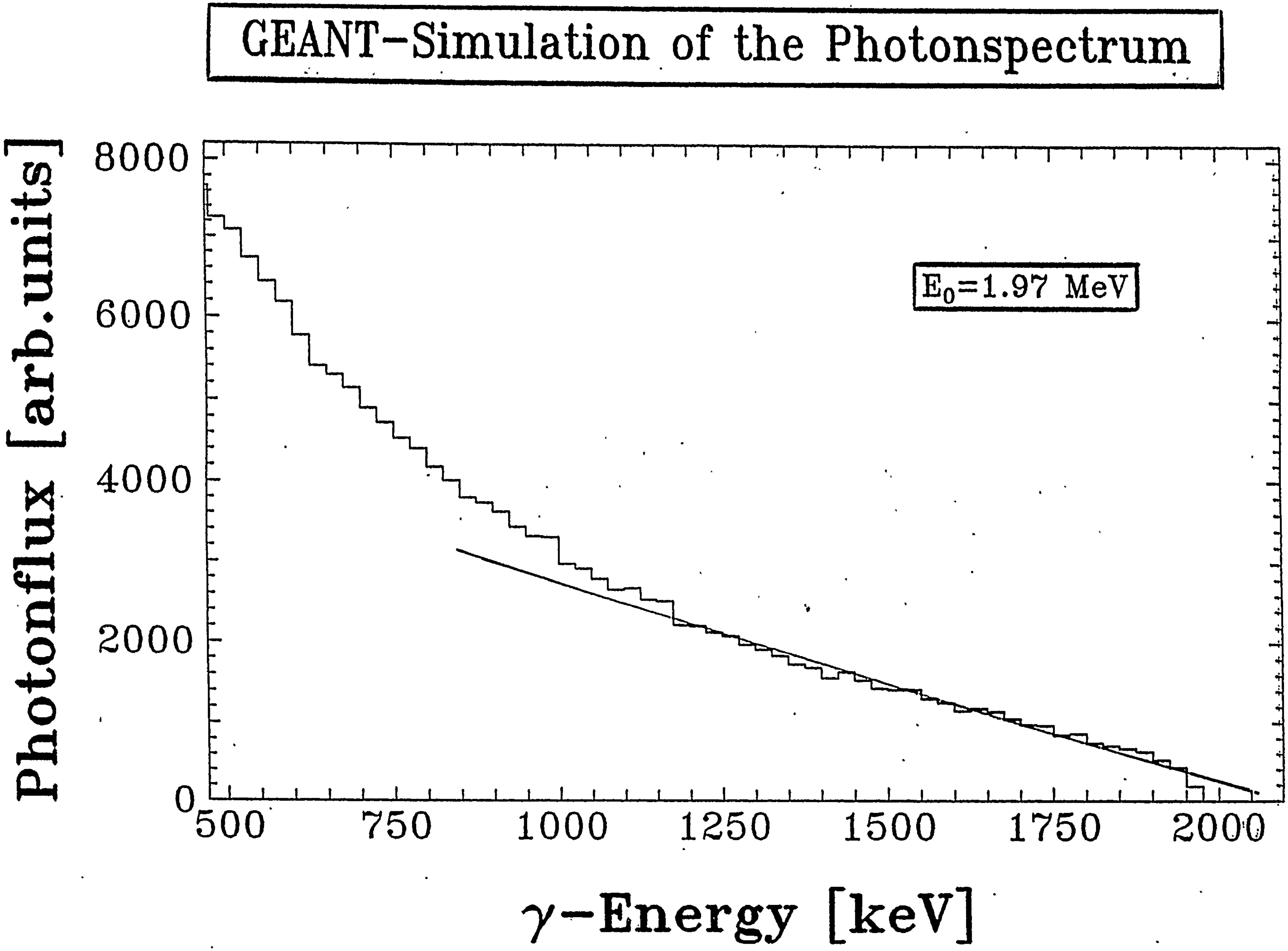
GEANT-Simulation of the Photonspectrum
Photonflux [arb.units]
8000
6000
4000
2000
0
500
750
1000
1250
1500
1750
2000
E_0=1.97 MeV
γ-Energy [keV]

Level Scheme of ^{115}In

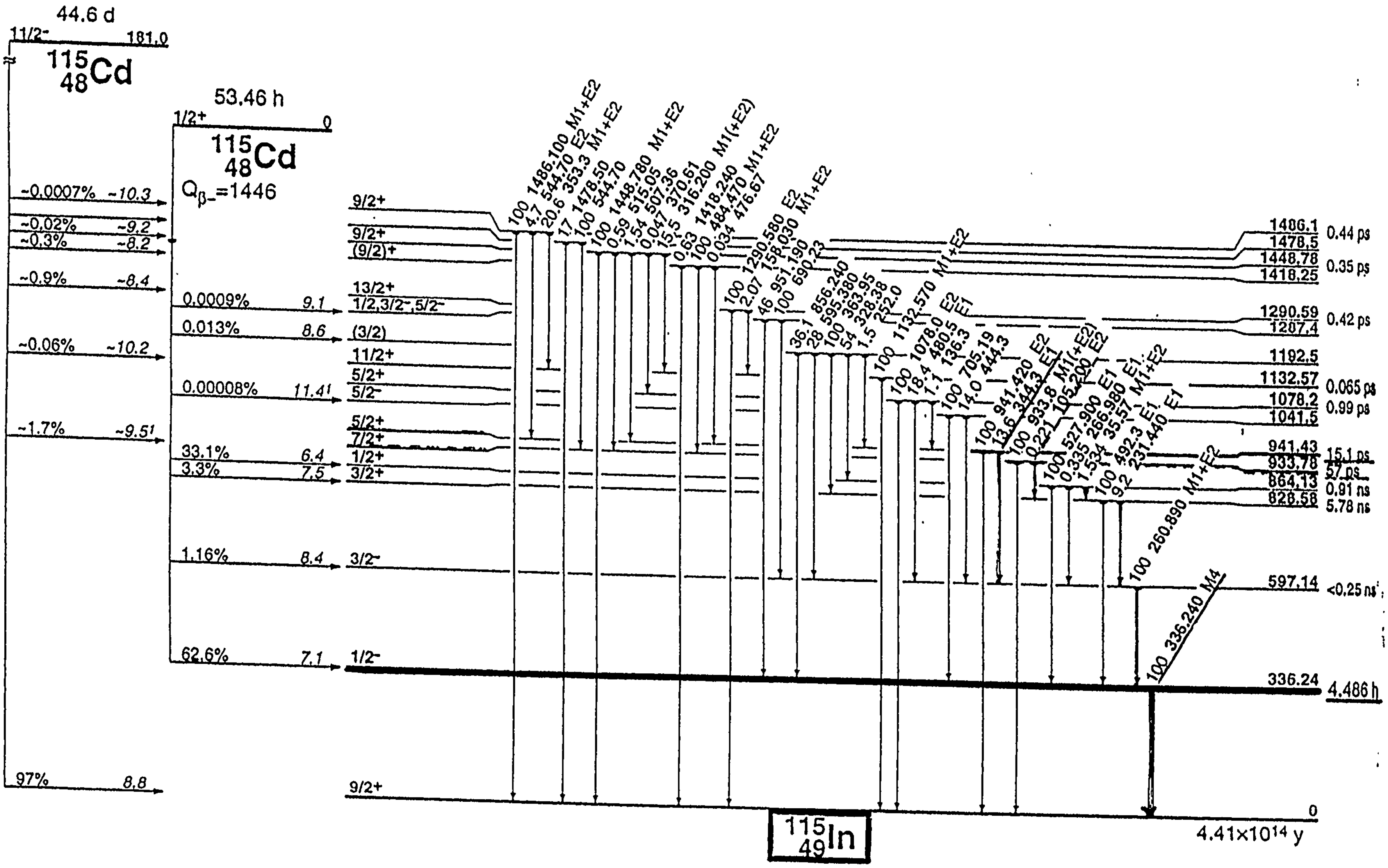

Threshold for Photoactivation of ^{115}In

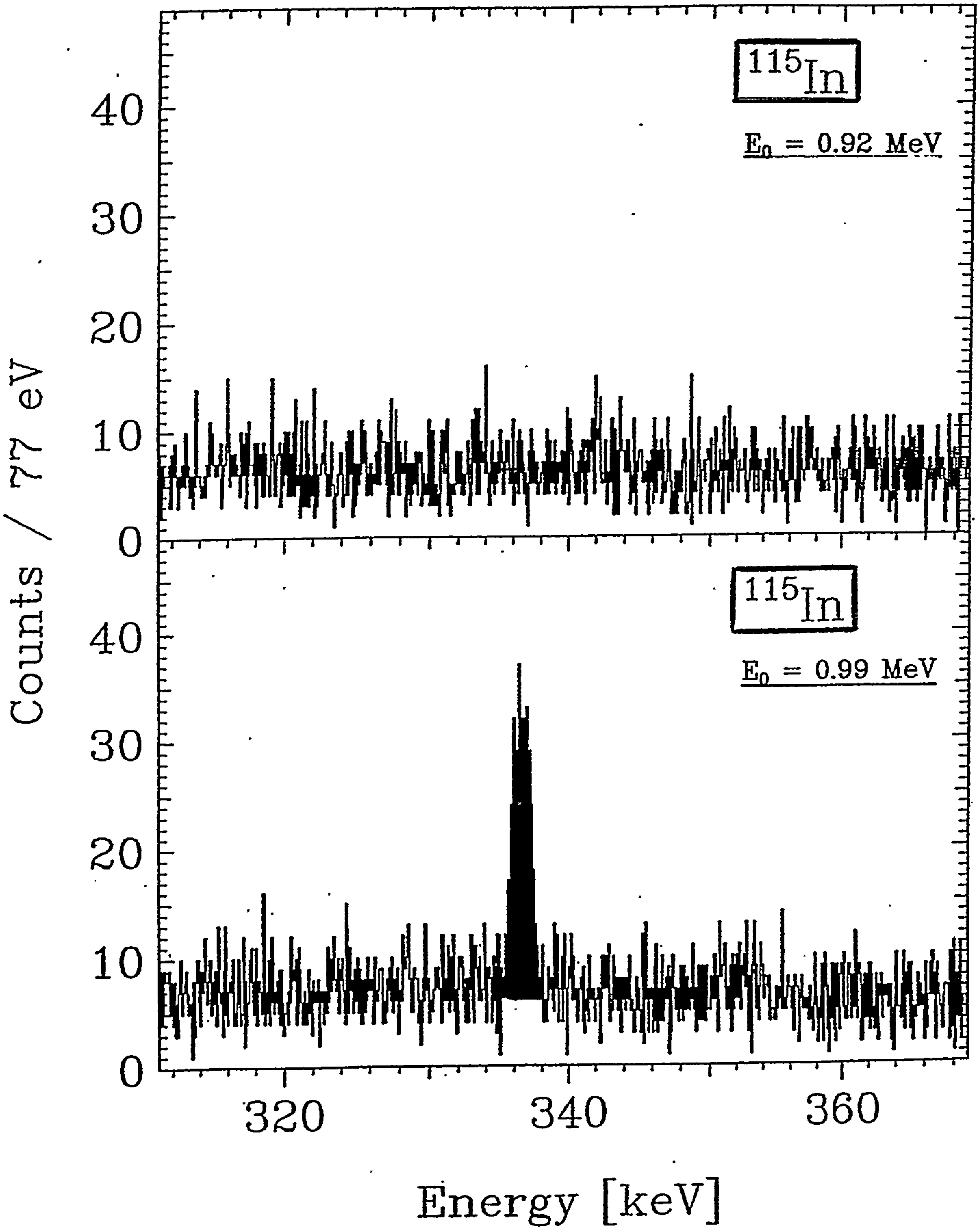

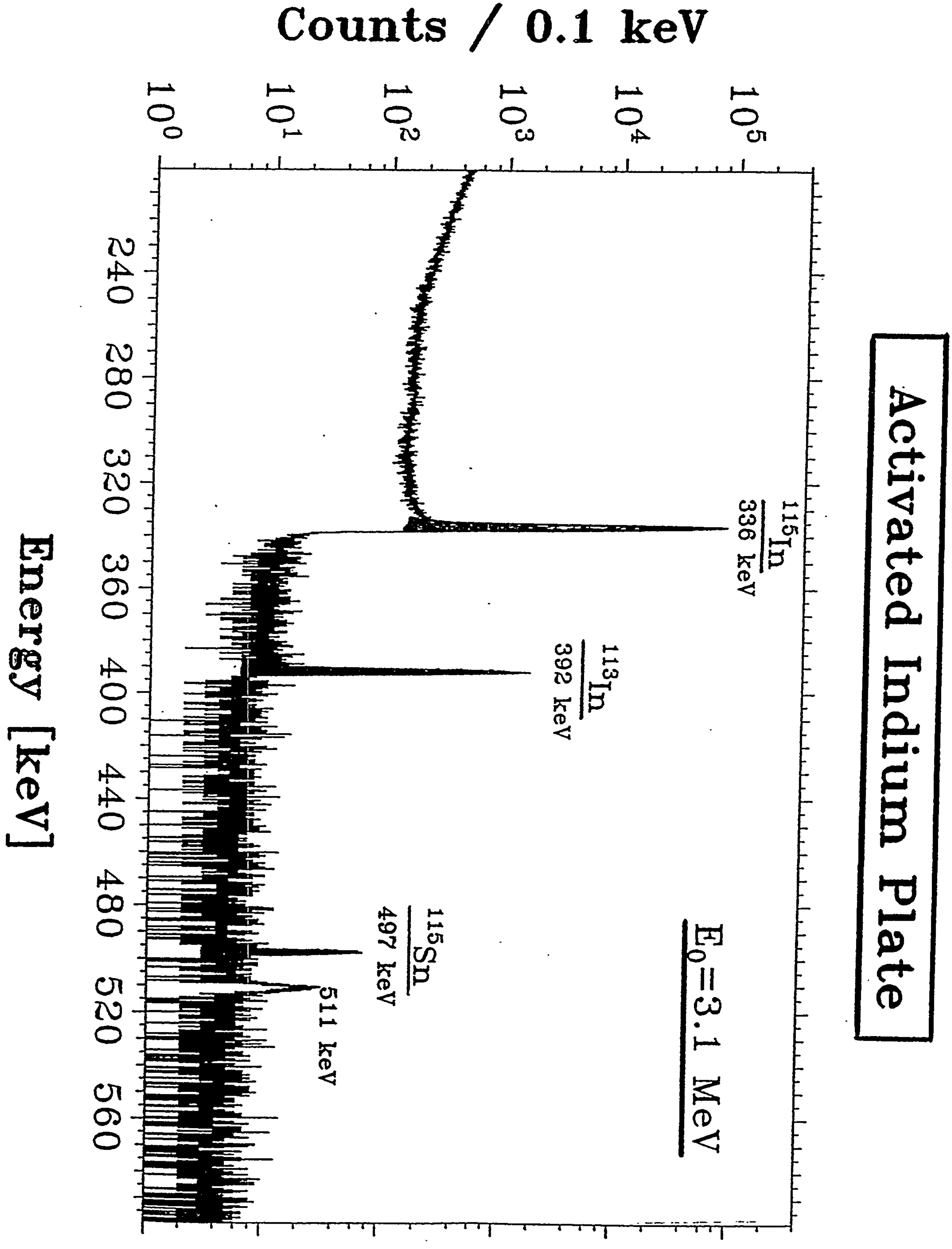
Activated Indium Plate
E_0=3.1 MeV
Counts / 0.1 keV
10^0
10^1
10^2
10^3
10^4
10^5
240
280
320
360
400
440
480
520
560
Energy [keV]
^{115}In
336 keV
^{113}In
392 keV
^{115}Sn
497 keV
511 keV

^{115}In Activation Yields

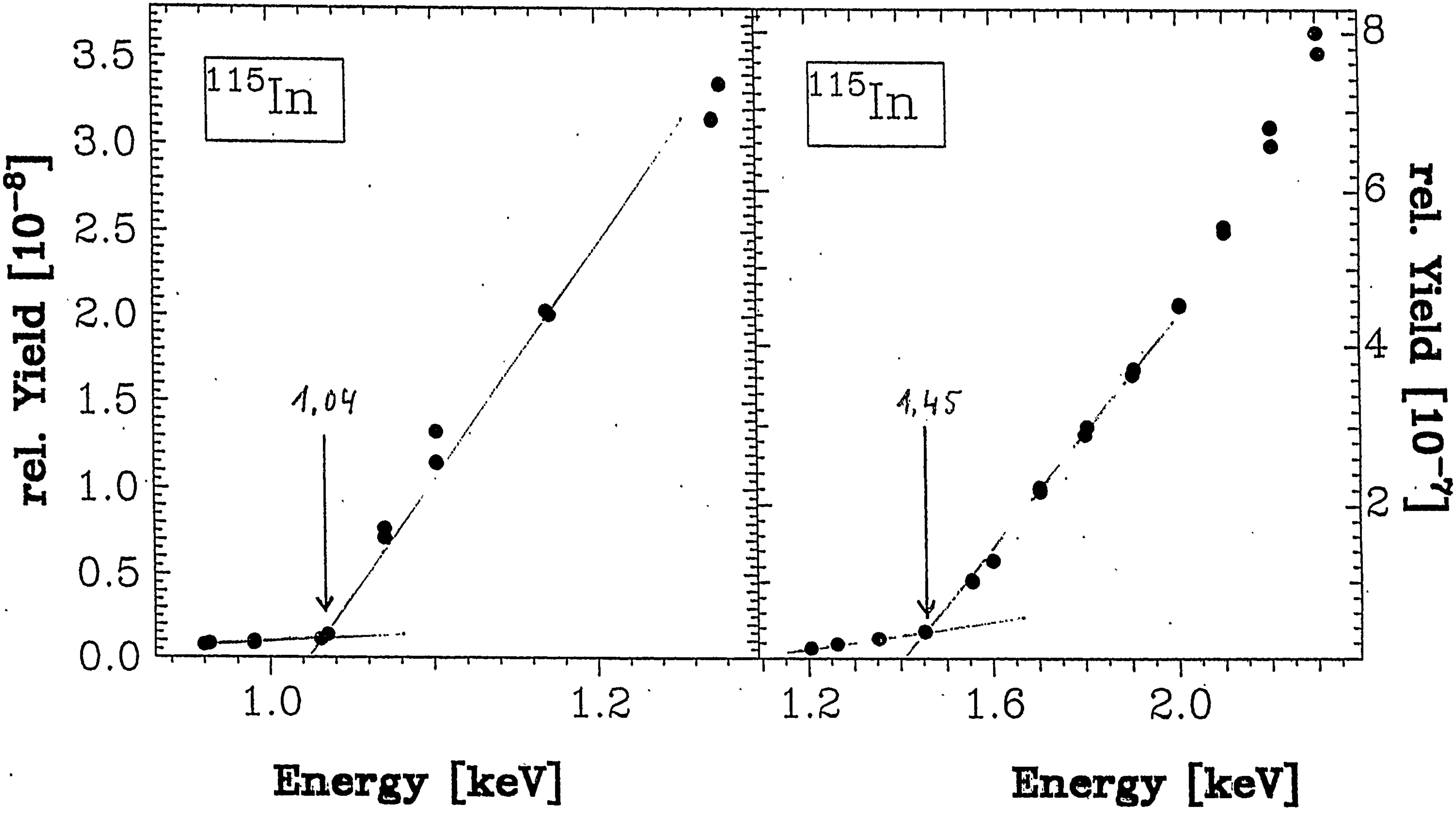

Activity Measurements

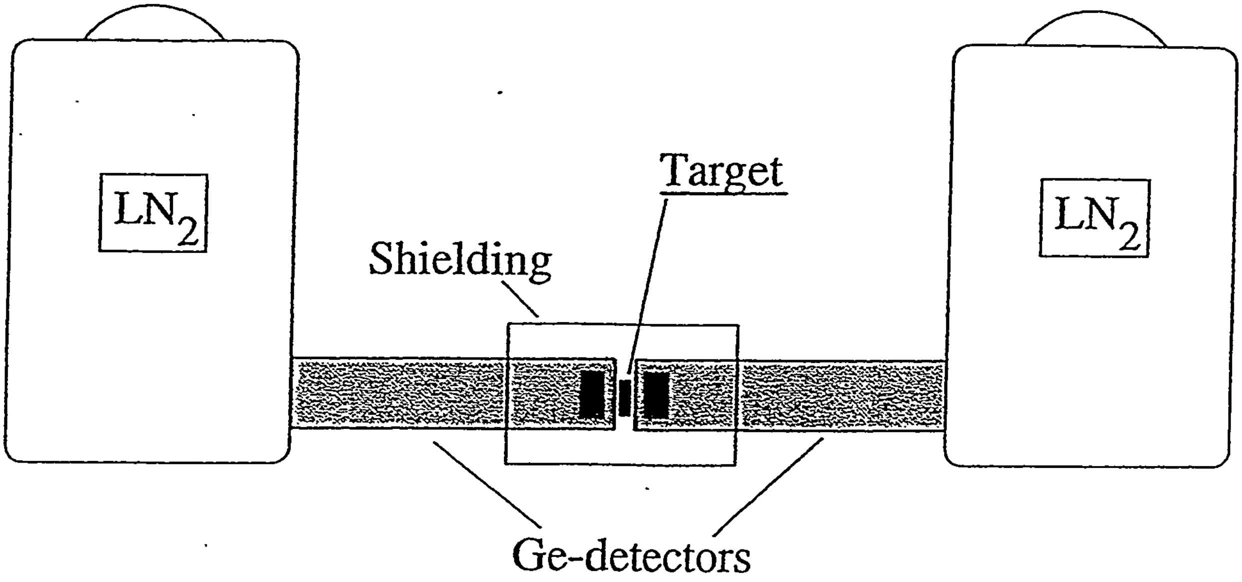

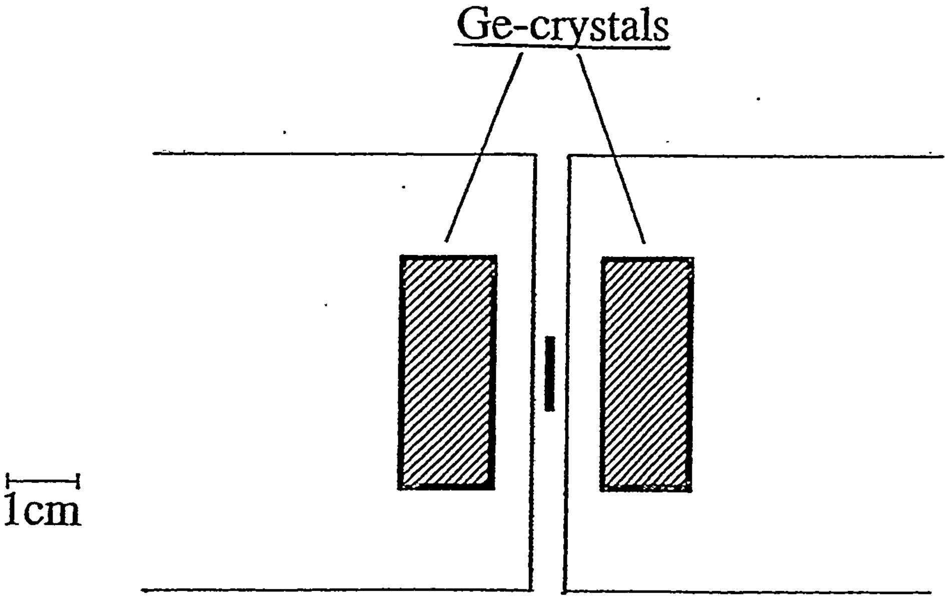

Targets used

- 150 mg Ta_2O_5 powder with an enrichment on ^{180}Ta of 5.45 %, Ø11.5 mm, packed into a graphite container:

  enr: 6.7 mg ^{180}Ta

  World's stock of enriched material !

- 150 mg Ta_2O_5 powder with natural abundance (0.012%) of ^{180}Ta, similar constructed as the enriched target:

  nat: 0.015 mg ^{180}Ta

- 1.5 g metallic Tantalum plate, Ø25 mm, with 0.2 mm thickness:

  blech: 0.18 mg ^{180}Ta

➡

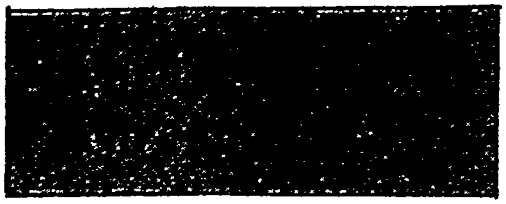

Photon Spectra of Activated Tantalum

metallic NATURAL TARGET ⟷ ENRICHED TARGET

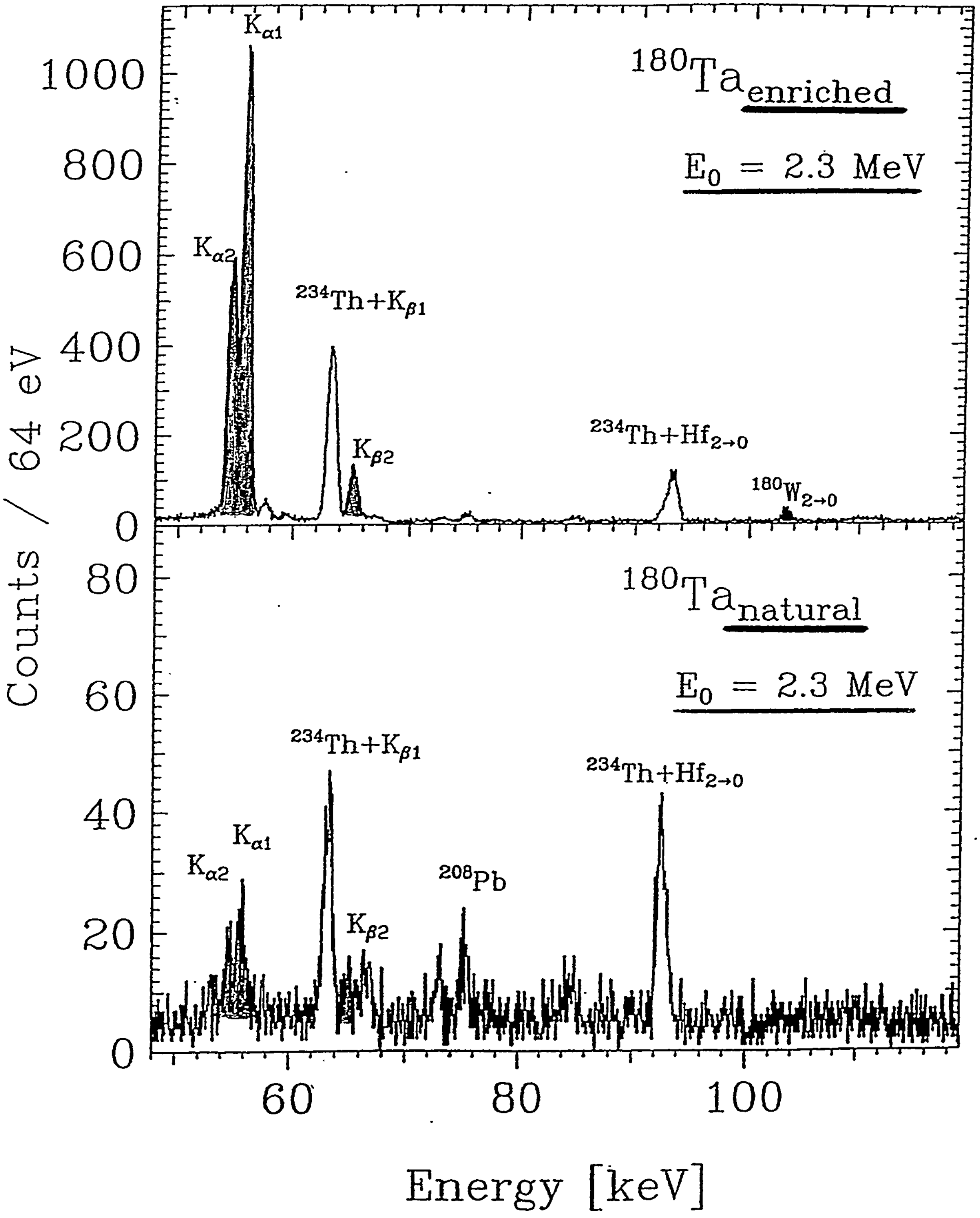

DARMSTADT-KARLSRUHE-MÜNCHEN-STUTTGART – COLLABORATION

Half-Life of ^{180g}Ta

EXPONENTIAL Y-SCALE

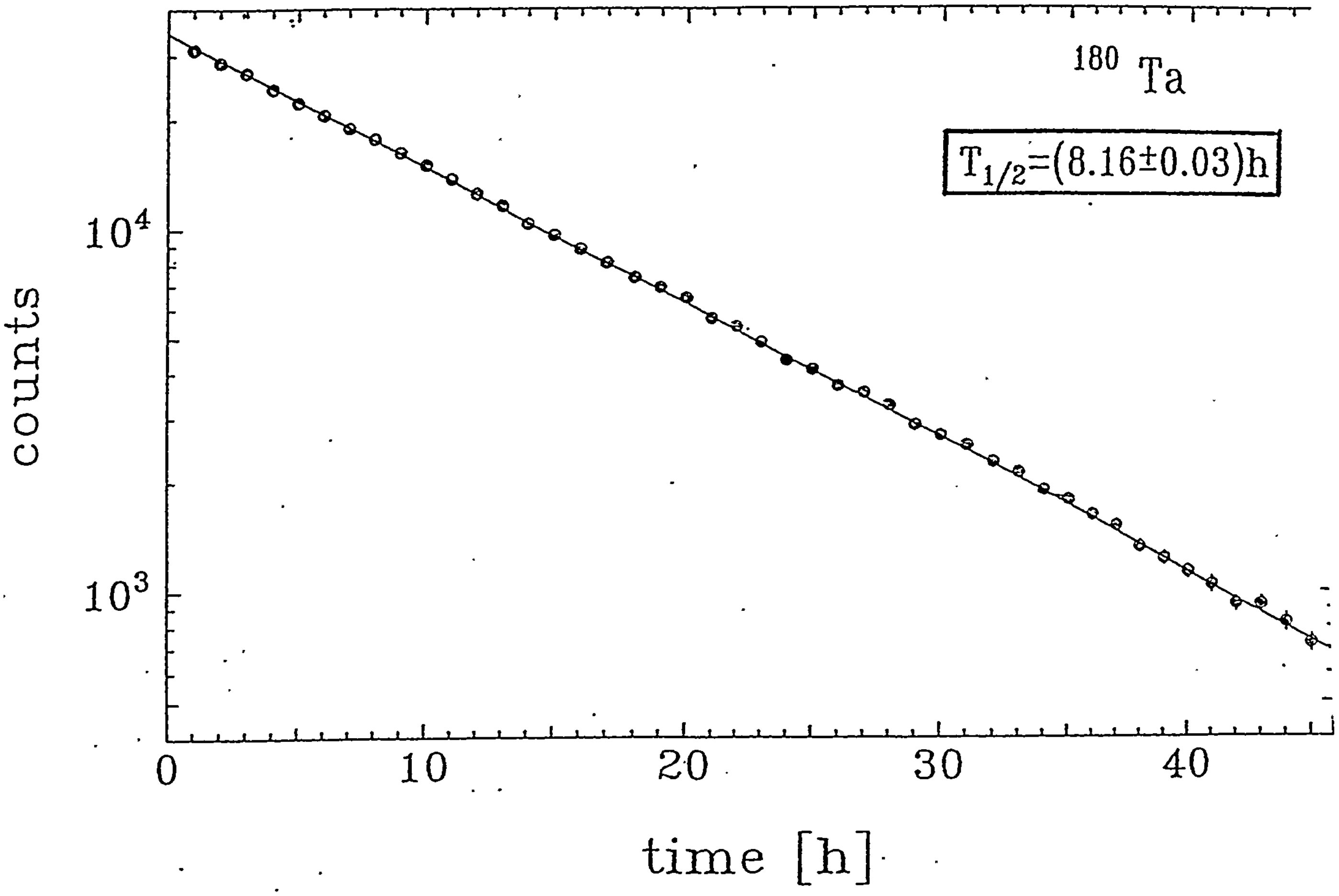

DARMSTADT-KARLSRUHE-MÜNCHEN-STUTTGART – COLLABORATION

^{180m}Ta - Photoactivation - Yields

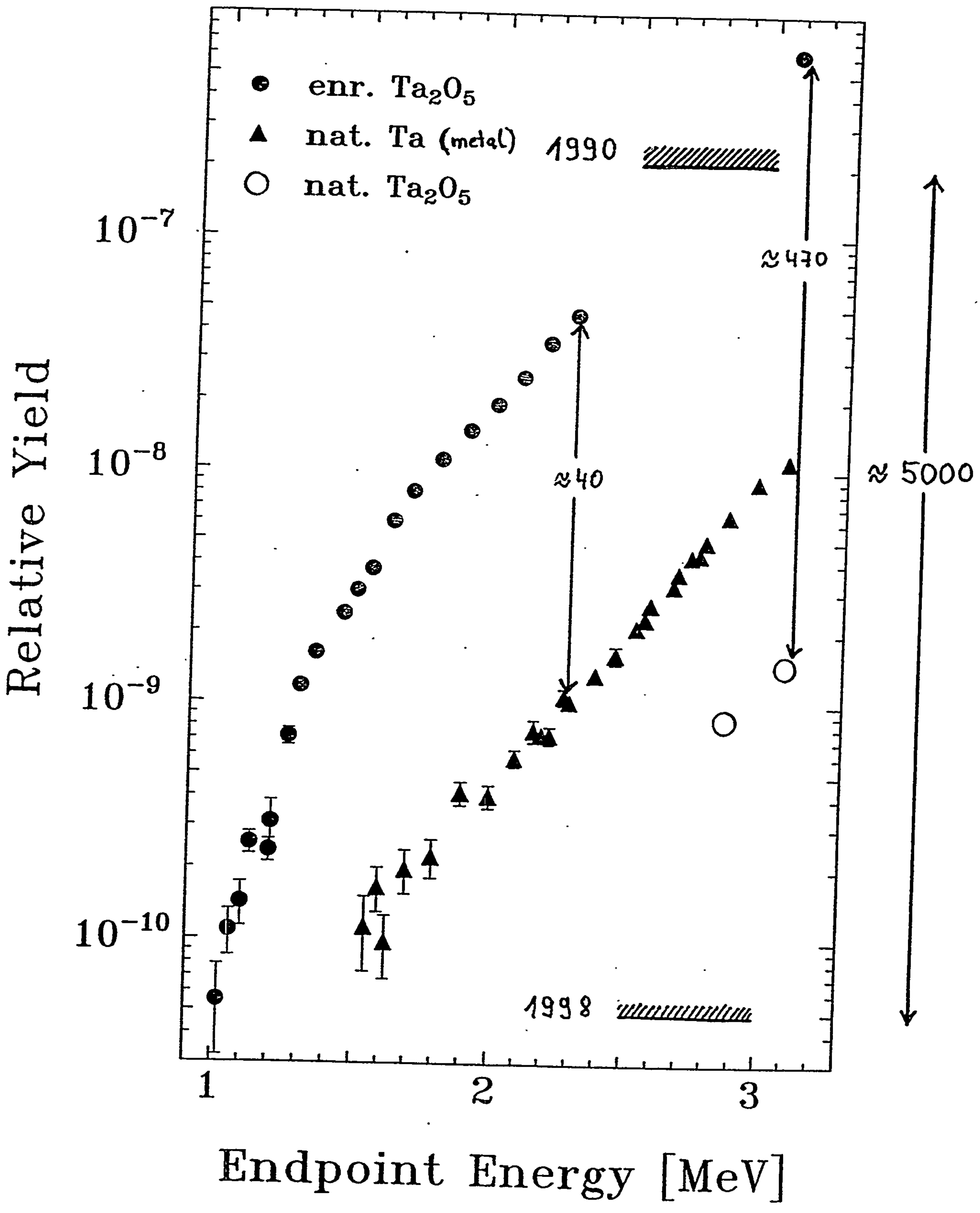

Breaks in the ^{180m}Ta Photoactivation Yield

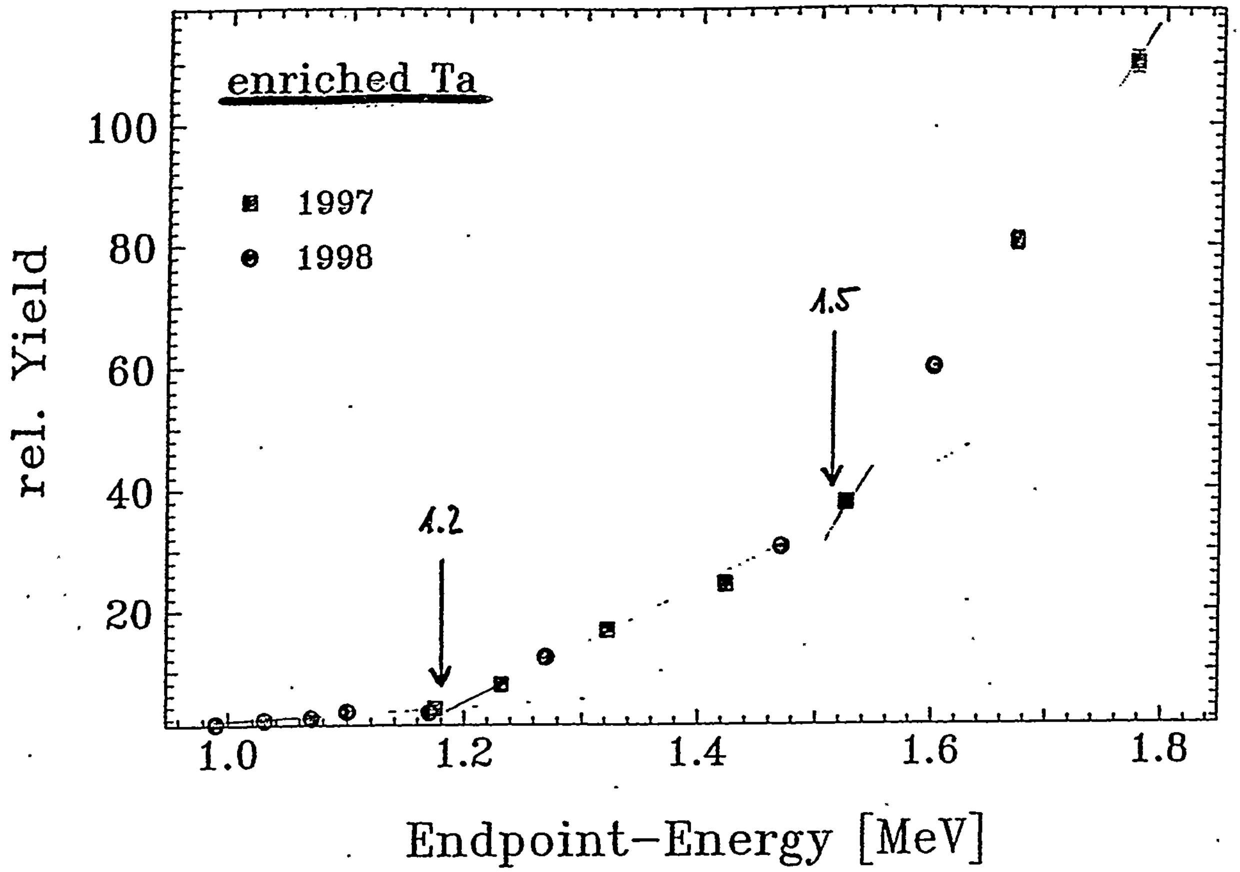

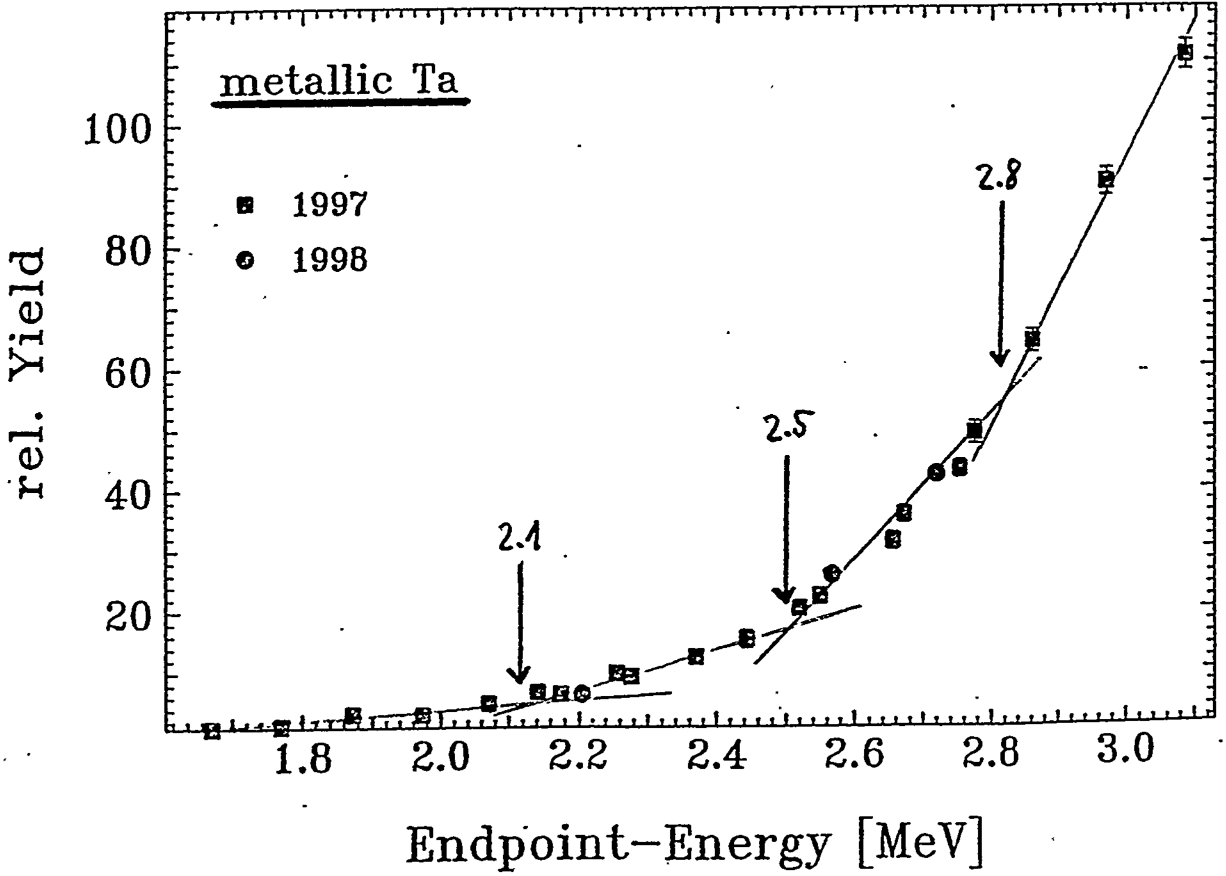

Cross-Section for an IS at 1010 keV

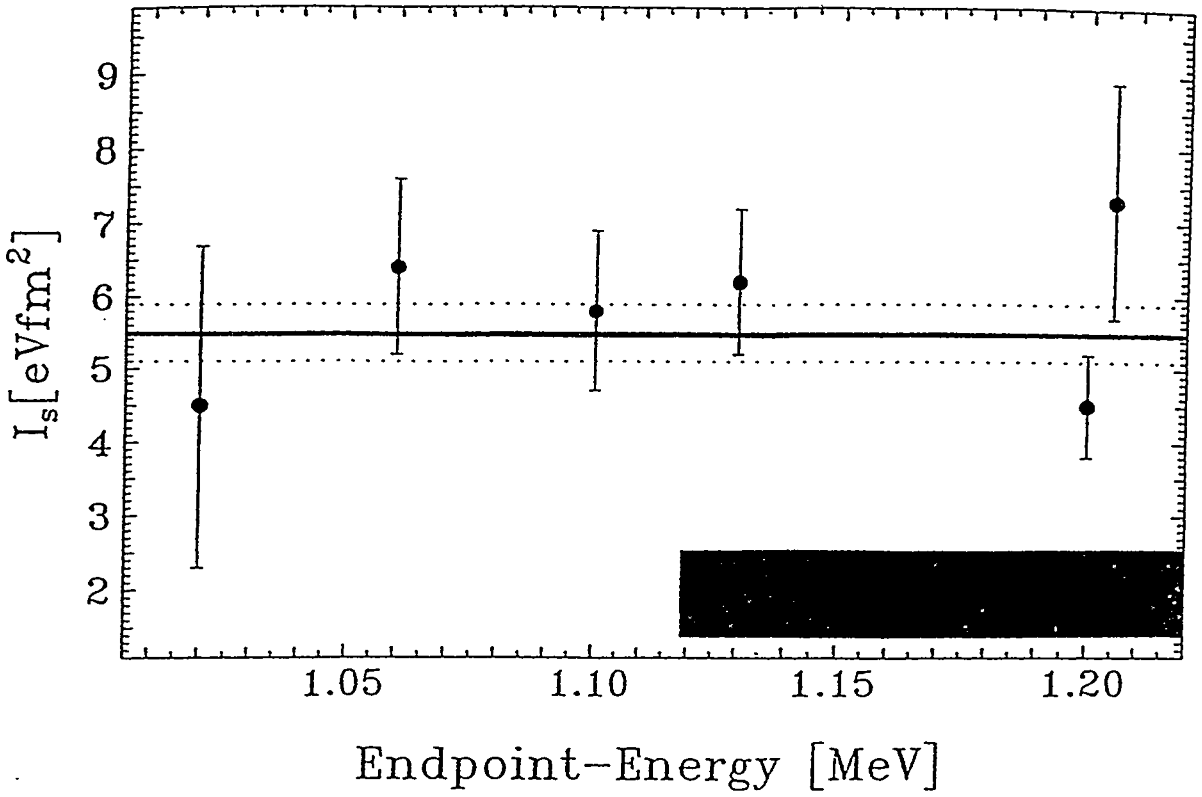

[redacted]

Planck Distribution

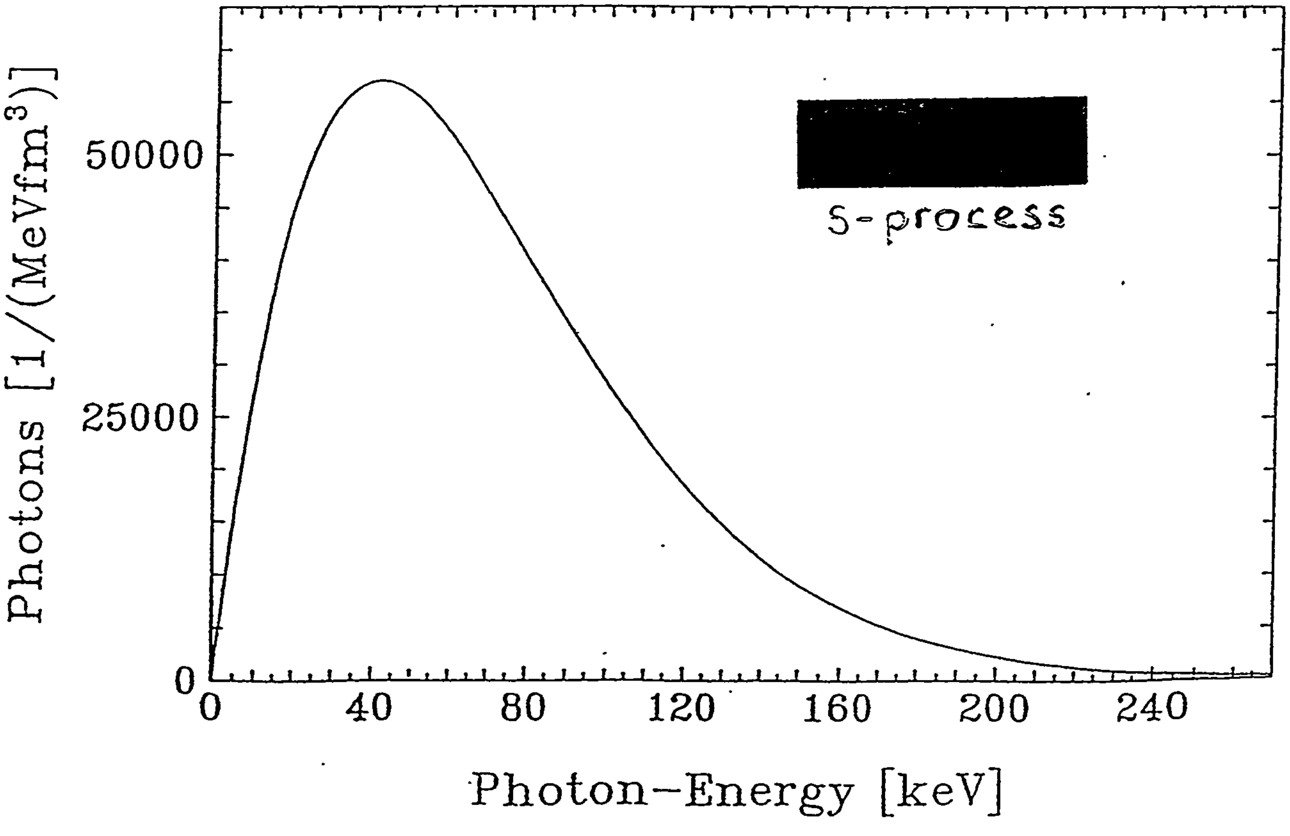

[redacted]

Effective Halflife of ^{180m}Ta

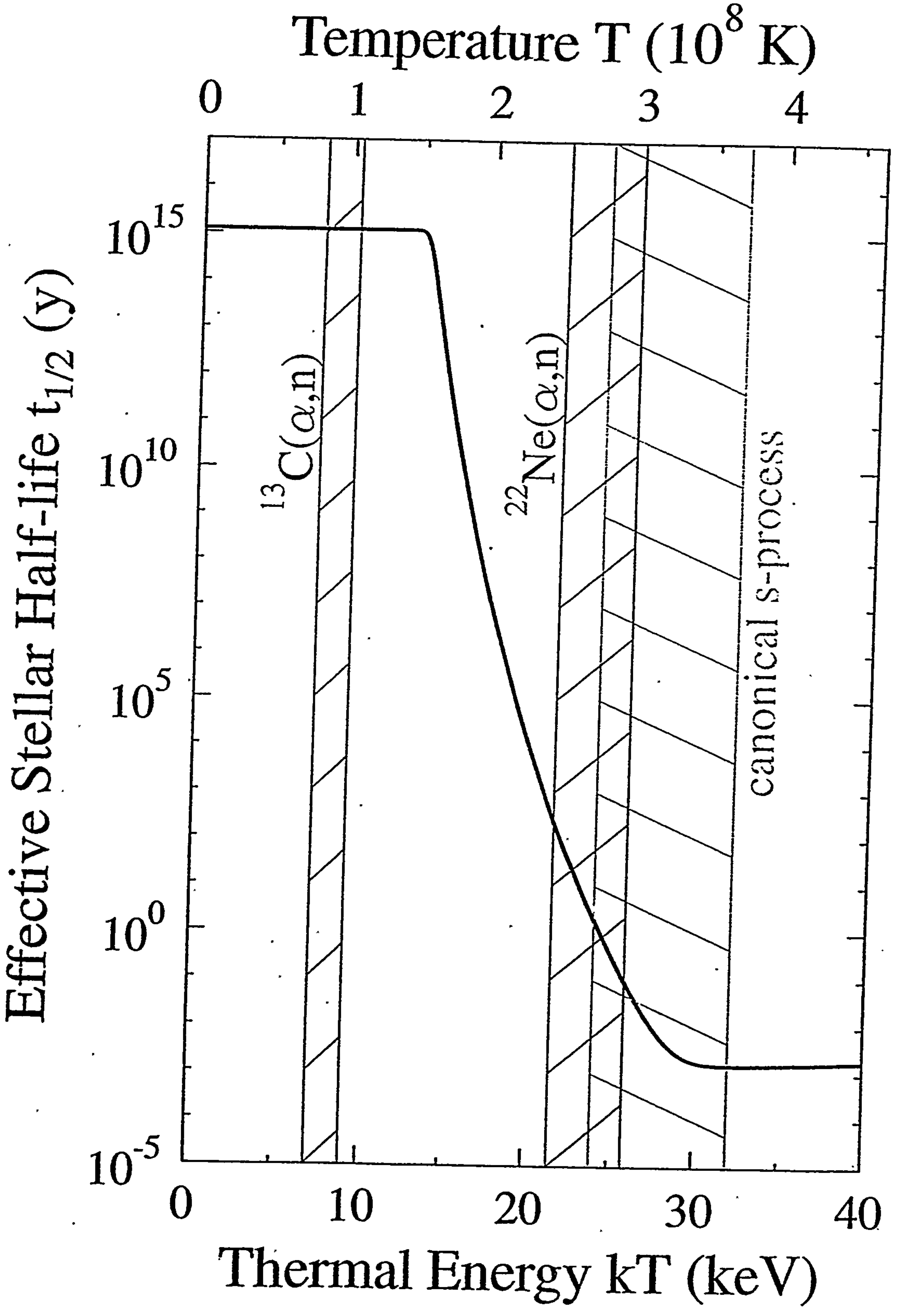

Summary

- **Sensitivity improved by a factor of 5000 compared to 1990**

  * Enriched target (5.5% ^{180m}Ta)
  * LEP-Detectors with
  good resolution (470 eV at 55 keV)
  high efficiency (ε_{abs}= 50 % at 60 keV)
  close geometry (80% of 4π)
  * High e^--current on radiation target (450 μA)

- **Depopulation of the isomer starts ≤1 MeV**

  Indication for further intermediate states at:
  1.2 MeV, 1.5 MeV, 2.1 MeV, 2.5 MeV, 2.8 MeV

- **Astrophysical Consequences:**

  Integrated cross-section for a level assumed at 1010 keV:

$$I_s = 5.5\pm0.4 \text{ eVfm}^2$$

➡ Upper limit for effective half-life of ^{180}Ta under s-process conditions (constant temperature of $T\approx3\bullet10^8$K assumed):

$$\boxed{t_{eff} < 1 \text{ year}}$$

(room temperature : $t_{eff} > 10^{15}$ years !)

➡ Need for dynamical stellar model calculations

Structure and EM Dissociation of ^{9}Be

A. Mengoni
ENEA, Bologna, Italy
University of Tokyo, Japan
RIKEN, Japan

and

T. Otsuka
University of Tokyo, Japan
RIKEN, Japan

The structure and electromagnetic dissociation of are discussed relevant to the nucleosynthesis of light elements.

Structure and EM dissociation of ^{9}Be

Alberto Mengoni
ENEA (Bologna) - UT (Tokyo) - RIKEN (Wako)

In collaboration with: T. Otsuka (University of Tokyo & RIKEN)

Workshop@Santa Fe, September 1999

Structure and EM excitation of $^9\mathrm{Be}$

Motivations:

1. **Astrophysics**
2. **Nuclear structure: the $1/2^+$ state movements**
3. **Somebody asked me to calculate the $^9\mathrm{Be} \rightarrow {}^8\mathrm{Be} + \gamma$ Coulomb dissociation cross section**

α-rich freeze out r-process paths

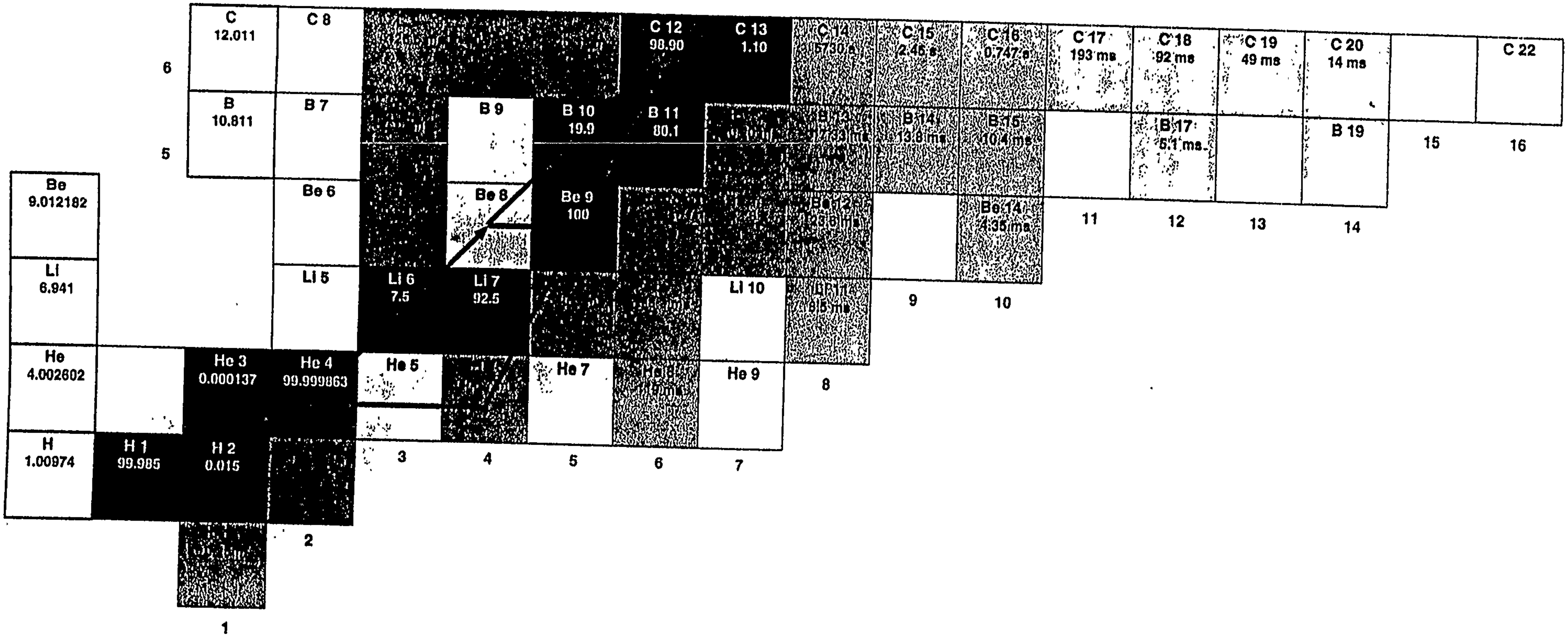

The α-rich freeze out r-process nucleosynthesis

- Phase: post-collapse of a Type II supernova
- Site: neutrino-heated high-entropy bubble
- Neutron densities: 10^{20-30} n/cm^3
- Status: NSE with α-induced recombinations (high photon-to-baryon ratio)
- Main quantities: expansion and cooling rates, reaction rates

The required α-induced reactions and corresponding rates to bridge the $A = 8$ instability gap are:

1. $\alpha(2\alpha, \gamma)^{12}\mathrm{C}$
2. $\alpha(\alpha n, \gamma)^{9}\mathrm{Be}(\alpha, n)^{12}\mathrm{C}$
3. $\alpha(2n, \gamma)^{6}\mathrm{He}(\alpha, n)^{9}\mathrm{Be}(\alpha, n)^{12}\mathrm{C}$

Reaction Rates

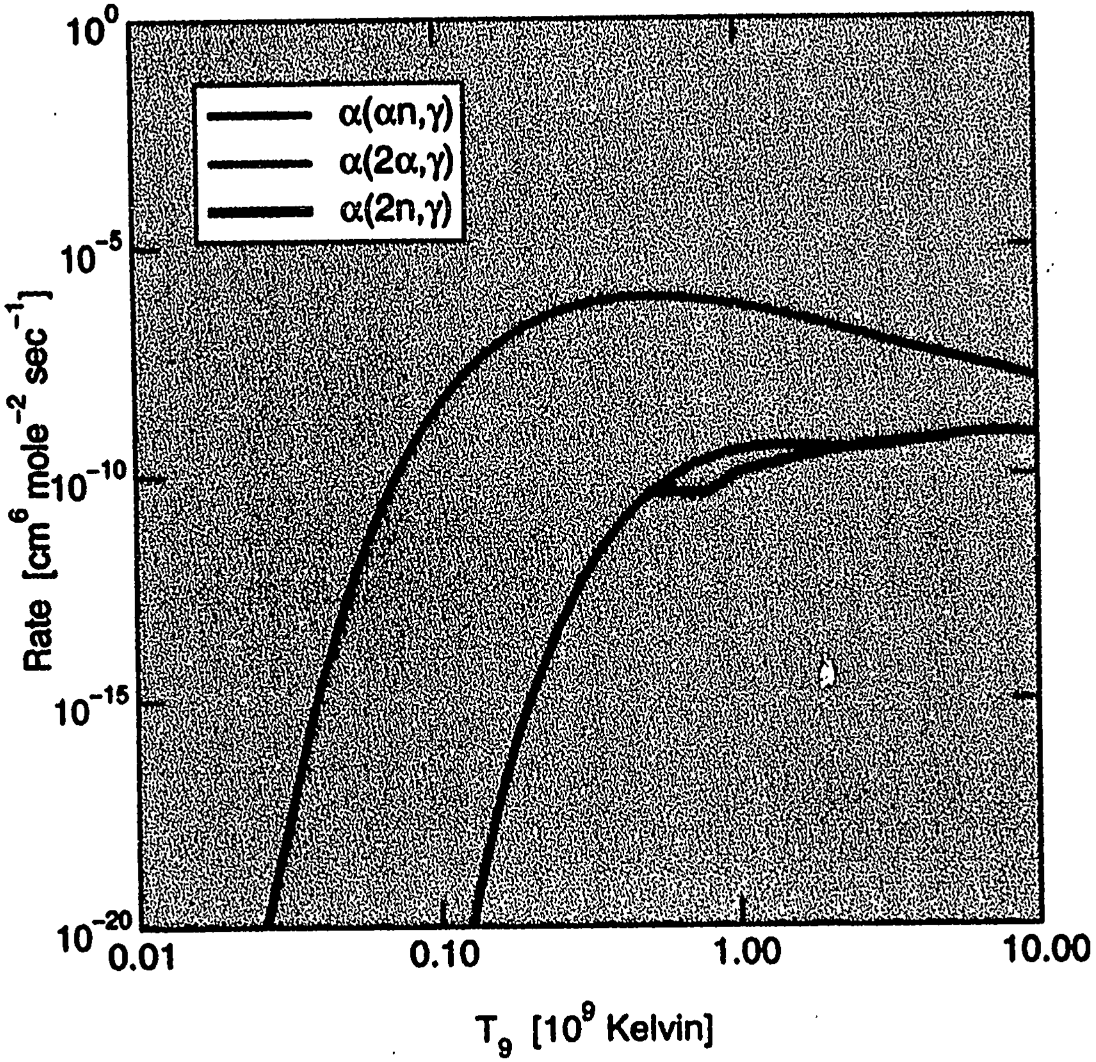

EM excitation of ^{9}Be

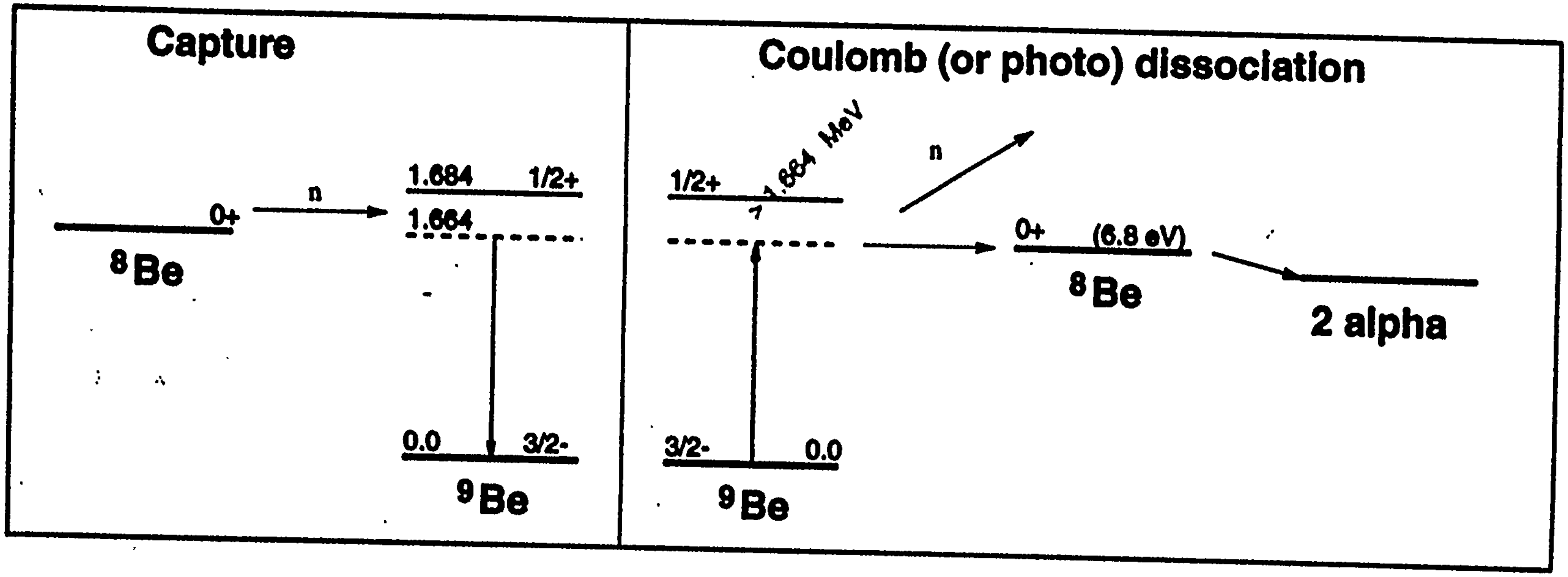

DRC cross section

We start from the wave functions Ψ_c and Φ_b of the continuum and of the bound-state respectively given by

$$\Psi_c(r) = \sum_{l_c j_c} i^{l_c} \frac{\psi_{E_c l_c j_c}(r)}{r} [[\hat{Y}_{l_c} \times \hat{\chi}_s]^{j_c} \times \hat{\chi}_I]^{J_c}$$

and

$$\Phi_b(r) = \sum_{l_b j_b} B_{j_b, J_b \alpha_b, I\alpha} \frac{\phi_{n_b l_b j_b}(r)}{r} [[\hat{Y}_{l_b} \times \hat{\chi}_s]^{j_b} \times \hat{\chi}_I]^{J_b}$$

The radial wave functions $\psi_{E_c l_c j_c}(r)$ and $\phi_{n_b l_b j_b}(r)$ are obtained by solving the scattering and the bound state problem respectively, in a given potential.

The matrix elements $Q^{(\mathrm{EL})}_{c\to b} =< \Psi_b \,||\, \hat{T}^{\mathrm{EL}} \,||\, \Phi_b >$ may be written as a product of three terms

$$Q^{(\mathrm{EL})}_{c\to b} = \mathcal{I}_{cb} \cdot B_b \cdot A_{cb}$$

with $\hat{T}^{\mathrm{EL}}_M = r^L Y_{LM}$ and $\mathcal{I}_{cb} = \int \psi^*_{E_c l_c j_c}(r) r^L \phi_{n_b l_b j_b}(r) dr$.

The capture cross section is given by

$$\sigma^{(\mathrm{EL})}_{c\to b} = \frac{8\pi(L+1)}{L[(2L+1)!!]^2} \frac{k_\gamma^{2L+1}}{\hbar v} \frac{1}{2s+1} \frac{1}{2I+1} \bar{e}^2_{\mathrm{EL}} \sum_{l_c j_c, l_b j_b} | Q^{(\mathrm{EL})}_{c\to b} |^2$$

Resonances and interference

In the presence of a resonant state, the cross section contains a Breit-Wigner plus an interference term

$$\sigma(E) = \sigma_{DRC}(E) + \sigma_{BW}(E) + 2[\sigma_{DRC}(E) + \sigma_{BW}(E)]^{1/2}\cos[\delta_r(E)]$$

with

$$\sigma_{BW}(E) = \pi\lambda_n^2 g_J \frac{\Gamma_n\Gamma_\gamma}{(E_r - E)^2 + \frac{1}{4}\Gamma^2}$$

and

$$\delta_r(E) = \tan^{-1}[\frac{\Gamma(E)}{2(E - E_r)}]$$

Interference effects in the $^{16}\mathrm{O}(n,\gamma)^{17}\mathrm{O}$

The p—wave resonance at 434 KeV in $n + {}^{16}\mathrm{O}$ provides a nice example of interference between the DRC and the compound capture mechanisms. The interference occurs among the p—wave component of the DRC and the p—wave neutron resonance. The interference effect is observed for both the transitions to the ground-state ($J^\pi = 5/2^+$) and in the first excited state ($J^\pi = 1/2^+$) in $^{17}\mathrm{O}$.

Model : DRC ($p \to s, d$ E1 transitions)
: Resonance + interference terms
Parameters: $E_r = 434$ KeV, $\Gamma_n = 45$ KeV
: $\Gamma_{\gamma 0} = 0.5$ eV, $\Gamma_{\gamma 1} = 0.5$ eV

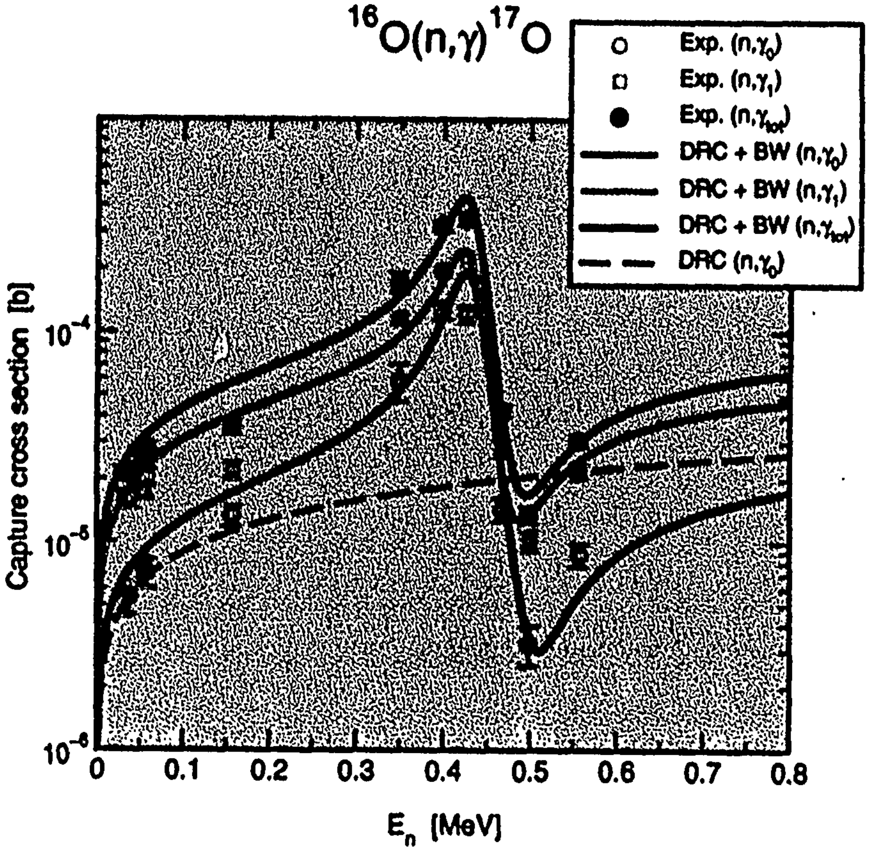

Fri Aug 27 11:30:53 1999

Direct & Inverse reactions

The time reversal invariance of nuclear reactions (detailed balance) provides a relation between the capture and the photo-nuclear cross sections

$$\boxed{\begin{array}{ccccccc} n & + & {}^{A}\mathrm{Z} & \rightarrow & {}^{A+1}\mathrm{Z} & + & \gamma \\ 1 & & 2 & & 3 & & 4 \end{array}}$$

$$\sigma_{\gamma,n} = \frac{k_n^2}{k_\gamma^2}\frac{2J_2+1}{2J_3+1}\,\sigma_{n,\gamma}$$

In the semiclassical limit (Coulomb trajectories) the cross section for Coulomb dissociation is related to the photo-nuclear cross section by the relation

$$\frac{d\sigma_{cd}^{\mathrm{EL}}}{dE_x} = \int 2\pi b db \frac{N_{\mathrm{EL}}(E_i, E_x, b)}{E_x}\sigma_{\gamma,n}^{\mathrm{EL}} = \frac{N_{\mathrm{EL}}(E_i, E_x)}{E_x}\sigma_{\gamma,n}^{\mathrm{EL}}$$

where E_x is the excitation energy and N_{EL} the virtual-photon number of multipolarity EL at given incident energy E_i and impact parameter b.

EM excitation of ^{9}Be: experimental data

$^{9}Be + \gamma \rightarrow {}^{8}Be + n$

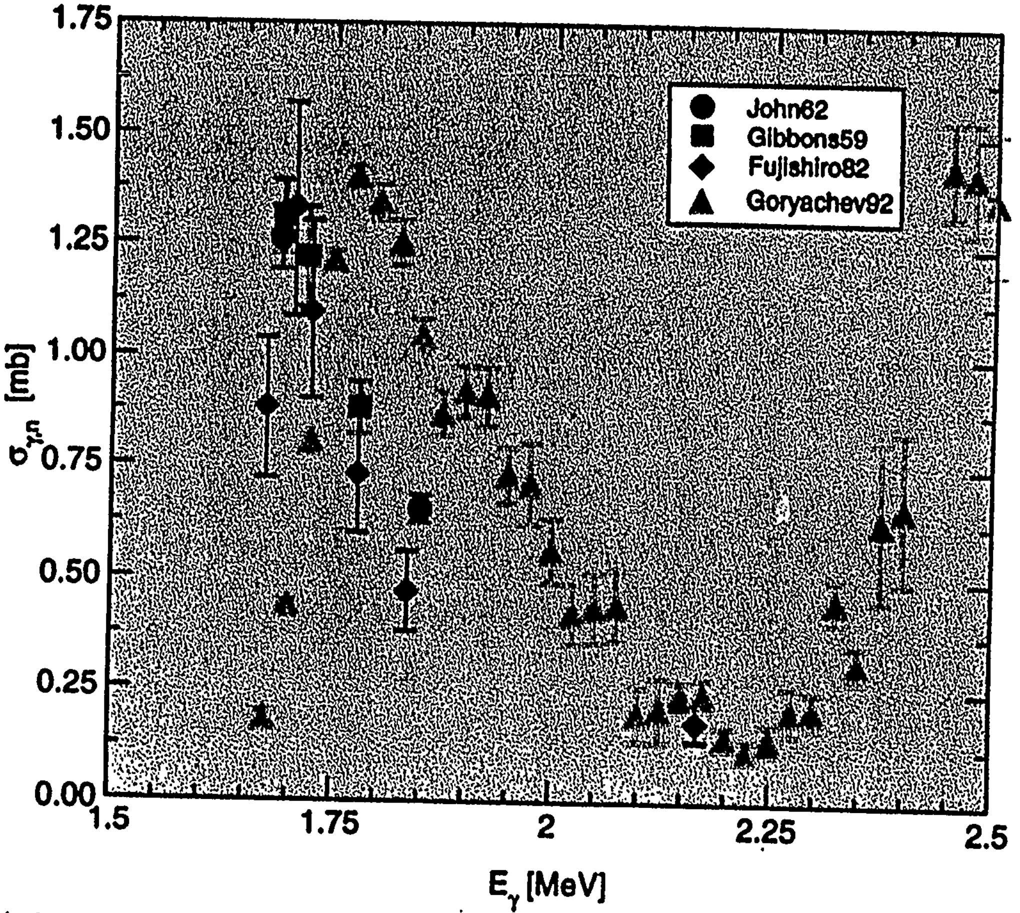

Tue Aug 24 16:01:31 1999

The $2s_{1/2}$ single-particle orbit and the ^{9}Be shell-model spectrum

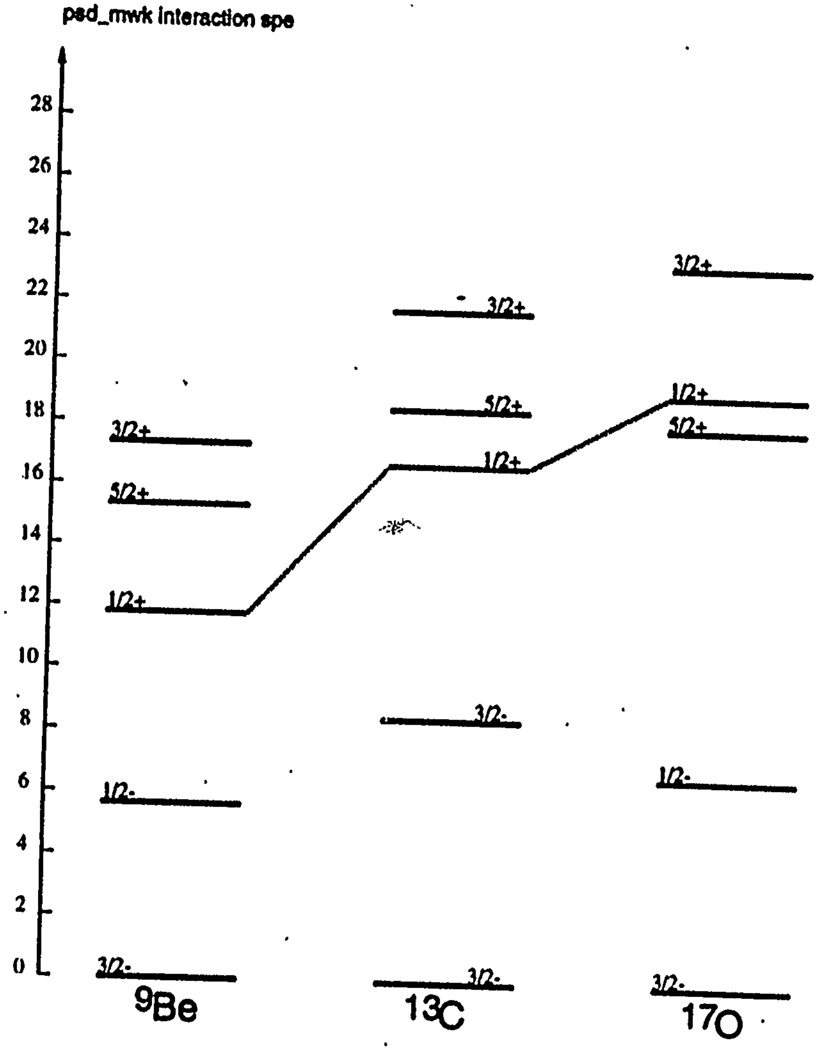

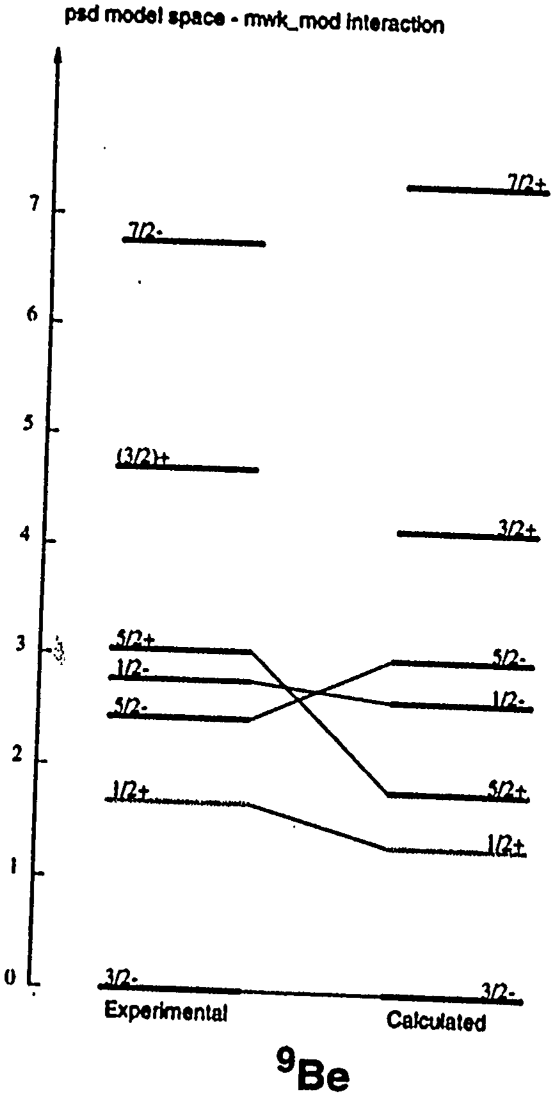

The $2s_{1/2}$ single-particle state in the mean field

The fact that the $1/2^+$ state in ^{9}Be is below the $5/2^+$ should NOT be surprising. In fact, even a simple HF calculation with the sk3 interaction shows this feature

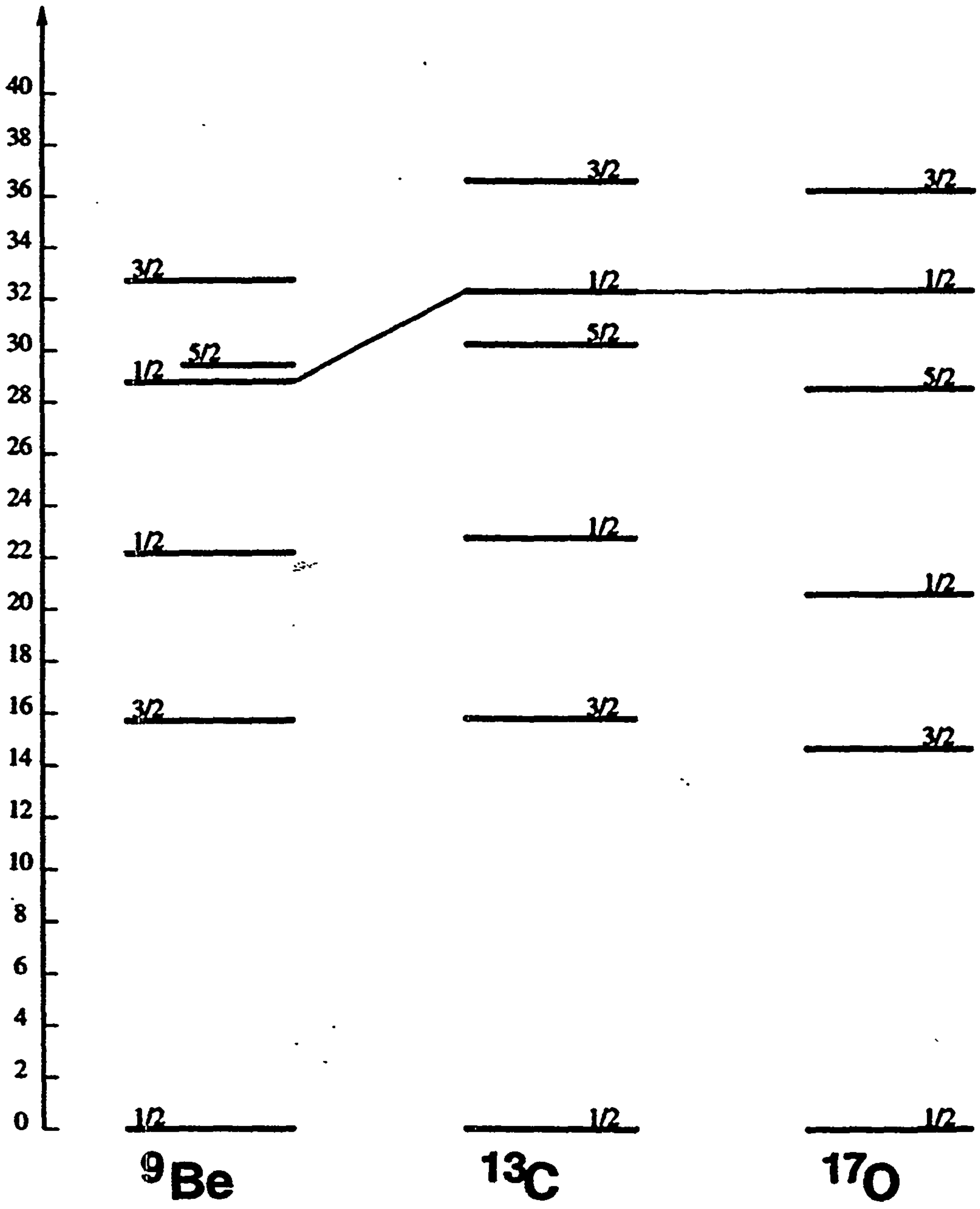

Shell model calculation

The shell-model Hamiltonian is

$$H = H_{core} + \sum_i \epsilon_i a_i^\dagger a_i + \sum_{i>j=1,k>l=1} v_{ijkl} a_i^\dagger a_j^\dagger a_l a_k$$

where ϵ_i is the energy of a the single-particle state and

$$v_{ijkl} \equiv < ij \mid V \mid kl > .$$

Here $\mid ij >$ is an antisymmetrised two-particle m-scheme state. The matrix elements $< ij \mid V \mid kl >$ can be derived from the J- and T-coupled two-body matrix elements

$$\begin{aligned} < j_1 m_1 t_{z1} j_2 m_2 t_{z2} \mid \ V \ \mid j_3 m_3 t_{z3} j_4 m_4 t_{z4} >= & \sum_{J,T} < j_1 j_2 \mid V \mid j_3 j_4 >^{JT} [(1+\delta_{12})(1+\delta_{34})]^{1/2} \times \\ & < j_1 m_1 j_2 m_2 \mid J m_1 + m_2 >< j_3 m_3 j_4 m_4 \mid J m_3 + m_4 > \times \\ & < 1/2 t_{z1} 1/2 t_{z2} \mid T t_{z1} + t_{z2} >< 1/2 t_{z3} 1/2 t_{z4} \mid T t_{z3} + t_{z4} > \end{aligned}$$

Shell model interactions

p model-space

1p1/2	1p3/2	
2.268	1.635	Cohen-Kurath p-shell
3.828	1.744	Kuo (core+polarization, Paris interaction)

psd model-space

1p1/2	1p3/2	1d3/2	1d5/2	2s1/2	
1.28	1.25	12.05	11.02	5.82	psdmwk (original)
1.28	1.25	7.28	6.25	1.48	psdmwk (modified)
1.68	1.38	11.86	10.43	5.34	MKI (Hoshino et al.)

psdmwk interaction

p-p-p-p	Millener (with modified s.p. energies)
sd-sd-sd-sd	Wildenthal (USD)
p-sd-p-sd	Millener-Kurath

Hoshino et al. (MKI)

p-p-p-p	Cohen-Kurath
sd-sd-sd-sd	Kuo (G-matrix)
p-sd-p-sd	Millener-Kurath

^{9}Be: p model-space with the Cohen-Kurath interaction

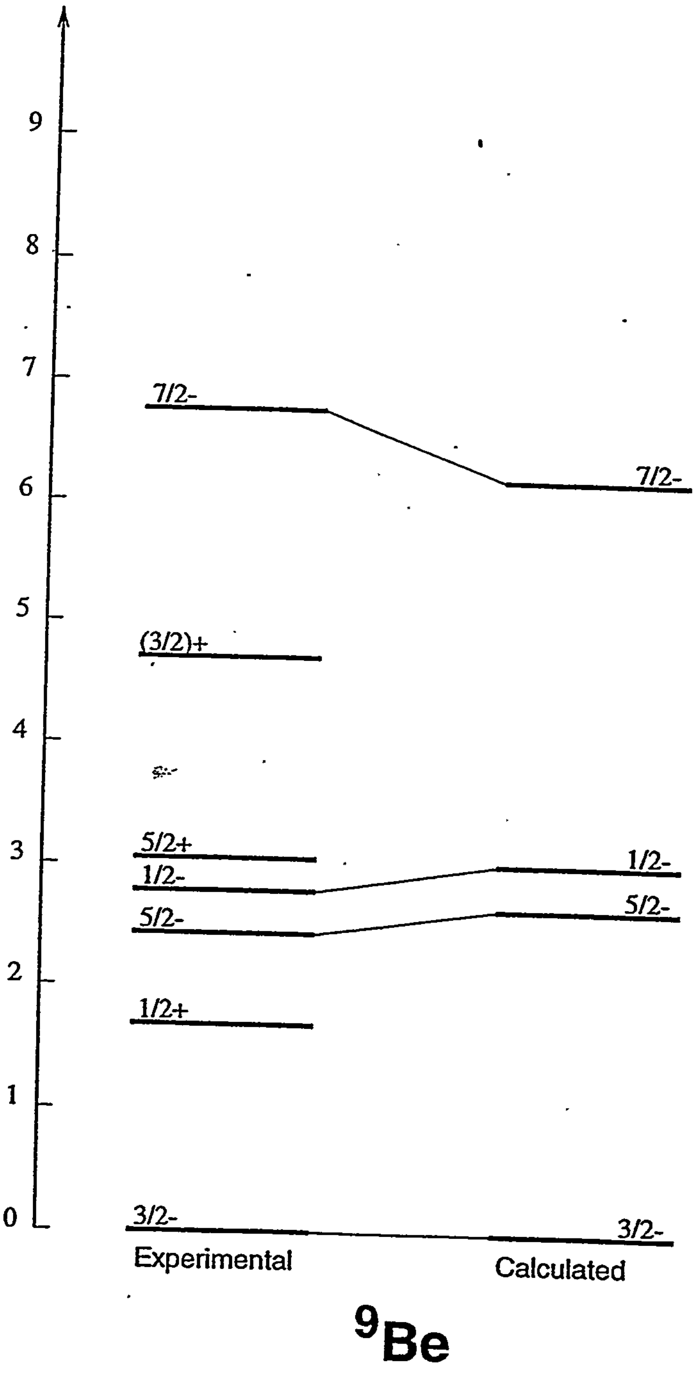

^{9}Be: psd model-space with the MWK interaction

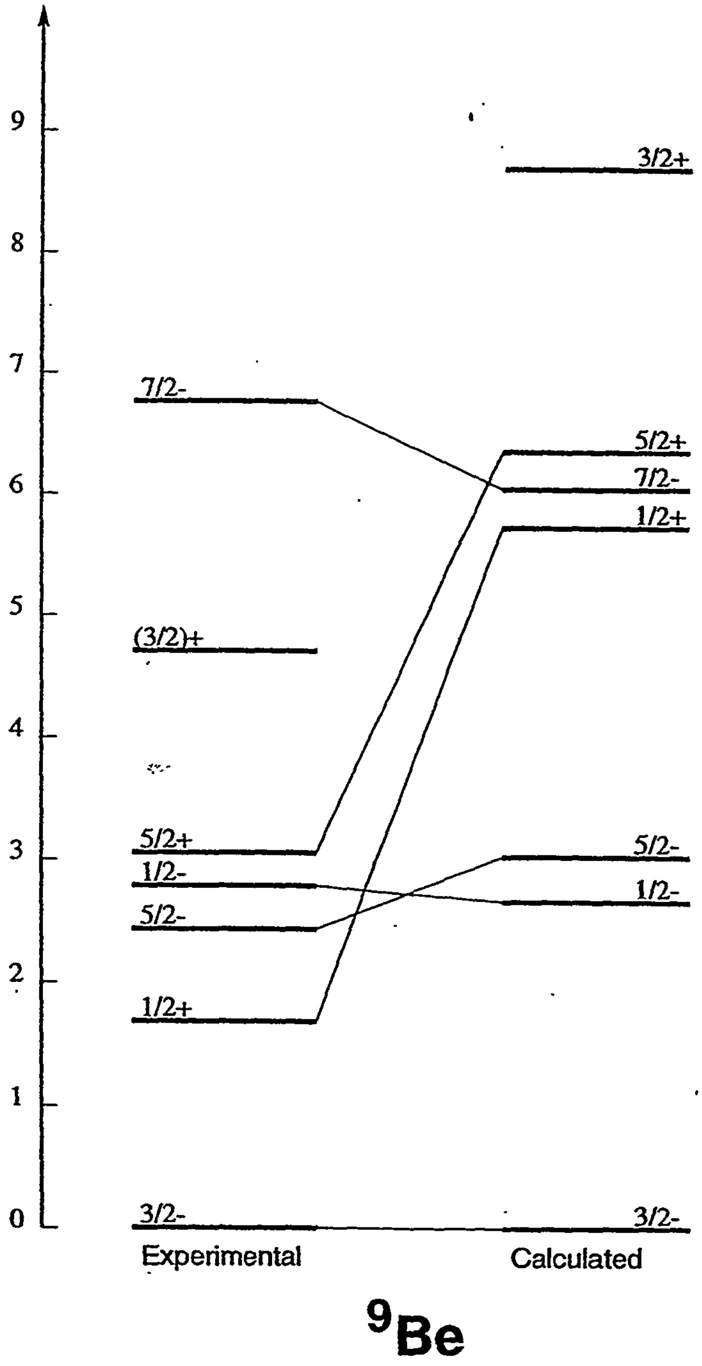

^{9}Be: psd model-space with a modified MWK interaction

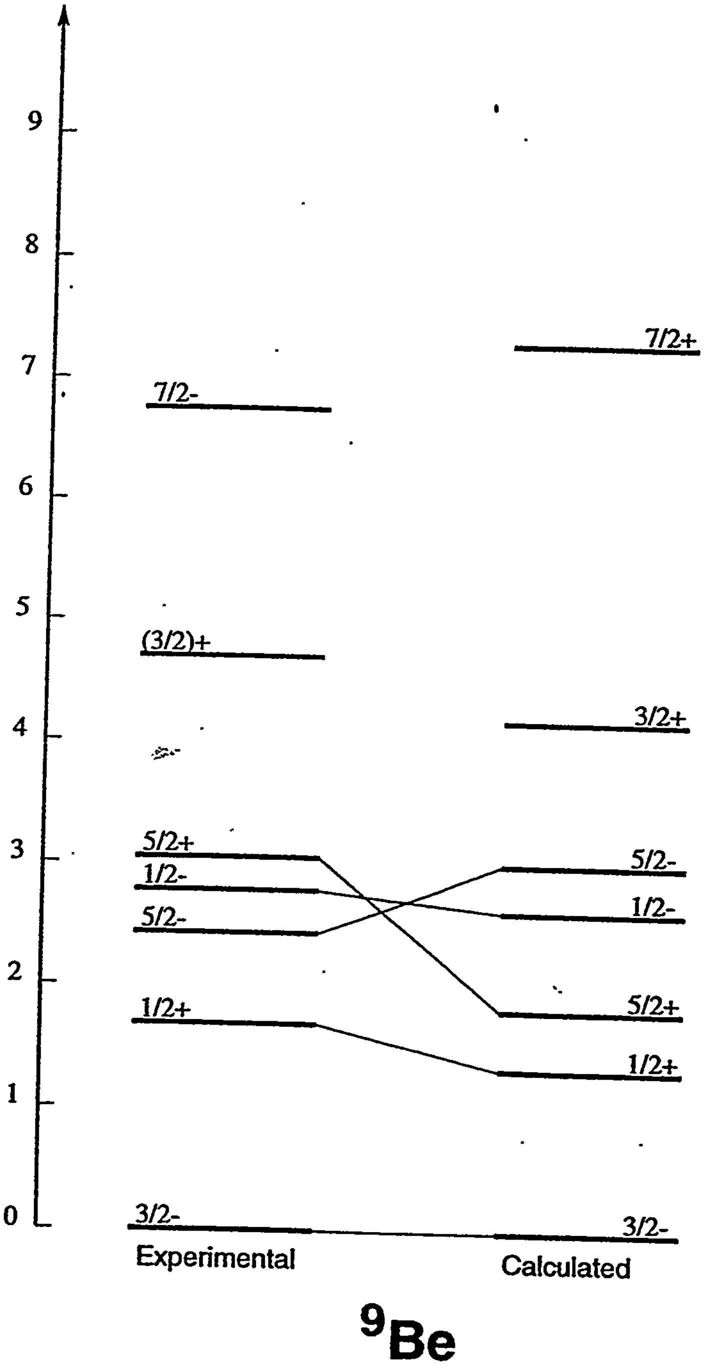

June 27, 1999

Wave functions

Information on the wave functions are reflected in the parentage amplitudes

$$S \equiv N < \text{cfp} >^2$$

where N is the number of particles in the orbit nlj and $< \text{cfp} >$ the coefficients of fractional parentage defined by

$$| J_f T_f \alpha_f(N) > = < (j)^N J_f T_f \alpha_f \{ | (j)^{N-1} J_c T_c \alpha_c > [\psi(J_c T_c \alpha_c)^{(N-1)} \times \phi(j)]^{J_f}$$

For the p model space with the Cohen-Kurath interaction we obtain:

S	$3/2^-$	(nlj)
0^+	0.58	$1p_{3/2}$
2^+	0.06	$1p_{1/2}$
	0.67	$1p_{3/2}$

For the psd model space with the MWK interaction we have:

S	$3/2^-$	(nlj)	$1/2^+$	(nlj)
0^+	0.57	$1p_{3/2}$	0.56	$2s_{1/2}$
2^+	0.05	$1p_{1/2}$	0.06	$1d_{3/2}$
	0.69	$1p_{3/2}$	0.25	$1d_{5/2}$

3-cluster Model

In the 3-cluster model of P. Descouvemont (*Phys. Rev.* **C39** (1989) 1557), a $\alpha - \alpha - n$ configuration was assumed. The $R_{\alpha-\alpha}$ was kept constant and the $R_{\alpha\alpha-n}$ was used as generator coordinate.

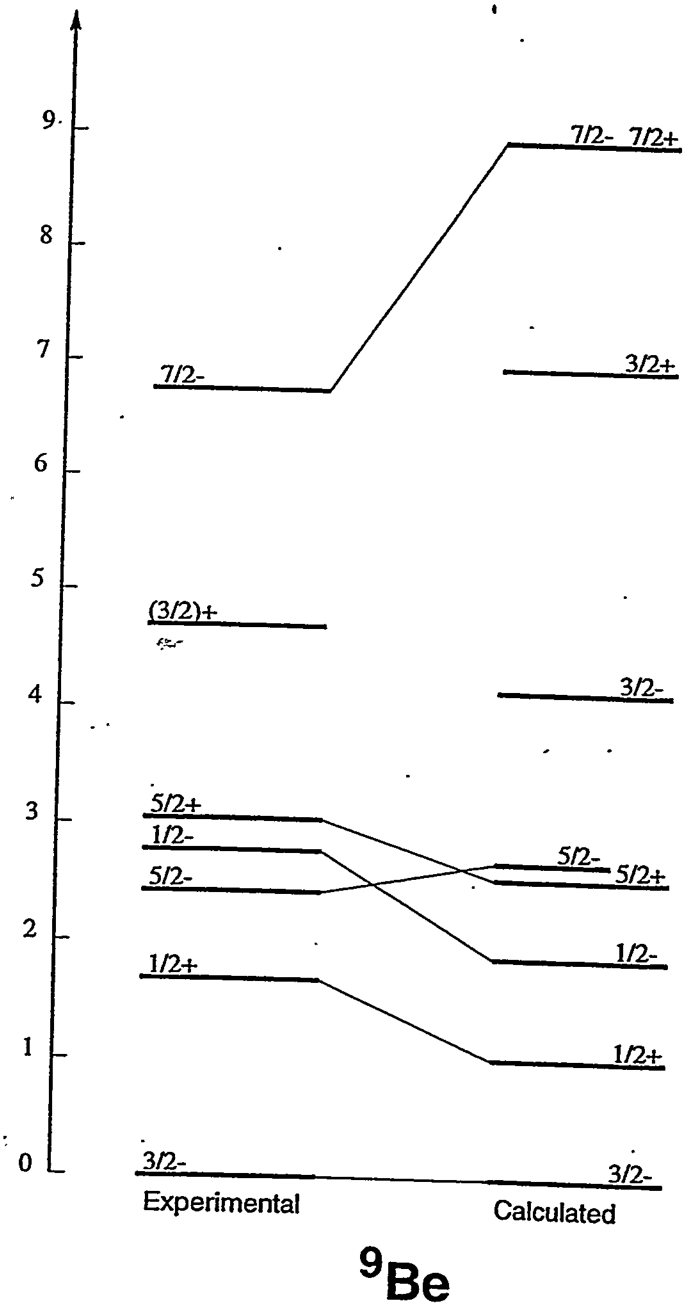

June 27, 1999

Stochastic variational method

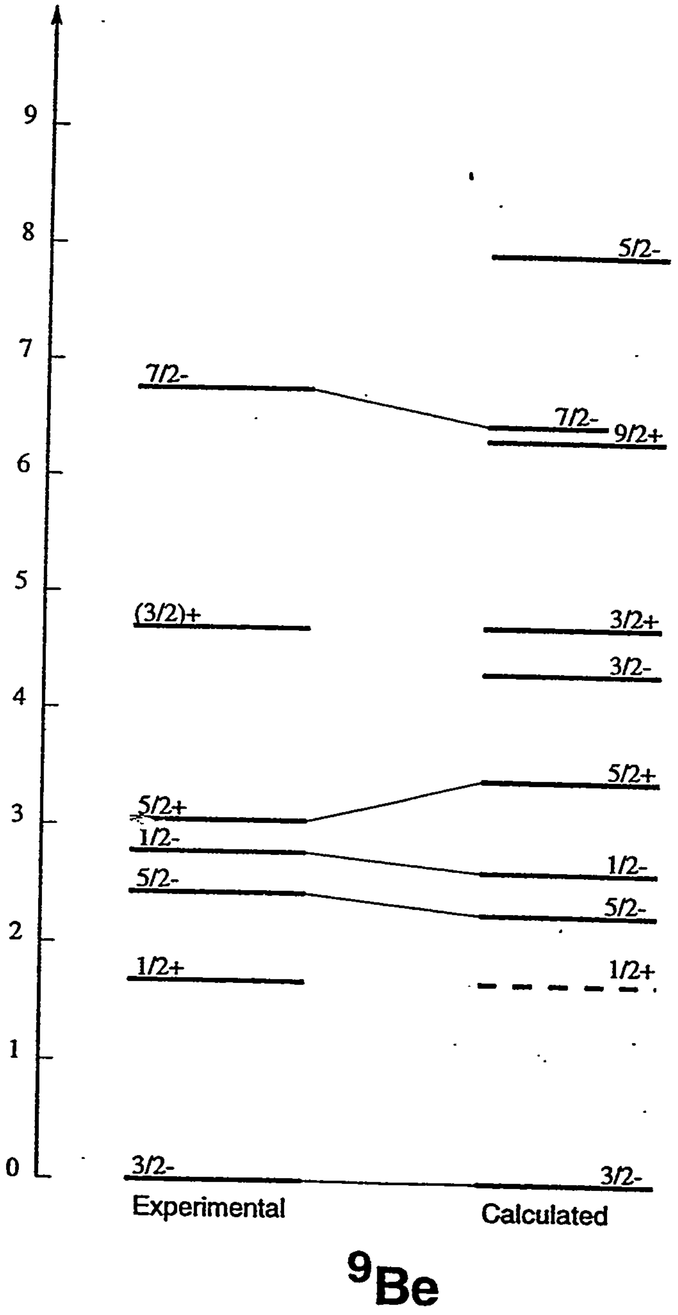

EM excitation of ^{9}Be: results

Model : DRC ($s \rightarrow p$ E1 transition)
: Breit-Wigner single-level resonance term
: Interference term included

Parameters : $E_r = 73.4$ KeV, $\Gamma_n = 217$ KeV
: $\Gamma_\gamma = 0.45$ eV

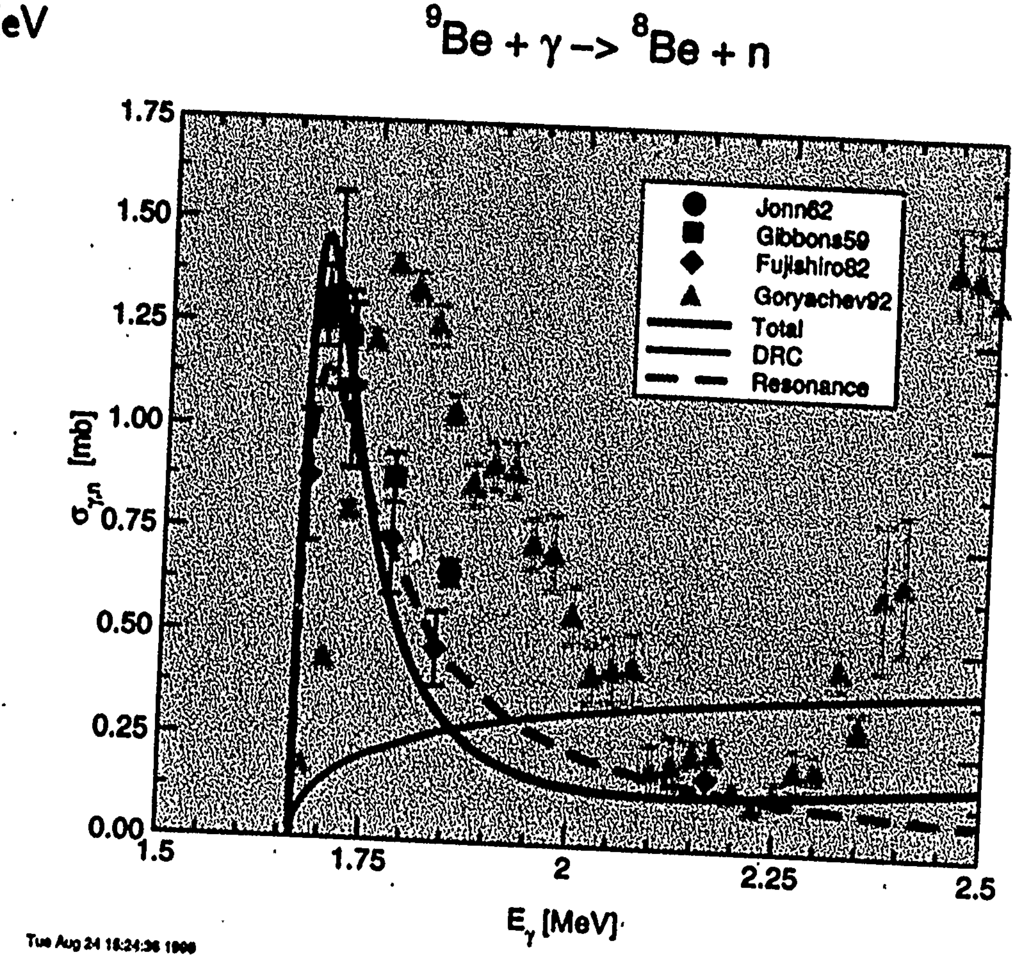

Neutron capture cross section for ^{8}Be

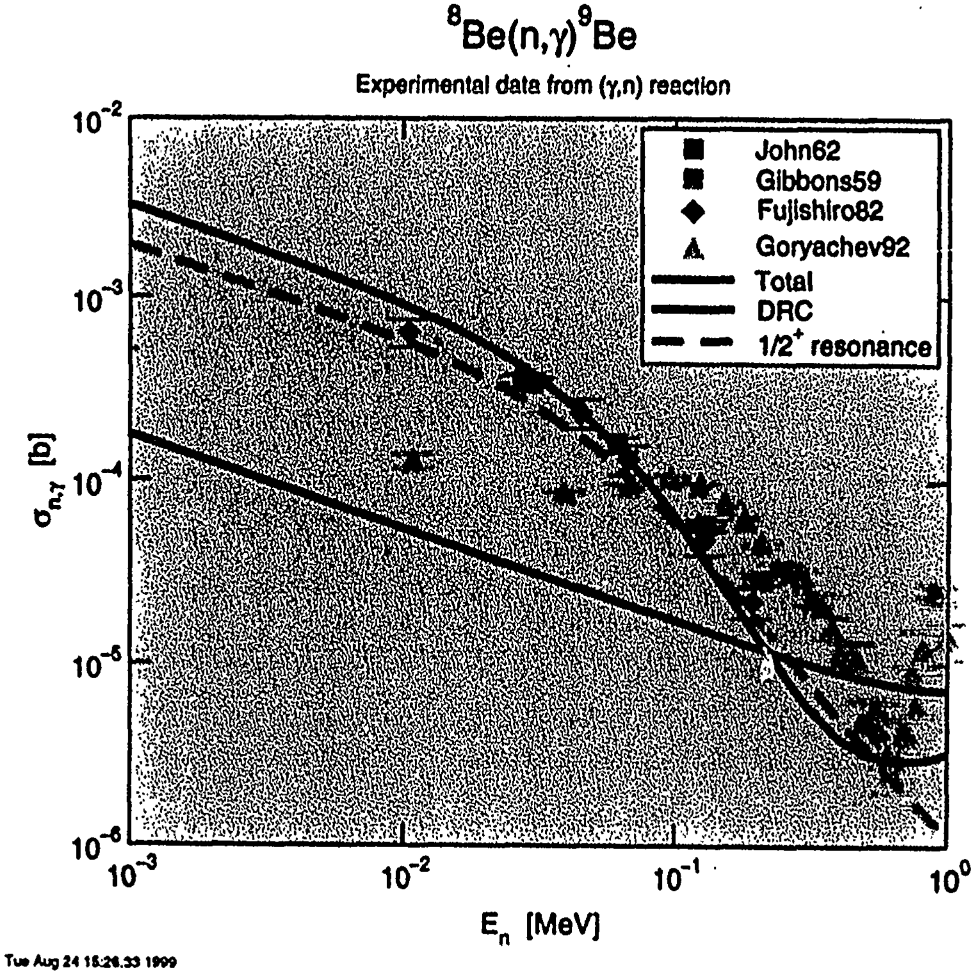

Conclusion

Neutron capture, photo and Coulomb dissociation reactions provide reliable and in some cases unique tools for investigating nuclear structure properties of light (stable AND unstable) nuclei.

SENSITIVITY OF SOLAR OSCILLATION FREQUENCIES TO ELEMENT ABUNDANCES AND COMPOSITION GRADIENTS

Joyce A. Guzik and Corinne Neuforge
XTA, MS B220
Los Alamos National Laboratory
Los Alamos, NM 87545

We are fortunate to live close enough to a pulsating star, the Sun, for which we can resolve the disk and thereby measure the frequencies of thousands of its global modes of oscillation. These nonradial p-modes travel to varying depths in the solar interior, and their frequencies have been measured in some cases to a precision of one part in a million; therefore they are extremely sensitive probes of solar interior structure. The process of using solar oscillations to determine the solar interior structure and test the physical input to solar models is called "helioseismology", analagous to the way that seismic waves are used to infer the Earth's interior structure.

The modern standard solar model generally has been successful in reproducing observed frequencies and the inferred sound speed of the solar interior. Nevertheless, discrepancies of several tenths of a percent in sound speed persist--these small differences are used as clues to refine the model initial assumptions and input physics. In this review we will discuss the degree to which helioseismology is sensitive to element abundances and composition gradients in the solar interior. We will discuss the sensitivity of helioseismic results to different recent solar element abundance determinations, including those of Ross and Aller (1976), Anders and Grevesse (1989), Grevesse and Noels (1993), and Grevesse and Sauval (1998). We will show the helioseismic evidence for diffusive settling of about 10 percent of the initial helium and 5 to 10 percent of heavier elements from the solar envelope convection zone during the Sun's 4.5 billion-year lifetime. Finally, we will discuss the implications of altering the solar central composition, or the composition gradient produced by nuclear burning of hydrogen to helium, on low-degree solar oscillation frequencies and the solar neutrino problem.

LA-UR- 99 - 4810

Approved for public release;
distribution is unlimited.

Title: SENSITIVITY OF SOLAR OSCILLATION FREQUENCIES TO ELEMENT ABUNDANCES

Author(s): Joyce A. Guzik and Corinne Neuforge

Submitted to: Proceedings of The Origin of the Elements In the Solar System: Implications of Post-1957 Observations, August 22-26, 1999, New Orleans, LA. To be published by Kluwer Academic.

Sensitivity of Solar Oscillation Frequencies to Element Abundances

JOYCE A. GUZIK AND CORINNE NEUFORGE
Applied Theoretical and Computational Physics Division, Los Alamos National Laboratory, XTA, MS B220, Los Alamos, NM 87545-2345

Key words: Sun--abundances; Sun--oscillations; Sun--diffusion

Abstract: We are fortunate to live close enough to a pulsating star, the Sun, for which we can resolve the disk and thereby measure the frequencies of thousands of its global modes of oscillation. These nonradial p-modes travel to varying depths in the solar interior, and their frequencies have been measured in some cases to a precision of one part in a million; therefore they are extremely sensitive probes of solar interior structure. The process of using solar oscillations to determine the solar interior structure and test the physical input to solar models is called "helioseismology", analogous to the way that seismic waves are used to infer the Earth's interior structure. The modern standard solar model generally has been successful in reproducing observed frequencies and the inferred sound speed of the solar interior. Nevertheless, discrepancies of several tenths of a percent in sound speed persist--these small differences are used as clues to refine the model assumptions and input physics. In this review we discuss the degree to which helioseismology is sensitive to element abundances and composition gradients in the solar interior.

1. INTRODUCTION

In this paper we give a general introduction to the assumptions and input physics used in the standard solar evolution model. We also provide a brief introduction to helioseimology, using 5-minute solar oscillation frequencies to infer the interior structure of the Sun. Finally we discuss results of the application of helioseismology to infer the Sun's interior element abundances and composition profile, and test models incorporating diffusive settling, radiative levitation, and mixing processes.

2. SOLAR MODELING

Solar modelers attempt to derive the interior structure of the present Sun by calculating its evolution from the onset of nuclear energy generation in the core to the present day, and comparing with observed quantities. The goal is to match the observed solar luminosity ($3.846 \pm 0.005 \times 10^{33}$ erg/sec (Willson et al. 1986), mass $1.9891 \pm 0.0004 \times 10^{33}$ g), radius 6.9599×10^{10} cm (Allen 1973), and surface Z/X abundance ratio 0.0245 ± 0.0015 (Grevesse & Noels 1993) at the present solar age 4.52 ± 0.04 billion years (Guenther 1989). The equations that are solved numerically include those for hydrostatic equilibrium; energy production due to nuclear reactions and conversion of potential energy into thermal energy as the Sun's core contracts; and energy transport from the interior to the surface via radiative diffusion or convection. The models are calculated assuming spherical symmetry, negligible mass loss or mass accretion, no rotation or magnetic fields, and that the Sun's luminosity is generated by conversion of core hydrogen to helium via nuclear reactions, principally via the proton-proton, but also CNO-cycles. We usually divide the Sun into several hundred mass shells from the center to the surface, and divide the evolution into several hundred timesteps. Typically, the initial helium mass fraction (Y_o), the initial mass fraction (Z_o) of elements heavier than H and He, and a parameter regulating the efficiency of convection (e.g., the mixing length to pressure scale height ratio, α), are adjusted to obtain the observed luminosity, radius, and surface Z/X abundance at the present solar age.

Some have also attempted, successfully, to evolve solar models that take into account the additional constraints of the observed solar Li abundance, which is believed to be reduced by a factor of 160 from the primordial value (Grevesse & Sauval 1998). Solar modelers have so far been unsuccessful in creating models that produce the neutrino fluxes observed by the GALLEX, SAGE, Homstake, Kamiokande, and Super-Kamiokande neutrino experiments (Bahcall, Basu, & Pinsonneault 1998), while retaining good agreement with observed oscillation frequencies.

Solving the equations requires physical data and other input, including radiative and conductive opacities (as a function of temperature, density, and element composition); equation of state tables giving the pressure, energy, and other thermodynamic quantities as a function of temperature, density and composition; nuclear reaction rates; and a treatment for convective energy transport. Most modern solar models use the OPAL (Iglesias, Rogers

& Wilson 1992; Iglesias & Rogers 1996) opacities; the OPAL (Rogers, Swenson & Iglesias 1996) or MHD (Dappen, Mihalas, Hummer, & Mihalas 1988) equation of state tables; and the nuclear reaction rates of Caughlan & Fowler (1988), Bahcall, Pinsonneault, & Wasserburg (1995), or those discussed by Brun et al. (1998). Since the OPAL opacity tables do not extend to temperatures below 6000 K, these have been supplemented by low-temperature opacity tables of, e.g., Kurucz (1992), Alexander & Ferguson (1994, 1995), or Neuforge (1993). While many modelers continue to use the mixing-length treatment of convection (Bohm-Vitense 1958), some have adopted the treatment of Canuto & Mazzitelli (1991, 1992) which allows for a spectrum of eddy length scales, or an attached envelope calibrated by 2-D or 3-D turbulence models (Rosenthal et al. 1998; Demarque, Guenther, & Kim 1997). It has also become standard (and essential) in modern solar models to incorporate some treatment of diffusive settling of helium and heavier elements (see, e.g. Cox, Guzik, & Kidman 1989; Thoul, Bahcall, & Loeb 1994).

3. INTRODUCTION TO HELIOSEISMOLOGY

Solar five-minute oscillations were discovered in 1960 by Leighton, Noyes, and Simon (1960) from Doppler velocities derived from spectral line profile variations. These velocity variations are manifested as waves on the solar surface with peak velocities of 1000 m sec^{-1}. They remain coherent for 6-7 periods over spatial scales of about 0.05 $R_\odot$ (Fig. 1). At first these waves were thought to be superficial phenomena related to convection cells near the surface, but were later interpreted by Ulrich (1970) and independently by Leibacher and Stein (1971) as the interference pattern of over 10 million global acoustic (sound, pressure) modes of oscillation, with frequencies between 1000 and 5000 μHz (periods ~5 minutes), and amplitudes less than 15 cm sec^{-1}. The Sun acts as a resonant acoustic cavity that traps these waves; they are reflected by the rapidly decreasing density as they travel toward the solar surface, and turned around (refracted) by the increasing sound speed as they travel toward the solar center. This discovery launched the new research field of helioseismology. Researchers made rapid progress in modeling solar evolution and pulsations, guided by attempts to match the properties of thousands of solar oscillation modes observed to very high accuracy. There are numerous excellent review articles (e.g. Christensen-Dalsgaard et al. 1996; Harvey 1995) that describe the properties of solar oscillations and their usefulness for inferring the Sun's interior structure.

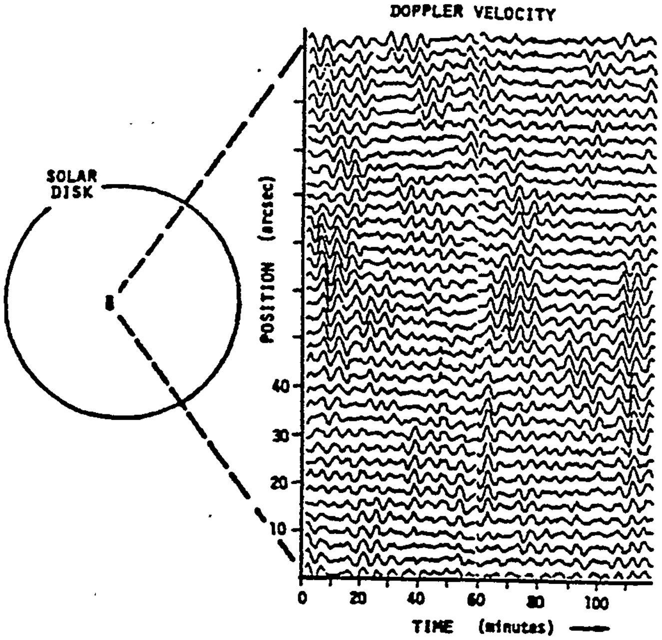

Figure 1. Wave packets seen in space- and time-resolved doppler velocity observations of the solar disk. These wave packets are actually the superposition of millions of acoustic resonance modes of oscillation that undergo constructive and destructive interference (from Toomre 1984).

Mathematically, solar oscillations can be described in terms of a set of normal modes (eigenmodes), consisting of a radial component, with the radial order n equal to the number of nodal points inside the Sun (Fig. 2), and an angular component represented by spherical harmonics $Y_{l,m}(\theta, \varphi)$ (Fig. 3). The angular degree l denotes the total number of nodal lines on the surface. Rotation (and to a lesser extent magnetic fields) breaks the spherical symmetry of the Sun. For example, for the Sun's slow rotation of about 26 days, each mode with the same degree l is split into $2l+1$ frequencies, separated by approximately the Sun's rotational frequency of about 0.45 μHz. The absolute value of the azimuthal order m, where $m = -l$, $(-l+1)$, . . ., 0, . . ., $(l-1)$, l, corresponds to the number of nodal lines through the symmetry axis (Fig. 3). Note (Fig. 2) that modes of low angular degree l penetrate deep within the solar interior, while modes of high degree turn around closer to the solar surface. Thus modes of different l can be used to probe different depths in the solar interior; by considering all of the modes, we can infer the entire interior structure.

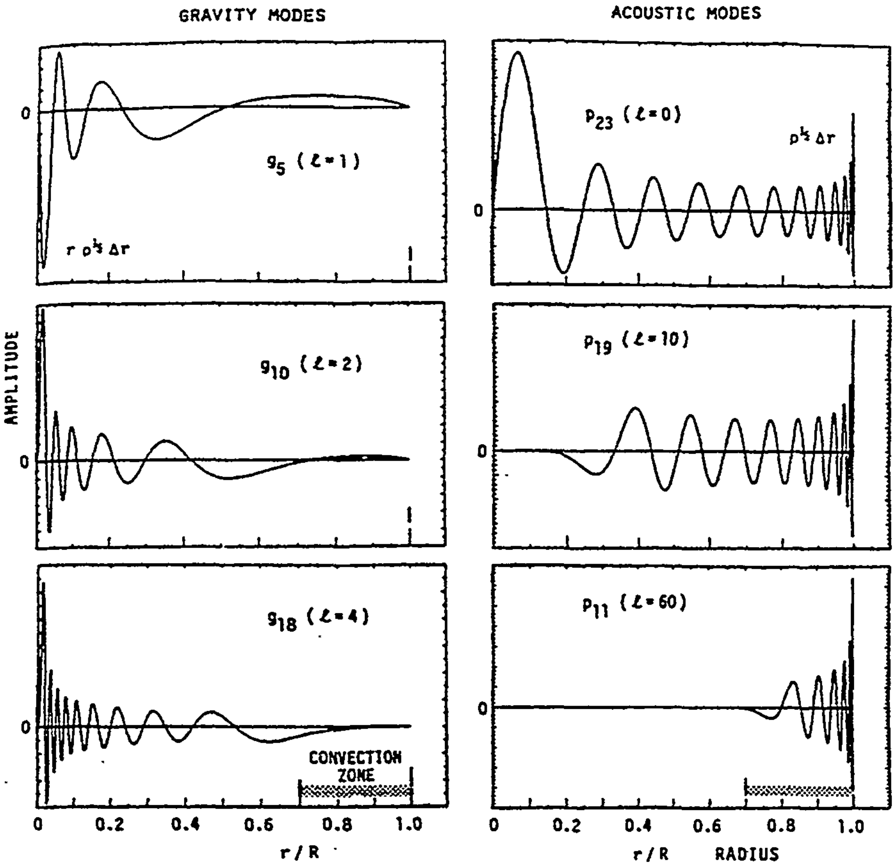

Figure 2. Scaled amplitudes versus radius of solar oscillation eigenmodes. The mode order *n* gives the number of nodes in the solar interior. The *g*-modes (left) have large amplitudes near the solar core, but are evanescent in the convection zone. The *p*-modes (right) propagate throughout the entire Sun, with modes of low angular degree *l* penetrating farthest into the solar interior (from Toomre 1984).

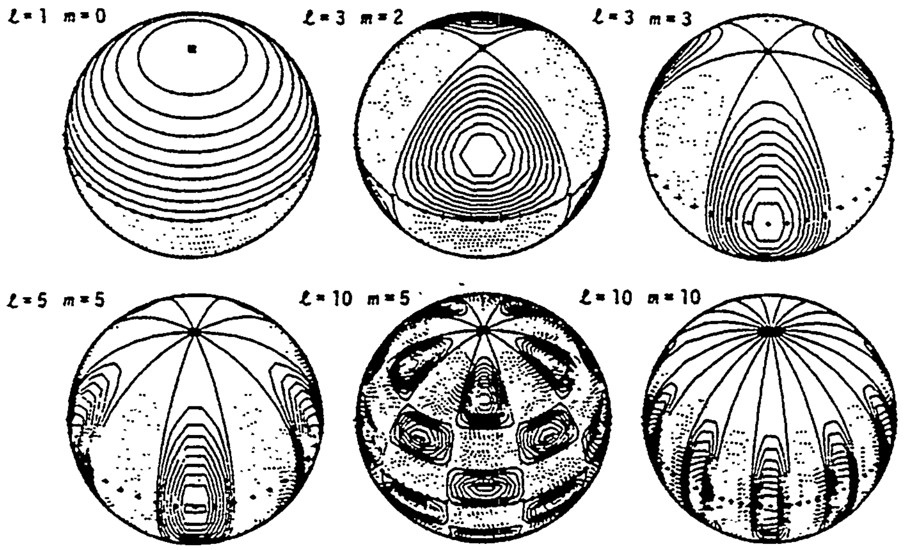

Figure 3. Doppler velocity contours for some eigenmodes of solar oscillation. The angular degree *l* gives the number of nodal lines on the solar surface, and the azimuthal order m gives the number of nodal lines through the symmetry axis (from Toomre 1984).

Since we can spatially resolve the solar disk, we can obtain the frequencies of modes from degrees $l = 0$ through ~1000. The discovery of nonradial oscillations in the Sun has also prompted searches for nonradial oscillations in Sun-like stars, and initiated the field of asteroseismology. For other stars, only frequencies of low-degree modes ($l = 0$, 1, 2, and maybe 3) can be measured from photometric variations, since for these modes amplitude variations averaged over the entire unresolved disk may not fully cancel out.

In addition to the pressure (*p*-) modes, theory also predicts another class of global nonradial modes, the gravity (*g*-) modes, with periods of about 40 minutes. For these waves, the restoring force is gravity instead of pressure. Gravity modes are complementary to *p*-modes, in that they have large amplitudes near the solar core (Fig. 2), while only a few of the lowest-degree *p*-modes reach the core. The *g*-mode frequencies would therefore be extremely useful for probing the solar core, and addressing the important questions of the core rotation rate and neutrino flux problem (see Rouse, these proceedings). However, gravity modes cannot propagate through the solar convection zone, and in spite of many claims, their existence has not been confirmed observationally. The lowest-degree gravity modes may have enough amplitude near the solar surface to eventually be detectable by long time-series space-based observations, for example by the SOHO spacecraft launched in November 1995.

The two approaches to helioseismic comparisons can be categorized as *forward* and *inverse* methods. The objective of the forward method is to test the physical input of solar and stellar models, and not necessarily to derive the absolute structure of the solar interior. In the forward approach, one generally uses the best available physical input to calculate solar evolution as described above, and directly compares the observed and calculated oscillation frequencies. The differences between predictions and observation are used to evaluate and suggest further refinements in physical input. For an excellent overview, see "Testing a Solar Model: The Forward Problem" (Christensen-Dalsgaard 1995). See Guzik & Swenson (1997) for the results of a recent standard solar model employing the forward method.

The objective of the inverse approach is to derive the internal structure of the Sun independent of the physical input of the models. One uses a reference model to derive weighting functions, or *Kernels*, that relate a specific change in model structure to a change in predicted frequency. The differences between observed frequencies and those of the calculated reference model (incorporating as well the observational errors), are used as input to back out differences between the reference model structure and the sun for such quantities as sound speed, density, adiabatic index Γ_1, or rotation rate as a function of radius. In the case of the solar rotation, the observed rotationally-produced frequency splittings are used to determine the internal rotation profile as a function of latitude as well as of radius. See paper by Rouse (these proceedings) for additional discussion of forward and inverse methods.

4. HELIUM AND HEAVY ELEMENT DIFFUSION

The diffusion of helium and the heavy elements is driven by the gravity and the temperature gradient (gravitational diffusion), the composition gradient (chemical diffusion) and the heat flow (thermal diffusion). A complete derivation of the diffusion and heat flow equations is given in Burgers (1969). In the Sun, the convective envelope is completely mixed and homogeneous in composition. Diffusion operates from the base of the envelope and makes the composition of the whole envelope vary with time. This implies that the present surface Z/X is different from the primordial one, Z_o/X_o.

4.1 Seismological Evidence for Helium Diffusion

Standard solar evolution models require an initial helium mass fraction (Y_o) of about 0.274 to generate the current solar luminosity. The models also predict that diffusive settling has reduced the envelope convection zone Y by about 0.026, and the mass fraction of heavier elements by about 5-10% over the Sun's 4.5 billion year lifetime. Helioseismology strongly supports this result. For example, Basu (1998) uses the signature in the oscillation frequencies of partial ionization of helium in the convection zone at 50-300,000 K to derive $Y=0.248 \pm 0.001$. Kosovichev's (1995) direct inversion for the hydrogen abundance profile in the solar interior show a discontinuity in X at the convection zone base, expected from helium draining out of the convection zone and accumulating near the base where the diffusion velocities become slower (Figure 4). Note also that the inversion shows the core hydrogen profile, and the expected depletion due to nuclear processing. The calculated sound speed profile below the solar convection zone also agrees better with the helioseismically-inferred profile when helium diffusion is included, as can be seen in Fig. 5 from Gabriel (1997).

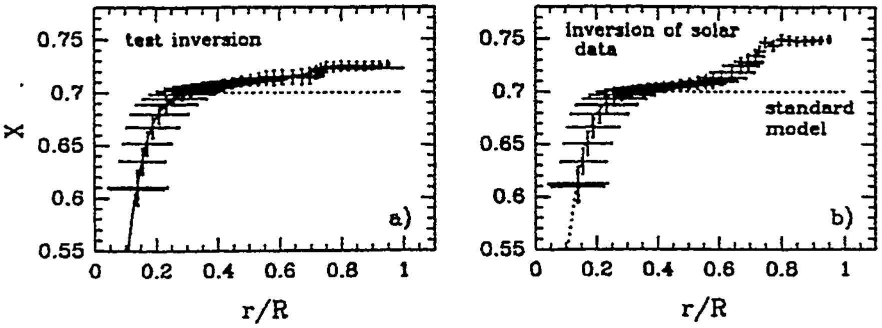

Figure 4. Inversion results for the solar interior hydrogen abundance (Kosovichev 1995). Panel a) shows how well the profile can be recovered for simulated oscillation data and a test model; panel b) shows the profile using actual solar oscillation data. The inversion shows a higher hydrogen abundance in the solar convection zone (outer 30% of the solar radius), due to diffusion.

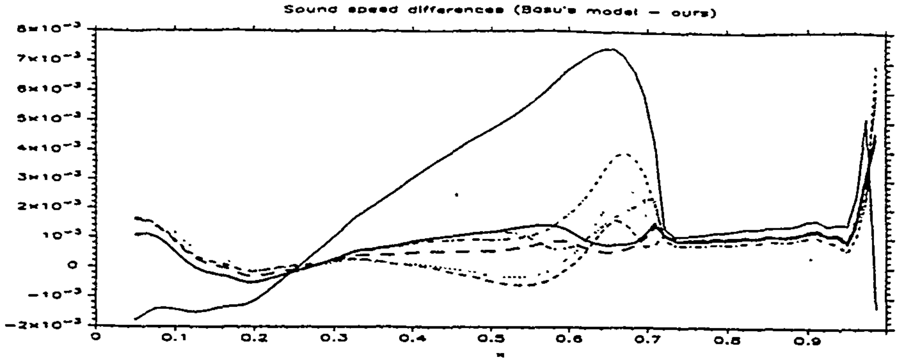

Figure 5. Sound speed profile differences between the models of Gabriel (1997) and the seismic reference model of Basu et al. (1997), as a function of the fractional radius. A model with helium and heavy element diffusion (dotted line) is in much better agreement with the seismic Sun than a model without diffusion (thin solid line).

Diffusion is a difficult problem to tackle and it needs to be treated using various approximations (see e.g. Michaud & Proffitt, 1993; Morel et al. 1997; Gabriel, 1997). Unfortunately, the solar models are not sensitive enough to discriminate between the different treatments of diffusion. Moreover, Figure 6 (Turcotte & Christensen-Dalsgaard, 1998a) shows that the differences between the primordial and the present surface abundances resulting from various prescriptions of diffusion are all smaller than the differences between the observed meteoritic and photospheric abundances. Recently, Turcotte et al. (1998) calculated solar models including radiative levitation and monochromatic opacities instead of Rosseland mean opacity tables, calculated for fixed relative abundances of the heavy elements. The various chemical species can indeed absorb a part of the net outgoing momentum flux carried by the photons and be pushed upwards, and, because all the elements do not settle at a common rate, their relative abundances vary with time. Figure 7 (Turcotte & Christensen-Dalsgaard, 1998b) shows that these major improvements appear to worsen slightly the calculated and inferred sound speed agreement. This may indicate that other compensating changes to input physics, such as in the opacities, may be needed to restore agreement.

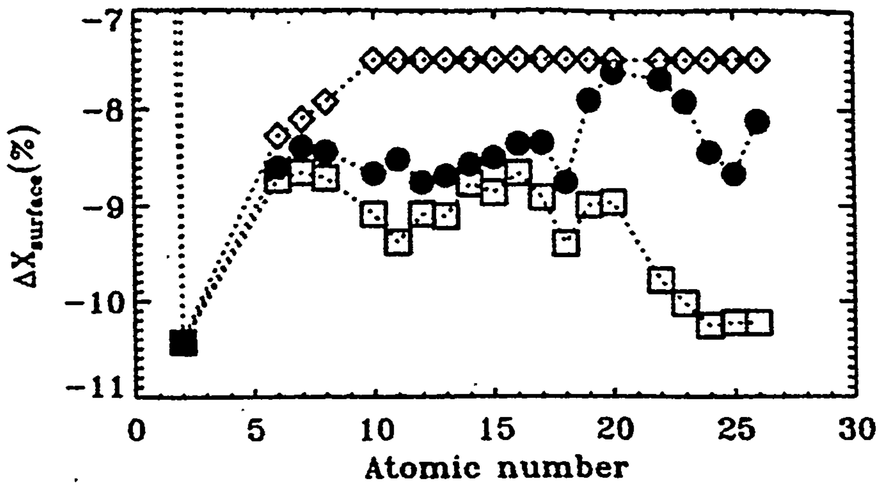

Figure 6. Fractional change of the surface abundances of all the elements included in the models of Turcotte et al. (1998), at the solar age and as a function of the atomic number. The models are: a solar model assuming a common settling rate for Z>8 (diamonds), the model including radiative forces and monochromatic opacities (filled circles) and a model including monochromatic opacities but with no radiative forces (squares).

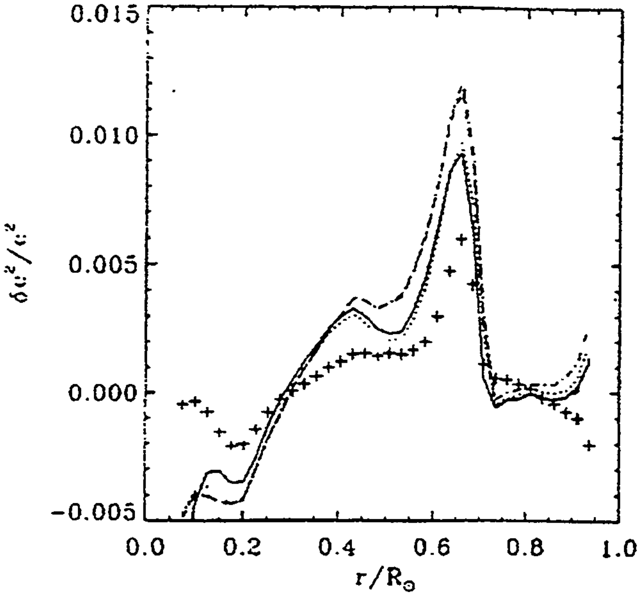

Figure 7. Relative differences in squared sound speed between the seismic reference model of Turck-Chièze et al. (1998) and theoretical models of Turcotte et al. (1998) in the sense (Sun)-(model), against fractional radius. The model calculated with no radiative forces and with Rosseland mean opacities (dotted line) appears to be better than the refined model calculated with radiative forces and monochromatic opacities (dash-dotted line).

5. THE SOLAR MIXTURE

The relative abundances of the heavy elements at the Sun's surface (the solar mixture) is used as an input in the computation of Rosseland mean opacity tables needed in model calculations, and Z/X provides a constraint in the modeling of the Sun. The most widely used solar abundances are those of Grevesse & Noels (1993).

Turcotte and Christensen-Dalsgaard (1998b) recalibrated a solar model with the Grevesse & Sauval (1998) revised solar abundances, presented in Table 1. Figure 8 shows that the new data increase the discrepancies between the inferred and calculated sound speed. The most important effects are due to the substantial reductions in Z/X and in the oxygen abundance: oxygen is the most abundant element after H and He and it dominates the opacity just below the convection zone. Nevertheless, the proposed changes for Z/X and oxygen are still within the uncertainties of the Grevesse and Noels (1993) composition.

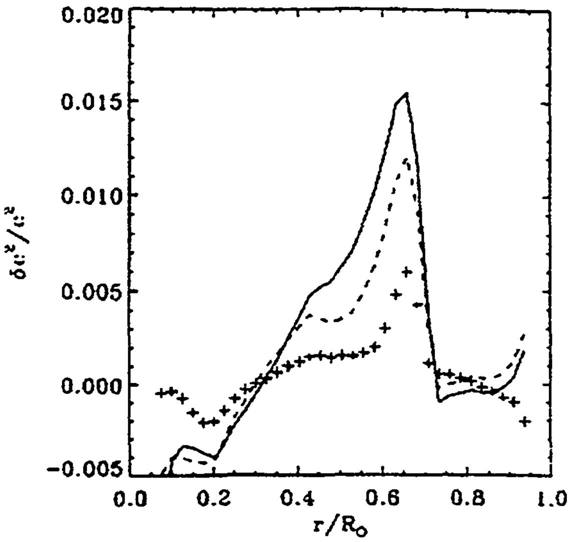

Figure 8. Relative differences in squared sound speed between the seismic reference model of Turck-Chièze et al. (1998) and theoretical models of Turcotte et al. (1998), in the sense (Sun)-(model), against fractional radius. The model calculated with the abundances of Grevesse & Noels (1993, dashed line) is in better agreement with the seismic data than the model calculated with the new abundances of Grevesse & Sauval (1998, solid line). Both models include monochromatic opacities but no radiative forces.

Table 1. Logarithmic C, N, O, S, and Ar abundances in number, relative to hydrogen (=12)

Element	Grevesse & Sauval (1998)	Grevesse & Noels (1993)
C	8.52 ± 0.06	8.55 ± 0.05
N	7.92 ± 0.06	7.97 ± 0.07
O	8.83 ± 0.06	8.87 ± 0.07
S	7.33 ± 0.11	7.21 ± 0.06
Ar	6.40 ± 0.06	6.52 ± 0.10
Z/X*	0.023	0.0245

*Z/X is the present surface mass fraction of heavy elements relative to hydrogen

6. ABUNDANCES THROUGH THE SOLAR INTERIOR

Turck-Chièze (1998) suggests that the small bumps superimposed on the general broad deviation in the squared sound speed differences between the model of Brun et al. (1998) and the sound speed inversion of Turck-Chièze et al. (1997, Figure 9) may result from the signature of the bound-bound processes of different heavy elements in the solar interior. Bound-bound processes give rise to a discontinuous opacity. For a given element, an incorrect abundance at the location where these processes are the most important will produce small discontinuities in the sound speed differences. A one percent effect in the total opacity will lead to a 0.1% effect on the sound speed profile, which should be observable. The seismic data could therefore give us access to the iron abundance near $0.2R_{\odot}$, the ^{3}He abundance at the edge of the nuclear core at $0.27R_{\odot}$, the silicon nd $0.4R_{\odot}$, the iron again around $0.6R_{\odot}$, and the oxygen near the ba he convection zone.

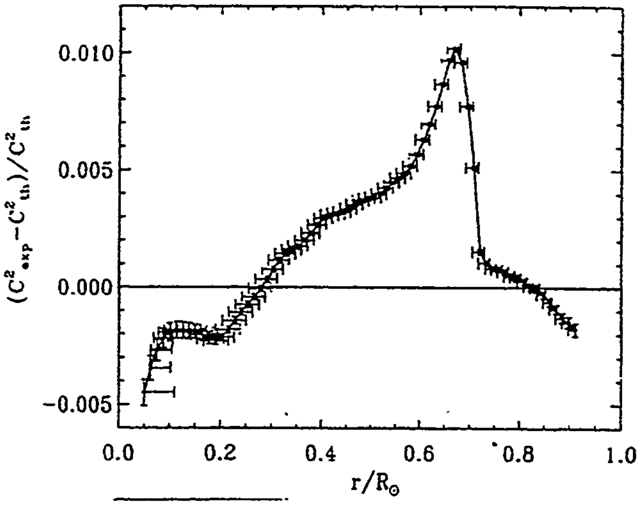

Figure 9. Relative differences in squared sound speed between the seismic reference model of Turck-Chièze et al. (1997) and the model of Brun et al. (1998). One can observe several small bumps superimposed on the general deviation in the squared sound speed differences.

7. THE SOLAR LITHIUM PROBLEM

Two explanations have been proposed to account for the depletion of ^{7}Li its presumed protosolar abundance to the present photospheric abundance: Mixing below the solar convection zone, induced by either differential rotation or gravity waves; and mass loss of about 0.1 solar masses early in the Sun's main-sequence lifetime. Both mechanisms have the advantage of smearing out the steep composition gradient at the base of the convection zone resulting from helium and element diffusion, and somewhat reducing the small remaining discrepancy between the inferred and calculated sound speed profiles.

Regarding the mass-loss scenario, Guzik & Cox (1995) and Morel, Provost, & Berthomieu (1997) conclude that the mass-loss phase must end quite early, no later than about 0.2-0.3 Gyr after the Sun arrives on the main sequence, to avoid ruining the good agreement with the sound speed of the models. The diffusion-produced composition gradient at the convection zone base is smoothed by the changing location of the convection zone boundary as the Sun loses mass. For example, Anderson et al. (1996) show for the Guzik & Cox model that a 0.3% difference in sound speed at the convection zone base is decreased to about 0.2%. However, in the early higher-mass phase, the increased nuclear energy generation rate steepens the resultant composition gradient in the core. Anderson et al. and Morel et al. show that if the mass loss phase does not end early enough, the core sound speed discrepancy is increased from 0-0.2% to about 0.4%.

Mixing induced by rotation or gravity waves, depending on the parametrization of the mixing, can do very well in improving the agreement in sound speed below the convection zone base (Gabriel 1997; Richard et al. 1996; Guenther & Demarque 1997). However, the mixing must not extend too deep to avoid ruining the good sound speed agreement in the solar core (Richard & Vauclair 1997).

8. CONCLUSIONS

Recent improvements to the physical input of the standard solar model have resulted in excellent agreement between the calculated and inferred solar structure, or between observed and calculated oscillation frequencies. Calculated low-degree p-mode frequencies agree with observation to within several μHz out of 3000 μHz, or a few tenths of a percent (Guzik & Swenson 1997). The inferred sound speed profile agrees with the profiles of standard solar evolution models to within 0.2% (Christensen-Dalsgaard et al. 1996). Helioseismology has provided clear evidence of diffusive settling of helium from the solar convection zone during the Sun's 4.5 billion year lifetime. Diffusive settling of about 5-10% of elements heavier than helium is expected as well, but the helioseismic signature is smaller due to the much smaller abundance of these elements. However, even small changes in element abundances, mixtures, and interior composition profiles alter the sound speed enough to be detectable by helioseismic methods. The oscillation frequency observations are so accurate that helioseismology promises to be a viable tool for helping to choose between alternative abundance mixtures, diffusion treatments, or proposed mixing processes.

REFERENCES

Alexander, D.R. & Ferguson, J.W. 1994, "Low-temperature Rosseland Opacities", ApJ, 437, 879

Allen, C.W. 1973, Astrophysical Quantities, 3rd Edition, (London: Athlone Press), p. 169

Anderson, E., et al. 1996, "The Seismic Structure of the Sun from GONG", in: "Sounding Solar and Stellar Interiors", eds. J. Provost and F.-X. Schmider, IAU, The Netherlands, p.151

Bahcall, J.N., Basu, S., & Pinsonneault, M.H. 1998, "How Uncertain are Solar Neutrino Predictions?," preprint astro-ph/9805135

Bahcall, J.N., Pinsonneault, M.H., & Wasserburg, G.J. 1995, "Solar Models with Helium and Heavy-element Diffusion", Rev. Mod. Phys. 67, 781

Basu, S. 1998, "Effects of Errors in the Solar Radius on Helioseismic Inferences", MNRAS 298, 719

Basu, S., Christensen-Dalsgaard, J., Schou, J., Thompson, M.J., Tomczyk, S. 1996, "The Sun's Hydrostatic Structure from LOWL Data", ApJ 460, 1064

Bohm-Vitense, E. 1958, "Uber die Wasserstoffkonvektionzone in Sternen verschiedener Effektivtemperaturen un Leuchtkräfte", Z. Astrophys. 45, 114

Brun, A.S., Turck-Chieze, S., Morel, P. 1998, "Standard Solar Models in the Light of New Helioseismic Constraints. I. The Solar Core", ApJ 506, 913

Burgers, J..M. 1969, Flow Equations for Composite Gases (New York: Academic)

Canuto, V.M. & Mazzitelli, I. 1991, "Stellar Turbulent Convection - A New Model and Applications", ApJ 370, 295

Canuto, V.M. & Mazzitelli, I. 1992, "Further Improvements of a New Model for Turbulent Convection in Stars", ApJ 389, 724

Caughlan, G.R. & Fowler, W.A. 1988, Atomic Nuclear Data Tables 40, p. 283

Christensen-Dalsgaard, J. 1995, "Testing a Solar Model: The Forward Problem", in: Proc. VI IAC Winter School "The Structure of the Sun", ed. T. Roca Cortes (Cambridge: Cambridge U. Press)

Christensen-Dalsgaard, J. et al. 1996, "The Current State of Solar Modeling", Science 272, 1286

Cox, A.N., Guzik, J.A., & Kidman, R.B. 1989, "Oscillations of Solar Models with Internal Element Diffusion", ApJ 342, 1187

Dappen, W., Mihalas, D., Hummer, D.G., & Mihalas, B.W. 1988, "The Equation of State for Stellar Envelopes. III - Thermodynamic Quantities", ApJ 332, 261

Demarque, P., Guenther, D.B., & Kim, Y.-C. 1997, "The Run of Superadiabaticity in Stellar Convection Zones. I. The Sun", ApJ 474, 790

Gabriel, M. 1997, "Influence of Heavy Element and Rotationally Induced Diffusions on the Solar Models", A&A 327, 771

Grevesse, N., Noels, A. 1993, "Cosmic Abundances of the Elements", in: "Origin and Evolution of the Elements", eds. N. Prantzos, E. Vangioni-Flam, M. Casse (Cambridge University Press, New York), p. 15

Grevesse, N., Sauval, A.J. 1998, "Standard Solar Composition", Sp. Sci. Rev. 85, 161

Guenther, D.B. & Demarque, P. 1997, "Seismic Tests of the Sun's Interior Structure, Composition, and Age, and Implications for Solar Neutrinos", ApJ 484, 937

Guenther, D.B. 1989, "Age of the Sun", ApJ 339, 1156

Guzik, J.A. & Cox, A.N. 1995, "Early Solar Mass Loss, Element Diffusion, and Solar Oscillation Frequencies", ApJ 448, 905

Guzik, J.A. & Swenson, F.J. 1997, "Seismological Comparisons of Solar Models with Element Diffusion Using the MHD, OPAL, and SIREFF Equations of State", ApJ 491, 967

Harvey, J. 1995, "Helioseismology", Physics Today 48, No. 10 (October 1995).

Iglesias, C.A. & Rogers, F.J. 1996, "Updated Opal Opacities", ApJ 464, 943

Iglesias, C.A., Rogers, F.J., & Wilson, B.G. 1992, "Spin-orbit Interaction Effects on the Rosseland Mean Opacity", ApJ 397, 717

Kosovichev, A.G. 1995, "Helioseismic Measurement of Element Abundances in the Solar Interior", Adv. Space Res. 15, (7) 95

Kurucz, R.L. 1992, ""Finding the "Missing" Solar Ultraviolet Opacity", Rev. Mexicana Astron. Astrofis. 23, 181

Leibacher, J. & Stein, R. F., 1971, "A New Description of the Solar Five-minute Oscillations", Astrophys. Lett. 7, 191

Leighton, R. B., Noyes, R. W., & Simon, G. W., 1962, "Velocity Fields in the Solar Atmosphere: I. Preliminary Report", ApJ 135, 474

Michaud, G., Proffitt, C.R. 1993, "Particle Transport Processes", in: "Inside the Stars", eds. A. Baglin and W.W. Weiss (San Fransisco, ASP), p. 246

Morel, P., Provost, J., Berthomieu, G. 1997, "Updated Solar Models", A&A 327, 349

Neuforge, C. 1993, "Low temperature Rosseland mean opacities", A&A 274, 818

Richard, O., & Vauclair, S. 1997, "Local mixing near the solar core, neutrino fluxes and helioseismology", A&A 322, 671

Richard, O., Vauclair, S., Charbonnel, C., & Dziembowski, W.A. 1996, "New Solar Models including Helioseismological Constraints and Light-element Depletion", A&A 312, 1000

Rogers, F.J., Swenson, F.J., & Iglesias, C.A. 1996, "OPAL Equation-of-State Tables for Astrophysical Applications", ApJ 456, 902

Rosenthal, C.S., Christensen-Dalsgaard, J., Nordlund, A., Stein, R.F., & Trampedach, R. 1998, "Convective Contributions to the Frequencies of Solar Oscillations," A&A, submitted

Thoul, A.A., Bahcall, J.N., & Loeb, A. 1994, "Element Diffusion in the Solar Interior", ApJ 421, 828

Toomre, J. "Overview of Solar Seismology: Oscillations as Probes of Internal Structure and Dynamics in the Sun," in: "Solar Seismology from Space", JPL Publication #84-84 (1984).

Turck-Chièze, S. 1998, "Composition and Opacity in the Solar Interior", Sp. Sci. Rev. 85, 125

Turck-Chièze, S., Basu, S., Berthomieu, G., Bonanno, A., Brun, A.S., Christensen-Dalsgaard, J., Gabriel, M., Morel, P., Provost, J., Turcotte, S., the GOLF team. 1998, "Sensitivity of the Sound Speed to the Physical Processes Included in the Standard Solar Model Framework", in: Proceedings of the SOHO6/GONG98 Workshop: "Structure and

Dynamics of the Interior of the Sun and Sun-like Stars", Boston USA, 1-4 June 1998 (ESA SP-418, 1998), p. 555

Turck-Chièze, S., Basu, S., Brun, A.S., Christensen-Dalsgaard, J., Eff-Darwich, A., Lopes, I., Perez Hernandez, F., Berthomieu, G., Provost, J., Ulrich, R.K., Baudin, F., Boumier, P., Charra, J., Gabriel, A.H., Garcia, R.A., Grec, G., Renaud, C., Robillot, J.M., Roca Cortes, T. 1997, "First View of the Solar Core from Golf Acoustic Modes", Sol. Phys. 175, 247

Turcotte, S., Christensen-Dalsgaard, J. 1998a, "Solar Models with Non-Standard Chemical Composition", Sp. Sci. Rev. 85, 133

Turcotte, S., Christensen-Dalsgaard, J. 1998b, "The Effect of Differential Settling on Solar Oscillation Frequencies", in: Proceedings of the SOHO6/GONG98 Workshop: "Structure and Dynamics of the Interior of the Sun and Sun-like Stars", Boston USA, 1-4 June 1998 (ESA SP-418, 1998), p. 561

Turcotte, S., Richer, J., Michaud, G., Iglesias, C.A., & Rogers, F.J. 1998, "Consistent Solar Evolution Model Including Diffusion and Radiative Acceleration Effects", ApJ 504, 539

Ulrich, R., 1970, "The Five-Minute Oscillations on the Solar Surface", ApJ 162, 993

Ulrich, R.K. & Rhodes, E.J., Jr. 1983, "Testing Solar Models with Global Solar Oscillations in the 5-minute Band", ApJ 265, 551

Willson, R.C., Hudson, H.S., Frolich, C., & Brusa, R.W. 1986, "Long-term Downward Trend in Total Solar Irradiance", Science 234, 1114

Linking Field Metal-Poor Stars and Globular Clusters

Corinne Neuforge
Los Alamos National Laboratory

Abstract

We have analyzed high resolution and high signal-to-noise spectra of 21 mildly metal-poor stars ([Fe/H] around -1). The correlations between the relative abundances of 16 elements have been studied, with a special emphasis on the neutron capture ones. This analysis reveals the existence of two sub-populations of field metal-poor stars, namely Pop IIa and Pop IIb. They differ by the behavior of the s-process elements versus the alpha and r-process elements. We suggest a scenario for the formation of metal-poor stars, which closely relates the origin of these stars to the evolution of globular clusters. According to this scenario, all thick disk and field halo stars were born in globular clusters from which they escaped, either during an early disruption of the proto-globular cloud (Pop IIa), or through a later disruption or an evaporation process of the cluster (Pop IIb). The chemical evolution of the globular clusters can be described in two phases. During the first one, massive stars in the proto-globular cluster cloud evolve, ending their lives as type II supernovae, and ejecting alpha elements and r-process elements into the interstellar medium. A second generation of stars forms out of this enriched ISM. The proto-globular cluster can become unstable and get disrupted, and those stars form Pop IIa. If it survives and forms a globular cluster, we get to the second phase, where intermediate mass stars reach the AGB, ejecting s-elements into the ISM through stellar winds or superwinds events. The matter released in the ISM by the AGB stars will be accreted by the lower mass stars, enriching the external layers of those stars in s-elements and accounting for Pop IIb.

Astron. Astrophys. 330, L33–L36 (1998)

ASTRONOMY
AND
ASTROPHYSICS

Letter to the Editor

Field halo stars: the globular cluster connection[*]

E. Jehin, P. Magain[**], C. Neuforge[***], A. Noels, and A.A. Thoul

Institut d'Astrophysique et de Géophysique, Université de Liège, 5, avenue de Cointe, B-4000 Liège, Belgium

Received 28 October 1997 / Accepted 14 November 1997

Abstract. High resolution and high signal-to-noise spectra of about 20 metal-poor stars have been analysed. The correlations between the relative abundances of 16 elements have been studied, with a special emphasis on the neutron-capture ones.

This analysis reveals the existence of two subpopulations of field halo stars, namely Pop IIa and Pop IIb. They differ by the behaviour of the s-process elements versus the α and r-process elements.

A scenario for the formation of these stars is presented, which closely relates the origin of field halo stars to the evolution of globular clusters. According to this scenario, the two subpopulations originate from two different stages in the globular cluster's chémical evolution.

1. Introduction

In traditional spectroscopic analyses of metal-poor stars, the mean abundance ratio of the chemical elements is discussed as a function of the overall metallicity, usually measured by the iron abundance [Fe/H]. The results are then compared to predictions from models of nucleosynthesis and chemical evolution of the Galaxy, and they are used to provide constraints on the sites and mechanisms for element synthesis. Unfortunately, these abundance ratios show rather considerable star-to-star scatter, therefore providing only weak constraints on the models.

With the improvement of observing and spectroscopic analysis techniques, it is now possible to reduce considerably the observational uncertainties in the abundance determinations, therefore decreasing the scatter in the abundance ratios. If the data are of sufficient quality, the remaining scatter is then mostly a genuine cosmic scatter which can be measured and analysed. We can investigate the cosmic scatter in relative abundances at a given metallicity and identify abundance correlations between several elements. Since the elements which are strongly correlated together have very likely been synthesized by the same nucleosynthetic processes in the same kinds of objects, we now have a new and efficient tool for identifying the sites and mechanisms of element synthesis at different stages of the galactic evolution. This new tool leads us to propose a scenario for the formation of field halo stars which links them to the globular clusters evolution.

2. Quality of the spectroscopic data

We have analysed a sample of about 20 dwarf and subgiant stars with [Fe/H] ~ -1, i.e. one tenth of the solar metallicity. This metallicity is generally assumed to correspond to the most metal-rich part of the halo of our Galaxy. The spectra were obtained with the Coudé Echelle Spectrometer (CES) fed by the 1.4m Coudé Auxiliary Telescope (CAT) at the European Southern Observatory (La Silla, Chile). Four spectral regions, chosen to contain lines of neutron-capture elements, were observed. The spectral resolution is of the order of 65 000 and the signal-to-noise ratio in the continuum is $\sim$ 250 for each spectrum. In order to reduce the analysis uncertainties, the lines were chosen to have similar dependences on the stellar atmospheric parameters (effective temperature, surface gravity, microturbulence velocity, overall metallicity) whenever possible. Moreover, the analysis was carried out differentially inside the sample, i.e., each star was compared to all other stars in the sample.

The sample of stars, together with some key abundance ratios and the total velocity with respect to the Local Standard at Rest, are presented in Table 1.

Following the traditional abundance analyses (e.g. Magain 1989, Edvardsson et al. 1993) we would show for example [Ti/Fe] as a function of [Fe/H]. The 1σ scatter in that plot for our sample amounts to 0.08 dex (20%). Is this scatter real or is it due to observational and/or analysis uncertainties? To answer this question we compare in Fig. 1 the values of [Ti/Fe] deduced from neutral lines with the ones deduced from lines of

---

[*] Based on observations carried out at the European Southern Observatory (La Silla, Chile)

[**] Maître de Recherches au Fonds National Belge de la Recherche Scientifique

[***] Chargé de Recherches au Fonds National Belge de la Recherche Scientifique

Table 1. Basic observational data, abundance ratios and total space velocity.

HD	b-y	[Fe/H]	[Ti/Fe]	[Y/Fe]	V(LSR)
22879	0.366	-0.892	+0.325	-0.033	131.4
25704	0.371	-0.894	+0.349	-0.174	132.2
59984	0.355	-0.755	+0.217	-0.195	52.2
61902	0.329	-0.727	+0.168	-0.264	87.0
63077	0.372	-0.831	+0.355	-0.070	152.1
63598	0.366	-0.856	+0.349	0.005	90.0
76932	0.360	-0.910	+0.332	0.045	120.9
78747	0.383	-0.730	+0.362	-0.050	29.5
79601	0.378	-0.668	+0.342	-0.151	42.0
97320	0.337	-1.220	+0.308	-0.150	91.0
111971	0.353	-0.737	+0.139	-0.218	31.9
126793	0.373	-0.800	+0.354	-0.102	10.8
134169	0.368	-0.804	+0.277	-0.193	40.8
152924	0.318	-0.708	+0.263	-0.196	45.0
189558	0.385	-1.129	+0.325	0.117	148.9
196892	0.346	-1.031	+0.342	0.048	126.2
199289	0.368	-1.074	+0.326	-0.138	72.5
203608	0.326	-0.677	+0.120	-0.223	51.0
215257	0.357	-0.804	+0.123	-0.309	77.5

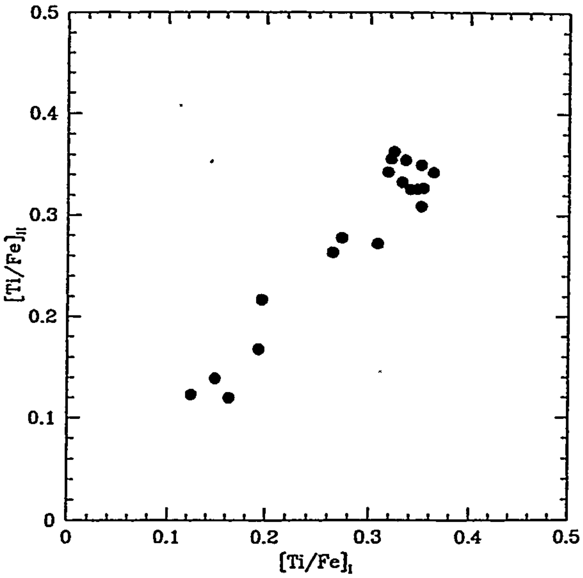

Fig. 1. Comparison of the values of [Ti/Fe] deduced from neutral lines, [Ti/Fe]$_I$, with those deduced from ionized lines, [Ti/Fe]$_{II}$

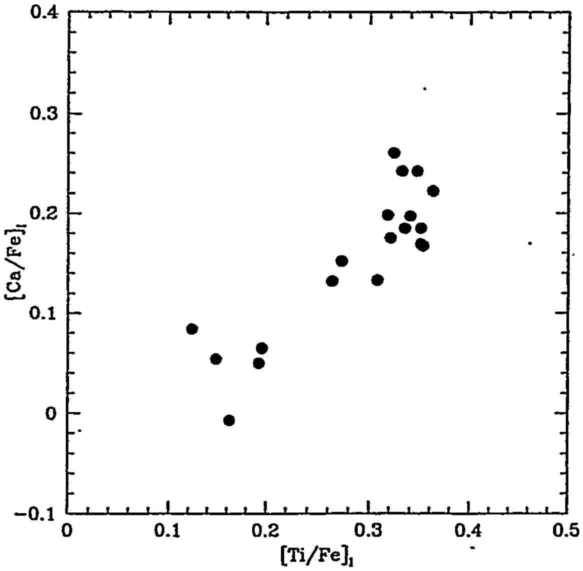

Fig. 2. Plot of [Ca/Fe] versus [Ti/Fe]

the singly ionized species. We can see a very nice correlation between those two values, with a scatter of only 0.026 dex (6%). Since the neutral and ionized lines have different dependences on the stellar atmospheric parameters, this shows that the scatter in element abundances due to analysis uncertainties does not exceed 6%. Therefore, the scatter in the abundance of Ti relative to Fe is real cosmic scatter. We will now investigate the cosmic scatter in the relative abundances of the other chemical elements.

3. Highlights of the abundance correlations

We find a close correlation between [Mg/Fe], [Ca/Fe] and [Ti/Fe], as illustrated in Fig. 2. This indicates that the so-called α-elements were synthesized by the same process in the same objects. We find a similar correlation between the abundances of Cr, Ni and Fe relative to Ti, indicating a common origin for these iron-peak elements.

We have also carried out this analysis for the neutron-capture elements, because we wanted to identify the sites and mechanisms for the synthesis of these elements in a relatively early phase of the galactic evolution. A first hint was put forward by Zhao and Magain (1991) who found that the elements Y and Zr are better correlated with Ti than with Fe. They suggested that this indicates that massive stars played a dominant role in the early nucleosynthesis of Y and Zr. Our results confirm their findings. For example, while the scatter of [Y/Fe] amounts to 0.12 dex (30%), the scatter of [Y/Ti] is only 0.07 dex (18%). Our new data allow us to go further than just compare the scatters, as shown in Fig. 3 where the values of [Y/Fe] versus [Ti/Fe] are plotted for each star in our sample. We see that [Y/Fe] is indeed correlated with [Ti/Fe], but this correlation is not simple. We can see two separate behaviours. For one subsample of the stars, the value of [Ti/Fe] increases with increasing [Y/Fe], while for the other subsample [Ti/Fe] is constant (and maximum) while [Y/Fe] increases. We find similar results when any of the elements Sr, Y and Zr is compared to any of the α-elements.

A very clean result is presented in Fig. 4, where the abundance of the prototypical r-process element Eu is compared to the Ti abundance. The correlation is nearly perfect. It allows us to conclude that, in general, the r-process element Eu is synthesized in the same objects as the α-elements, i.e. most probably in the supernova explosion of massive stars, confirming the generally accepted scenario. We notice the absence of a vertical feature similar to the one obtained for [Y/Fe]. Instead, it is re-

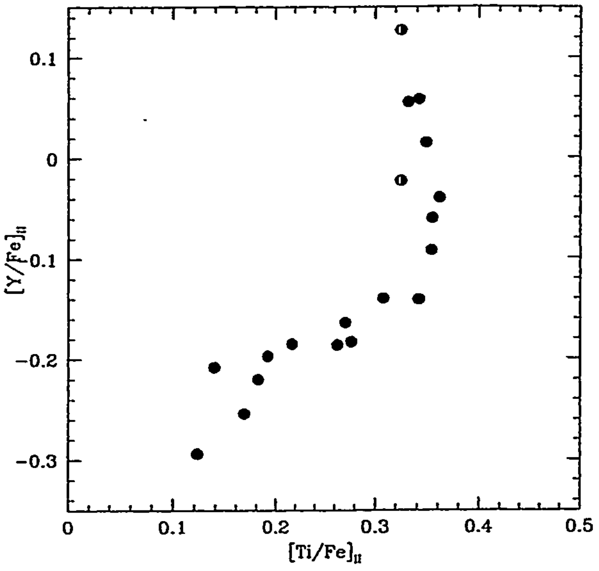

Fig. 3. Plot of [Y/Fe] versus [Ti/Fe]

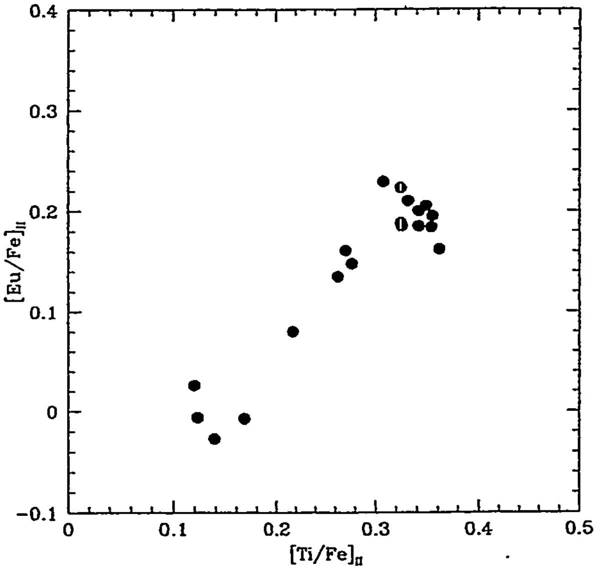

Fig. 4. Plot of [Eu/Fe] versus [Ti/Fe]

placed by a clumping of the points at the maximum value of [Ti/Fe] and [Eu/Fe].

4. Tentative scenario

According to the results presented above, we can distinguish between two separate stellar populations. Roughly 50% of the stars in our sample show a range of moderate overabundances of the α-elements and a slowly varying abundance of the s-process elements relative to the iron peak. The other 50% of the stars in the sample show a constant (and maximum) overabundance of the α-elements relative to the iron-peak elements, and varying s-process abundances. This behaviour must be related to nucleosynthesis processes.

The first interpretation which comes to mind is to relate one of these populations to the most metal-rich part of the halo and the other to the most metal-poor part of the disk. This interpretation is somewhat similar to what has been recently proposed by Nissen and Schuster (1997). However, upon examination of the kinematical data for our sample, there is no clear distinction between these populations on this basis alone, both populations containing high velocity stars typical of halo kinematics.

We therefore propose an alternative interpretation in which the halo stars can be divided into two sub-classes of Pop II stars, namely Pop IIa and Pop IIb, forming the two branches in Fig. 3. The stars belonging to the disk do not exhibit such correlations in their element abundances, unless they are very metal-poor. We will discuss these points in more details in a subsequent paper. In the following, we propose a scenario explaining the origin of the two sub-classes of halo stars.

4.1. General picture

First we assume a burst of star formation with at least some massive stars. As these massive stars evolve and end their lives in supernova (SN) explosions, α-elements and r-process elements are ejected in the surrounding interstellar matter (ISM). A second generation of stars will form out of this continuously enriched ISM. These stars will form the Pop IIa stars, with values of [α/Fe] and [r/Fe] increasing with time. The slope in [Y/Fe] versus [Ti/Fe] for Pop IIa stars indicates an overproduction of Y relative to Fe in massive stars. Our results show the same tendency for Sr and Zr.

Assume now that after this burst phase no more massive stars are formed. The lower mass stars are either still reaching the main sequence or in a more evolved phase, maybe already processing s-elements. These elements will be ejected through stellar wind or superwind events and will contaminate the surrounding ISM. After the SN phase, the ISM was already enriched in α and r-process elements, showing a unique [α/Fe] and [r/Fe]. The interstellar matter will continue to condense in new stars, now with a constant value of [α/Fe] and increasing values of [s/Fe]. These stars will form the Pop IIb stars.

Note that [Eu/Fe] shows a perfect correlation with [α/Fe] in Pop IIa stars, as expected. The points representative of Pop IIb stars are clumped at the maximum value of [α/Fe] and [r/Fe], i.e. at the values reached at the end of the massive stars outburst. This shows that, if produced by lower mass stars, it must be in the same proportions as Fe.

4.2. Globular clusters and EASE scenario

We now suggest that the formation of the field halo stars takes place in the globular clusters (GCs). This requires two reasonable assumptions. The first one is that the evaporation of low mass stars from GCs happens since the early phases of the evolution of the cluster and accounts for the field Pop II stars. The second one is that the matter ejected by SNe and stellar winds, although generally assumed to be mostly expelled from the cluster, nevertheless contributes to the enrichment of the lower

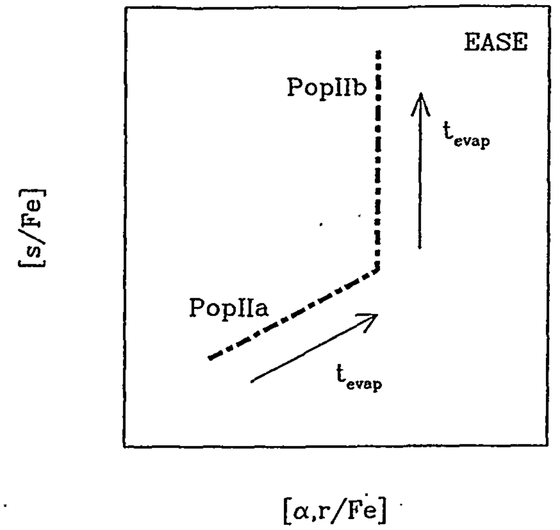

Fig. 5. EASE scenario. Here, t_{evap} is the time elapsed between the cluster formation and the evaporation of the star from the cluster

mass stars, first by mixing with the ISM and then by accretion at the surface of already formed stars. The possibility of self-enrichment by SNe has been discussed by Smith (1986, 1987) and Morgan and Lake (1989).

In the early phase of the GC evolution, massive stars will form SNe until all stars more massive than about $8M_\odot$ have completed their evolution. This fixes the end of the α and r elements synthesis and the maximum value of [α/Fe] observed in Fig. 3. The second phase will lead to a relative enrichment of s elements only.

Our two phases scenario nicely explains the features observed in Fig. 3. Pop IIa stars are evaporated during the massive stars outburst, [α/Fe] increasing with time, and the Pop IIb stars escape later in the evolution of the cluster, after the end of the SN phase. The stars located at the top of the vertical branch are those which have escaped the cluster in the most advanced phases of its evolution. A schematical illustration is given in Fig. 5.

The range of metallicity at a given location in Fig. 3 corresponds to stars evaporated from clusters of various global enrichments (due to different initial mass functions) and, thus, different present day metallicity. As the evolution time for a star of a given mass is about the same in all GCs, it is no surprise that the abundance ratios, contrary to the metallicity, do not depend on the cluster from which the halo stars have evaporated.

The similar numbers of Pop IIa and Pop IIb stars suggest that either the evaporation was much more efficient in the early phases of the GC evolution or that a large fraction of Pop IIa stars originate from GCs which have been disrupted during the massive stars outburst. This is in agreement with the view that GCs with a flat mass function are weakly bound (Meylan and Heggie, 1997). This is also in agreement with the recent work of Brown et al. (1995), where they develop a model for the early dynamical evolution and self-enrichment of GCs.

The EASE (Evaporation/Accretion/Self-Enrichment) scenario also nicely explains the larger metallicity range covered by the field halo stars, extending to much lower metallicities than the GCs. The very metal-poor stars would be evaporated from the GCs at a very early stage of the outburst phase, when the self-enrichment of the cluster was still very low.

Acknowledgements. This work has been supported by contracts ARC 94/99-178 "Action de Recherche Concertée de la Communauté Française de Belgique" and Pôle d'Attraction Interuniversitaire P4/05 (SSTC, Belgium).

References

Brown J.H., Burkert A., and Truran J.W., 1995, ApJ 440, 666
Edvardsson B., Andersen J., Gustafsson B., Lambert D.L., Nissen P.E., Tomkin J., 1993, A&A 275, 101
Magain P., 1989, A&A 209, 211
Meylan G., Heggie D.C., 1997, A&AR 8, 1
Morgan S., Lake G., 1989, ApJ 339, 171
Nissen P.E., Schuster W., 1997, A&A, in press
Smith G., 1986, PASP 99, 67
Smith G., 1987, ApJ 306, 565
Zhao G., Magain P., 1991, A&A 244, 425

This article was processed by the author using Springer-Verlag LaTeX A&A style file *L-AA* version 3.

Astron. Astrophys. 341, 241–255 (1999)

ASTRONOMY
AND
ASTROPHYSICS

Abundance correlations in mildly metal-poor stars*

E. Jehin, P. Magain, C. Neuforge***, A. Noels, G. Parmentier, and A.A. Thoul**

Institut d'Astrophysique et de Géophysique, Université de Liège, 5, Avenue de Cointe, B-4000 Liège, Belgium

Received 9 July 1998 / Accepted 29 September 1998

Abstract. Accurate relative abundances have been obtained for a sample of 21 mildly metal-poor stars from the analysis of high resolution and high signal-to-noise spectra. In order to reach the highest coherence and internal precision, lines with similar dependency on the stellar atmospheric parameters were selected, and the analysis was carried out in a strictly differential way within the sample.

With these accurate results, correlations between relative abundances have been searched for, with a special emphasis on the neutron capture elements.

This analysis shows that the r elements are closely correlated to the α elements, which is in agreement with the generally accepted idea that the r-process takes place during the explosion of massive stars.

The situation is more complex as far as the s elements are concerned. Their relation with the α elements is not linear. In a first group of stars, the relative abundance of the s elements increases only slightly with the α elements overabundance until the latter reaches a maximum value. For the second group, the s elements show a rather large range of enhancement and a constant (and maximum) value of the α elements overabundance.

This peculiar behaviour leads us to distinguish between two sub-populations of metal-poor stars, namely Pop IIa (first group) and Pop IIb (second group).

We suggest a scenario of formation of metal-poor stars based on two distinct phases of chemical enrichment, a first phase essentially consisting in supernova explosions of massive stars, and a second phase where the enrichment is provided by stellar winds from intermediate mass stars. More specifically, we assume that all thick disk and field halo stars were born in globular clusters, from which they escaped, either during an early disruption of the cluster (Pop IIa) or, later, through an evaporation process (Pop IIb).

Key words: stars: abundances – stars: Population II – nuclear reactions, nucleosynthesis, abundances – Galaxy: evolution

1. Introduction

The chemical composition of the solar system is now known with a high accuracy from the spectroscopic studies of the solar photosphere as well as from the analysis of the carbonaceous chondrites (Anders and Grevesse 1989, Grevesse et al. 1996). Moreover, theoretical models of stellar evolution and nucleosynthesis allow the identification of the most likely sites and mechanisms for the formation of the chemical elements. Combining them with simple models for the chemical evolution of the Galaxy, one can reproduce reasonably well the solar system abundances.

However, the solar system only provides a single data point, both in the time evolution of the Galaxy and in the spatial distribution in the disk. It is thus important to gather additional data in order to have an insight of the chemical composition of the interstellar matter at different epochs since the formation of the Galaxy.

As time goes by, more and more metals are synthesized in the stellar interiors and ejected in the surrounding environment, so that the overall metallicity slowly increases. Although the correlation of metallicity with time is not a perfect one, unevolved metal-poor stars give a picture of the chemical conditions at earlier phases of the galactic evolution.

Up to now, spectroscopic analyses of metal-poor stars have essentially consisted in determining abundance ratios as a function of metallicity. These ratios are supposed to show the evolution of the nucleosynthetic processes with time. Unfortunately, these results generally show a rather large scatter, which is either of cosmic origin or due to observational uncertainties. In the latter case, this prevents any meaningful comparison with the theoretical models. On the other hand, if the scatter reflects an intrinsic cosmic dispersion, it should be accounted for in the models.

In order to find the origin of that scatter, we must improve the accuracy of the abundances. This requires both high quality data and a careful spectroscopic analysis.

Send offprint requests to: E. Jehin

* Based on observations obtained at the European Southern Observatory, La Silla, Chile.

** Maître de Recherches au Fonds National de la Recherche Scientifique (Belgium)

*** Chargé de Recherches au Fonds National de la Recherche Scientifique (Belgium)

Table 1. Basic photometric data

HD	ID	V	b−y	V−K	c_1
22879	1	6.70	0.366	1.478	0.274
25704	2	8.12	0.371	1.53	0.275
59984	3	5.92	0.355	1.423	0.335
61902	4	8.24	0.329	1.29	0.361
63077	5	5.38	0.372	1.53	0.273
63598	6	7.94	0.366	–	0.299
76932	7	5.83	0.360	1.475	0.299
78747	8	7.73	0.383	–	0.296
79601	9	8.00	0.378	–	0.306
97320	10	8.19	0.337	1.31	0.305
111971	11	8.05	0.353	–	0.304
126793	12	8.19	0.373	1.44	0.291
134169	13	7.68	0.368	1.464	0.309
152924	14	8.02	0.318	1.24	0.379
189558	15	7.74	0.385	1.575	0.269
193901	16	8.67	0.376	1.52	0.221
194598	17	8.35	0.343	1.38	0.269
196892	18	8.24	0.346	1.37	0.307
199289	19	8.29	0.368	1.42	0.264
203608	20	4.22	0.326	1.23	0.310
215257	21	7.42	0.357	1.53	0.310

Table 2. Model parameters

HD	$T_{\rm eff}$ (K)	$\log g$ (cgs)	[Fe/H]	ξ (km/s)
22879	5774	4.1	−1.00	1.0
25704	5715	3.9	−1.05	1.1
59984	5860	3.8	−0.85	1.3
61902	6054	3.9	−0.85	1.3
63077	5717	4.0	−0.90	0.9
63598	5779	3.9	−0.95	1.1
76932	5798	3.9	−1.00	1.0
78747	5676	3.8	−0.80	1.0
79601	5716	3.8	−0.75	1.1
97320	6000	4.1	−1.30	1.2
111971	5880	4.0	−0.85	1.1
126793	5783	3.9	−0.90	1.3
134169	5782	3.8	−0.90	1.2
152924	6132	3.9	−0.80	1.4
189558	5628	3.8	−1.20	1.2
193901	5703	4.4	−1.15	0.8
194598	5920	4.2	−1.20	1.0
196892	5925	4.0	−1.10	1.2
199289	5808	4.1	−1.15	1.2
203608	6112	4.3	−0.80	1.3
215257	5769	3.8	−0.90	1.3

Here, we report on the results of such a detailed analysis and we investigate the underlying reasons for the remaining scatter – if any. We look at correlations between different abundance ratios at a given metallicity. Strongly correlated elements are likely to have been processed in the same astrophysical sites. Therefore, the identification of such correlations can provide fruitful insights on the nucleosynthesis of these elements. This allows us to suggest a scenario for the formation of metal-poor stars. Preliminary results have already been presented briefly in Jehin et al. (1998).

2. Observations and data reduction

We have selected a sample of 21 unevolved metal-poor stars (Tables 1 and 2), with roughly one tenth of the solar metallicity ([Fe/H] ~ -1 [1]). This corresponds more or less to the transition between the halo and the disk.

The observations were carried out with the Coudé Echelle Spectrometer (CES) fed by the 1.4 m Coudé Auxilliary Telescope (CAT) at the European Southern Observatory (La Silla, Chile). The long camera was used with a Loral CCD detector (ESO #38) having 2688×512 pixels of 15×15 μm each.

The exposure times were chosen in order to reach a signal-to-noise ratio (S/N) of at least 200 in all spectral regions. The spectra were collected during two observing runs, in January 1996 (8 nights) and July 1996 (11 nights), the last one having been carried out in remote control from the ESO headquarters in Garching bei München. All stars were observed in four wavelength bands, each band having a width of about 50Å. These spectra are centered around 4125, 4325, 4584 and 4897Å.

The data reduction consisted in:

1. background subtraction on the basis of the mean level measured on the parts of the CCD not illuminated by stellar light;
2. flat-fielding, using the spectrum of an internal lamp;
3. wavelength calibration, using the stellar lines themselves to define the calibration curve, thus automatically correcting for the radial velocity;
4. definition of the continuum, in the form of a low order Spline fitted through a number of pre-defined continuum windows;
5. equivalent widths (EWs) measurements, by Gaussian and Voigt function fitting, the first method being preferred for the weak lines and the second in the case of the stronger ones (for which the Lorentzian damping wings contribute significantly to the EW). The table listing the nearly 2000 EWs measurements is available in electronic form from CDS.

3. Determination of the atmospheric parameters

3.1. *Effective temperature*

The effective temperatures $T_{\rm eff}$ were determined from the Strömgren b−y and Johnson V−K colour indices, using the calibration of Magain (1987) which is based on the infrared flux method (Blackwell and Shallis 1977). The sources of b−y measurements are Schuster and Nissen (1988), Olsen (1994) and Carney (1983). The V−K colours were obtained from Carney (1983), Alonso et al. (1994) and from some unpublished

---

[1] We adopt the usual spectroscopic notation: $[A/B] \equiv \log_{10}(N_A/N_B)_\star - \log_{10}(N_A/N_B)_\odot$ for elements A and B.

measurements by P. Magain with the ESO 1 m telescope on La Silla. When several values were available for the same star, the average was taken.

The adopted effective temperature is a mean of the two determinations and is listed in Table 2. The agreement between the temperatures deduced from the two colour indices is quite good, the mean difference amounting to 45 K, with an r.m.s. scatter of 40 K in the individual determinations.

All these stars being in the solar neighbourhood (distances range from 9 to 80 pc), the interstellar reddening should be negligible. The internal precision of the effective temperatures may thus be estimated from the comparison of the two photometric determinations. The scatter of 40 K in the T_{eff} differences corresponds to an uncertainty of 28 K ($40/\sqrt{2}$) in the individual values and of 20 K in the mean T_{eff} from the two colour indices. This high internal precision can be checked from the differential excitation equilibria of FeI. The excitation equilibria indicate effective temperatures which agree quite well with the photometric values: the scatter of the excitation temperatures around the photometric ones amounts to 57 K, while the expected scatter, on the basis of a precision of 20 K on the photometric values and 45 K on the excitation values, amounts to 50 K. The 7 K difference is completely negligible and shows that the internal precision of our effective temperatures is indeed very high.

3.2. Metallicity

For the first step, the model metallicities were taken from previously published analyses. This is not a crucial parameter in metal-poor stars model atmospheres as the continuous opacity is dominated by the contribution of the negative hydrogen ion and hydrogen itself is the main electron donor. Nevertheless, the model metallicities were redetermined on the basis of our set of FeI lines. The latter values were used in the subsequent analysis.

3.3. Surface gravity

Surface gravities are usually determined by requiring FeI and FeII lines to indicate the same abundance. However, this procedure is affected by several uncertainties. For example, the iron abundance derived from FeI lines is quite sensitive to T_{eff} and unfortunately the zero-point of the T_{eff} scale of metal-poor stars may be uncertain by as much as 100 K, causing errors in [Fe/H] of about 0.10 dex and errors in the spectroscopic gravities of the order of 0.25 dex. For other uncertainties, see for e.g the discussion in Nissen et al. (1998). To avoid these problems, we decided (1) to determine the surface gravity from the Strömgren c_1 index, using the calibrations of VandenBerg and Bell (1985) for the adopted temperatures and metallicities; (2) to always derive relative abundances from the comparison of lines of the same ionization stage and, thus, of the same dependence on surface gravity.

Table 3. Data for the 2.52 eV CaI lines in HD 76932: wavelength λ, excitation potential χ, oscillator strength $\log gf$, equivalent width EW and damping enhancement factor f_6 over the Unsöld formula.

λ (Å)	χ (eV)	$\log gf$	EW (mÅ)	f_6
5260.390	2.52	−1.719	8.6	1.4
5261.710	2.52	−0.579	54.2	1.4
6161.295	2.52	−1.266	23.4	2.0
6163.754	2.52	−1.286	25.3	2.0
6166.440	2.52	−1.142	29.1	2.0
6169.044	2.52	−0.797	49.9	2.0
6169.564	2.52	−0.478	66.3	2.0
6493.788	2.52	−0.109	83.4	0.8
6499.654	2.52	−0.818	47.9	0.8

3.4. Microturbulence velocity

Microturbulence velocities ξ are obtained, as usual, by forcing a set of lines of the same element and same ionization stage but with different EWs to indicate the same abundance. In our observations, only the FeI lines are suitable for such a determination. The precision of the microturbulence determinations, estimated by linear regression, is better than 0.1 km s^{-1}. The adopted model parameters for the 21 stars are listed in Table 2.

4. Method of analysis

4.1. A strictly differential analysis

Our stellar sample is rather homogeneous in terms of atmospheric parameters: all the stars are dwarfs or subgiants with $3.8 < \log g < 4.4$, have roughly solar temperatures with $5620\,\text{K} < T_{\text{eff}} < 6140\,\text{K}$ and a narrow range of metallicity ($-1.3 <$ [Fe/H] < -0.7). A differential analysis within the sample is thus indicated, especially as we are interested in distinguishing minute variations from star to star and, so, need the highest possible internal precision.

As a first step, all stars were analysed with respect to HD 76932, one of the brightest stars in our sample, having average atmospheric parameters. The zero points of the element abundances in HD 76932 were determined from lines with laboratory gf-values (Table 3). When lines from two ionization stages were available, the abundance of the ion was forced to agree with that of the neutral.

The microturbulence velocity in the atmosphere of HD 76932, which must be known in order for this differential analysis to be carried out, was determined from a set of CaI lines with the same excitation potential, precise laboratory gf-values (Smith and Raggett 1981) and a suitable range of EWs (Table 3). These lines were observed with the same instrument in the context of another programme. A value of $\xi = 1.0$ km/s has been obtained.

It is possible to reduce even further the uncertainties in the relative gf-values by analysing each star with respect to each other and derive mean gf-values from the whole sample. This reduces the scatter in the line abundances for an individual star but has no effect on the mean abundances of one star relative to another, provided that exactly the same lines are used in both stars. Since this is not the case for all stars, we only used this global differential analysis whenever justified, i.e. when the number of lines of a given species is large enough and when the line sample varies from star to star. Such an analysis was performed for FeI, FeII, TiI, TiII, CrI, CrII and NiI.

4.2. *Model atmospheres and line analysis*

The abundance analysis was carried out with model atmospheres constructed individually for each star. The usual assumptions of Local Thermodynamic Equilibrium (LTE) and plane parallel (horizontally homogeneous) atmospheres were made. These models were calculated on the basis of the temperature stratifications ($T(\tau)$ relations) of Kurucz (1993). Given the $T(\tau)$ relation, the gas pressure, the electron pressure and the continuous absorption were computed with a programme based on the Gustafsson et al. (1975) subroutines.

When more than one line of the same species was measured for a star, the mean abundance value and the standard deviation were computed. Whenever possible, the analysis was restricted to lines having EWs between 5 and 50 mÅ. Using weaker lines would lead to increased random errors (and possibly some systematic overestimates), while stronger lines are very sensitive to microturbulence and damping. In a few cases, however, especially for Mg, rather strong lines had to be used, while only very weak lines were available for Zr, Sm and Ce. The damping constants γ were computed with the Unsöld formula (Gray 1972), with an empirical enhancement factor of 1.5.

The 93 spectral lines used in the abundance analysis are listed in Table 4. They were selected after a careful inspection of the stellar and solar spectra. The lines were chosen as far as possible to be free of blends affecting the EW measurements.

5. Element abundances

5.1. *Iron peak elements*

We have obtained the abundances of four iron peak elements, namely V, Cr, Fe and Ni (Table 5). They all have a rather large number of clean lines and the line-to-line scatter of the abundances is small ($<\sigma>\sim$ 0.03). In the case of Fe and Cr, both neutral and ionized lines are available.

Our iron abundances are based on 34 FeI and 3 FeII transitions. The zero point for iron was obtained from 3 FeI lines with accurate oscillator strengths from the Oxford group (Blackwell et al. 1982a and references therein). The iron ionization equilibrium is satisfied to a good accuracy ($<[\mathrm{Fe/H}]_{\rm I}-[\mathrm{Fe/H}]_{\rm II}>=$ $+0.011 \pm 0.051$), the small scatter confirming the photometrically determined surface gravities.

From the 6 CrI and 4 CrII lines available in our spectra, we find that the chromium abundance in metal-poor stars scales like the iron one. The scatter around the mean is very small in both cases: 0.030 dex for $[\mathrm{Cr/Fe}]_{\rm I}$ and 0.032 dex for $[\mathrm{Cr/Fe}]_{\rm II}$. The agreement between the neutral and ionized lines is satisfactory: $<[\mathrm{Cr/H}]_{\rm I}-[\mathrm{Cr/H}]_{\rm II}>=$ $+0.002 \pm 0.050$. The zero point was

Table 4. Atomic line data. The six columns give, respectively, the element and its ionization stage, the wavelength, the excitation potential of the lower level, the differential log gf determined from our analysis, the absolute log gf from the literature and the EW in the spectrum of HD 76932.

El.	λ (Å)	χ (eV)	log gf dif.	log gf abs.	HD 76932 (mÅ)
Mg I	4571.102	0.00	−5.014	−5.550	76.0
Ca I	4108.532	2.71	−0.547		31.9
Ca I	4578.559	2.52	−0.415	−0.697	48.5
Sc II	4314.091	0.62	0.378	−0.040	98.1
Sc II	4320.749	0.61	0.147	−0.210	87.8
Ti I	4112.716	0.05	−1.648	−1.758	13.9
Ti I	4870.136	2.25	0.501	+0.358	16.0
Ti I	4885.088	1.89	0.497		29.0
Ti I	4913.622	1.87	0.267	+0.160	20.7
Ti II	4316.802	2.05	−1.498		34.2
Ti II	4330.245	2.05	−1.552		32.7
Ti II	4330.708	1.18	−1.892		53.8
Ti II	4563.766	1.22	−0.599		105.4
Ti II	4568.328	1.22	−2.752		17.6
Ti II	4571.982	1.57	−0.100		124.0
Ti II	4583.415	1.16	−2.739		19.6
Ti II	4589.953	1.24	−1.446		70.4
Ti II	4874.014	3.09	−0.809		22.5
Ti II	4911.199	3.12	−0.493		34.7
V I	4111.787	0.30	−0.047	+0.408	42.6
V I	4115.177	0.29	−0.407	+0.071	28.1
V I	4330.024	0.00	−1.148	−0.631	13.7
V I	4577.184	0.00	−1.618	−1.048	5.6
V I	4594.126	0.07	−1.232	−0.672	10.7
V I	4875.492	0.04	−1.355	−0.807	9.3
Cr I	4111.358	2.90	−0.442		11.5
Cr I	4129.184	2.91	+0.246		35.4
Cr I	4580.062	0.94	−1.580		38.2:
Cr I	4600.757	1.00	−1.376	−1.276	43.5
Cr I	4870.816	3.08	+0.162		25.8
Cr I	4885.774	2.54	−2.117	−1.055	5.5
Cr II	4558.650	4.07	−0.465		55.5
Cr II	4588.204	4.07	−0.686		47.2
Cr II	4592.057	4.07	−1.293		23.5
Cr II	4884.598	3.86	−2.083		9.0
Fe I	4109.062	3.29	−1.464		36.0
Fe I	4112.323	3.40	−1.701		20.1
Fe I	4114.451	2.83	−1.366		56.5
Fe I	4114.942	3.37	−1.644		22.8
Fe I	4120.212	2.99	−1.290		53.8
Fe I	4124.489	3.64	−2.219		4.7
Fe I	4125.886	2.84	−2.056		28.3
Fe I	4126.191	3.33	−0.963		57.5
Fe I	4126.857	2.84	−2.763		7.8
Fe I	4132.908	2.84	−0.997	−0.960	71.0
Fe I	4136.527	3.37	−1.573		25.1
Fe I	4137.005	3.41	−0.679		62.2
Fe I	4137.415	4.28	−0.961		17.4
Fe I	4566.524	3.30	−2.228		10.7:

Table 4. (continued)

El.	λ (Å)	χ (eV)	log gf dif.	log gf abs.	HD 76932 (mÅ)
Fe I	4574.225	3.21	−2.419		8.4
Fe I	4574.728	2.28	−2.889		18.3
Fe I	4587.134	3.57	−1.727		14.7
Fe I	4595.365	3.30	−1.712		26.6
Fe I	4596.416	3.65	−2.169		6.0
Fe I	4598.125	3.28	−1.529		34.2
Fe I	4602.008	1.61	−3.182	−3.154	30.2
Fe I	4602.949	1.48	−2.195	−2.220	76.0
Fe I	4875.881	3.33	−1.900		18.2
Fe I	4885.434	3.88	−1.045		30.3
Fe I	4886.337	4.15	−0.735		33.4
Fe I	4896.442	3.88	−1.931		6.2
Fe I	4907.735	3.43	−1.804		18.3
Fe I	4908.032	4.22	−1.562		7.4
Fe I	4910.020	3.40	−1.348		38.5
Fe I	4910.330	4.19	−0.742		30.0
Fe I	4910.570	4.22	−0.754		31.4
Fe I	4911.782	3.93	−1.687		9.0
Fe I	4917.235	4.19	−1.025		19.9
Fe I	4918.015	4.23	−1.212		14.4:
Fe II	4128.742	2.58	−3.668		24.4
Fe II	4576.339	2.84	−3.047		41.0
Fe II	4582.833	2.84	−3.280		30.8
Ni I	4331.651	1.68	−2.146	−2.100	31.6
Ni I	4600.364	3.60	−0.499		24.2
Ni I	4604.996	3.48	−0.252	−0.250	38.4
Ni I	4606.226	3.60	−0.921		11.3:
Ni I	4873.446	3.70	−0.459	−0.380	22.1
Ni I	4904.418	3.54	−0.079		45.0
Ni I	4912.025	3.77	−0.739		12.4
Ni I	4913.978	3.74	−0.569		17.3
Ni I	4918.371	3.84	−0.140		29.9
Sr I	4607.338	0.00		0.280	14.9
Y II	4883.690	1.08	+0.074	0.070	42.3
Y II	4900.124	1.03	−0.072	−0.090	38.7
Zr II	4317.321	0.71		−1.380	8.3
Ba II	4130.657	2.72		0.560	18.8
La II	4322.505	0.17	−0.938		5.4
La II	4333.763	0.17	−0.152	−0.160	22.4
Ce II	4137.655	0.52	+0.065		10.2
Ce II	4562.367	0.48	−0.080	0.330	9.1
Nd,II	4109.450	0.32	+0.548	0.519	20.0
Nd II	4314.512	0.00	−0.292	−0.226	8.4
Sm II	4318.936	0.28		−0.270	6.4
Eu II	4129.724	0.00		0.204	38.8

fixed from the oscillator strengths of Blackwell et al. (1984, 1986b) for Cr I.

Nickel is represented in our spectra by 9 clean Ni I lines. The three absolute log gf available for the zero point calibration are from Doerr and Kock (1985) and the recent determinations from Wickliffe and Lawler (1997).

Because of the lack of hyperfine structure (HFS) data for our V I lines, we have restricted our analysis to 6 lines with EWs smaller than 30 mÅ (except 4111.787Å which is slightly stronger but had to be included for our most metal-poor stars). Using accurate transition probabilities from Whaling et al. (1985) we have derived gf-values for each V I line. Absolute abundances were thus computed and compared with the results obtained from the differential analysis. The very small scatter around the mean difference ($< \sigma > \sim$ 0.02) reflects the high internal accuracy of the two sets of gf-values. The relative abundances of iron peak elements are listed in Table 5.

5.2. *α elements*

The magnesium abundance is obtained from a single Mg I line, the calcium abundance from two neutral lines and the titanium abundance from a first set of 4 Ti I lines and a second set of 8 Ti II lines.

Only the rather strong intercombination Mg I line (~70 mÅ) at 4571 Å is available in our spectra for the Mg abundance determination. The deduced abundance is thus more sensitive to the microturbulence velocity ξ.

The line-to-line scatter in the deduced titanium abundances is ~ 0.025. The ionization equilibrium of titanium confirms, once again, the validity of the photometric surface gravities: $<[\mathrm{Ti/H}]_{\mathrm{I}} - [\mathrm{Ti/H}]_{\mathrm{II}} >= +0.016 \pm 0.044$. The zero point was determined from 3 accurate Ti I gf-values (Blackwell et al. 1982b, 1986a).

The relative abundances are given in Table 6.

5.3. *Heavy elements*

For the sake of clarity, we shall distinguish between the light s-process elements (Sr, Y, Zr), the heavy s-process elements (Ba, La, Ce) and the mixed or r-process elements (Nd, Sm, Eu). This is of course an oversimplification, several processes contributing in variable proportions to the synthesis of each of them.

For Sr, we used the neutral resonance line at 4607.34 Å with an oscillator strength log gf = 1.92 ± 0.06 (Migdalek and Baylis (1987)), a value which is in agreement with both experimental and theoretical determinations.

The agreement between our two lines of Y II is always very good, with a mean difference of 0.02 between the two line abundances. The absolute log gf used were determined from measurements of radiative lifetimes and branching ratios (Hannaford et al. 1982).

The only Zr II line available in our spectra has an accurate laboratory oscillator strength (Biémont et al. 1981).

The only Ba line available is the 4130 Å Ba II line. The abundances were computed with 9 HFS components but the HFS effect turns out to be very small. The transition probability was taken from Gallagher (1967). This line is slightly blended

Table 5. Iron peak element abundances and line-to-line scatter

ID	$[\mathrm{Fe/H}]_{\mathrm{I}}$	$[\mathrm{Fe/H}]_{\mathrm{II}}$	$[\mathrm{V/Fe}]_{\mathrm{I}}$	$[\mathrm{Cr/Fe}]_{\mathrm{I}}$	$[\mathrm{Cr/Fe}]_{\mathrm{II}}$	$[\mathrm{Ni/Fe}]_{\mathrm{I}}$
1	−0.892(16)	−0.888(12)	−0.032(36)	−0.111(28)	−0.107(26)	−0.082(32)
2	−0.960(26)	−1.001(19)	0.015(33)	−0.124(33)	−0.109(30)	−0.093(37)
3	−0.755(27)	−0.755(07)	−0.103(32)	−0.098(43)	−0.128(15)	−0.112(33)
4	−0.727(23)	−0.693(16)	−0.102(36)	−0.098(51)	−0.130(49)	−0.122(29)
5	−0.831(22)	−0.840(10)	0.030(35)	−0.079(38)	−0.052(56)	−0.070(33)
6	−0.856(27)	−0.970(25)	−0.046(66)	−0.101(41)	−0.099(41)	−0.086(36)
7	−0.910(29)	−0.910(12)	−0.039(37)	−0.089(35)	−0.089(22)	−0.083(31)
8	−0.730(20)	−0.857(11)	−0.033(34)	−0.098(55)	−0.070(17)	−0.084(32)
9	−0.668(23)	−0.760(17)	0.008(29)	−0.072(26)	−0.023(24)	−0.074(31)
10	−1.220(17)	−1.179(31)	−0.095(82)	−0.124(32)	−0.108(46)	−0.080(35)
11	−0.737(27)	−0.748(25)	−0.136(30)	−0.157(56)	−0.105(33)	−0.134(30)
12	−0.800(24)	−0.864(17)	−0.001(55)	−0.113(47)	−0.117(31)	−0.080(30)
13	−0.804(32)	−0.823(10)	−0.069(37)	−0.107(43)	−0.086(15)	−0.095(46)
14	−0.708(28)	−0.675(41)	−0.106(140)	−0.088(62)	−0.102(49)	−0.082(32)
15	−1.129(34)	−1.093(30)	−0.037(38)	−0.098(51)	−0.132(40)	−0.108(38)
16	−1.071(25)	−1.043(06)	−0.200(58)	−0.154(38)	−0.143(31)	−0.232(44)
17	−1.126(30)	−1.074(28)	−0.139(57)	−0.164(33)	−0.141(76)	−0.185(45)
18	−1.031(21)	−1.025(13)	−0.024(81)	−0.082(45)	−0.064(33)	−0.077(37)
19	−1.074(32)	−1.100(18)	−0.023(63)	−0.142(45)	−0.065(48)	−0.055(39)
20	−0.677(29)	−0.636(07)	−0.079(51)	−0.109(93)	−0.133(30)	−0.086(37)
21	−0.804(29)	−0.814(15)	−0.160(90)	−0.162(36)	−0.088(39)	−0.136(43)

on the red wing with a Ce II line but the error on the deduced differential abundances should not exceed 5%.

For the La II line at 4333 Å, we have adopted the transition probability calculated by Gratton and Sneden (1991) from the experimental lifetime measurements of Arnesen et al. (1977a, 1977b) and Andersen et al. (1975). No HFS was included because de EWs never exceed 30 mÅ. This line is slightly blended by a CH line but no correction was applied.

Two lines of Ce II are measurable in our spectra but are located in very crowded regions. Moreover, these two lines are not available for all the stars. For the zero point, we have adopted the transition probability given by Gratton and Sneden (1991) for the 4562 Å line, determined by renormalizing the values of Corliss and Bozman (1962) to the lifetimes results of Andersen et al. (1975). The abundance derived for HD 97320 is very uncertain.

The Nd II lines are also not easy to measure and are not available for all stars. We have performed an inverse solar analysis to obtain $\log gf$ values, but the zero point is somewhat uncertain.

The Sm abundance was derived from a single weak Sm II line, and the zero point deduced from the oscillator strength given by Biémont et al. (1989).

The Eu II line at 4129.724 Å has both a large HFS and a significant isotopic shift. Each of the two isotopes has 16 HFS components (Woolf et al. 1995). They were all included, based on the data from Broström et al. (1995) for the isotopic shift (4578 MHz). The 32 HFS components were calculated using data from Becker et al. (1983), Villemoes and Wang (1994) and Möller et al. (1993). A laboratory gf-value ($\log gf = 0.204 \pm 0.027$), determined from lifetimes and relative line intensities (Biémont et al. 1982) was used. The isotopic ratio was assumed to be identical to the meteoritic value. For each star we have computed synthetic spectra between 4129.5 and 4130.1 Å including also 5 Fe I lines with $\log gf$ from Grevesse and Sauval (private communication). The macroturbulence velocities were determined from a set of 5 clean Fe I lines in this spectral window. The Eu

Table 6. α element abundances and line-to-line scatter

ID	[Mg/Fe] I	[Ca/Fe] I	[Ti/Fe] I	[Ti/Fe] II
1	0.344	0.197(37)	0.249(20)	0.234(22)
2	0.269	0.133(82)	0.217(74)	0.180(46)
3	0.239	0.065(39)	0.105(32)	0.126(27)
4	0.077	0.050(59)	0.102(32)	0.077(21)
5	0.344	0.175(27)	0.230(46)	0.264(22)
6	0.299	0.185(37)	0.260(29)	0.258(35)
7	0.366	0.242	0.241(31)	0.241(21)
8	0.322	0.260(24)	0.233(32)	0.271(38)
9	*	0.198(24)	0.227(25)	0.251(23)
10	0.303	0.169(55)	0.260(20)	0.217(57)
11	0.096	0.054(47)	0.058(30)	0.048(29)
12	0.341	0.185(27)	0.244(28)	0.263(23)
13	0.326	0.152(86)	0.182(39)	0.186(14)
14	0.234	0.132(88)	0.173(44)	0.172(49)
15	0.398	0.242(42)	0.256(62)	0.234(34)
16	0.164	0.119(60)	0.071(38)	0.101(34)
17	0.139	0.177	0.120(52)	0.091(43)
18	0.324	0.222(39)	0.272(29)	0.251(31)
19	0.338	0.167(46)	0.262(40)	0.235(20)
20	0.152	−0.007(60)	0.072(35)	0.029(23)
21	0.063	0.084(33)	0.033(44)	0.032(27)

Table 7. Heavy element abundances and line-to-line scatter

ID	[Sr/Fe]I	[Y/Fe]II	[Zr/Fe]II	[Ba/Fe]II	[La/Fe]II	[Ce/Fe]II	[Nd/Fe]II	[Sm/Fe]II	[Eu/Fe]II
1	−0.099	−0.033(13)	0.155	0.180	0.241(39)	0.007(13)	−0.103(21)	0.208	0.188
2	−0.119	−0.174(19)	−0.009	0.078	0.141(104)	−0.105(31)	−0.055	0.170	0.161
3	−0.231	−0.195(09)	−0.020	0.048	0.120	−0.125	−0.190(18)	0.017	0.080
4	−0.236	−0.264(32)	−0.027	−0.005	0.067(26)	−0.165(16)	−0.251	0.007	−0.007
5	−0.127	−0.070(19)	0.084	0.092	0.220(13)	−0.134	−0.114(51)	0.164	0.195
6	−0.145	0.005(54)	0.195	0.145	0.200(80)	−0.104(39)	−0.093(33)	0.287	0.205
7	−0.086	0.045(15)	0.190	0.119	0.198	−0.050	−0.098	0.242	0.210
8	−0.170	−0.050(19)	0.159	0.109	0.208	−0.064	−0.064(60)	0.187	0.162
9	−0.233	−0.151(21)	0.054	0.055	0.147	−0.165(63)	−0.073(19)	0.218	0.185
10	0.003	−0.150(34)	*	0.060	0.100	−0.189	0.046	0.267	0.229
11	−0.314	−0.218(32)	−0.153	0.026	0.126	−0.074	−0.258(27)	−0.126	−0.027
12	−0.118	−0.102(20)	0.174	0.141	0.258	−0.067(39)	−0.136(25)	0.191	0.184
13	−0.276	−0.193(39)	0.027	0.057	0.117(61)	−0.104(45)	−0.202(15)	0.051	0.148
14	−0.279	−0.196(48)	−0.070	−0.086	0.072(62)	−0.167	−0.293	−0.022	0.135
15	0.002	0.117(31)	0.363	0.396	0.338(95)	0.112(66)	−0.033(54)	0.229	0.223
16	−0.383	−0.207(49)	*	0.147	0.288	0.076	−0.016	0.374	0.363
17	−0.351	−0.230(31)	−0.106	−0.015	0.175	−0.023	−0.025	0.283	0.214
18	−0.103	0.048	0.353	0.155	0.275(16)	0.056(28)	−0.104(25)	0.313	0.200
19	−0.198	−0.138(35)	0.109	0.038	0.276(134)	0.008(111)	*	0.117	0.185
20	−0.254	−0.223(20)	−0.032	0.038	0.135(22)	−0.045(20)	−0.203(07)	0.149	0.026
21	−0.329	−0.309(16)	−0.095	0.054	0.079(33)	−0.123	−0.286	0.016	-0.006

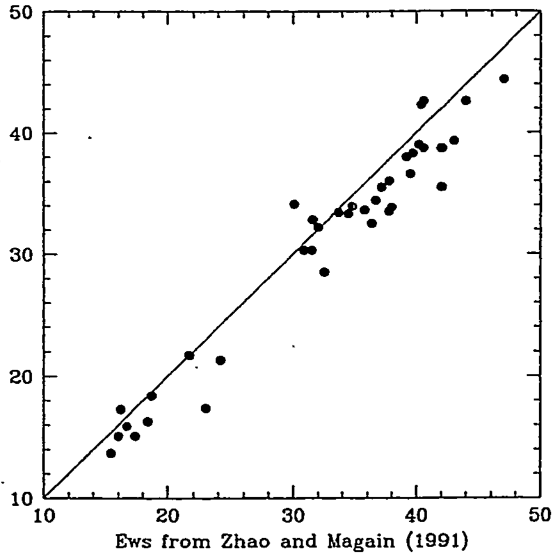

Fig. 1. Comparison of our EWs with those measured by Zhao and Magain (1991)

abundance was adjusted until the synthetic and observed spectra matched.

The abundances of the neutron capture elements relative to Fe are given in Table 7.

6. Estimation of the uncertainties

We now discuss the uncertainties on the abundances. First, we consider the errors which act on single lines and, secondly, those which affect whole sets of lines.

In the first category, we have the uncertainties on the line parameters, i.e., the random errors on EWs, on oscillator strengths, on damping constants,...

They can be estimated by comparing the results from different lines of the same element. With 30 FeI lines (5 mÅ < EW < 70 mÅ), the scatter varies somewhat from star to star (from 0.016 to 0.034) with a mean value of 0.027 dex. We find similar values for other elements having a significant number of lines in our spectra (NiI, TiII,...).

Our EW measurements for the 10 stars which also appear in Zhao and Magain (1991) are plotted in Fig. 1. The small systematic difference is due to a non-linearity of the CCD used by Zhao and Magain, which accounts for an overestimate of about 5% in their EWs (Gosset and Magain 1993). Apart from that, the agreement is very good, with a scatter of 1.5 mÅ only. Thus, if the two studies were of the same quality, the precision on the EWs would be 1 mÅ. For typical lines having EWs of 25 mÅ the corresponding error on the abundance is of the order of 0.02 dex.

Considering these two different estimates (0.027 and 0.02 dex), the total abundance error coming from EW measurements can be assumed to amount to $0.025/\sqrt{N}$, where N is the number of lines measured.

The second category of errors are essentially model errors, such as uncertainties on the effective temperature, surface gravity, microturbulence velocity, overall metallicity and temperature structure. We estimate uncertainties in the differential $T_{\rm eff}$ values due to errors in observed photometric indices to be about 20 K (see Sect. 3.1). In $\log g$ the total errors may approach 0.2 dex, resulting from errors in the c_1 index, and uncertainties in the calibration of VandenBerg and Bell (1985). If there is a system-

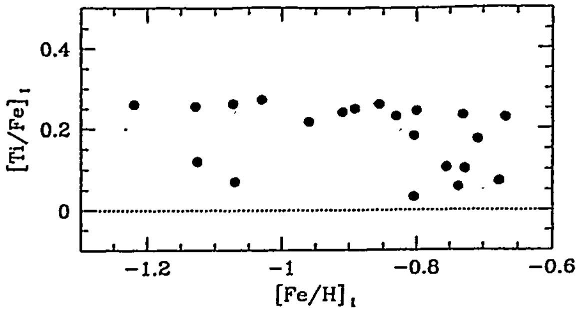

Fig. 2. Traditional plot: the abundance of Ti relative to Fe versus [Fe/H]

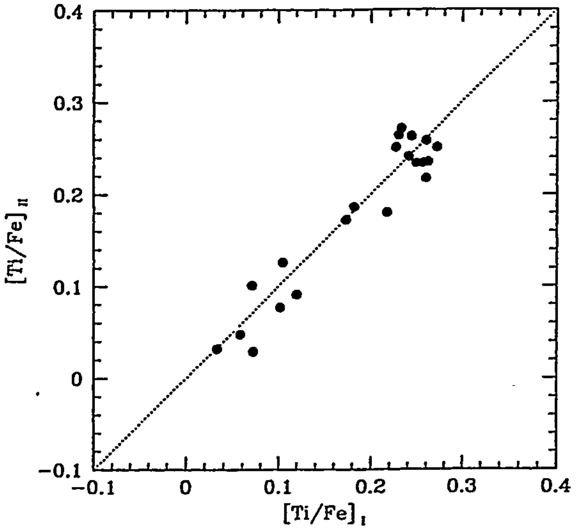

Fig. 3. Comparison of the values of [Ti/Fe] determined from ionic and from neutral lines

atic error in T_eff, it will affect our $\log g$ determination. However, the three ionization equilibria available confirm the differential photometric gravities (Sects. 5.1 and 5.2). A systematic error on all surface gravities will not change the abundance ratios. Moreover, the comparison with the "Hipparcos parallax-based gravities" of Nissen et al. (1998) for the four stars in common shows that, if present, such a systematic error is very small, of the order of 0.12 ± 0.03 dex.

The variations of the abundance ratios due to changes on effective temperature (+20K), surface gravity (+0.2 dex), model metallicity (+0.2 dex) and microturbulence velocity (+0.1 dex) are summarized in Table 8 for a typical star. The total uncertainty never exceeds some 10% for all abundance ratios.

In Fig. 2, we show the abundance of titanium relative to iron as deduced from the neutral lines versus [Fe/H]. It appears that the scatter in [Ti/Fe], which amounts to 0.08 dex, is much larger than the estimated error on that abundance ratio (0.013). It seems therefore that the observed scatter is not due to analysis uncertainties and could be genuine cosmic scatter.

We confirm this result by comparing the values of [Ti/Fe] deduced from neutral lines with those obtained from the ionized lines, as shown in Fig. 3. We see that the correlation between the two ratios is close to perfect, the remaining scatter amounting to 0.025 dex only, which is compatible with the estimated errors (0.024 dex). These two determinations of [Ti/Fe] are completely independent since the sensitivity of the ionic lines to errors on the model parameters is different from that of the neutral lines.

Table 8. Influence of errors in the model parameters on the HD 199289 abundances

Element abundance	ΔT_eff +20K	$\Delta \log g$ +0.2	Δ [Fe/H] +0.2	$\Delta\xi$ +0.1	Rms sum
[Fe/H] I	+0.014	+0.010	−0.001	−0.009	0.019
[Fe/H] II	+0.002	+0.090	+0.014	−0.008	0.091
[Cr/Fe] I	+0.002	+0.002	+0.003	+0.002	0.005
[Cr/Fe] II	−0.003	+0.002	−0.005	−0.004	0.007
[Ti/Fe] I	+0.002	−0.003	+0.002	+0.006	0.007
[Ti/Fe] II	+0.000	−0.003	−0.005	−0.010	0.012
[Mg/Fe] I	+0.010	+0.020	−0.007	−0.012	0.026
[Ca/Fe] I	−0.003	−0.007	+0.004	+0.005	0.010
[V/Fe] I	+0.007	−0.005	+0.002	+0.009	0.013
[Ni/Fe] I	−0.001	+0.004	+0.001	+0.002	0.005
[Sr/Fe] I	+0.003	−0.003	+0.000	+0.005	0.007
[Y/Fe] II	+0.006	+0.004	+0.005	−0.002	0.009
[Zr/Fe] II	+0.007	−0.012	+0.008	+0.007	0.017
[Ba/Fe] II	+0.001	−0.009	+0.000	+0.003	0.010
[La/Fe] II	+0.008	+0.000	+0.009	+0.003	0.012
[Ce/Fe] II	+0.009	−0.008	+0.011	+0.006	0.017
[Nd/Fe] II	+0.008	−0.013	+0.017	+0.004	0.023
[Sm/Fe] II	+0.009	−0.012	+0.011	+0.007	0.020
[Eu/Fe] II	+0.009	−0.025	+0.011	+0.003	0.029

We conclude that the observed scatter is indeed of cosmic origin and that the high precision of our results allows us to investigate the correlations between different relative abundances.

7. Abundance correlations

7.1. *α elements*

In Fig. 4 we show the abundance of Mg relative to Fe, [Mg/Fe], as a function of [Ti/Fe], and [Ca/Fe] versus [Ti/Fe]. These two figures show that the three α-elements Mg, Ca and Ti behave in the same way, which means that they were synthesized by the same nucleosynthetic process in similar objects. This is in agreement with the generally accepted view that the α-elements are mainly produced in supernova explosions of massive stars (Arnett 1991, Thielemann et al. 1993, Woosley and Weaver 1995).

7.2. *Iron peak elements*

The abundances of Cr and Fe relative to Ti are displayed in Fig. 5. The correlation is very good, with a scatter of only 0.023 dex. The second part of the same figure shows the same comparison for Ni and Fe. Here again, the correlation is remarkable ($\sigma = 0.013$) for all but two stars, which appear to be somewhat depleted in nickel. These two stars, which also display other abundance anomalies (as we shall see below) are identified by open symbols in this figure and the following ones.

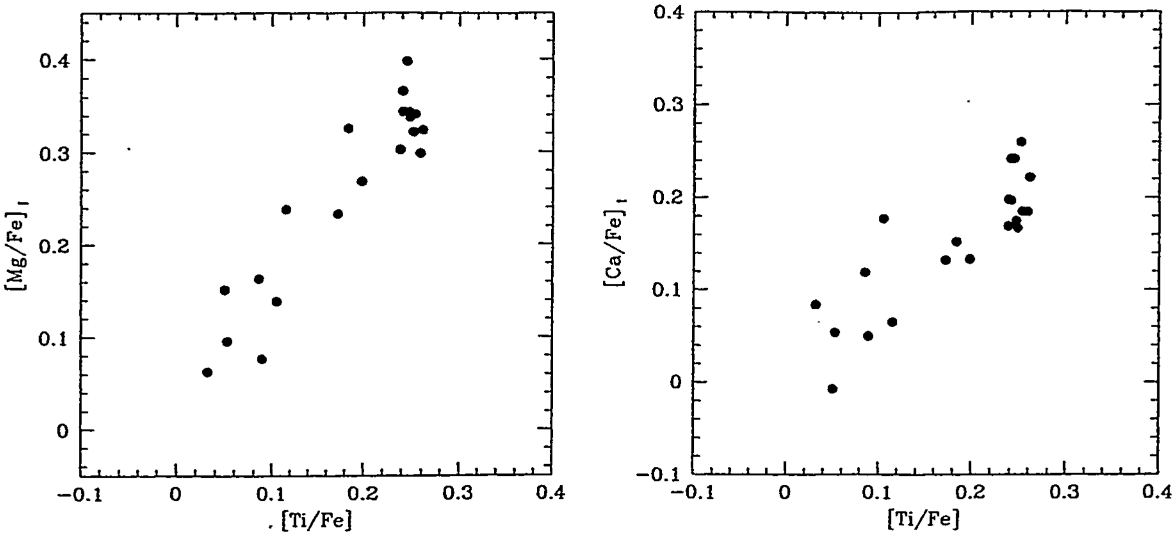

Fig. 4. Correlation diagrams for [Mg/Fe] and [Ca/Fe] versus [Ti/Fe]

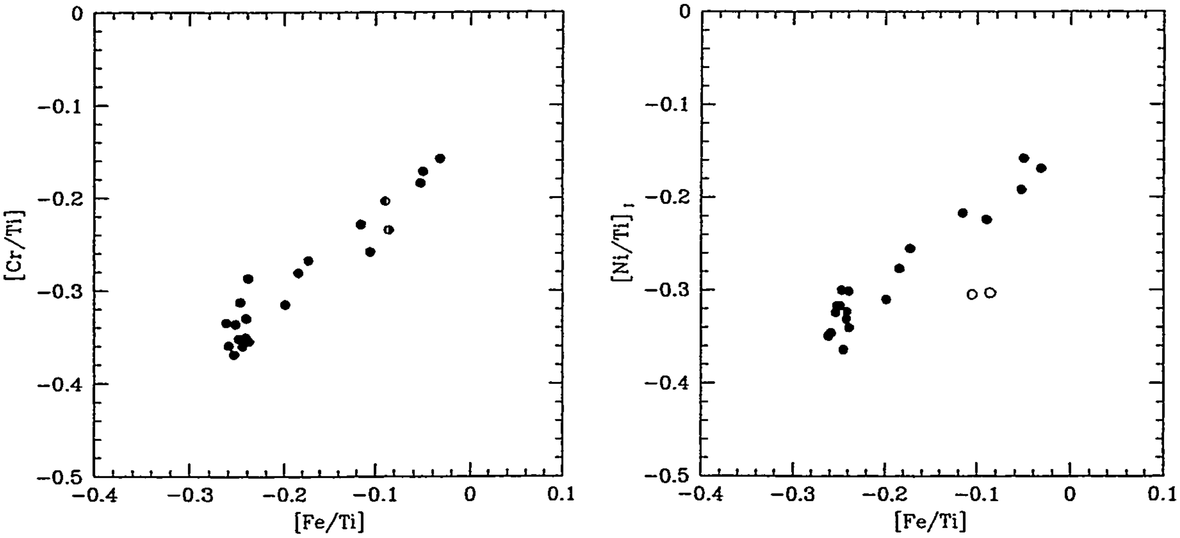

Fig. 5. Correlation diagrams for [Cr/Ti] and [Ni/Ti] versus [Fe/Ti]

While the even iron peak elements correlate very well with each other, the situation appears different for the odd element vanadium. As shown in Fig. 6, the vanadium abundance does not correlate well with the other iron peak ones. The correlation is only slightly better with the α-elements. It is difficult to draw any conclusion without investigating the behaviour of the other odd iron peak elements Mn and Co.

7.3. Neutron capture elements

We wanted to carry out the same analysis for the neutron capture elements, in order to distinguish between the s and r processes at an early stage of the galactic evolution, and to identify the most likely sites for their formation. A correlation plot for a typical s element, yttrium, is shown in Fig. 7, together with the corresponding diagram for the r element europium. The difference between the behaviours of Y and Eu is striking. Apart for the two "anomalous" stars, there is a one-to-one correlation between the r-process element Eu and the α-element Ti. All points are located on a single straight line with a slope close to 1 and ending with a clumping at the maximum value of [Ti/Fe].

In contrast, the diagram of the s-process element Y is much more complex. Here, we do not have a simple correlation with the α-elements, but rather, two distinct behaviours. For about half of the stars, corresponding to low values of [Ti/Fe], there is a correlation between [Y/Fe] and [Ti/Fe], but the slope is significantly smaller than 1.

The remaining stars have a constant (and maximum) [Ti/Fe] and increasing values of [Y/Fe], starting at the maximum value reached by the first group. We refer to such an abundance correlation as a *two branches diagram*.

Such a strikingly different behaviour needs to be confirmed by other r and s elements. Fig. 8 shows the same correlation diagram for the other light s-process elements Sr and Zr, which

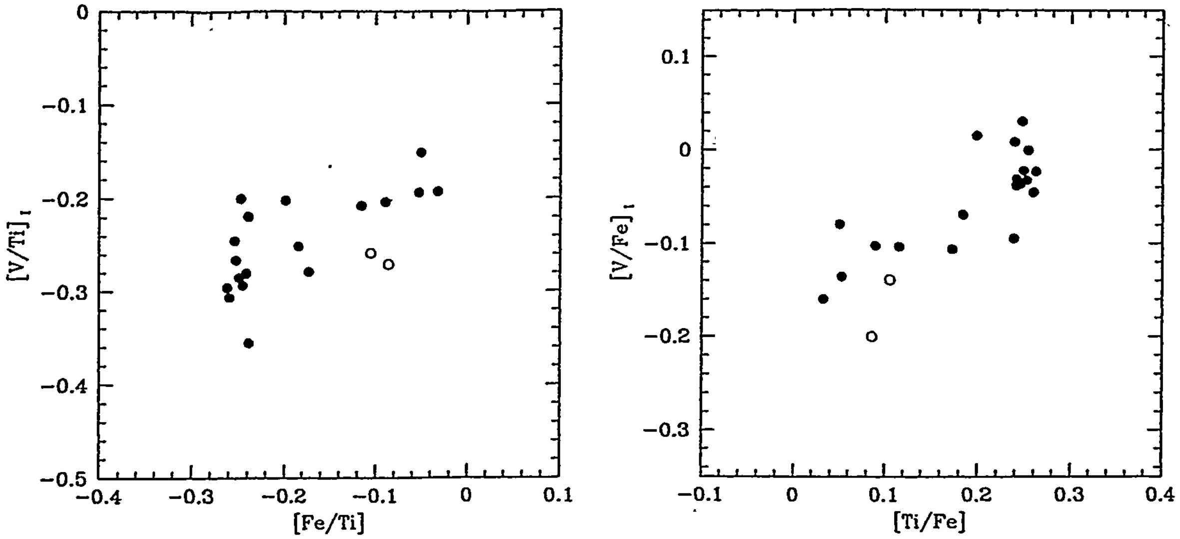

Fig. 6. Correlation diagrams for [V/Ti] versus [Fe/Ti] and [V/Fe] versus [Ti/Fe]

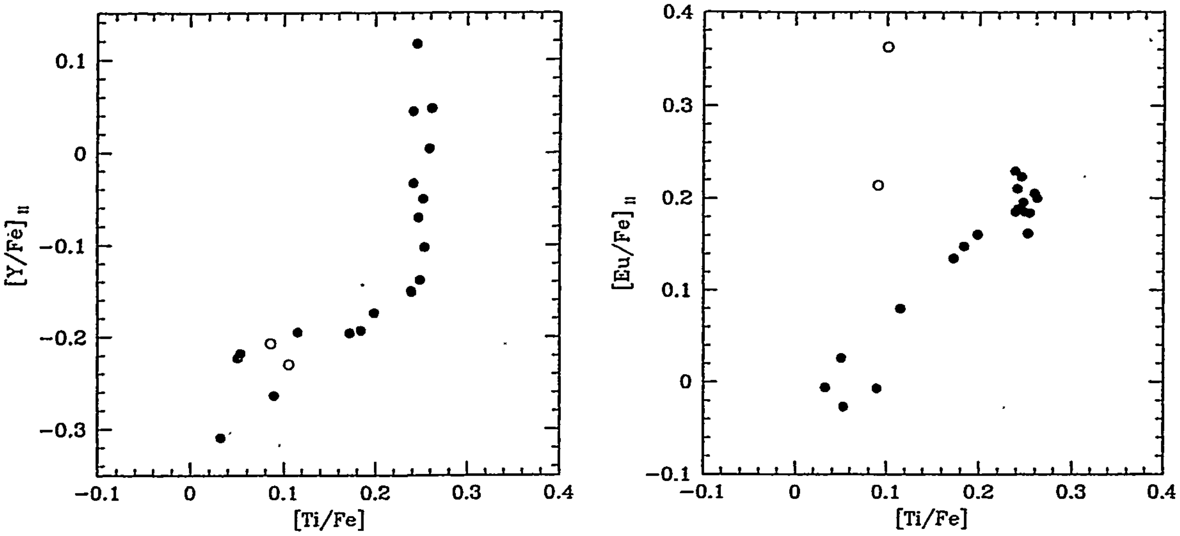

Fig. 7. Correlation diagrams for [Y/Fe] and [Eu/Fe] versus [Ti/Fe]

agree very well with the diagram for Y, although the Sr and Zr results are based on the analysis of a single line, which is moreover very weak in the case of Zr. The three light *s*-process elements Sr, Y and Zr thus show a common pattern. We propose an explanation for these *two branches diagrams* in Sect. 9.

The heavy *s*-process elements Ba, La and Ce have been considered together in Fig. 9 since the available spectroscopic data were of slightly lower quality. Despite the larger scatter, these elements all follow the same trend. Once again, we can distinguish two groups of stars, the first one with variable [Ti/Fe] and a second vertical one at the maximum value of this abundance ratio.

The slope for the first group of stars is not as well defined as in the case of the lighter *s* elements. This may be due to the lower quality of the data, but might also reflect a different nucleosynthetic history. The latter hypothesis is supported by the fact that at least one of the anomalous stars, which perfectly fits in the light *s* diagrams, now shows up again as overenriched in heavier *s* elements.

The cases of Nd and Sm are illustrated in Fig. 10. These elements, formed by both neutron capture processes in the solar system, display a pattern intermediate between those of the *r*-process element Eu and the heavy *s*-process ones. For low values of [Ti/Fe], [Nd/Fe] and [Sm/Fe] are roughly constant, except for the two anomalous stars, which are relatively enriched. Near the maximum value of [Ti/Fe], a looser clumping appears, with a dispersion which is intermediate between those of the *r* and *s* elements.

As we have seen earlier, the two stars HD 193901 and HD 194598 represented by open symbols in the correlation diagrams, display a number of abundance anomalies: a lower Ni abundance (Fig. 5b), a probable overabundance in heavy *s*-process elements (Fig. 9) and, above all, a higher abundance in *r*-process products (Figs. 7b, 10). If, as stated by Anders and

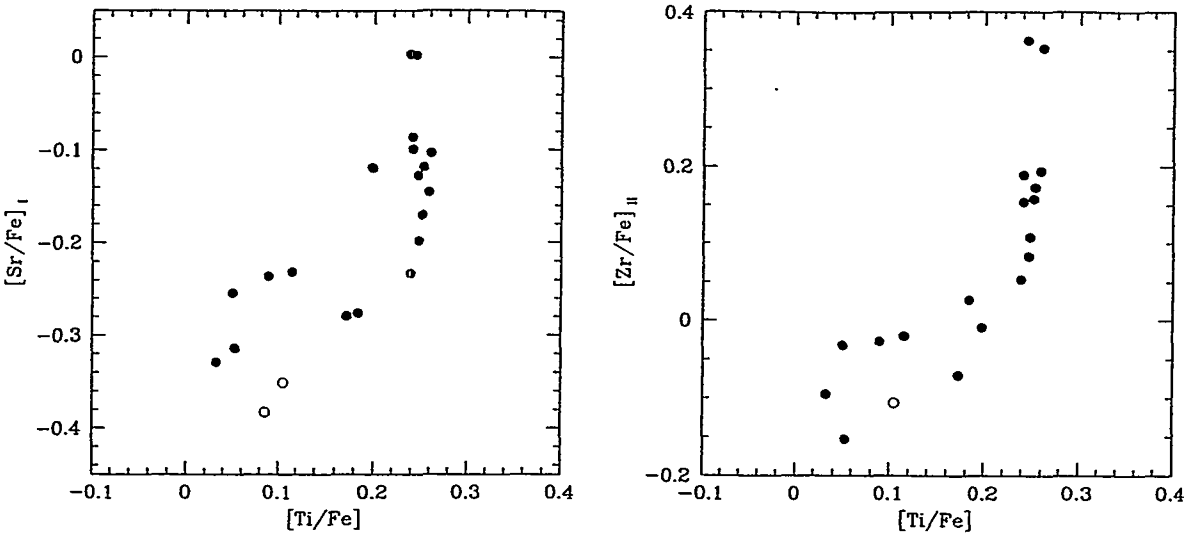

Fig. 8. Correlation diagrams for [Sr/Fe] and [Zr/Fe] versus [Ti/Fe]

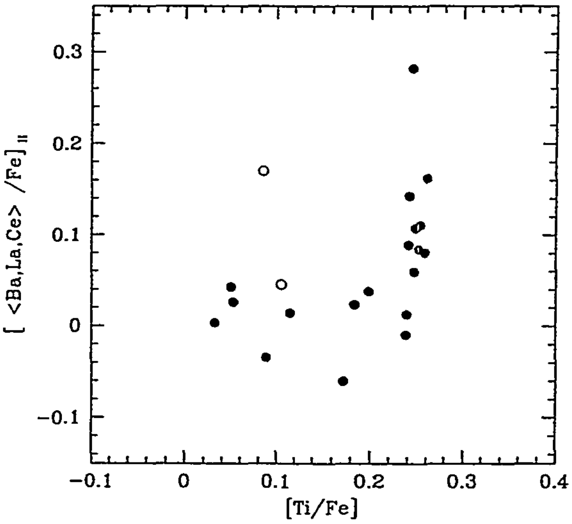

Fig. 9. Correlation diagram for [$< Ba, La, Ce >$/Fe] versus [Ti/Fe]

Grevesse (1989), Ni is the even iron peak element with the smallest contribution from explosive nucleosynthesis, this behaviour might be explained by a different nucleosynthetic history, namely an enhanced contribution from explosive processes compared to equilibrium ones.

8. Kinematics of the stars

The kinematical data are summarized in Table 9. The radial velocities were selected from several sources: Barbier-Brossat et al. (1994), Wilson (1953), Evans (1967), Gratton and Sneden (1991), Lindgren and Andersen (private communications). The radial velocities are known to about ±2 km s^{-1} for most of the stars. The proper motions and parallaxes used to calculate the galactic velocities were taken from the Hipparcos Catalogue (1997). The calculation of the galactic space velocities U, V and W with respect to the LSR is based on the method presented in Johnson and Soderblom (1987). The corrections applied to the observed velocities for the solar motion are (-10.4,+14.8,+7.3) km s^{-1} in (U,V,W) (Mihalas and Routly 1968).

Table 9. Kinematic data. Radial velocity v_R, parallax π, proper motion in right ascension μ_α and in declination μ_δ, and the deduced galactic velocity components with respect to the LSR: U, V, W. (U is positive towards the galactic anticentre)

ID	v_R (km/s)	π (mas)	μ_α (mas/yr)	μ_δ (mas/yr)	U (km/s)	V (km/s)	W (km/s)
1	118.0	41.07	689.67	−214.34	98.36	−70.97	−37.11
2	52.0	19.02	347.27	413.51	118.63	−49.50	1.44
3	57.4	33.40	−92.20	−167.52	19.33	−36.24	−10.81
4	−1.0	12.01	−12.86	−201.75	−80.07	17.71	−31.50
5	102.6	65.79	−220.83	1722.89	135.33	−43.40	46.89
6	62.0	20.14	152.49	−239.09	−39.46	−71.50	9.89
7	120.8	46.90	244.35	213.46	38.23	−76.80	77.39
8	−1.0	25.16	−64.62	−132.59	−20.41	16.88	−18.56
9	32.0	18.66	−157.82	−56.85	9.35	−18.72	−29.12
10	51.1	17.77	159.19	−201.28	−83.37	−5.22	−30.28
11	−10.0	15.34	−45.01	79.26	7.83	17.55	30.87
12	−9.0	17.71	−12.45	−64.29	2.99	15.15	−7.15
13	28.5	16.80	0.71	−14.74	−26.66	12.72	22.12
14	31.0	13.72	−63.25	17.68	−34.98	−11.53	20.66
15	−14.7	14.76	−309.16	−365.29	−84.12	−113.76	50.62
16	−172.0	22.88	539.73	−1055.93	145.69	−230.16	−66.03
17	−247.0	17.94	117.90	−549.71	66.11	−262.10	−23.53
18	−30.0	15.78	44.38	−428.55	−12.17	−113.75	−26.24
19	−16.5	18.94	169.40	−283.37	37.84	−51.77	−11.21
20	−29.4	108.50	81.08	800.68	2.69	58.83	13.47
21	−33.6	23.66	150.64	331.61	55.35	29.86	52.98

Upon examination of Table 9, our sample appears to contain thick disk and halo stars. However, there is no clear distinction between these two populations in Figs. 7a, 8 and 9, since thick disk stars are found on both branches in these plots.

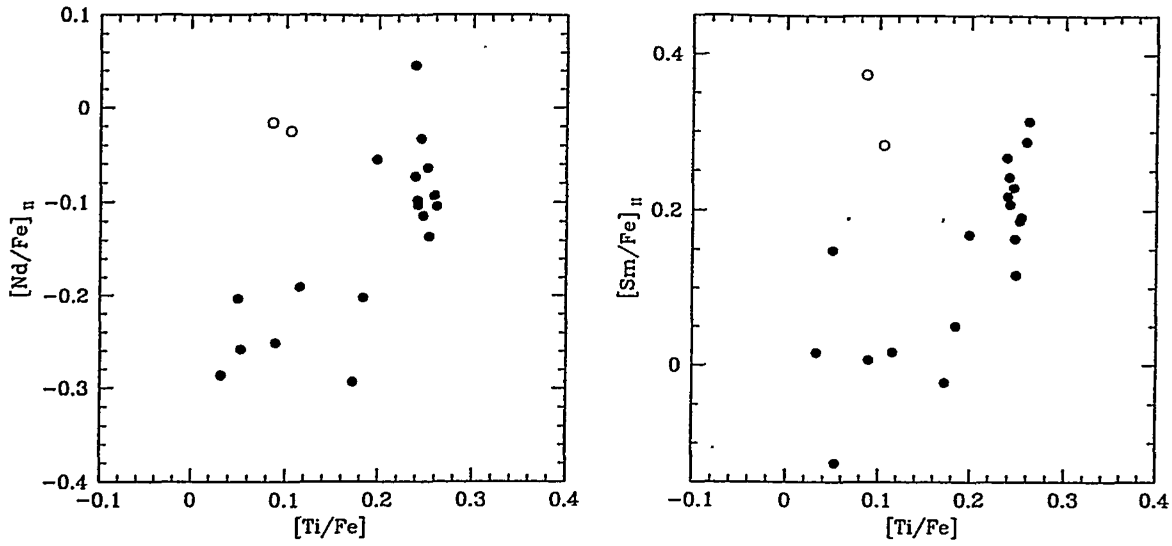

Fig. 10. Correlation diagrams for [Nd/Fe] and [Sm/Fe] versus [Ti/Fe]

This result seems to disagree with the analysis of Nissen and Schuster (1997, NS), who have selected two samples of stars on the basis of their kinematical properties and covering about the same metallicity range as ours. While their halo stars are indeed found in both branches of our diagram, all their disk stars display maximum [α/Fe] values. Some of our disk stars undoubtedly have low [α/Fe]. The apparent disagreement might be due to the fact that both samples contain a relatively small number of stars and that, by accident, all disk stars selected by NS have a high [α/Fe].

It may be of interest to note that the two stars which seem to display some anomalous abundances are just these which have the most halo-like kinematic properties. However, it is difficult to conclude on the basis of only two stars. We plan to extend the analysis to other metal-poor stars with kinematics more typical of the halo.

9. The "Two branches diagram"

9.1. *Universality of the "Two branches diagram"*

The analysis of the correlations between the relative abundances of a number of elements for stars with roughly 0.1 of the solar metallicity leads us to distinguish between two stellar populations, corresponding to distinct branches in the diagram (e.g. Fig. 7a): (a) a fraction of the stars have a range of moderate over-abundances of the α-elements and either a constant or slowly varying abundance of the s-process elements relative to the iron peak, and (b) the others show a constant (and maximum) over-abundance of the α-elements relative to the iron-peak elements, and a range in s-process abundances. This behaviour must be related to nucleosynthesis processes.

Since our sample contains a limited number of stars, its astrophysical significance may be checked by including the results of other analyses. In Fig. 11, we have added the NS stars as well as the sample of Zhao and Magain (1991, ZM). The quality of those data is almost as good as the quality of the data presented here. The ZM data extend our sample towards stars of lower metallicity. The stars in Fig. 11 have metallicities $-2 \leq$ [Fe/H] ≤ -0.6. The zero points have been fixed by comparing the results obtained for the stars in common (3 with NS, 10 with ZM), for which we have kept the results obtained here with a more precise analysis. We see that all these metal-poor stars follow the same trend, independently of their metallicity.

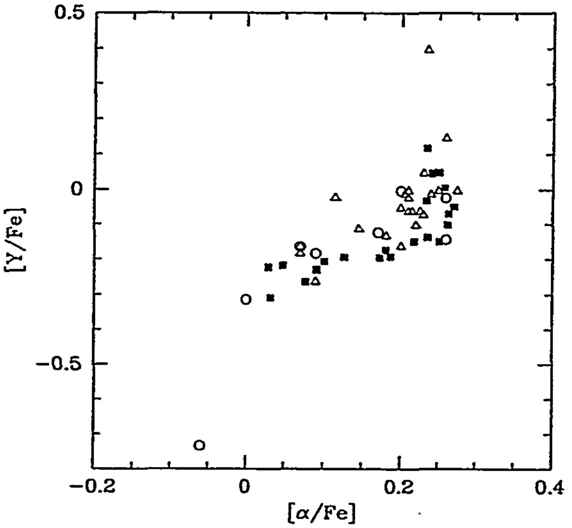

Fig. 11. Correlation diagram for [Y/Fe] versus [α/Fe] with our data (full squares), the data of Zhao and Magain (1991) (open circles) and the data of Nissen and Schuster (1997) (open triangles). Only stars with [Fe/H] < -0.6 are plotted

As our metallicity range for (thick) disk stars is rather limited towards metal-poor stars, we have added in Fig. 12 the data obtained by Edvardsson et al. (1993) for disk stars of various metallicities. The difference in zero-points between the two analyses has been corrected on the basis of 10 stars in common. We see that these disk stars definitely *do not* follow the relation obtained for metal-poor stars, but scatter mostly through the upper left

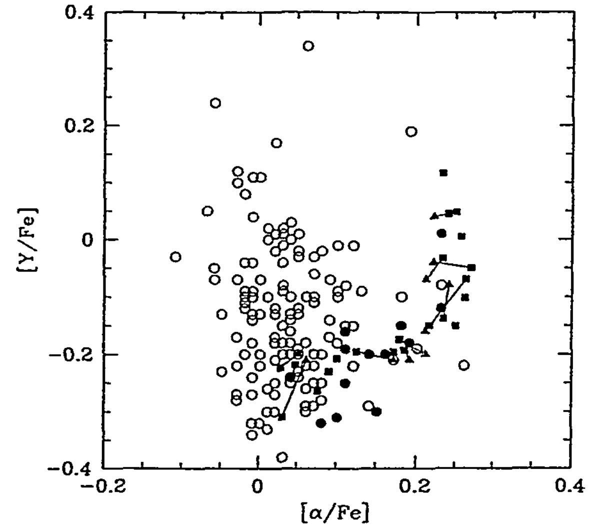

Fig. 12. Correlation diagram for [Y/Fe] versus [α/Fe] with our data (full squares), the data of Edvardsson et al. (1993) for [Fe/H] > −0.6 (open circles), for [Fe/H] < −0.6 (full circles) and for the stars also included in our work (full triangles), joined by lines to their counterparts

part of the diagram. Taking into account the larger error bars in Edvardsson et al. (1993) data, our metal-poor stars define the lower right envelope of this domain. This envelope also contains the lowest metallicity stars of Edvardsson et al. (1993).

On the basis of these two comparisons, a cutoff in metallicity at [Fe/H] ~ -0.6 seems to emerge. For stars of higher metallicity, the *two branches diagram* does not apply. Lower metallicity stars follow a universal relation described by the *two branches diagram*. We shall refer to the slowly varying branch stars as Population IIa and to the vertical branch as Population IIb.

9.2. Interpretation

9.2.1. General picture

We now briefly describe a possible scenario for the formation and origin of these metal-poor stars, which provides an explanation for the universal relation described above. This scenario will be developed in more details in a forthcoming paper. It takes place in the early stages of the chemical evolution of the Galaxy. We distinguish two separate phases in the evolution of the metal-poor stars.

Phase 1

At first, we assume that there is a burst of star formation, consisting essentially of massive stars. As these stars evolve and become supernovae (SNe), α-elements and r-process elements are formed and then ejected in the surrounding interstellar matter (ISM). New stars are formed from this ISM, which is enriched in those α and r-process elements. These stars correspond to Pop IIa.

Phase 2

As time goes on, the lower mass stars are either still contracting towards the main sequence or have reached a more evolved phase, maybe already processing s elements. These evolved stars are known to have strong stellar winds and to undergo superwind events. The newly formed s elements are thus ejected into the surrounding ISM, previously enriched in α- and r-process elements. New born stars formed from this ISM will keep a constant value for [α/Fe] but will be enriched in s elements. They will belong to Pop IIb.

Another possibility is that already formed lower mass stars can accrete gas from the s-process enriched winds. In this case, the s-process enrichment will show up in the external layers only, at least if the convective envelope is not too large. These stars will also belong to Pop IIb, although their internal chemical composition will be that of Pop IIa at the bottom of the vertical branch.

9.2.2. Globular cluster scenario

In this subsection, we will be more specific as to the environment in which our two-phases scenario could occur.

As we have shown in Sect. 9.1, the *two branches diagram* seems to define a universal relation for stars more metal-poor than [Fe/H] ~ -0.6. In particular, it should therefore apply to all halo stars.

Since the halo is also populated by globular clusters (GCs, see the recent review by Meylan & Heggie 1997), we have searched for a connection between them and the field halo stars (FHS), and we propose the following EASE (Evaporation/Accretion/Self-Enrichment) scenario:
(1) all FHS were born in (proto-) GCs;
(2) GCs have undergone a chemical evolution;
(3) some of the GCs were disrupted at an early stage in their evolution, the lower mass stars forming Pop IIa;
(4) in the GCs which have survived, accretion of matter from AGB stars modifies the surface composition of the cluster stars;
(5) some low mass stars evaporate from the GCs or get dispersed in the halo when the GC is disrupted. They form Pop IIb FHS.

The relation between the thick disk and field halo stars on the one hand and GCs on the other hand is substantiated by the similarities in kinematic properties and metallicity distributions between:
(1) the FHS and the GCs more metal-poor than [Fe/H] ~ -1 ("halo GCs");
(2) the thick disk stars and the GCs more metal-rich than [Fe/H] ~ -1 ("disk GCs");
(Zinn 1985, Armandroff 1989, Harris 1998).

A few authors (Cayrel 1986; Smith 1986, 1987; Morgan and Lake 1989) have considered the possibility of GCs self-enrichment by SNe and, through simple and qualitative arguments, have shown that this was indeed possible under certain conditions.

In a recent paper, Brown et al. (1995) have developed a more detailed model for the early dynamical evolution and self-enrichment of GCs which supports the first part of our scenario. They show that the SN explosions of the first generation stars trigger the formation of an expanding shell, decelerated by the surrounding hot ISM, in which second generation stars can form.

They also discuss the conditions for a GC to survive this phase of chemical self-enrichment.

While the second generation stars are forming, the proto-GC may become unstable and disruption can occur. This can happen at any time during the SNe phase. It is important to notice that, at the time of disruption, the metallicity is fixed by the rate of mixing of the enriched matter expelled by SNe with the pre-existing ISM, i.e., by the ratio of the mass of the processed material to the mass of the ISM. On the other hand, the value of [α/Fe] depends on the mass distribution of the Type II SNe which have exploded by the time of disruption. Of course, only the less massive stars are still visible now. They form Pop IIa and they appear somewhere on the slowly varying branch, depending on the time at which disruption of the proto-GC occurred. All stars originating from a given proto-GC should have the same [α/Fe] value but stars coming from different proto-GCs will have different values. Since the disrupted proto-GC has not completed its chemical evolution, some of the stars dispersed in the halo may have a much lower metallicity than the lowest ones presently observed in the GCs, independently of their respective [α/Fe].

The GC can also survive the SNe phase. When all stars more massive than about 8 $M_\odot$ have exploded as SNe, the α and r elements synthesis stops, leading to a typical value of [α/Fe]. Such a view is supported by the analysis of Carney (1996) who finds that GCs do not show any significant variations in [α/Fe] despite wide variations in [Fe/H], age and kinematics.

According to Fig. 7, our scenario requires this typical value of [α/Fe] to be the maximum value observed in the *two branches diagram*, which in turn implies an increase of [α/Fe] with time in a given proto-GC. The end of the SNe phase must indeed correspond to the bottom of the vertical branch. Such an increase with time, i.e., with decreasing mass of the progenitor, is in agreement with the theoretical yields computed by Woosley & Weaver (1995) although such results are still rather uncertain since other computations (e.g. Thielemann et al. 1993) show different behaviours. Moreover, such an interpretation of Fig. 7 implies a nearly solar [Ti/Fe] for the most massive SNe, which is also in agreement with some of the models computed by Woosley & Weaver (1995).

The fact that [Y/Fe] increases with [Ti/Fe] for Pop IIa stars would indicate that the ratio of the Y yield to the Fe yield increases with decreasing mass of the SN progenitor (Fig. 7). On the other hand, the roughly constant value obtained for the heavy s elements (Ba, La, Ce) observed in Fig. 9 suggests that the ratio of the yields (Ba,La,Ce)/Fe does not vary significantly with the mass of the progenitor.

In a second phase, intermediate mass stars evolve until they reach the AGB where they enrich their envelope in s-process elements due to dredge-ups during the thermal pulses. Through stellar winds or superwinds, those enriched envelopes are ejected and they pollute the surrounding less massive stars by accretion.

No new stars would be formed at this stage because the remaining ISM is probably too diffuse. During the subsequent evolution of the GC, some of these surface enriched low mass stars evaporate and form Pop IIb. Those stars can also get dispersed in the halo when the GC gets disrupted (e.g., when crossing the disk).

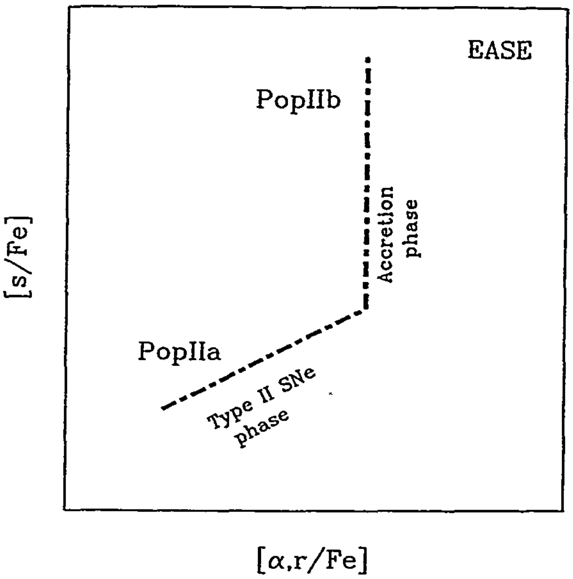

Fig. 13. EASE scenario.

For a typical r element like Eu, the behaviour of [Eu/Fe] versus [α/Fe] (Fig. 7) is completely different, showing a perfect correlation in Pop IIa stars and an absence of the vertical s-process feature, replaced by a clumping of the points representative of Pop IIb stars at the constant value of [α/Fe] and [r/Fe], characteristic of the end of the massive stars outburst. This shows that, if also produced by lower mass stars, it must be in roughly the same proportions as Fe.

Our EASE scenario nicely explains the features observed in the *two branches diagrams*. It is schematically displayed in Fig. 13.

Pop IIa stars mostly originate from disrupted proto-GCs, their [α/Fe] depending on the moment at which disruption occurs. Pop IIb stars escape later in the evolution of the cluster, after the end of the SN phase.

This EASE scenario can also explain the larger metallicity range covered by the FHS, extending to much lower metallicities than the GCs. The very metal-poor stars have escaped from the proto-GCs at a very early stage of the outburst phase, when the chemical enrichment of the cloud was still very low.

Acknowledgements. This work has been supported by contracts ARC 94/99-178 "Action de Recherche Concertée de la Communauté Française de Belgique" and Pôle d'Attraction Interuniversitaire P4/05 (SSTC, Belgium). We wish to thank J. Andersen and H. Lindgren for providing radial velocities for some of the stars and N. Grevesse and J. Sauval for some of the atomic data. We also thank N. Grevesse and G. Meylan for fruitful discussions. The Simbad database, operated at CDS, Strasbourg, France, has been used in this project.

References

Alonso A., Arribas S., Martinez-Roger C., 1994, A&ASS 107, 365

Anders E., Grevesse N., 1989, Geochimica et Cosmochimica Acta 53, 197

Andersen T., Poulsen O., Ramanujam P.S., Petrakiev-Petkov A., 1975, Sol. Phys. 44, 257

Armandroff T.E., 1989, AJ 97, 375

Arnesen A., Bengtsson A., Halling R., et al., 1977a, Phys. Scr. 16, 31

Arnesen A., Bengtsson A., Halling R., Noreland T., 1977b, J. Phys. B 10, 565

Arnett D., 1991, In: Frontiers of Stellar Evolution. ASP Conf. Ser. 20, 389

Barbier-Brossat M., Petit M., Figon P., 1994, A&ASS 108, 603

Becker O., Enders K., Werth G., Dembczynski J., 1993, Phys. Rev. A 48, 3546

Biémont E., Grevesse N., Lowe R.M., Hannaford P., 1981, ApJ 248, 867

Biémont E., Kerner C., Meyer G., Träger F., zu Putlitz G., 1982, A&A 107, 166

Biémont E., Grevesse N., Hannaford P., Lowe R.M., 1989, A&A 222, 307

Blackwell D.E., Shallis M.J., 1977, MNRAS 180, 177

Blackwell D.E., Menon S.L.R., Petford A.D., 1984, MNRAS 207, 533

Blackwell D.E., Petford A.D., Simmons G.J., 1982a, MNRAS 201, 595

Blackwell D.E., Booth A.J., Menon S.L.R., Petford A.D., 1986a, MNRAS 220, 289

Blackwell D.E., Booth A.J., Menon S.L.R., Petford A.D., 1986b, MNRAS 220, 303

Blackwell D.E., Booth A.J., Petford A.D., Shallis M.J., Leggett S., 1982b, MNRAS 199, 21

Broström L., Mannervik S., Royen P., Wännström A., 1995, Phys. Scr. 51, 330

Brown J.H., Burkert A., Truran J.W., 1995, ApJ 440, 666

Carney B.W., 1983, AJ 88, 623

Carney B.W., 1996, PASP 108, 900

Cayrel R., 1986, A&A 168, 81

Corliss C.H., Bozman W.R., 1962, Experimental Transition Probabilities for Spectral lines of Seventy Elements (NBS Monograph 32) (Washington: GPO)

Doerr A., Kock M., 1985, J. Quant. Spectrosc. Radiat. Transfer 33, 307

ESA, 1997, 'The HIPPARCOS Catalogue'. ESA SP-1200, ESTEC, Nordwijk

Edvardsson B., Andersen J., Gustafsson B., et al., 1993, A&A 275, 101

Evans D.S., 1967, Catalogue of Stellar Radial Velocities. IAU Symp. 30, 57

Gallagher A., 1967, Phys. Rev. 157, 24

Gosset E., Magain P., 1993, ESO Messenger 73, 13

Gratton R.G., Sneden C., 1991, A&A 241, 501

Gratton R.G., Sneden C. 1994, A&A 287, 927

Gray D.F., 1972, The Observation and Analysis of Stellar Photospheres. Wiley, New York

Grevesse N., Noels A., Sauval A.J., 1996, Cosmic Abundances. ASP Conf. Series Vol. 99, 117

Gustafsson B., Bell R.A., Eriksson K., Nordlund A., 1975, A&A 42, 407

Hannaford P., Lowe R.M., Grevesse N., Biémont E., Whaling W., 1982, ApJ 261, 736

Harris W.O., 1998, preprint astro-ph/9801201

Jehin E., Magain P., Neuforge C., Noels A., Thoul A.A., 1998, A&A 330, L33

Johnson D.R.H., Soderblom D.R., 1987, AJ 93, 864

Kurucz R.L., 1993, ATLAS9 Stellar Atmosphere Programs and 2 km/s grids. Kurucz CD-ROM No 13

Magain P., 1987, A&A 181, 323

Meylan G., Heggie D.C., 1997, A&AR 8, 1

Migdalek J., Baylis W.E., 1987, Can. J. Phys. 65, 1612

Mihalas D., Routly P.M., 1968, Galactic Astronomy. Freeman and Co.

Möller W., Hürnermann H., Alkhazov G., Panteleev V., 1993, Phys. Rev. Lett. 70, 541

Morgan S., Lake G., 1989, ApJ 339, 171

Nissen P.E., Schuster W.J., 1997, A&A, 326, 751

Nissen P.E., Høg E., Schuster W.J., 1998, Proc. of Hipparcos Venice 97 Symposium. ESA SP-402, in press

Olsen E.H.; 1994, A&AS 106, 257

Schuster W.J., Nissen P.E., 1988, A&ASS 73, 225

Smith G., 1986, PASP 99, 67

Smith G., 1987, ApJ 306, 565

Smith G., Raggett D. St J., 1981, J.Phys. B: At. Mol. Phys. 14, 4015

Thielemann F.K., Nomoto K., Hashimoto M., 1993, In: Prantzos N., et al. (eds.) Origin and Evolution of the Elements. Cambridge Univ. Press, p.297

VandenBerg D.A., Bell R.A., 1985, ApJSS 58, 561

Villemoes P., Wang M., 1994, Z. Phys. D 30, 19

Whaling W., Hannaford P., Lowe R.M., Biémont E., Grevesse N., 1985, A&A 153, 109

Wickliffe M.E., Lawler J.E., 1997, ApJSS 110, 163

Wilson R.E., 1953, General Catalog of Stellar Radial Velocities. Carnegie Inst. of Washington, Washington, D.C.

Wiese W.L., Martin G.A., 1980, NSRDS-NBS 68 (U.S. Gov. Printing Office, Washington, DC)

Woolf V.M., Tomkin J., Lambert D.L., 1995, ApJ 453, 660

Woosley S.E., Weaver T.A., 1995, ApJSS 101, 181

Zhao G., Magain P., 1991, A&A 244,425

Zinn R., 1985, ApJ 293, 424

Thermal Neutron Capture Cross Sections and Resonance Integrals of Radioactive Fission Products

Hideo Harada*, Shoji Nakamura*, and Toshio Katoh*

**Japan Nuclear Cycle Development Institute, Tokai-works,*
Tokai-mura, Naka-gun, Ibaraki-ken 319-1194 Japan

Abstract

Accurate data on neutron capture cross sections of radioactive fission products are important for the study of nuclear transmutation as well as nuclear synthesis. The present authors have measured the thermal neutron capture cross sections (σ_0) and resonance integrals (I_0) of ^{134,135,137}Cs, ^{90}Sr, ^{99}Tc, and ^{129}I, which are important fission products from the viewpoint of nuclear transmutation. Some characteristic activation methods using reactor neutrons have been developed for example:

(1) Triple neutron capture reaction ^{133}Cs(n, γ) ^{134}Cs(n, γ) ^{135}Cs(n, γ) ^{136}Cs was utilized and the ratio of the γ-ray yields between ^{134}Cs and ^{136}Cs was measured. The cross section of a short-lived nucleus ^{134}Cs has been deduced using stable ^{133}Cs target. Effectiveness using multi-neutron capture reaction was shown.

(2) To extend the possibility of neutron capture cross section measurement for various kinds of RI targets, a conventional Knudsen-cell-based Q-mass analyzer was developed. The isotope ratio of ^{135}Cs/^{137}Cs samples was measured using the analyzer. This ratio and the ratio of activity of ^{136}Cs to that of ^{137}Cs in the irradiated target were measured for deduction of the σ_0 and I_0 of ^{135}Cs.

The values of cross sections obtained differ very much from those of previous ones. Our measurement methods and results will be briefly reviewed.

Workshop on the Origin of the Heavy Elements

- Astrophysical models and experimental challenges -

Eldorado Hotel, Santa Fe, New Mexico, September 3-4, 1999

Thermal Neutron Capture Cross Sections and Resonance Integrals of Radioactive Fission Products

Hideo Harada*, Shoji Nakamura*, and Toshio Katoh*

**Japan Nuclear Cycle Development Institute, Tokai-works,*

Tokai-mura, Naka-gun, Ibaraki-ken 319-1194 Japan

$T_{1/2}$	Main F P nuclei
>5000y	^{93}Zr, ^{79}Se, ^{126}Sn, ^{107}Pd ^{129}I, ^{135}Cs, ^{99}Tc, (^{14}C)
>100y	^{94}Nb, ^{166m}Ho, ^{158}Tb, ^{108m}Ag
>30y	^{151}Sm, ^{121m}Sn, ^{90}Sr, ^{137}Cs
<30y	^{152}Eu, ^{85}Kr, ^{134}Cs etc.

Thermal Neutron Capture Cross Sections (σ_0) and Resonance Integrals(I_0) of Important Fission Product Nuclides for Transmutation Studies

Nuclide	Half-Life	Previous Data (Author and reported year)	Data of JNC
^{137}Cs	30 years	$\sigma_{eff}=0.11\pm0.03$ b (Stupegia '60)	$\sigma_0=0.25\pm0.02$ b $I_0=0.36\pm0.07$ b ('90,93)
^{90}Sr	29 years	$\sigma_{eff}=0.8\pm0.5$ b (Zeisel '66)	$\sigma_0=15.3\pm^{1.3}_{4.2}$ mb $I_0\leqq0.16$ b ('94)
^{99}Tc	2.1 × 10^5 years	$\sigma_0=20\pm2$ b $I_0'=186\pm16$ b (Lucas '77)	$\sigma_0=22.9\pm1.3$ b $I_0=398\pm38$ b ('95)
^{129}I	1.6 × 10^7 years	$\sigma_0=27\pm2$ b $I_0=36\pm4$ b (Eastwood '58)	$\sigma_0=30.3\pm1.2$ b $I_0=33.8\pm1.4$ b ('96)
^{127}I	(stable)	$\sigma_0=4.7\pm0.2$ b $I_0=109\pm5$ b (Friedmann '83)	$\sigma_0=6.40\pm0.29$ b $I_0=162\pm8$ b ('99)
^{135}Cs	3 × 10^6 years	$\sigma_0=8.7\pm0.5$ b $I_0=61.7\pm2.3$ b (Baerg '58)	$\sigma_0=8.3\pm0.3$ b $I_0=38.1\pm2.6$ b ('97)
^{134}Cs	2 years	$\sigma_{eff}=134\pm12$ b (Bayly '58)	$\sigma_{eff}=141\pm9$ b ('99)
^{133}Cs	(stable)	$\sigma_0=30.4\pm0.8$ b $I_0=461\pm25$ b (Baerg '60)	$\sigma_0=29.0\pm1.0$ b $I_0=298\pm16$ b ('99)

σ_0 : the thermal neutron capture cross section at υ_n=2,200 m/s.
σ_{eff} : the effective cross section.
I_0 : the resonance integral.
I_0' : the reduced resonance integral with the 1/υ part subtracted.

Measurements of σ_0 and I_0

Reaction rate

$$R \equiv \int_0^{\infty} \sigma_{(v)} \cdot n_{(v)} v dv$$

assumption :

$$n_{(v)} = n(1-f)\rho_m(v) + nf\rho_e(v)$$

where

$$\rho_m = \frac{4}{\sqrt{\pi}} \cdot \frac{v^2}{v_T^3} \cdot e^{-\left(\frac{v}{v_T}\right)^2},$$

$$\rho_e = \frac{\sqrt{\mu}\, v_T}{v^2} \Delta(\mu kT : \text{step func.})$$

$$R = nv_0\sigma_0 \,[gG_{th} + r\sqrt{\frac{T}{T_0}} \cdot S_0 G_{epi}$$

where

$$g = \frac{\hat{\sigma}_m}{\sigma_0} = \frac{1}{\sigma_0 v_0} \int_0^{\infty} \sigma_{(v)} \rho_{m(v)} dv$$

G = self-shielding coef.

$$r = \frac{\sqrt{\pi\mu}}{4} \cdot f$$

$$S_0 = \sqrt{\frac{4}{\pi}} \cdot \frac{I_0'}{\sigma_0}$$

where

$$I_0' = \int_0^\infty \left[\sigma(v) - \hat{\sigma}_m \frac{v_0}{v}\right] \frac{\Delta dE}{E}$$

$$\frac{R}{\sigma_0} = \phi_1 + \phi_2 \cdot S_0 G_{epi}$$

for irradiation without a Cd shield

$$\frac{R'}{\sigma_0} = \phi_1' + \phi_2' \cdot S_0 G_{epi}$$

for irradiation with a Cd shield

Data used for the determination of nv_0 and $r(T/T_0)^{1/2}$ from radioactivities in flux monitors

Nuclear reaction	σ_0 (b)	g	G_{th}	s_0	G_{epi}
$^{59}Co(n,\gamma)^{60}Co$	37.2	1.00	1.00	1.83	1.00
$^{197}Au(n,\gamma)^{198}Au$	98.8	1.01	1.00	17.02	1.00
$^{98}Mo(n,\gamma)^{99}Mo$	0.130	1.00	1.00	53	0.85

Level Scheme

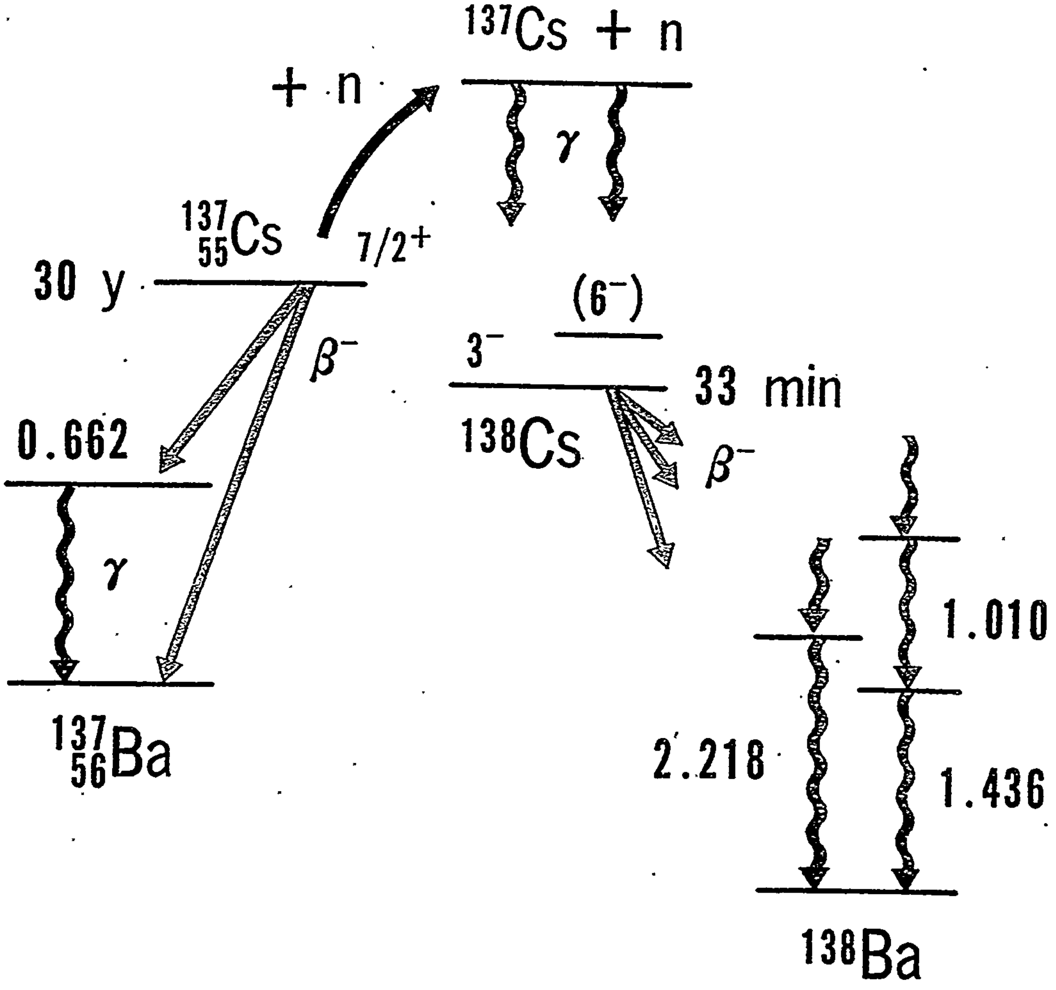

Stupegia's Experiments

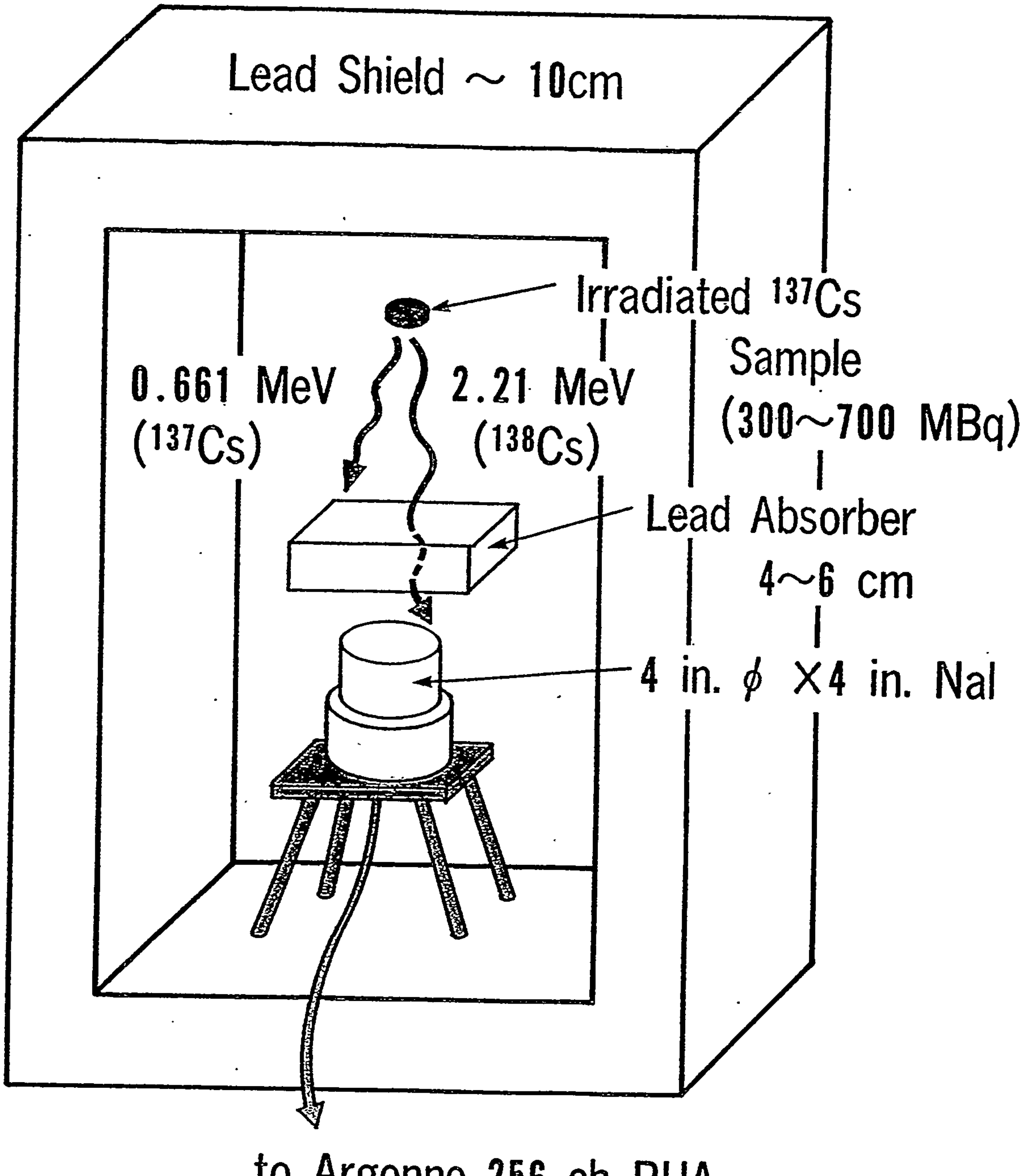

to Argonne 256 ch PHA

J. Nucl. Energy 12 16 ('60)

Argonne, CP-5,

Pneumatic tube

$\phi_{th} \sim 10^{13}$ n/cm²/s, $r\sqrt{\frac{T}{T_0}} \sim 0.003$

$\sigma_\gamma = 0.110 \pm 0.033$ b

relative to Au

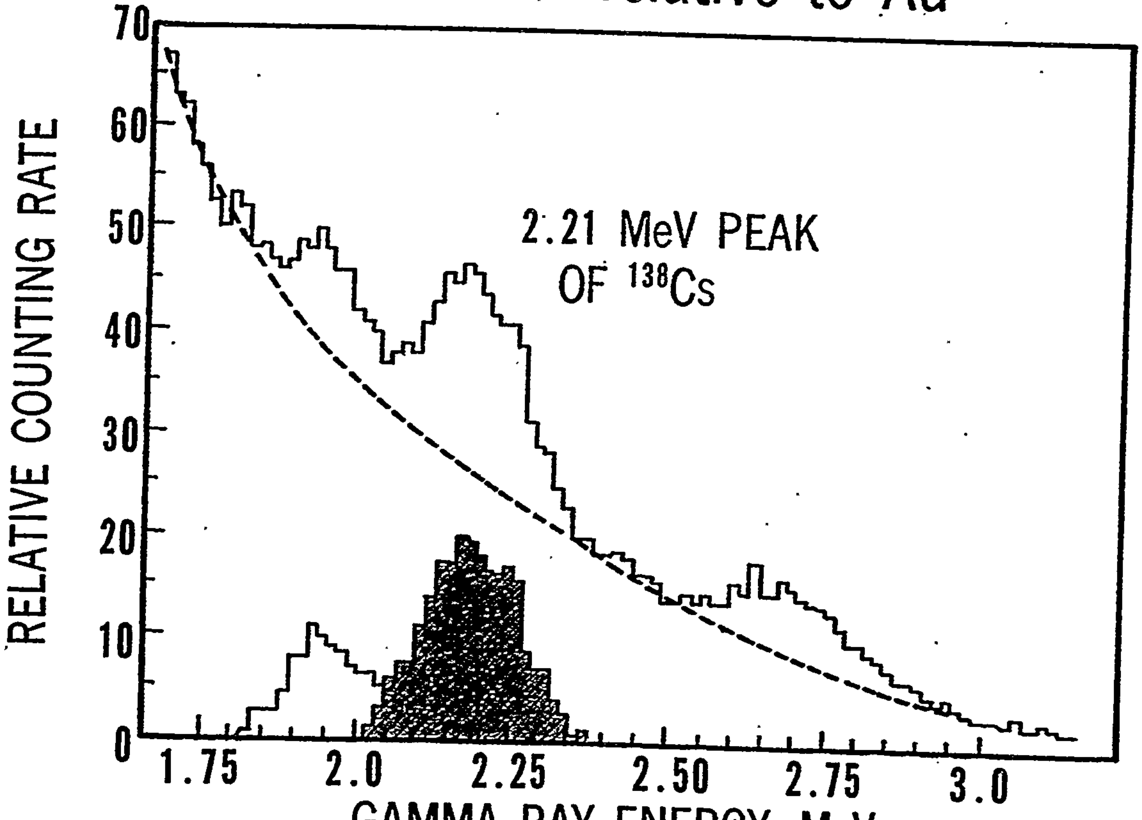

Gamma-ray spectrum of ^{138}Cs
in the presence of ^{137}Cs target.

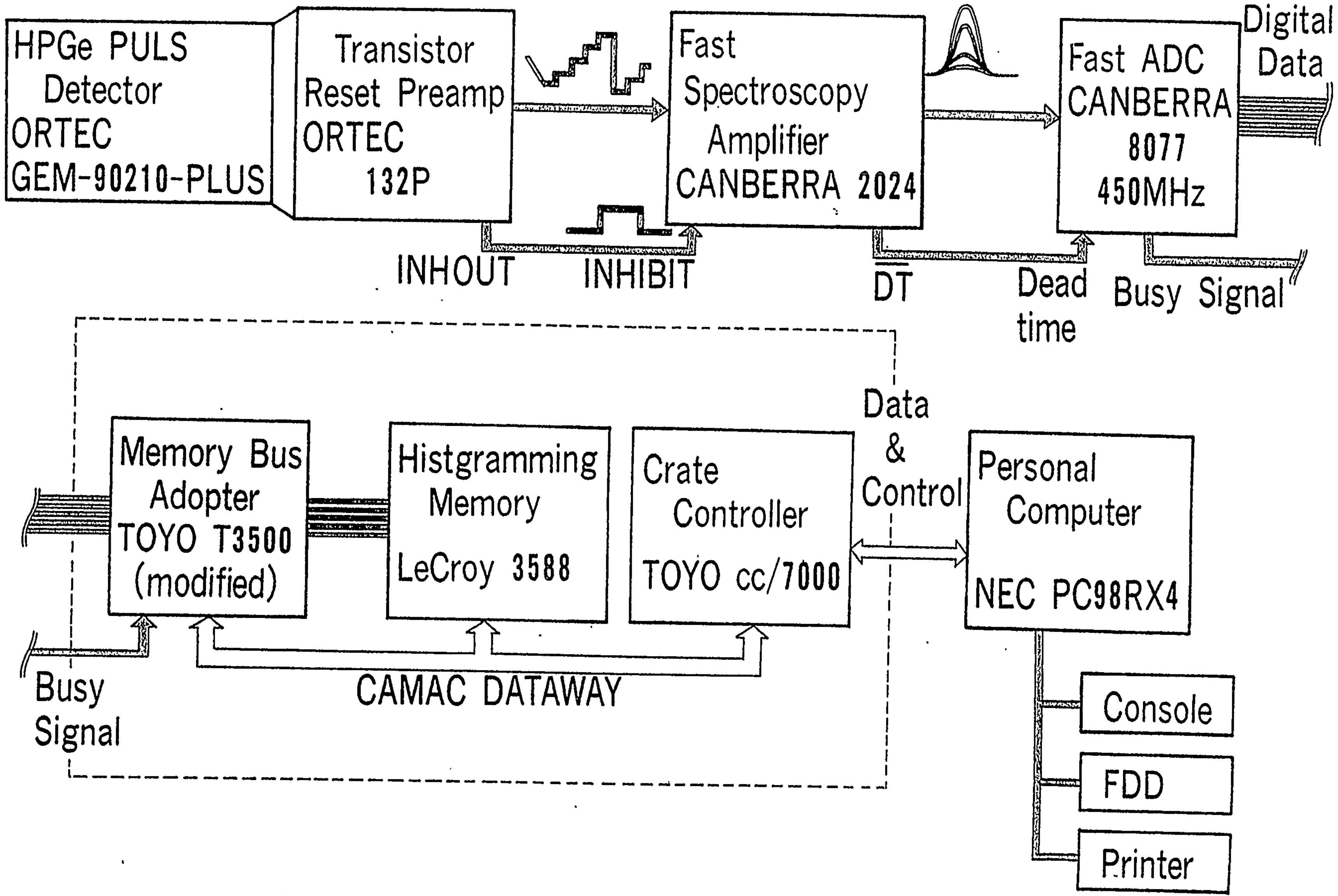

High Count Rate Spectroscopy Systems

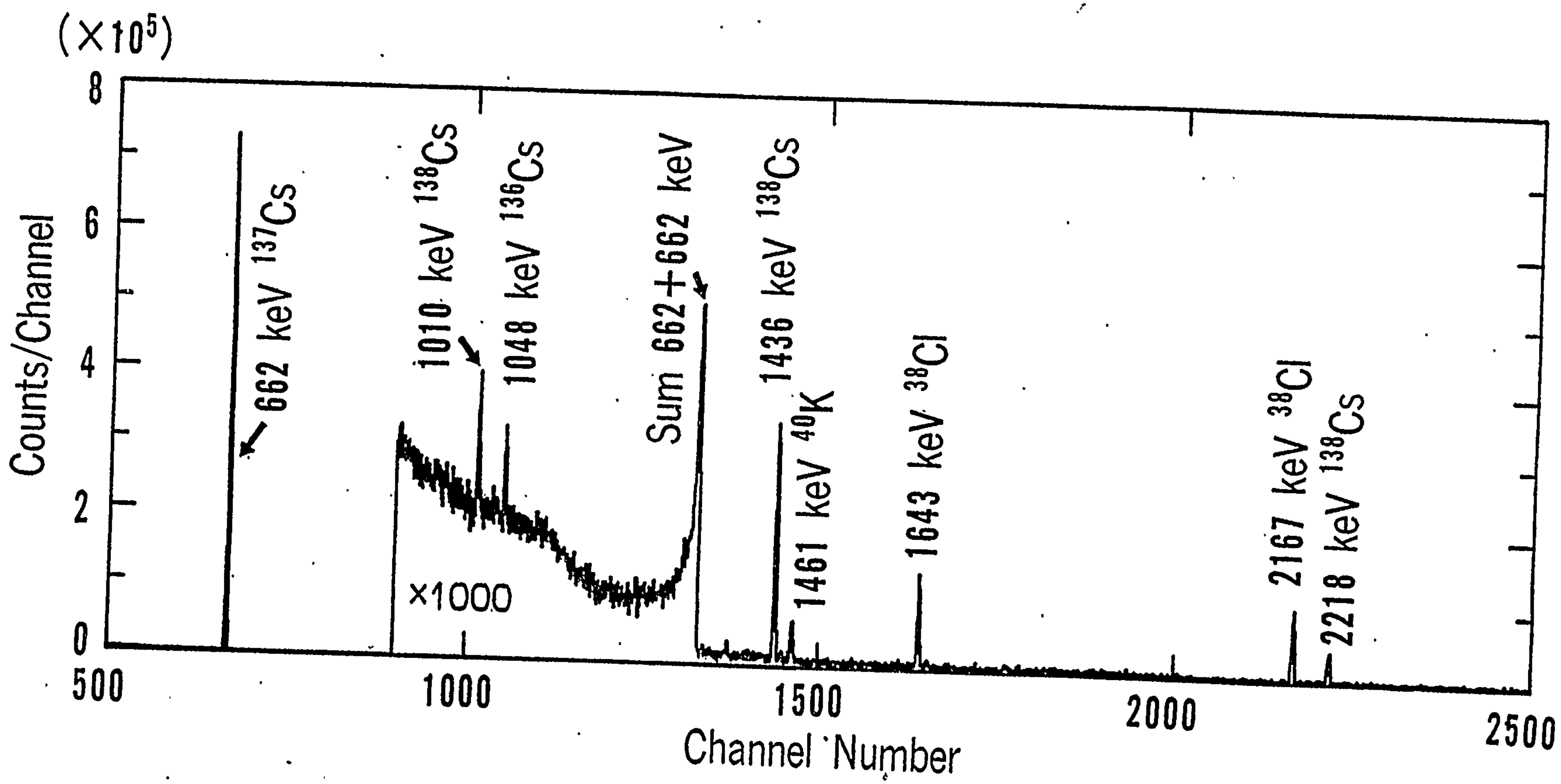

Gamma-ray spectrum obtained from neutron-irradiated and chemically purified ^{137}Cs sample in 10-min measurement

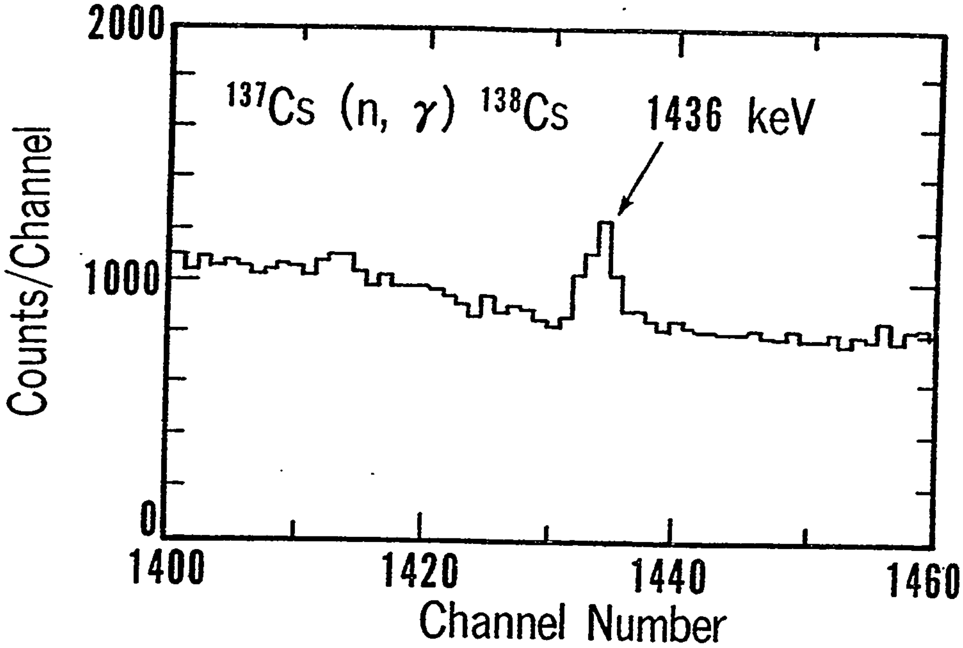

γ-ray spectrum : Chemical purification
was NOT performed

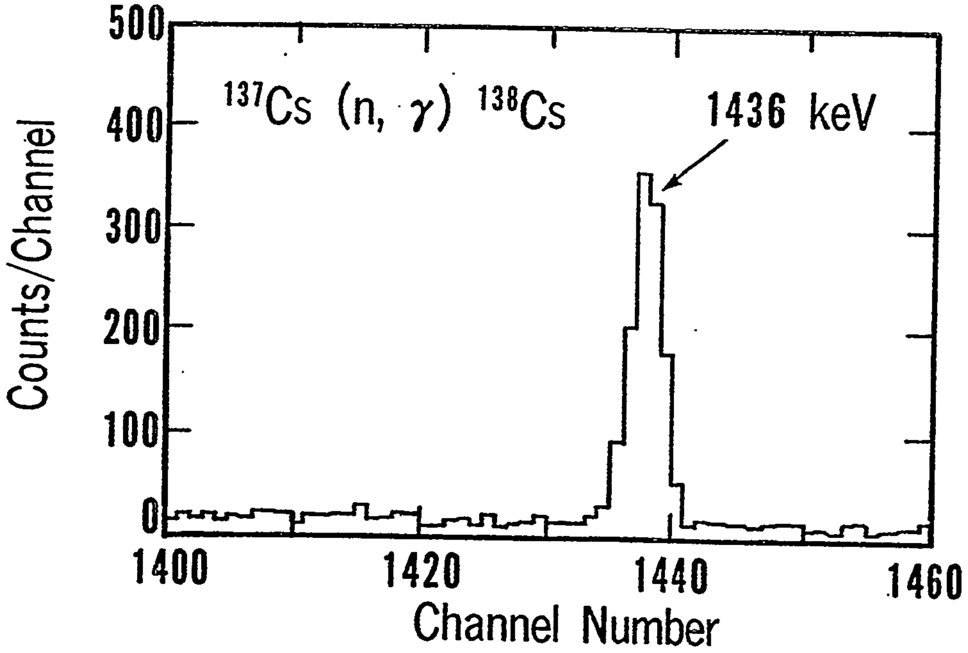

γ-ray specturm : Chemical purification
was performed

三重中性子捕獲反応
Triple Neutron Capture Reaction

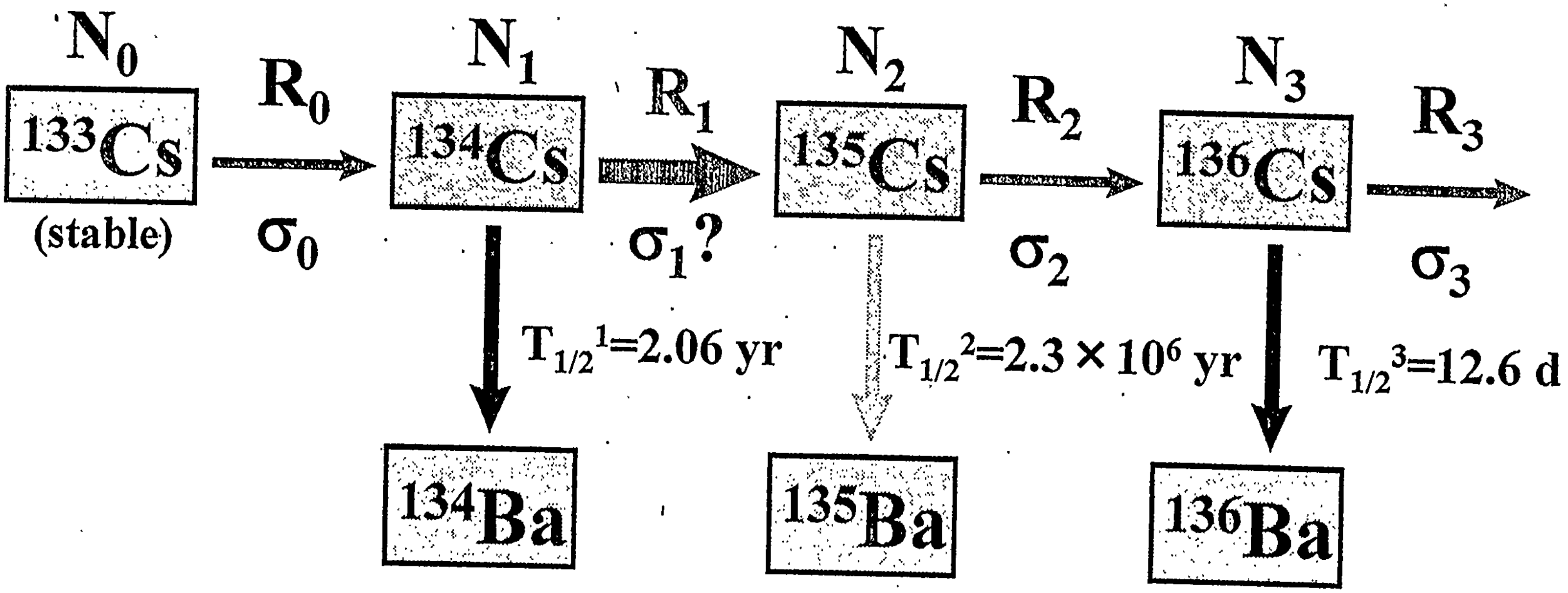

N_0 ^{133}Cs (stable) $\xrightarrow[\sigma_0]{R_0}$ N_1 ^{134}Cs $\xrightarrow[\sigma_1?]{R_1}$ N_2 ^{135}Cs $\xrightarrow[\sigma_2]{R_2}$ N_3 ^{136}Cs $\xrightarrow[\sigma_3]{R_3}$

^{134}Cs $\to$ ^{134}Ba　$T_{1/2}{}^{1}=2.06$ yr

^{135}Cs $\to$ ^{135}Ba　$T_{1/2}{}^{2}=2.3\times10^{6}$ yr

^{136}Cs $\to$ ^{136}Ba　$T_{1/2}{}^{3}=12.6$ d

$\lambda_i=\ln 2/T_{1/2}{}^{i}$

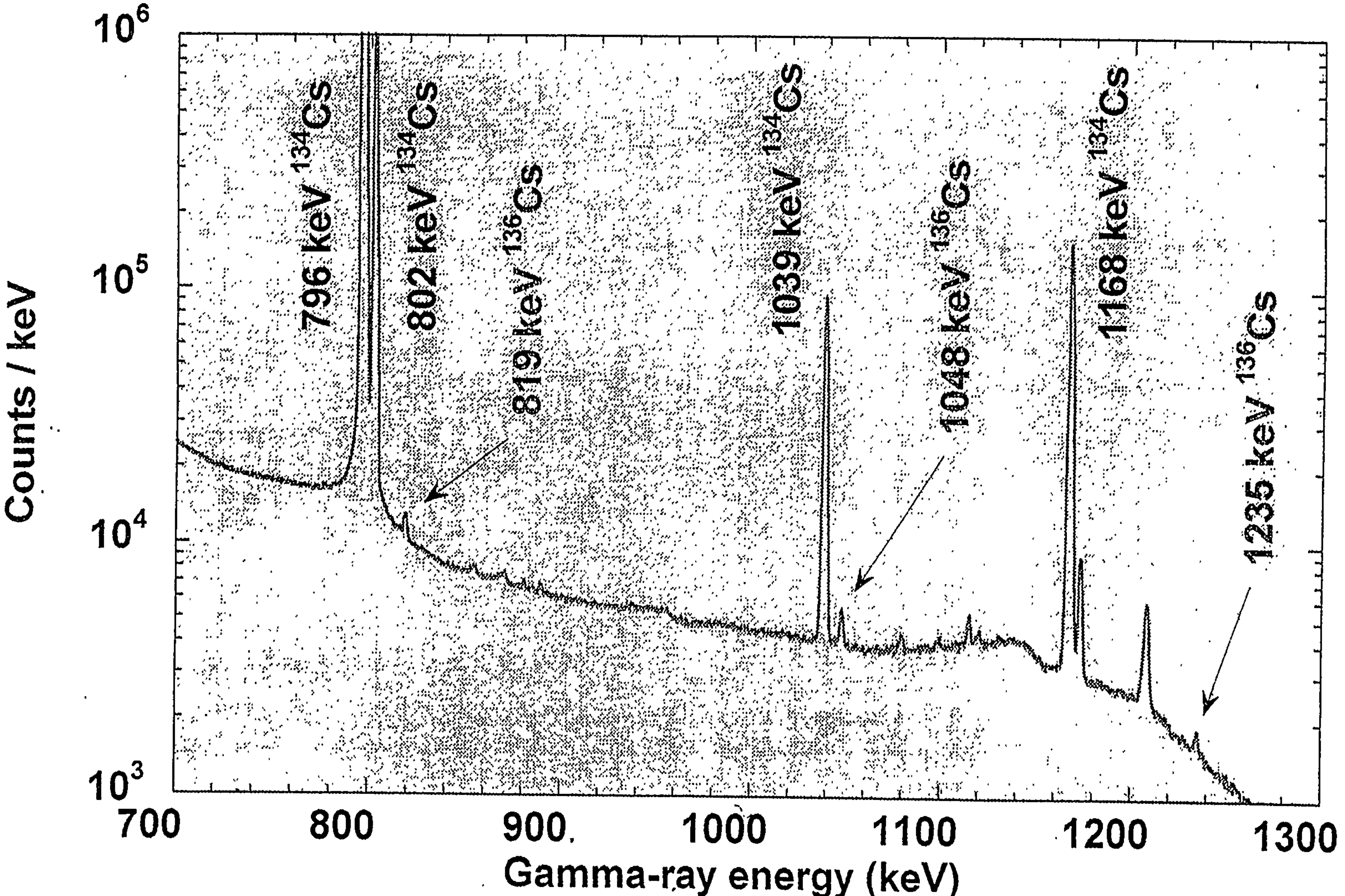

Gamma-ray spectra of Cs sample irradiated with reactor neutrons

Thermal Neutron Capture Cross Section of ^{135}Cs(n,γ) Reaction

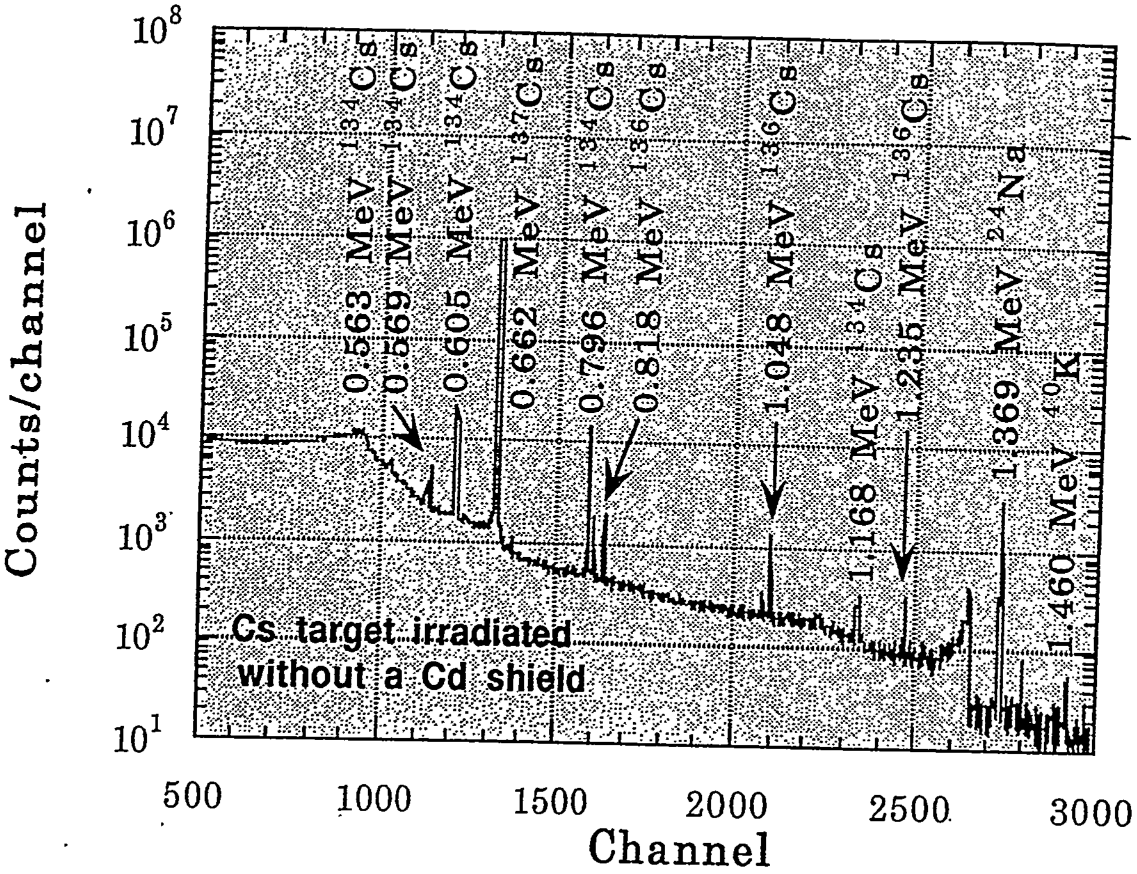

	Baerg ('58)	Sugarman('49)	PNC data
σ_0 (b)	8.7±0.5	14.5±4	8.3±0.3
I_0 (b)	61.7±2.3	----------	37.9±2.7

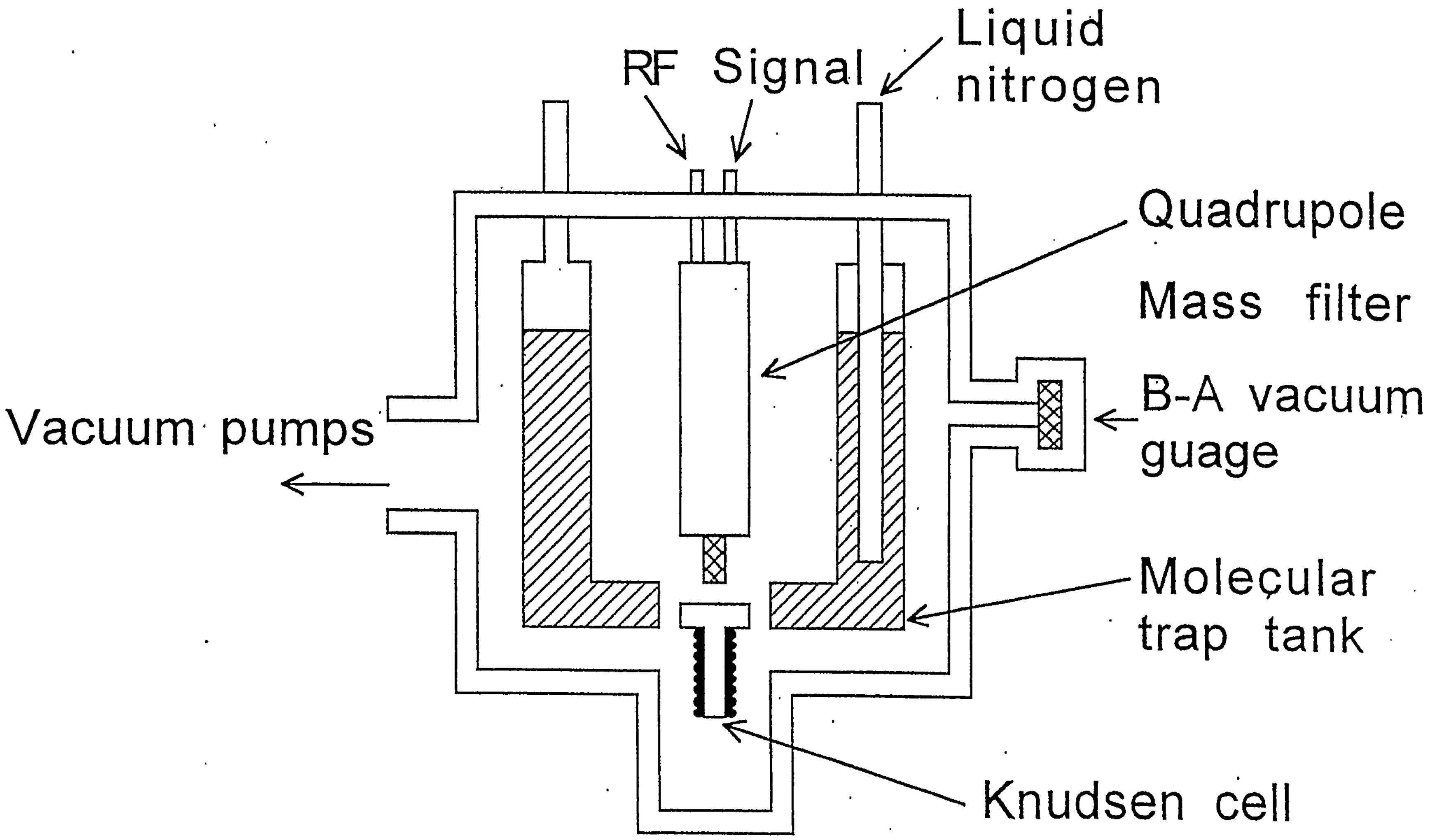

Vacuum chamber and molecular trap

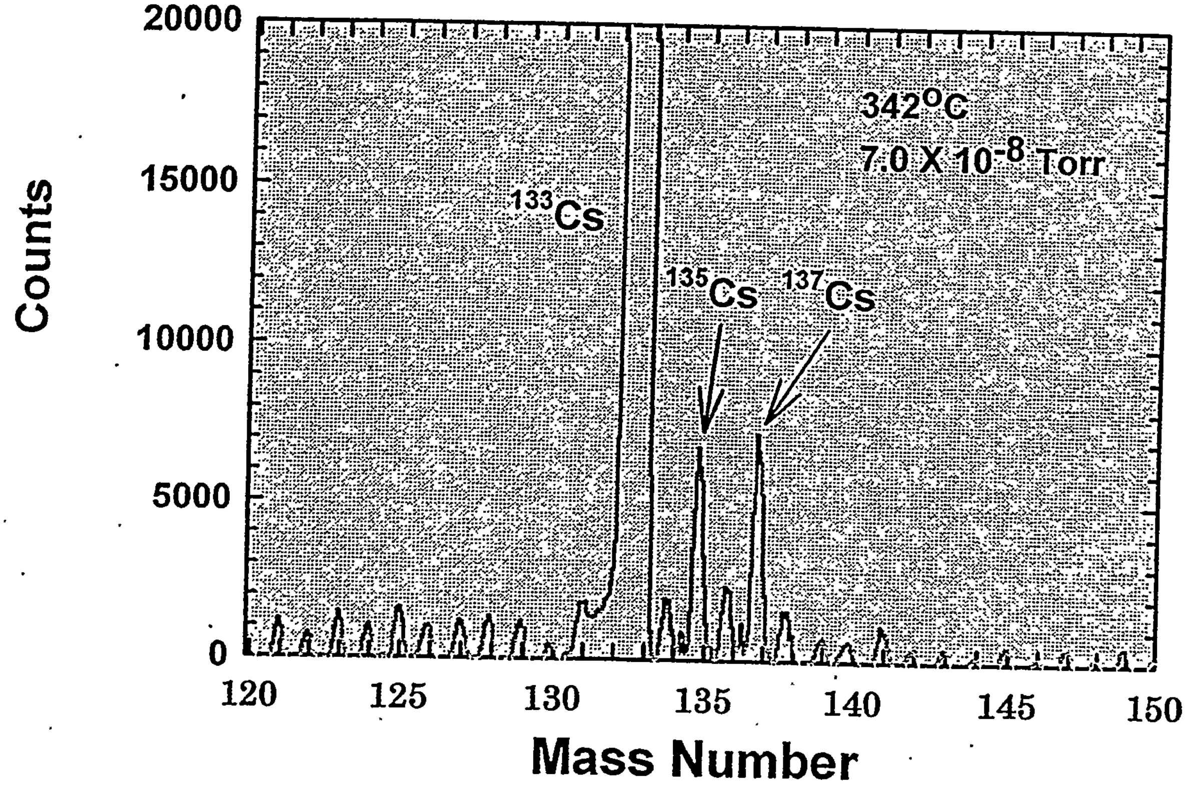

A mass spectrum of a ^{135}Cs/^{137}Cs sample heated in the Knudsen cell to the temperature of about 340°C.

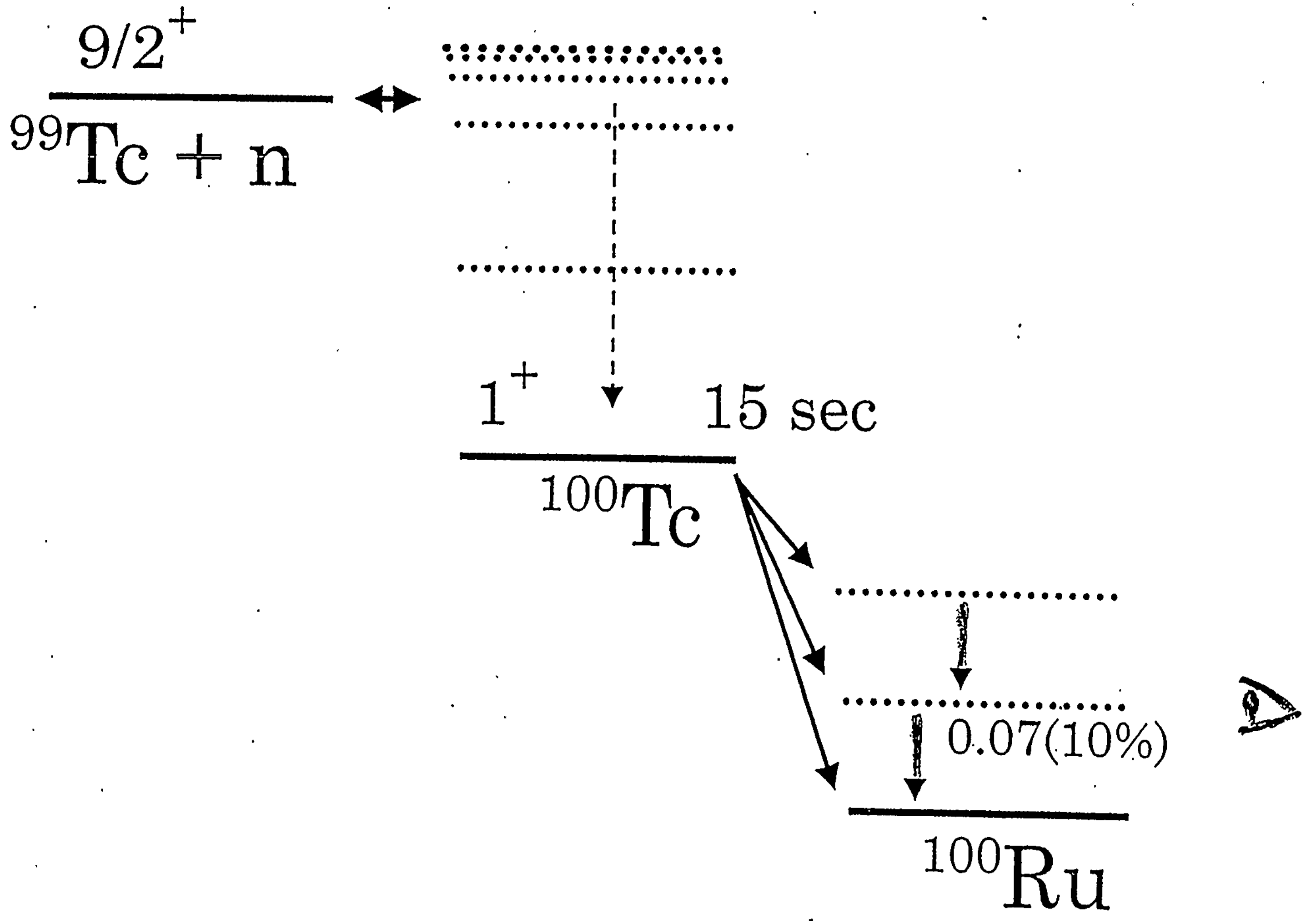
9/2$^+$
^{99}Tc + n
1$^+$
15 sec
^{100}Tc
0.07(10%)
^{100}Ru

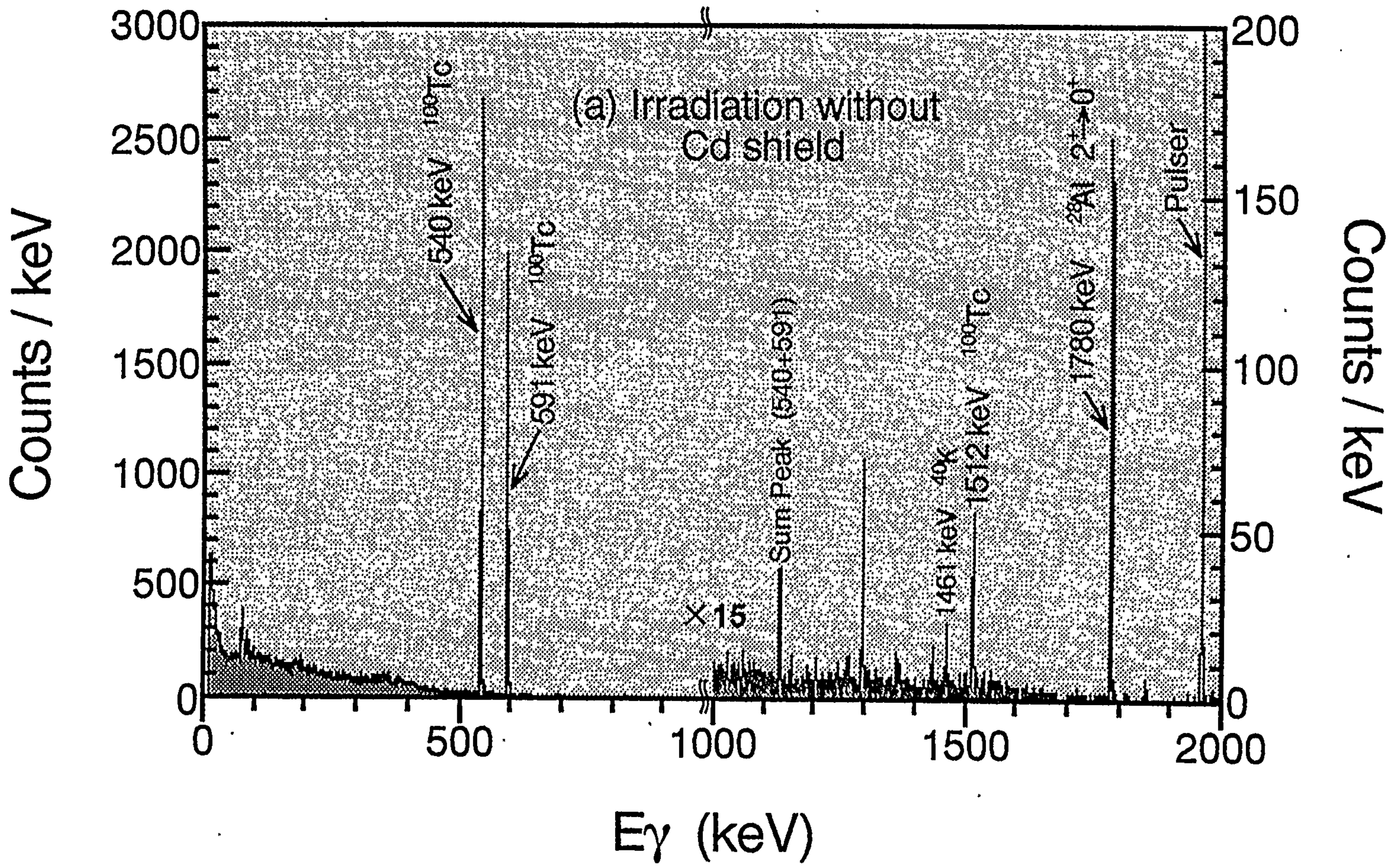
(a) Irradiation without
Cd shield
540 keV ^{100}Tc
591 keV ^{100}Tc
Sum Peak (540+591)
1461 keV ^{40}K
1512 keV ^{100}Tc
1780 keV ^{28}Al $2^+ \to 0^+$
Pulser
×15
Counts / keV
Counts / keV
Eγ (keV)
0
500
1000
1500
2000
2500
3000
0
50
100
150
200
0
500
1000
1500
2000

Comparison of thermal neutron cross section and resonance integral of the $^{99}Tc(n,\gamma)^{100}Tc$ reaction

	σ_0	I_0	I'_0	Reference
Present	22.9 ± 1.3	398 ± 38	388 ± 38	
Lucas	20 ± 2		186 ± 16	(16)
JENDL-3	19.7	312		(17)
ENDF/B-VI	19.5	351		(18)

Future Plan

- Reduce Experimental Errors -

$\gamma\gamma$-coincidence → Efficiency Calibration

$\beta\gamma$-coincidence → γ-intensity per decay

Measurement Accuracy <2%

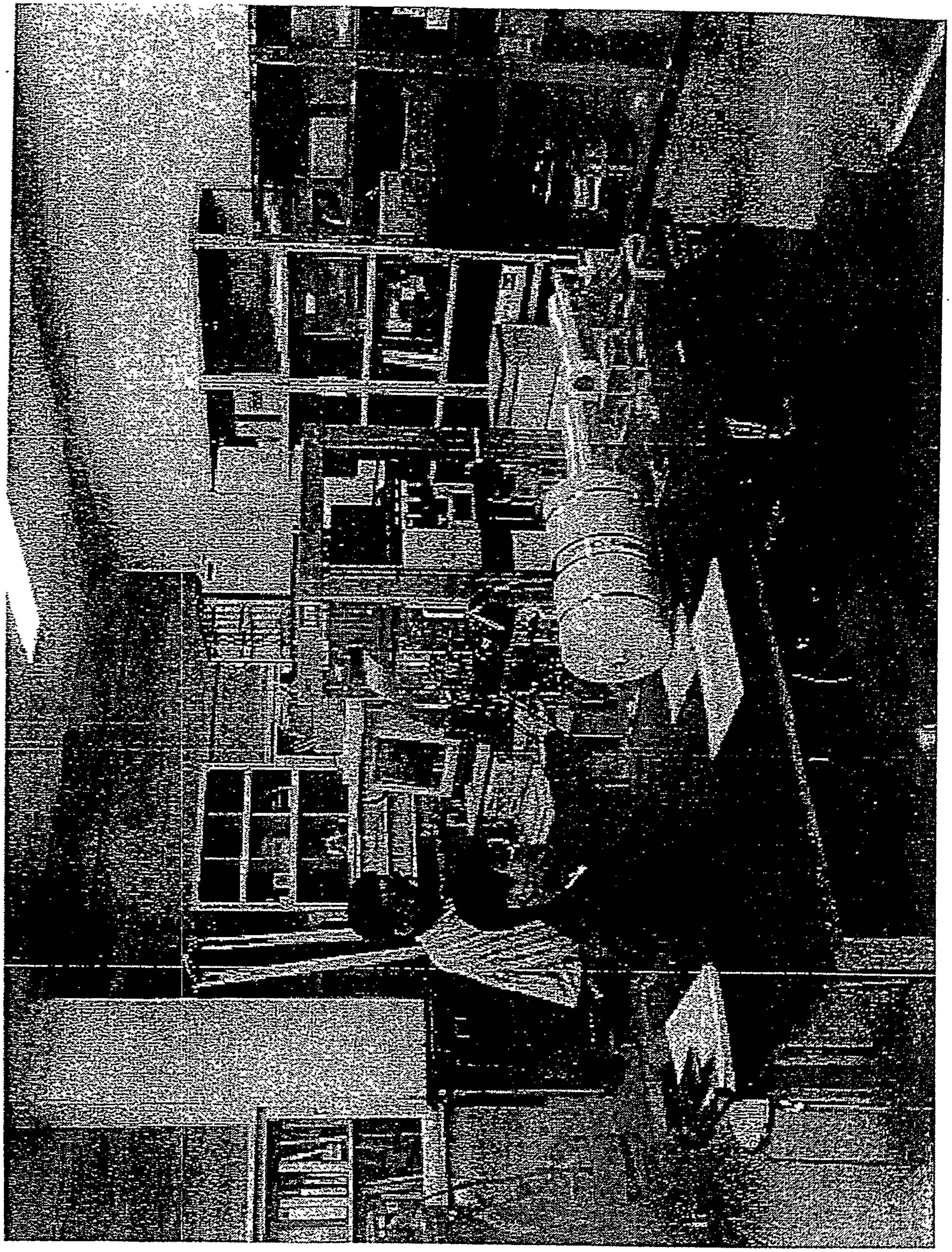

Other Important FP to be measured

^{93}Zr, ^{79}Se, ^{126}Sn, ^{107}Pd

Neutron Time-of-Flight Spectrometer GNEIS at the 1-GeV Proton Synchrocyclotron of PNPI

O. A. Shcherbakov, A. B. Laptev, G. A. Petrov,
A. S. Vorobyev

Petersburg Nuclear Physics Institute, Gatchina
Leningrad District, 188355
Russia

The PNPI Synchrocyclotron facility and its research program based on the spallation neutron source are discussed.

Neutron Time-of-Flight Spectrometer GNEIS at the 1-GeV Proton Synchrocyclotron of PNPI

O.A. Shcherbakov, A.B. Laptev, G.A. Petrov
A.S. Vorobyev

Petersburg Nuclear Physics Institute, Gatchina
Leningrad district, 188355, Russia
shcherba@hep486.pnpi.spb.ru

B.P. Konstantinov Petersburg Nuclear Physics Institute
Russian Academy of Sciences

RESEARCH AREAS:

- elementary particle physics
- nuclear and atomic physics
- physics of the condensed matter
- molecular and radiation biophysics

MAIN RESEARCH FACILITIES:

- 1 GeV proton synchrocyclotron
- 18 MWt reactor WWR-M
- 100 MWt high flux reactor PIK (under construction)

Internet URL http://www.pnpi.spb.ru

PNPI SYNCHROCYCLOTRON
general information

Diameter of the magnet pole pieces	685 cm
Width of the gap between poles	50 cm
Magnet weight	8,000 t
Electric power supplied	1 MWt
Frequency range	30 – 13 MHz
Accelerating voltage	10 kV
Repetition rate	40-60 Hz
Internal beam intensity	< 3 • A
Extraction coefficient	30 %
Duty cycle coefficient	50 %

proton beam characteristics

particle	E (GeV)	• E/E (%)	Intensity (s^{-1})	channel number	comment
proton	1	1	$6 \cdot 10^{12}$	P1,P2,P3,P4	
proton	1	1	10^{8}	P2	medical small size beam 3 mm x 5 mm
proton	1	0.03	10^{10}	P2	spectrometry beam, time gate extraction

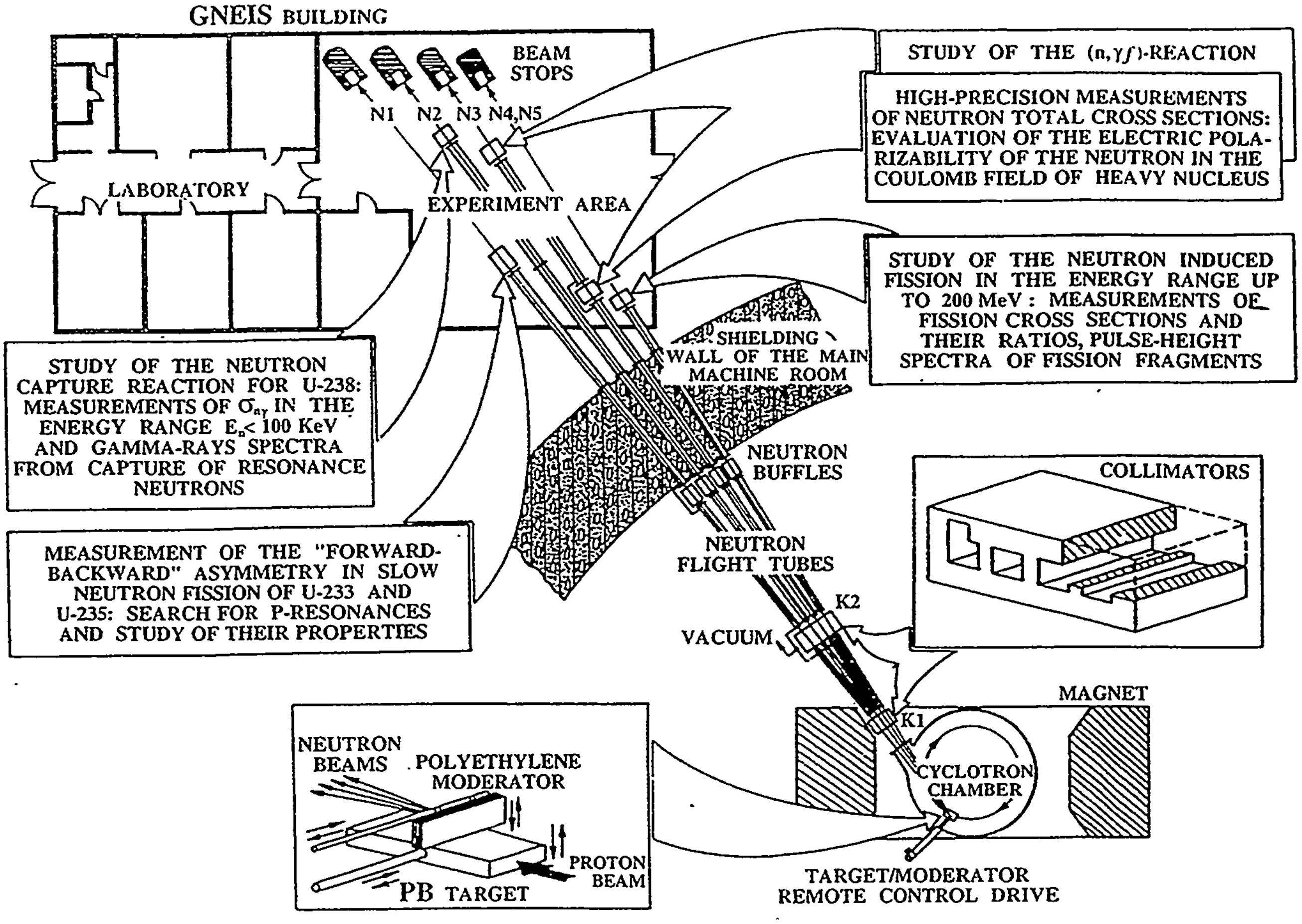

Fig.1. General layout of the Gatchina neutron time-of-flight spectrometer GNEIS

Pulsed neutron source:

- internal water-cooled rectangular lead target	40 cm x 20 cm x 5 cm
- rectangular polyethylene moderator	30 cm x 10 cm x 5 cm
- duration of the fast neutron pulse	~ 10 ns
- repetition rate	< 50 Hz
- average fast neutron intensity	~ $3\cdot10^{14}$ n/s

Spectrometer:

- number of evacuated flight paths (one beam N5 axis looking at the target and others N1-4 looking at the moderator)	5
- length of flight paths	35 – 50 m
- experimental area (GNEIS building)	45 x 30 m^2

Reference: N.K. Abrosimov et al., Nucl.Inst.Meth., A242 (1985)121

Study of the (n,γf)-reaction in Neutron Resonances of U235 and Pu239.

O.A. Shcherbakov, A.B. Laptev, G.A. Petrov

Experimental studies on the two-step (n,γf)-reaction give unique information not only about fission process itself, but also about the structure of highly excited states in heavy nuclei, both in 1-st and 2-nd wells of the fission barrier, and radiative transitions between them. The fission γ-ray multiplicity has been measured in neutron resonances of ^{235}U and ^{239}**Pu**. The experimental prefission widths $\Gamma_{\gamma f}$ have been obtained from the observed correlations between the multiplicity of fission-γ-rays and reciprocal fission width Γ_f^{-1} of resonances. The experimental and calculated prefission width $\Gamma_{\gamma f}$ is shown in Fig.2 for the 4⁻-resonances of ^{235}U and 1⁺-resonances of ^{239}**Pu** as function of the ratio of the **E1** and **M1** components in the prefission γ-ray spectrum. The comparison of the experimental and calculated $\Gamma_{\gamma f}$-widths shows predominance of the **M1** radiation in compound nucleus ^{236}U and that of **E1** radiation in the prefission spectra of γ-transitions between the highly excited states. It was also found that the best agreement between experiment and calculations is obtained by using the model of intermediate damping of the vibrational states in the second well and the GDR model.

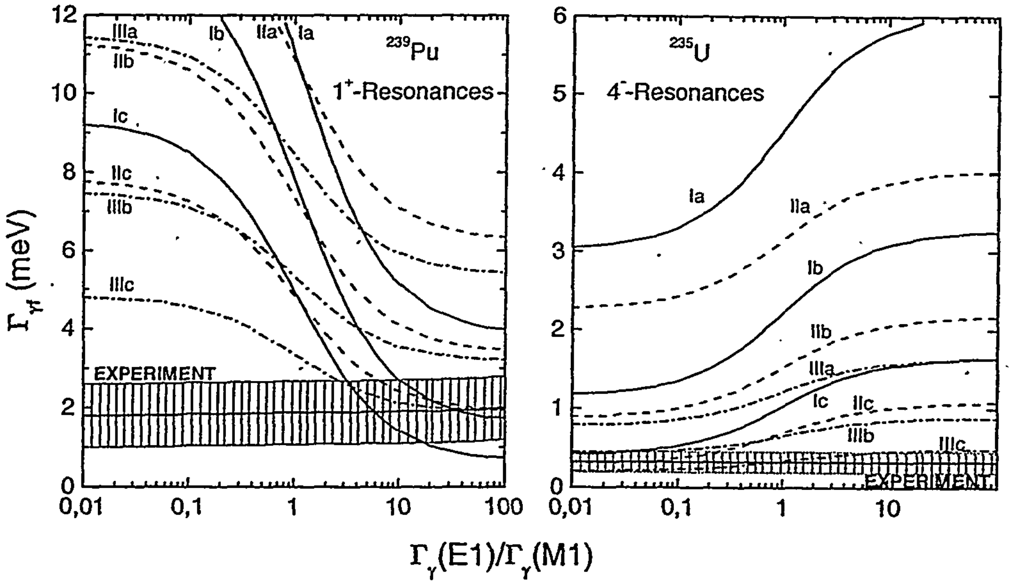

Fig.2. Experimental and calculated widths $\Gamma_{\gamma f}$ for 1⁺-resonances of ^{239}**Pu** and 4⁻-resonances of ^{235}**U**. Calculation model: **I**- single-humped fission barrier, **II**,**III**- double-humped barrier (complete and intermediate damping of the vibrational states in the second well, respectively); **a**- single-particle model (Weisskopf) for probabilities of γ-transitions; **b**,**c** – GDR model (Axel-Brink, Lorentzian-shaped probability of partial γ-transitions proportional to E_γ^4 and E_γ^5, respectively).

In another experiment at the GNEIS, the pulse-height spectra of fission gamma-rays have been measured in isolated resonances of ^{239}**Pu** in the energy range from 10 eV to 91 eV. The difference pulse-height spectra for weak (Γ_f <10 meV) and strong (Γ_f >10 meV) 1⁺-resonances show a few structures that could be interpreted as prefission gamma-transitions between the levels at excitation energy 1-3 MeV below the neutron binding energy B_n.

Measurements of the capture cross-section of ^{238}U in energy range E_n<100 keV and gamma-ray spectra from the capture of resonanse neutrons: study of the nature of the 721.6 eV resonance.

O.A. Shcherbakov and A.B. Laptev

Two lowest energy resonance clusters in the subthreshold fission cross-section of ^{238}U are dominated by the 721.6 eV and 1211.4 eV resonances. Anomalously small capture width of the 721.6 eV resonance (~ 4.7 meV) is a strong evidence that this resonance is not usual (class-I, corresponding the first well of fission barrier) compound state. If the 721.6 eV resonance is predominantly class-II (corresponding to the second well) in character, then not only its radiative width Γ_γ should be small, but the capture γ-ray spectrum of this resonance should be softer than that of other s-wave resonances (class-I). Prior to present measurements, J.C. Browne (1976) observed a much softer • -ray spectrum for the 721.6 eV resonance than for neighboring resonances, whereas H. Weigmann et al. (1975) found no difference. To resolve this contradiction, the capture • -ray spectra in isolated neutron resonances of ^{238}U in the energy range from 400 eV to 1300 eV have been measured at the GNEIS. The data obtained have been processed after the slightly modified method of Weigmann et al. The idea was to detect a γ-decay branch within the second well using two different bias values for the γ-ray registration: lower **B1** and upper **B2**. Then, for value of **B2** larger than $\mathbf{B_n}$- $\mathbf{E_{II}}$ (2 MeV, height of the second minimum), the ratio of resonance area **A.** measured with two biases **B1** and **B2**: **R** = **A.** (bias **B2**)/**A.** (bias **B1**) should be smaller for the resonance having major class-II fraction than for ordinary class-I resonances because the softer class-II component will be under the upper bias **B2** for this resonance.

The results of the present measurements and those of Weigmann et al (Geel) are shown in Fig. 3. As it is seen from our data, the capture γ-ray spectrum of the 721.6 eV resonance is much softer than that of the neighboring s-wave resonances. Our data enable to make a conclusion that the 721.6 eV resonance is predominantly class-II by nature. As for the 1211.4 eV resonance, both our data and the results of Weigmann et al show that there are no solid arguments to consider this resonance as a class-II state.

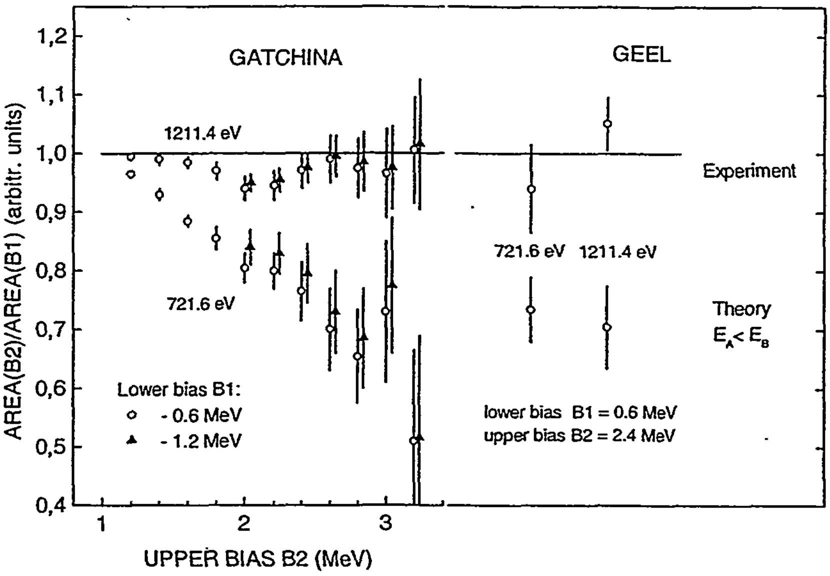

Fig. 3. Results of the capture γ-ray measurements for resonances of U238.

Estimation of the Neutron Polarizability from Analysis of the Total Cross-Sections of Lead-208 and Carbon

I.S. Guseva, A.B. Laptev, G.A. Petrov and O.A. Shcherbakov

The results of the total cross section measurements for ^{208}**Pb** and **C** from 1 eV to 20 keV performed at the GNEIS facility for the purpose of estimating α_n are given in this report and shown in Fig. 4, the given errors are statistical ones.

The method employed for evaluation of α_n for ^{208}**Pb** is described in detail in ref. Guseva, I. S., Preprint 1969, PNPI, Gatchina, 1994. Fitting results for ^{208}**Pb** are presented in fig. 5. Points are experimental total cross section after the Schwinger and solid-state corrections and contribution of radiative absorption having been subtracted. The reduced χ^2 is equal 2.5 . The neutron polarizability obtained is α_n = $(2.4\pm1.1)\cdot10^{-3}$ fm^3 and the amplitude of neutron-electron interaction is $a_{ne} = -(1.78\pm0.25)\cdot10^{-3}$ fm . Fitting results for carbon are presented in fig. 6, the value of reduced χ^2 is equal 1.7 .

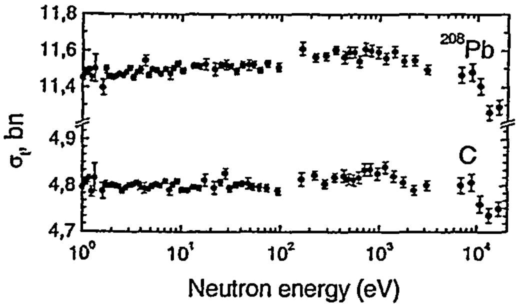

Fig. 4. Measured total cross sections of ^{208}Pb and C.

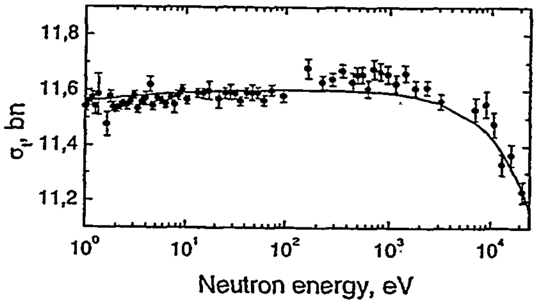

Fig. 5. Fitting results for ^{208}Pb.

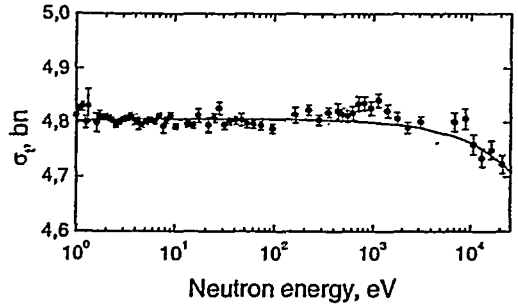

Fig. 6. Fitting results for C.

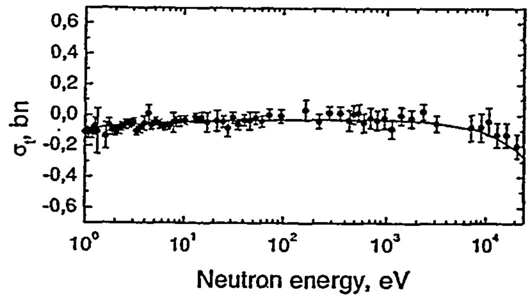

Fig. 7. Fitting results for difference $\sigma(^{208}\text{Pb}) - 2.42\cdot\sigma(\text{C})$.

To eliminate influence of the distortions caused by uncertainties of experimental background the difference $\sigma(^{208}\mathbf{Pb}) - \mathbf{2.42}\cdot\sigma(\mathbf{C})$ used for the neutron polarizability estimation. Fitting results for this difference are shown in fig. 7. Using this method, the polarizability was obtained near the same value $\alpha_n = (2.44\pm1.32)\cdot10^{-3}$ fm^3 . The value obtained for amplitude of neutron-electron interaction is $a_{ne} = -(1.75\pm0.27)\cdot10^{-3}$ fm , the value of reduced χ^2 is equal 0.7 .

Measurement of the forward-backward asymmetry in slow neutron fission

A.M. Gagarsky, S.P. Golosovskaja, A.B. Laptev, A.K. Petukhov, G.A. Petrov, V.E. Sokolov and O.A. Shcherbakov

Parameters and decay properties of low energy **p**-resonances in heavy fissile nuclei are practically unknown because of the difficulties existing when generally accepted method are used. The new method to obtain such information is the study of the neutron energy dependence of the forward-backward asymmetry of angular distribution of fission fragments which is the result of s- and **p**-wave interference in neutron capture

$$W(\bullet) = 1 + \alpha_{fb}\cdot(\mathbf{p}_n\cdot\mathbf{p}_f)$$

where $\mathbf{p}_n$ and $\mathbf{p}_f$ are the neutron and light fragment momenta. The principal advantage of this method if compared with the other asymmetry-measurements: a non-polarized neutron beam can be used. The measurements of the forward-backward asymmetry coefficient α_{fb} for ^{235}U and ^{233}U from 1 eV to 136 eV have been performed at the GNEIS. The results obtained for ^{235}U in the energy range from 1 eV to 21 eV are shown in Fig. 8.

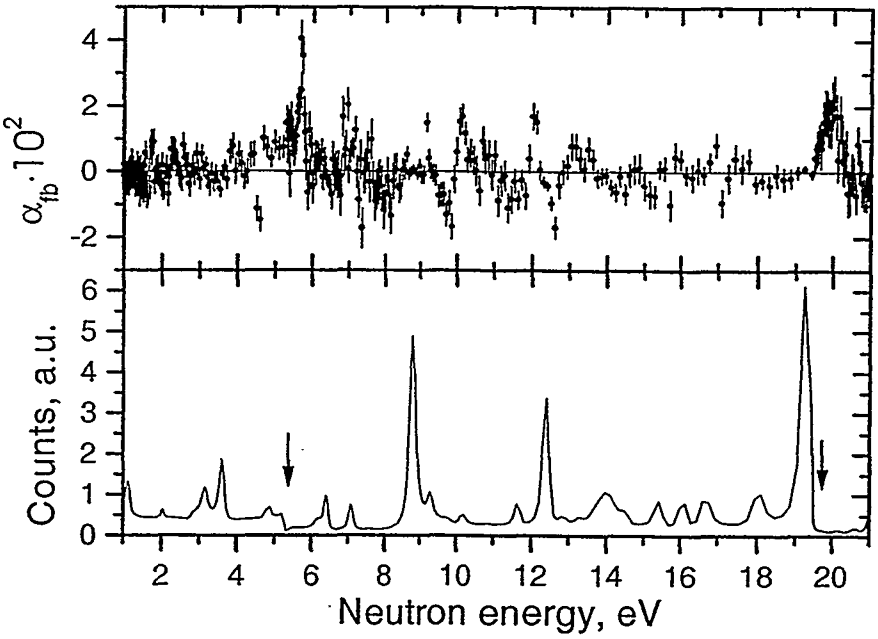

Fig. 8. Energy dependence of the asymmetry coefficient α_{fb} and fission yield for ^{235}U.

Several irregularities caused by **p**-resonances have been observed in energy dependence of the coefficient α_{fb}. Estimations of the main **p**-resonance parameters have been made. Fitting analysis of the data gives that the average total width of the **p**-resonances is some greater than that of s-resonances. For example in case of ^{235}U $\langle\Gamma_{fp}\rangle = (200 \pm 50)$ meV and $\langle\Gamma_{fs}\rangle = (140 \pm 10)$ meV. On the base of analysis of this data, the evaluation of fast direct fission (without compound nucleus stage) contribution to the total fission cross section was obtained. It was found to be lower than $5\cdot10^{-2}$ at 95 % - level of reliability.

The information obtained in these measurements is very important for the fundamental investigations of the **P**- and **T**-parity violation effects that are expected to be resonancely enhanced in a vicinity of **p**-resonances.

Neutron induced fission cross-sections of U233, U238, Th232, Np237 and Pu239 relative to U235 from 1 MeV to 200 MeV

O.A. Shcherbakov, A.B. Laptev, G.A. Petrov, A.S. Vorobyev, A.Yu. Donets, A.V. Fomichev and Yu.V. Tuboltsev

There is a long standing need in information about fission of heavy nuclei induced by the particles at intermediate energies. Regular experimental studies of fission in this energy region started comparatively recently, mainly due to the increased capabilities of modern neutron sources and experimental techniques. Among new applications of the fission data above 20 MeV, the most important are accelerator-driven transmutation of waste reactor materials and energy production, peaceful use of weapon plutonium, accelerator and spaceship shielding, radiation therapy.

During the last decade, the measurements of neutron-induced fission cross-sections for some long-lived actinides in the energy range above 20 MeV with continuous spectrum neutrons have been systematically performed only at the WNR/LANSCE facility in Los Alamos and the GNEIS facility in Gatchina. Analysis of the experimental data available in the energy range 20-200 MeV, as well as experience in producing evaluated fission cross-sections below 20 MeV, shows that new independent measurements aimed to improve fission cross-section data base in the energy range above 20 MeV are necessary. At the same time, calculation methods for the fission cross-sections of actinide nuclei at intermediate energies are still under development, except some codes such as ALICE and HETC. In such situation, the semi-empirical formulae based on the few known experimental data are used to estimate the fission cross-sections. These formulae can give not only the systematics for fission cross-section at a certain energy point but also its energy dependence.

Fission cross-section ratios for U233, U238, Th232, Pu239 and Np237 relative to U235 have been measured using a 50-m flight path. A system of few iron, brass and lead collimators gives the beam diameter of 18 cm at the fission chamber location. The last series of the measurements were carried out with the use of "clearing" magnet placed at 30 m from the source-target. This magnet removes charged particles produced in the collimators and filters from the neutron beam.

The fission reaction rate was measured using a fast parallel plate ionization chamber with electrode spacing 7 mm and filled with methane working gas. The fission chamber contained 6 foils of oxide fissile material 200 μg/cm^2 thick and 18 cm in diameter deposited onto 0.015 cm thick aluminum backings. Also, a weak Cf252 deposit was applied on each fissile foil to match the gains of electronics. The distances between the neutron production target and each fissile foil were determined using C^{12} neutron transmission resonances. For each isotope under investigation, the time-of-flight and pulse height spectra were accumulated.

The results of present measurements are shown in Fig.9,10,11. To obtain fission cross-sections from the measured ratios, the recommended data for fission cross-section of U235 (INDC-368, IAEA, 1997) have been used. The error bars represent the statistical errors only (one standard deviation). The solid lines show JENDL-3.2 data in the energy range below 20 MeV. Also shown are the data of measurements carried out at the WNR/LAMPF facility in Los-Alamos by P.W. Lisowski et al. (1992) and the data of systematics (T. Fukahori, 1998).

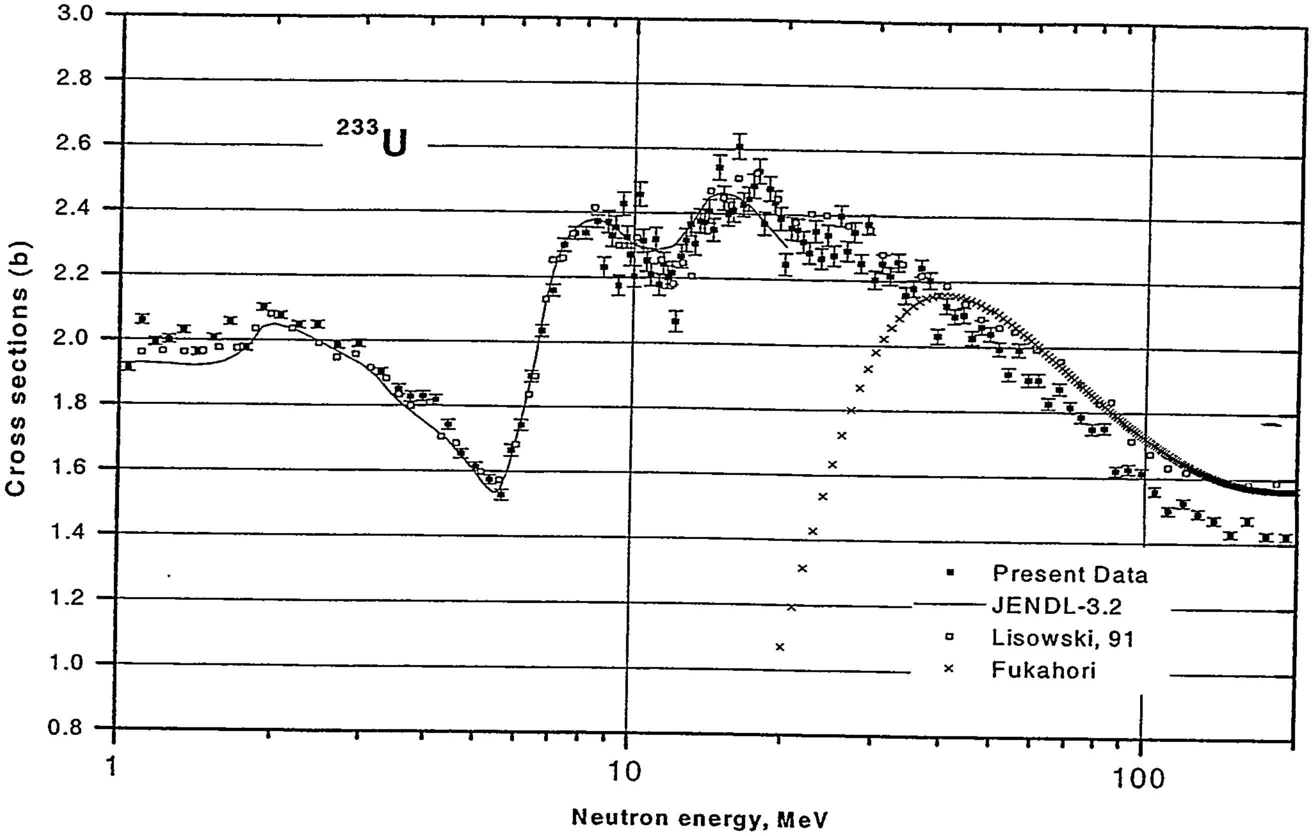

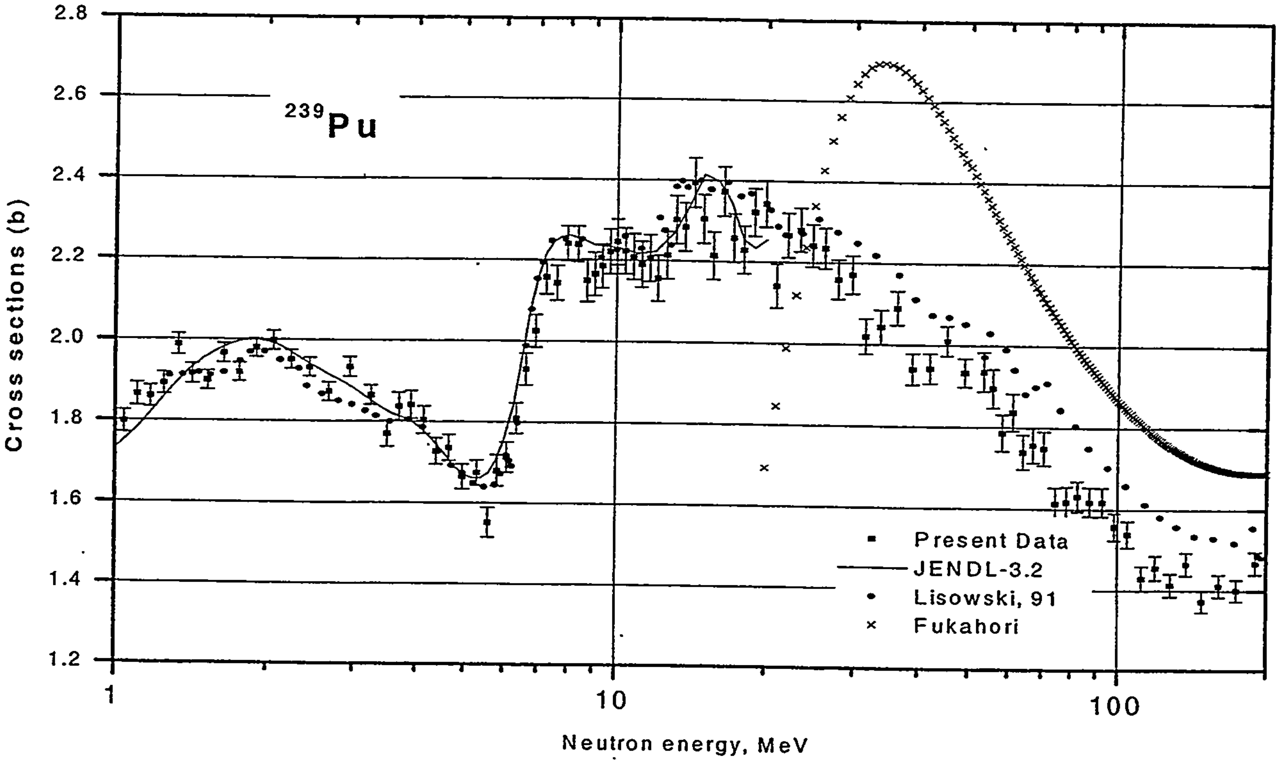

Fig.9. Fission cross sections of U233 and Pu239 in the energy range from 1 to 200 MeV.

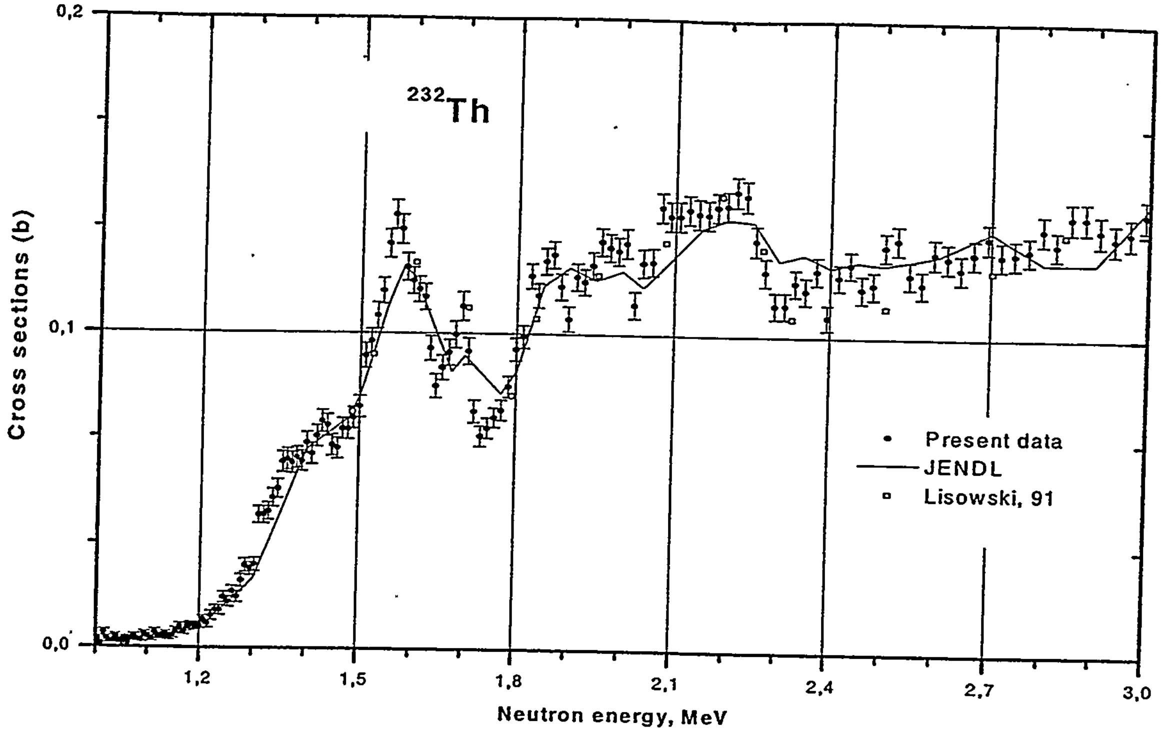

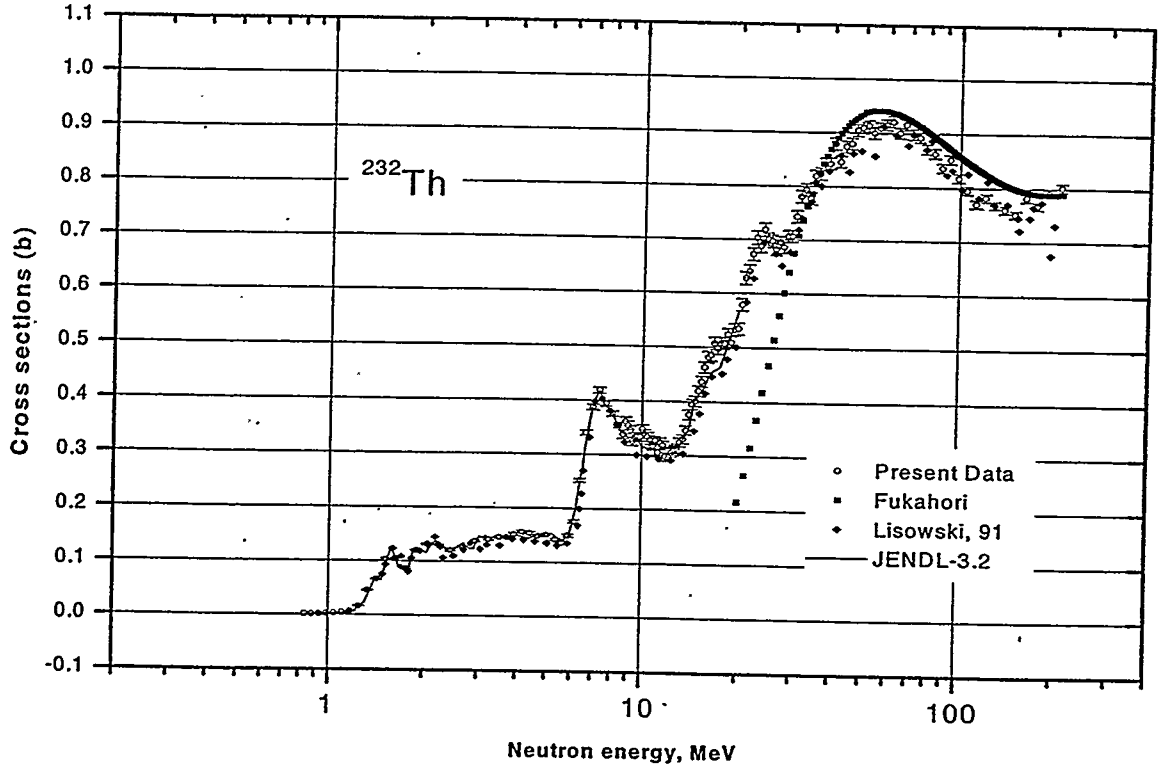

Fig. 10. Fission cross section of Th232 in the energy range from 1 to 200 MeV.

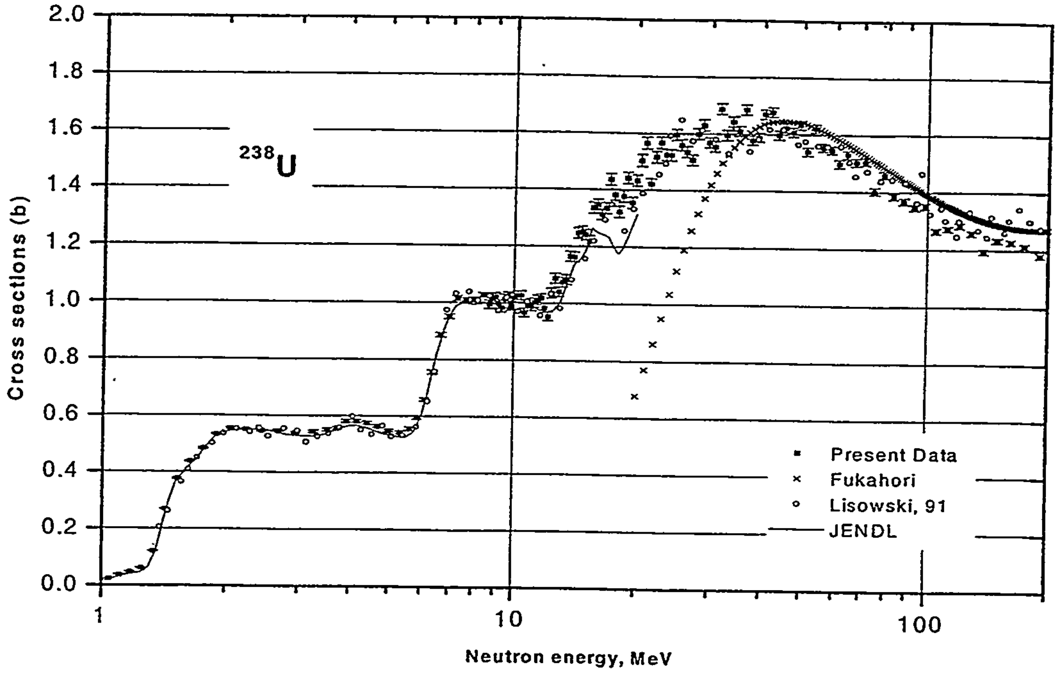

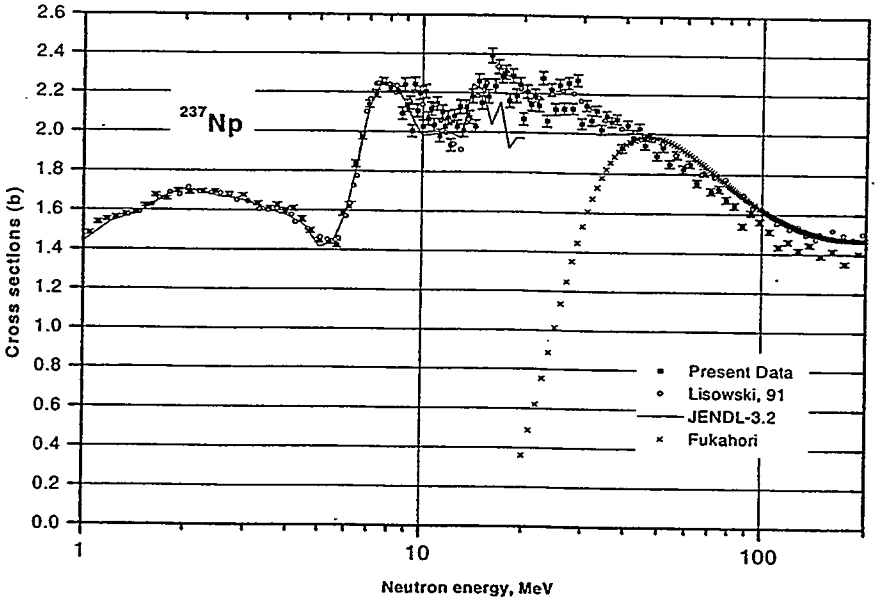

Fig. 11. Fission cross sections of U238 and Np237 in the energy range from 1 to 200 MeV

The use of a 4π γ-detector at spallation sources

René Reifarth, Michael Heil, and Franz Käppeler

Forschungszentrum Karlsruhe, Institut für Kernphysik, Hermann-von-Helmholtz-Platz 1,
D-76344 Eggenstein-Leopoldshafen, GERMANY

Neutron spallation sources offer a new possibility for investigating neutron induced reactions, e.g. neutron capture and neutron induced fission. Due to the higher neutron fluxes compared with other sources and the specific time structure, measurements even on radioactive samples are possible. The neutron energy at spallation sources ranges usually from the thermal region up to several hundred MeV. The main experimental problems at such sources are high count rates, background due to neutron beam halo, and background from sample-scattered neutrons, which are subsequently reacting in the detector system. In order to plan for state of the art equipment it was investigated if a 4π γ-detector similar to the Karlsruhe BaF_2 array [Wis90] can be used under the different conditions of a spallation source, and what kind of improvements would be required.

These problems were studied by means of the detector simulation tool GEANT [GEA93]. The first step was to show that the experimental data obtained with the 4π setup at the Karlsruhe Van-de-Graaff accelerator can be reproduced by the simulation. To this end the complete geometry with 42 individual detector modules including the 80 cm neutron flight path was linked to the GEANT code. The γ-response could almost perfectly be reproduced for monoenergetic γ-rays as well as for γ-cascades from neutron captures in various materials [Uhl93a,Uhl93b]. The response to keV neutrons was even sensitive enough to reveal small differences compared to the measured data due to superseeded barium cross sections in the data base of GEANT. In a second step the detector geometry and the neutron energy range were modified according to the different situation at a spallation source in order to study the corresponding neutron sensitivity as well as possibilities of background discrimination. It was found that the problem of neutron induced background can be solved by using a combination of neutron moderator around the sample and absorbers between the various modules. The count rate problem can be managed using higher detector granularity and advanced data acquisition systems.

[GEA93]	GEANT *Detector Description and Simulation Tool*, CERN (1993).
[Uhl93a]	M. Uhl and J. Kopecky, "Neutron capture cross section and gamma ray strength functions" in Nuclei in the Cosmos, eds. F. Käppeler and K. Wisshak (IOP, Bristol, 1993), pp. 259-266.
[Uhl93b]	M. Uhl private communications (1993).
[Wis90]	K. Wisshak, K. Guber, F. Käppeler, J. Krisch, H. Müller, G. Rupp, F. Voss, Nucl. Instr. Methods A292 (1990) 595.

The possible use of a 4π γ-detector at spallation sources

GEANT simulations

René Reifarth, Michael Heil, Franz Käppeler

Content

- Karlsruhe setup: simulations & experiments
- Simulations for the CERN neutron beam
- Possible improvements
- Other channels
- Conclusions

Karlsruhe setup

4π BaF_2 array at VdG

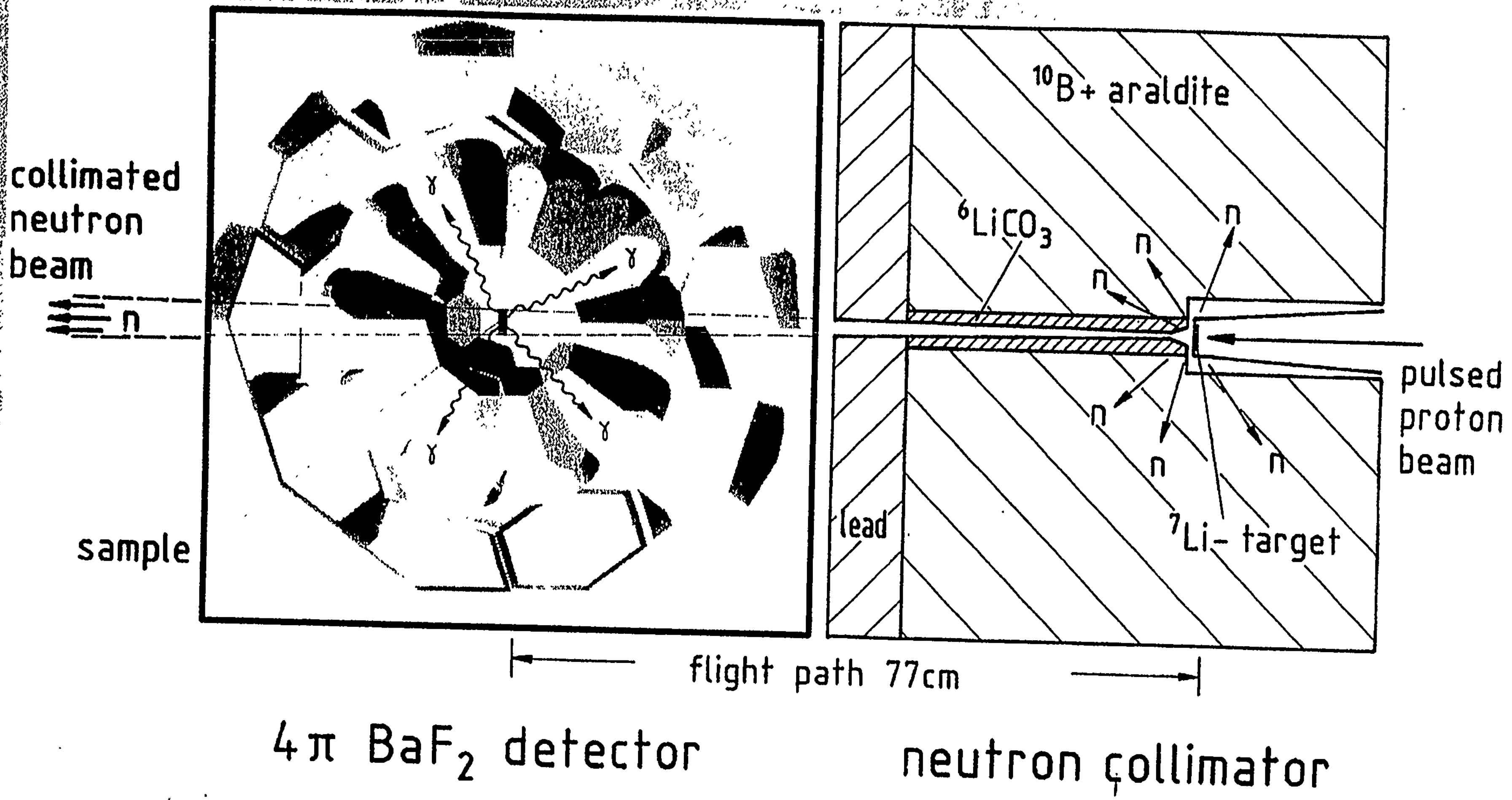

Simulated 4π BaF_2 detector

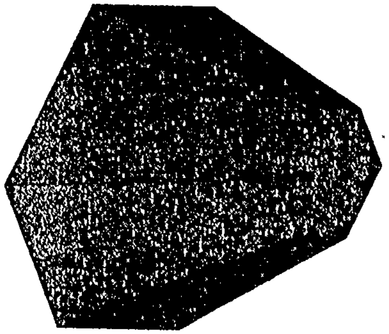

30 hexagons

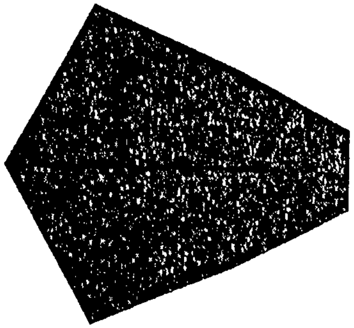

12 pentagons

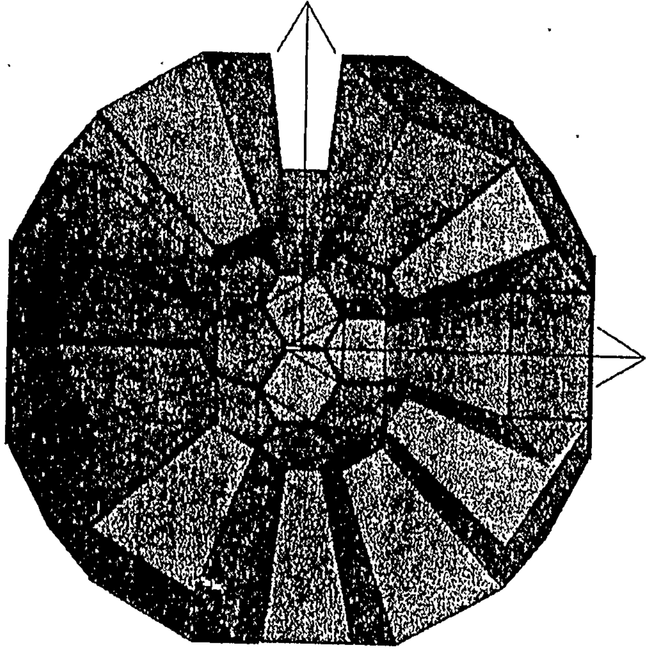

- equal solid angle
- 15 cm length
- 90 % total efficiency

Response to monoenergetic γ's

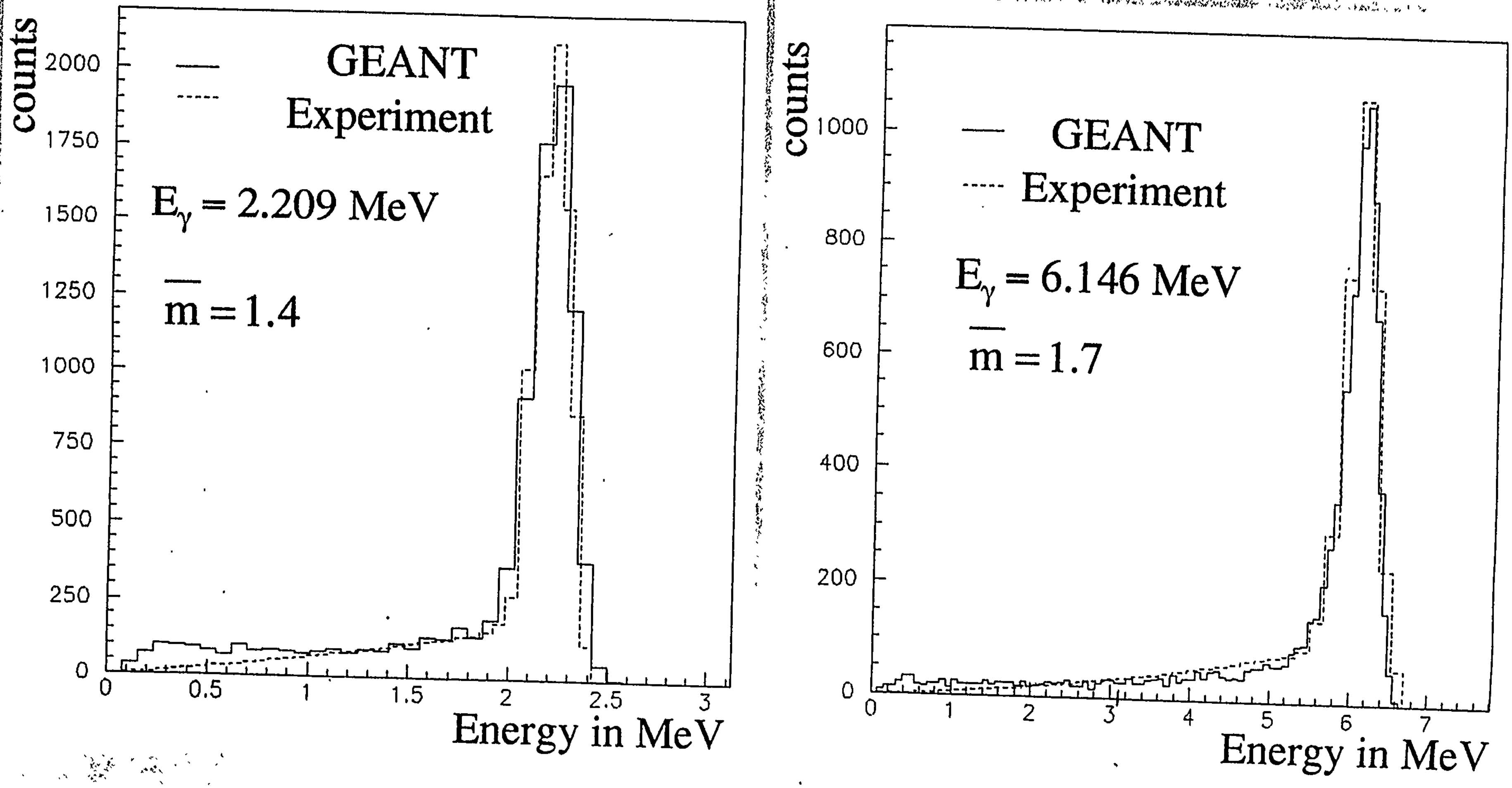

Karlsruhe setup

Response to ^{155}Gd(n,γ) cascades

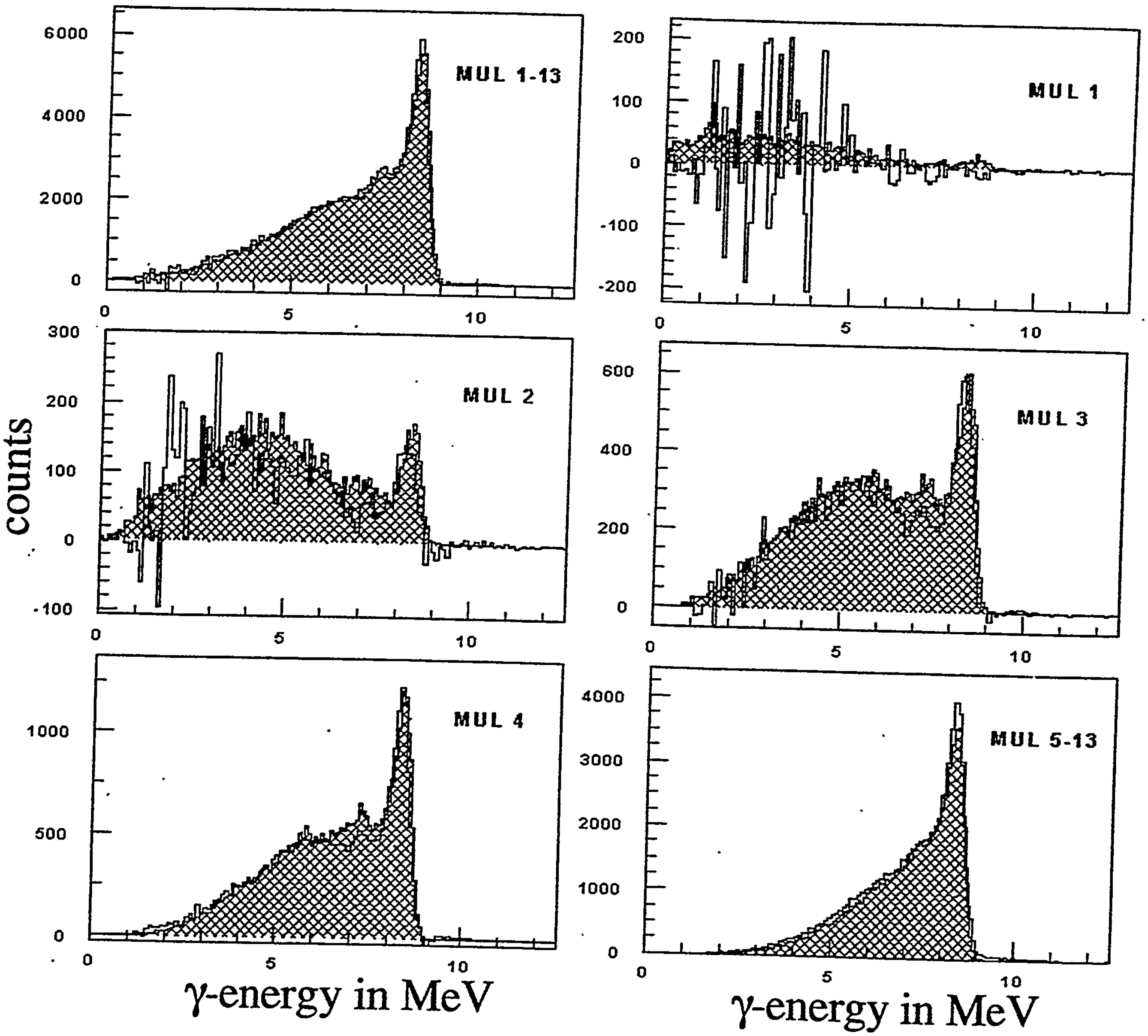

Karlsruhe setup

^{197}Au(n,γ)

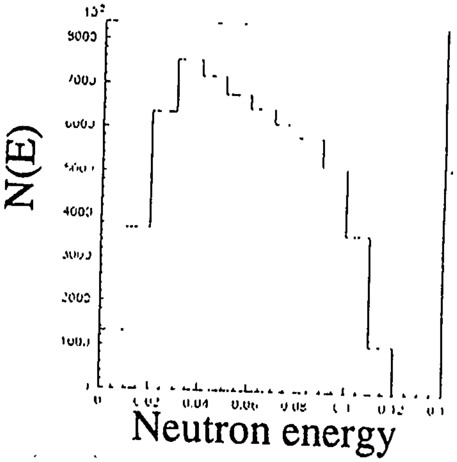

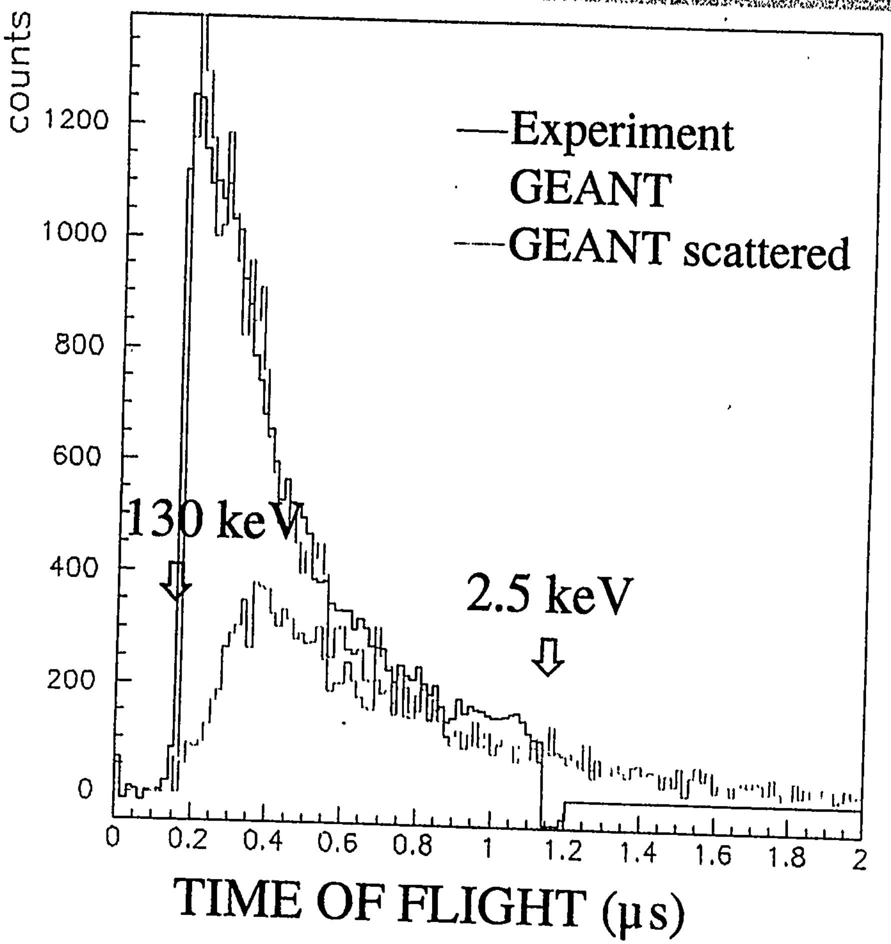

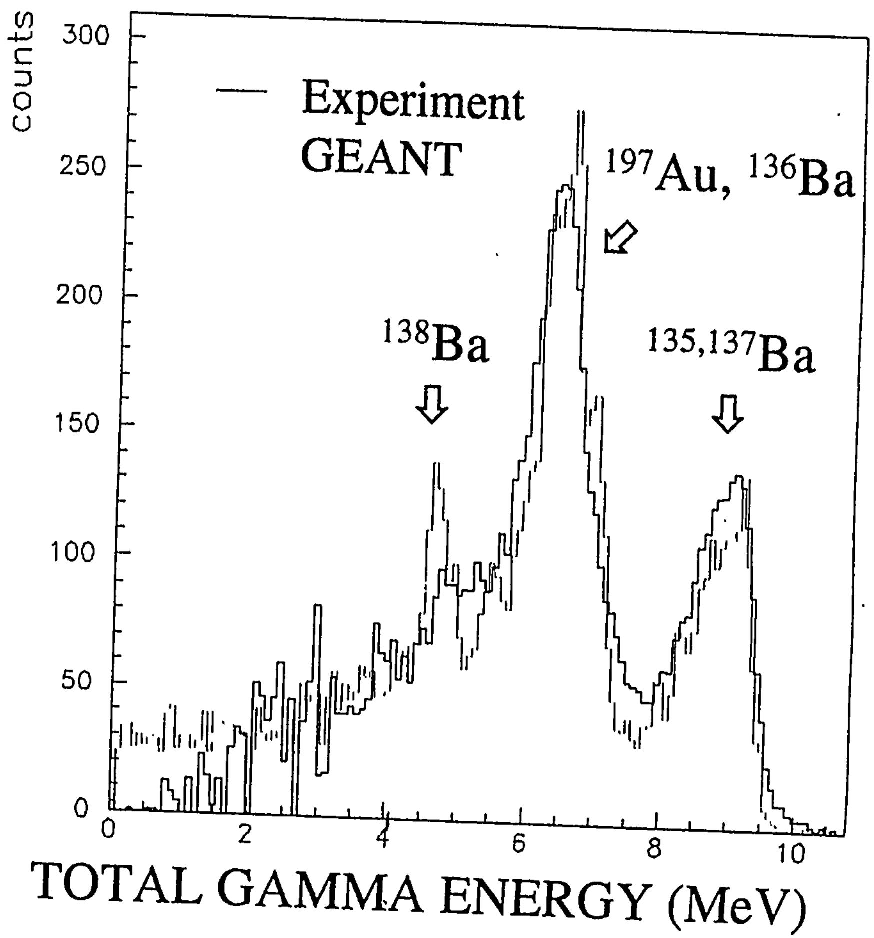

^{197}Au(n,γ) at CERN neutron beam

response to stellar neutrons , **5 g gold**

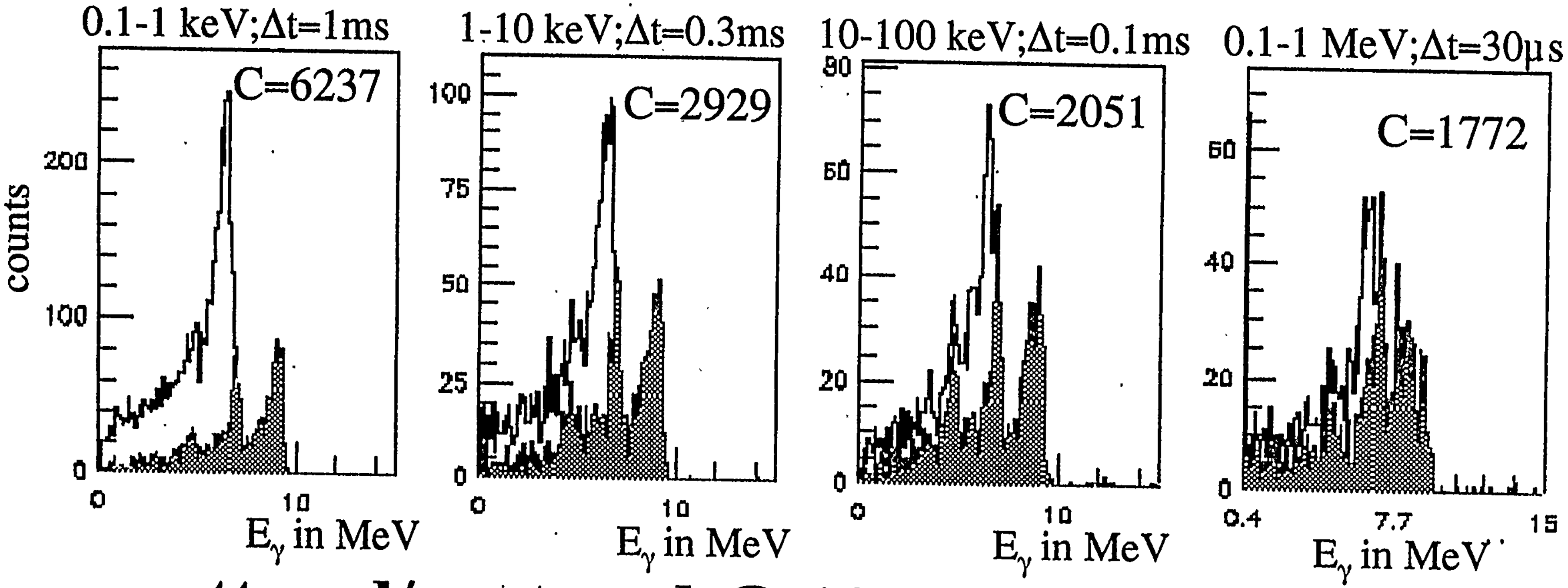

0.1-1 keV;Δt=1ms

1-10 keV;Δt=0.3ms

10-100 keV;Δt=0.1ms

0.1-1 MeV;Δt=30μs

scattered/captured @ 10 .. 100 keV : 1.54

100 μg gold sample possible

Karlsruhe setup

^{197}Au(n,γ) - TOF cuts

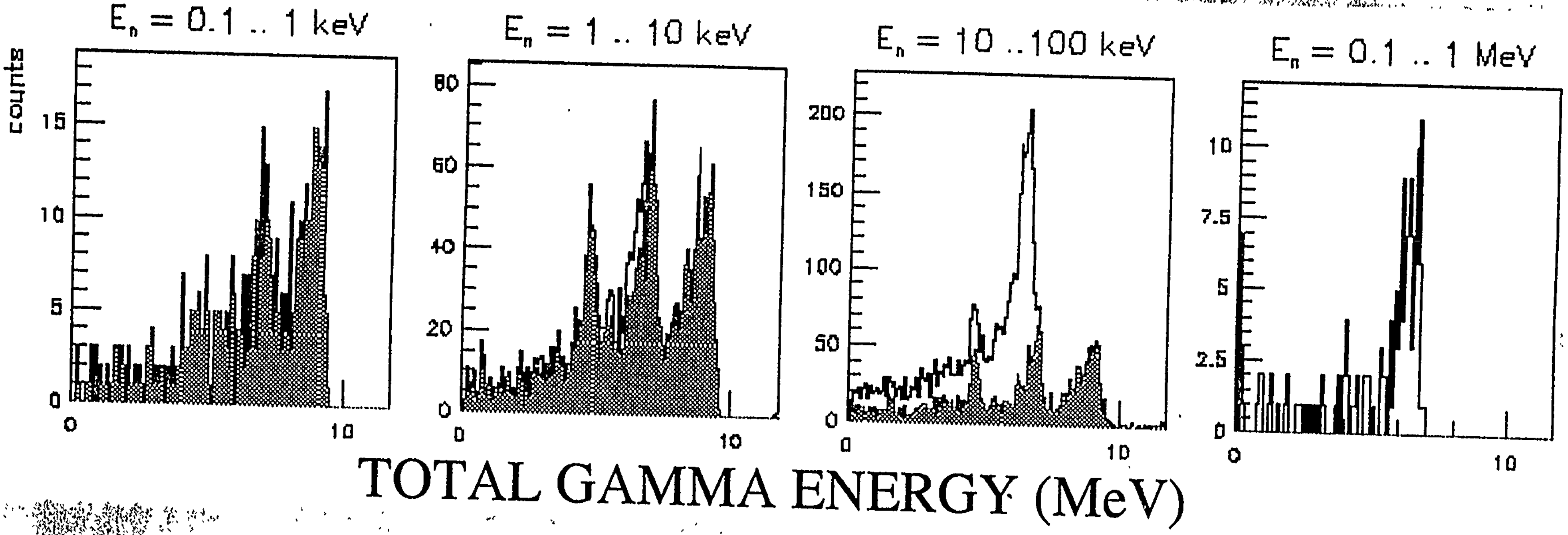

scattered/captured @ 10 .. 100 keV : 0.82

^{197}Au(n,γ)

response to high energy neutrons

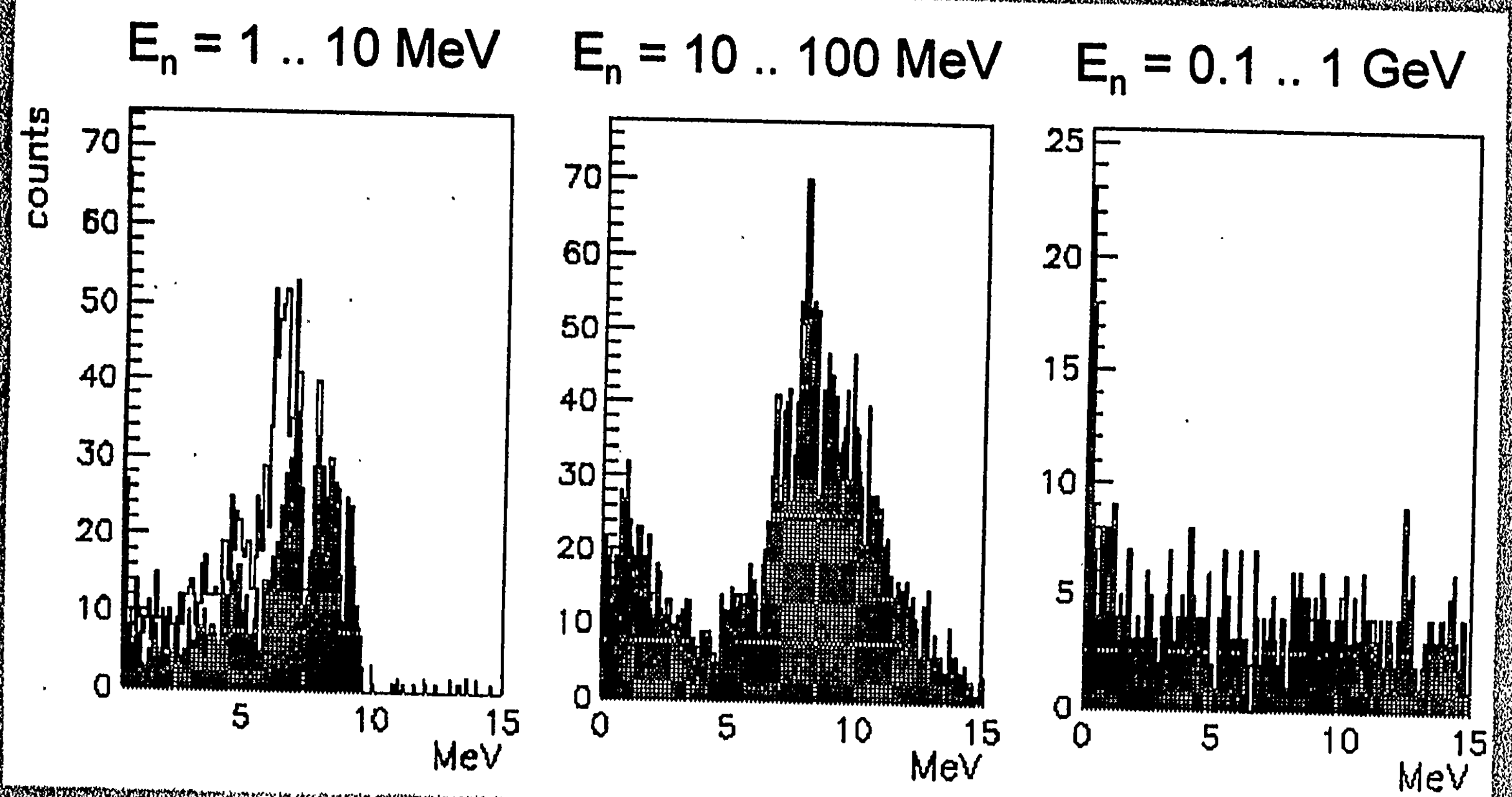

- no significant contribution to later TOF cuts
- no (n,γ), but (n,X)

Radial profile of beam (detector at 200m)

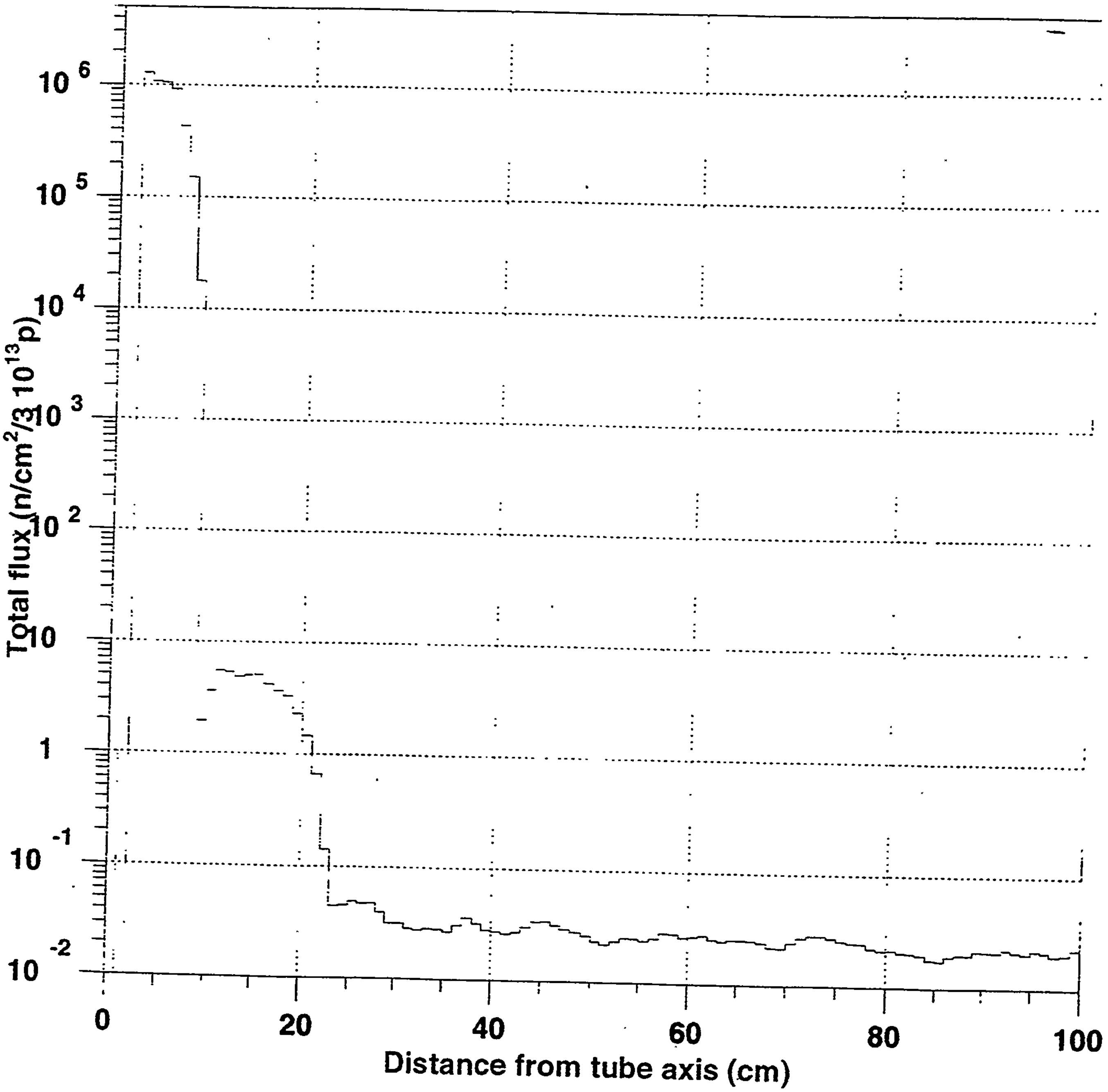

Influence of **BEAM HALO**

core diameter:	30 mm
halo diameter:	80 mm
flux ratio (core/halo):	$2 \cdot 10^5$
gold sample:	$100\ \mu g/cm^2 \cong 0.7$ mg

scattering background / Halo: 0.5

⇨ **Halo NOT negligible!**

for samples < 1 mg

Influence of **BACKING**

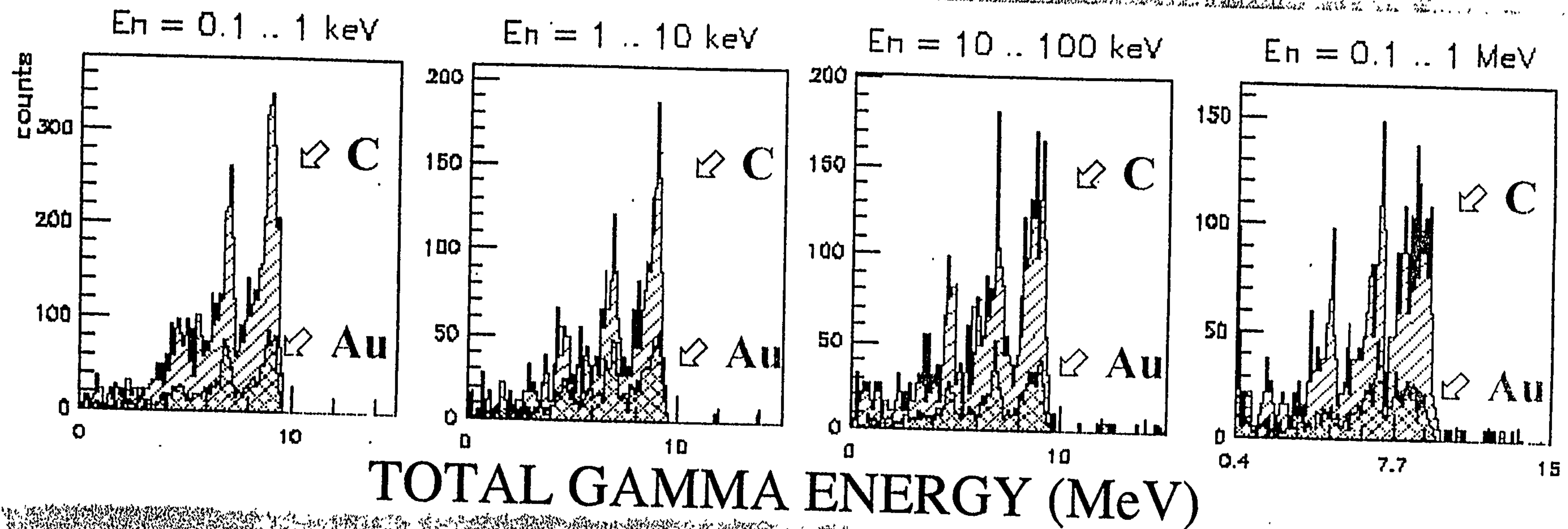

Gold sample: 100 µg/cm²
Carbon backing: 100 µg/cm²

backing/sample @ 10 .. 100 keV : 4.0

⇨ small sample diameters preferable

CeF_3 crystals

$^{197}Au(n,\gamma)$ CERN setup

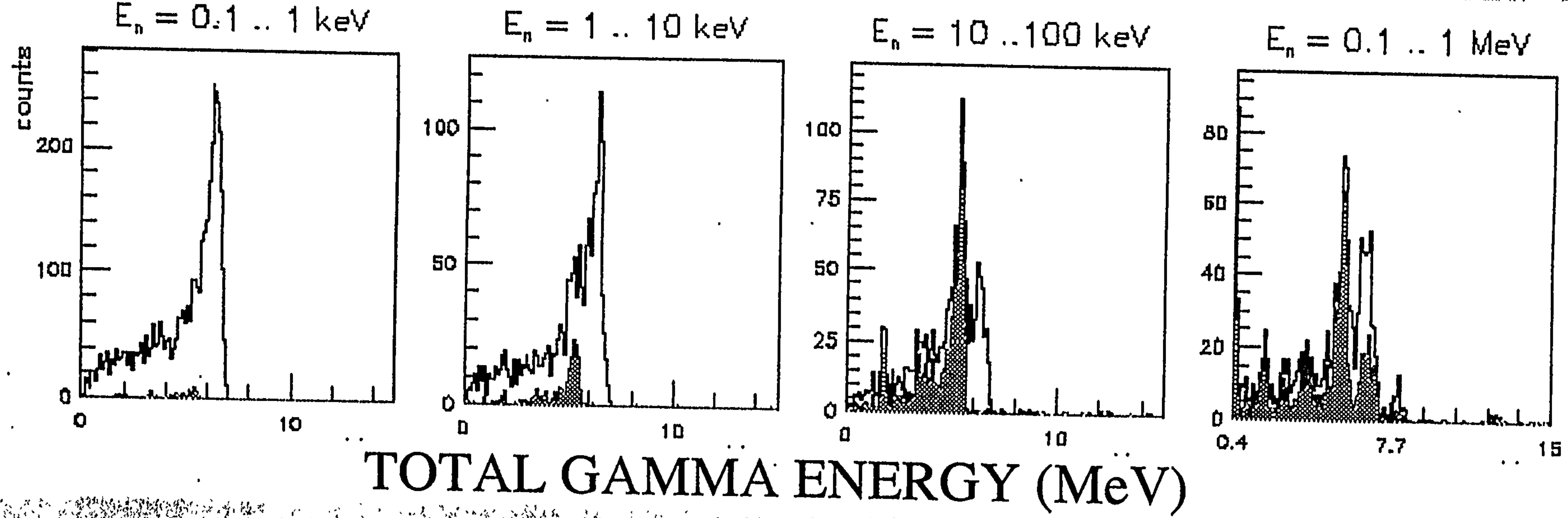

scattered/captured @ 10 .. 100 keV : 1,04

background reduction by **factor 1.5**

BaF_2: 1.54

But: no fast component!

Possible improvements

Moderator around sample

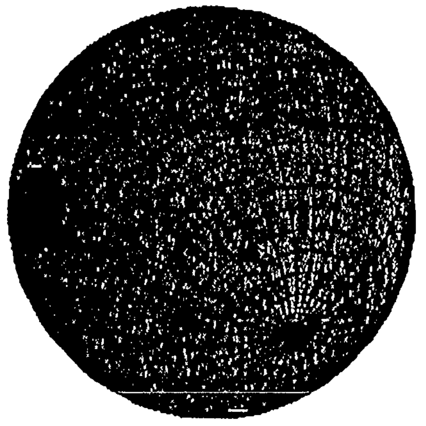

^{197}Au(n,γ), CERN setup, 6 cm ^{6}LiH sphere, BaF$_2$ array

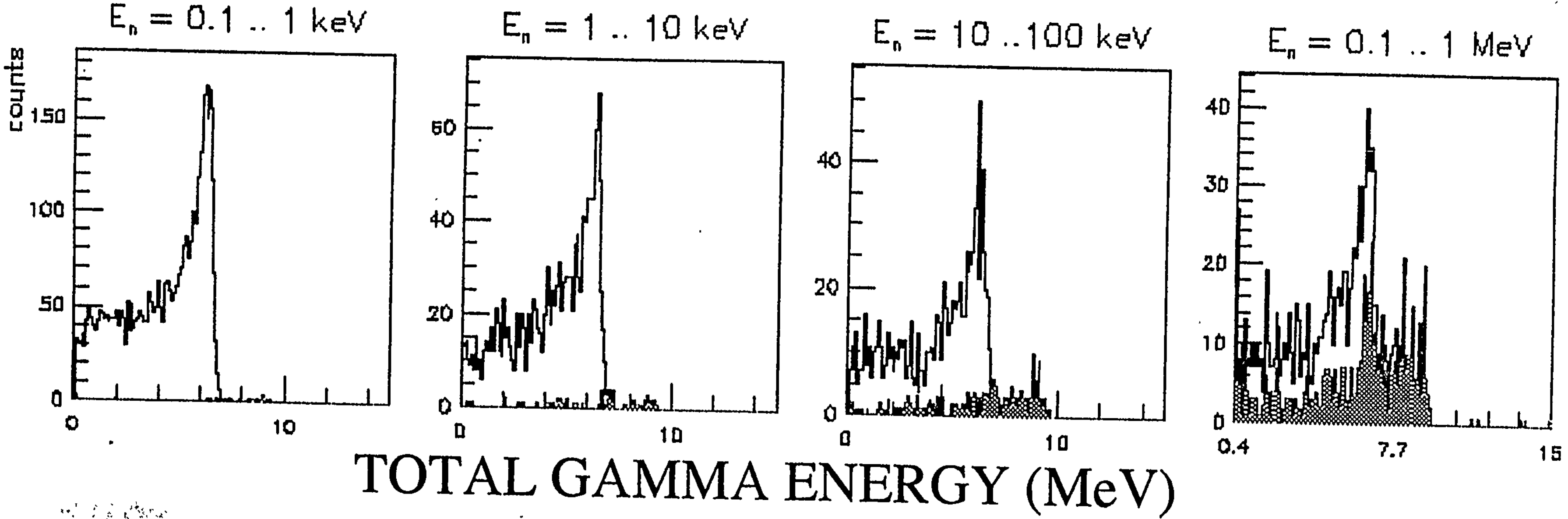

scattered/captured @ 10 .. 100 keV : 0.23

≈ 1.7 l **^{6}LiH** ≈ 1.4 kg ⇨ background reduction by **factor 7**

Possible improvements

Moderator around sample, ^{10}B layers between BaF_2 crystals

^{197}Au(n,γ), CERN setup, 6 cm ^{6}LiH, 1.8 mm ^{10}B

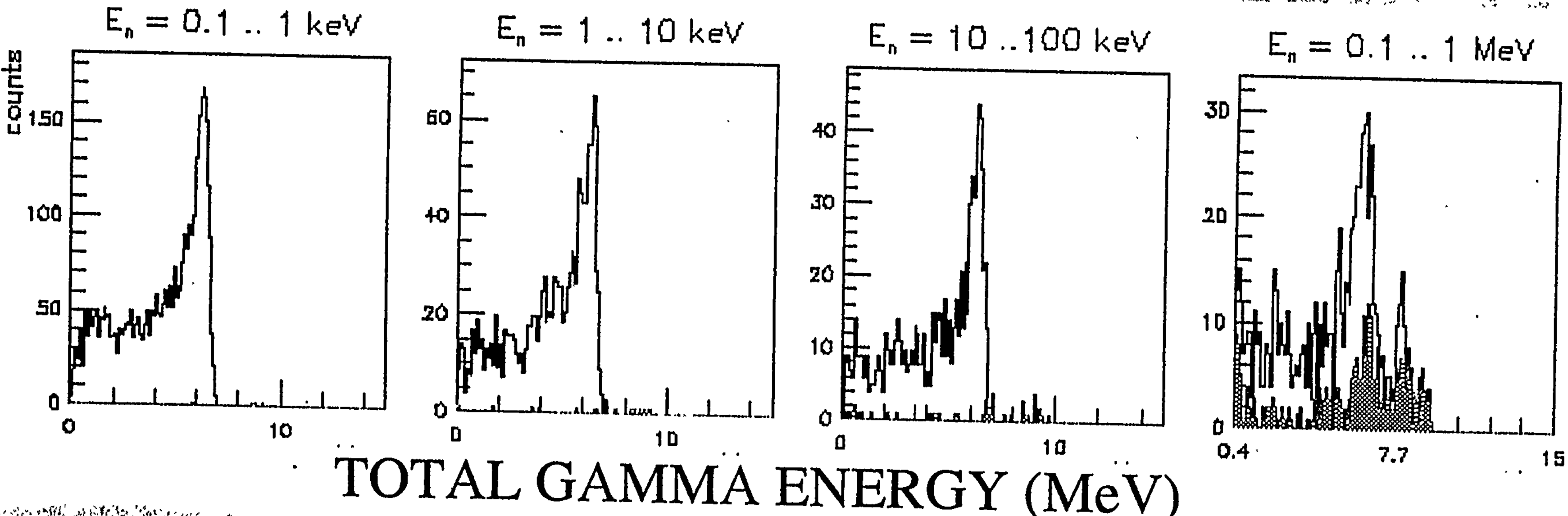

scattered/captured @ 10 .. 100 keV : 0.058

≈ 1.8 l **^{6}LiH** & 1.7 l **^{10}B** ⇨ background reduction by **factor 25**

Possible improvements

Higher granularity

162 crystals instead of 42

👍

- Count rate reduction per crystal: factor 2.7
- 6 cm ^{6}LiH & ^{10}B more efficient: factor 1.3

👎

- More PM
- More electronics

Summary

Setup	Scattered / Captured
• 42 crystals BaF_2	1.5
• 42 BaF_2 with 6 cm ^6LiH	0.23
• 42 BaF_2 with ^6LiH and ^{10}B	0.058
• 162 BaF_2 with ^6LiH and ^{10}B	0.044
• CeF_3	1.0
• 162 modules C_6F_6 (60 cm)	0.036

Neutron induced fission

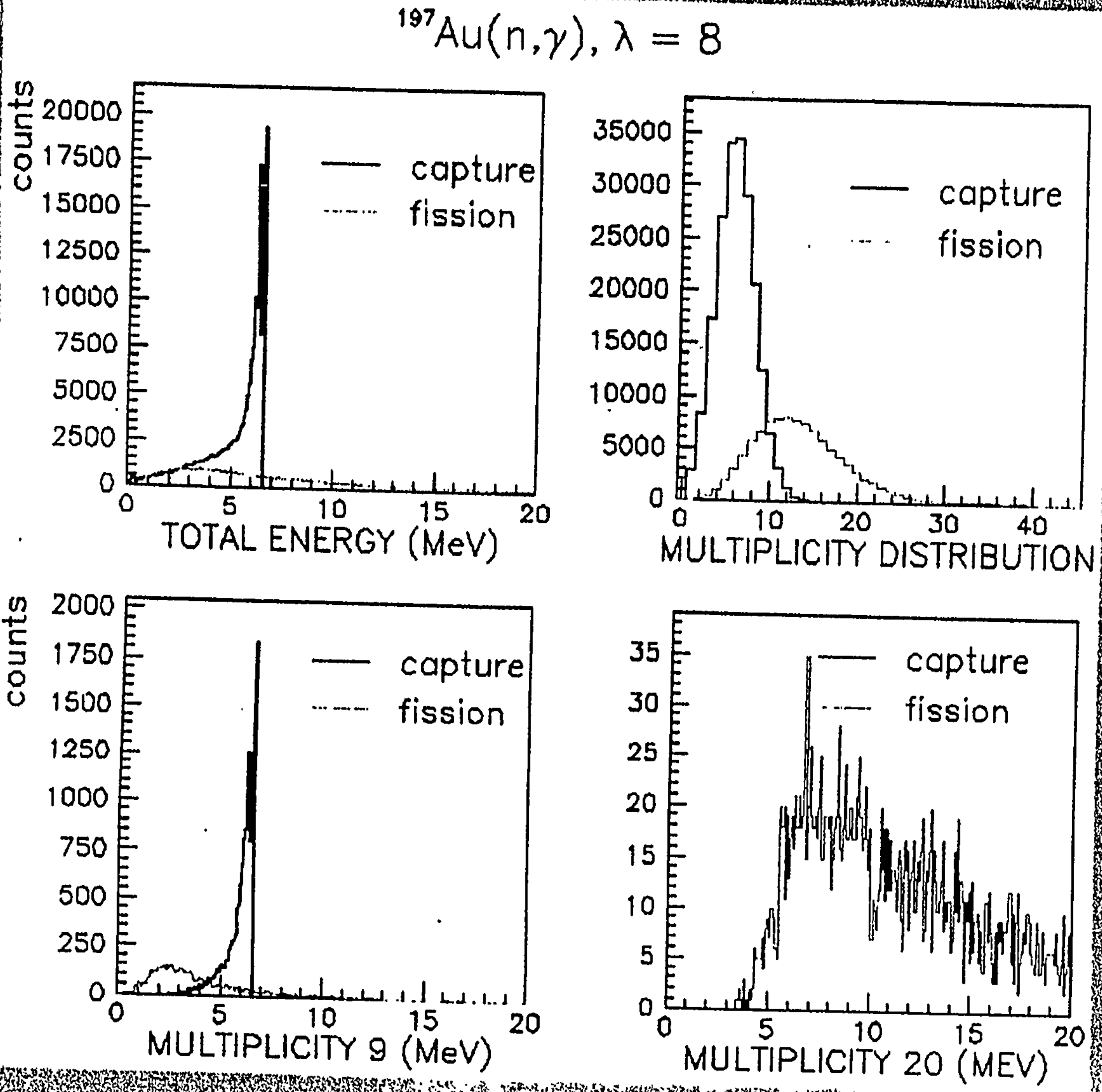

- $\sigma_{capture} = 1.5\ \sigma_{fission}$
- sample centered in the detector
- *energy & multiplicity cuts possible*

Conclusions

- 4π γ-detector **CAN BE USED** at spallation sources
- background from scattered neutrons can be handled, reduction by factor 25 possible (LiH, B)
- efficient tool also for other channels
- quality of neutron beam **crucial**, halo $< 5 \cdot 10^{-6}$!

Plans for Measurements at Oak Ridge

Paul Koehler
Oak Ridge National Laboratory

Plans for neutron measurements at ORELA will be discussed. Both neutron capture cross sections and (n,alpha) reactions will address s process and p-process nucleosynthesis.

“ORELA” Astrophysics

- Some Relevant Astrophysics
- The ORELA Facility
- Near Future Plans

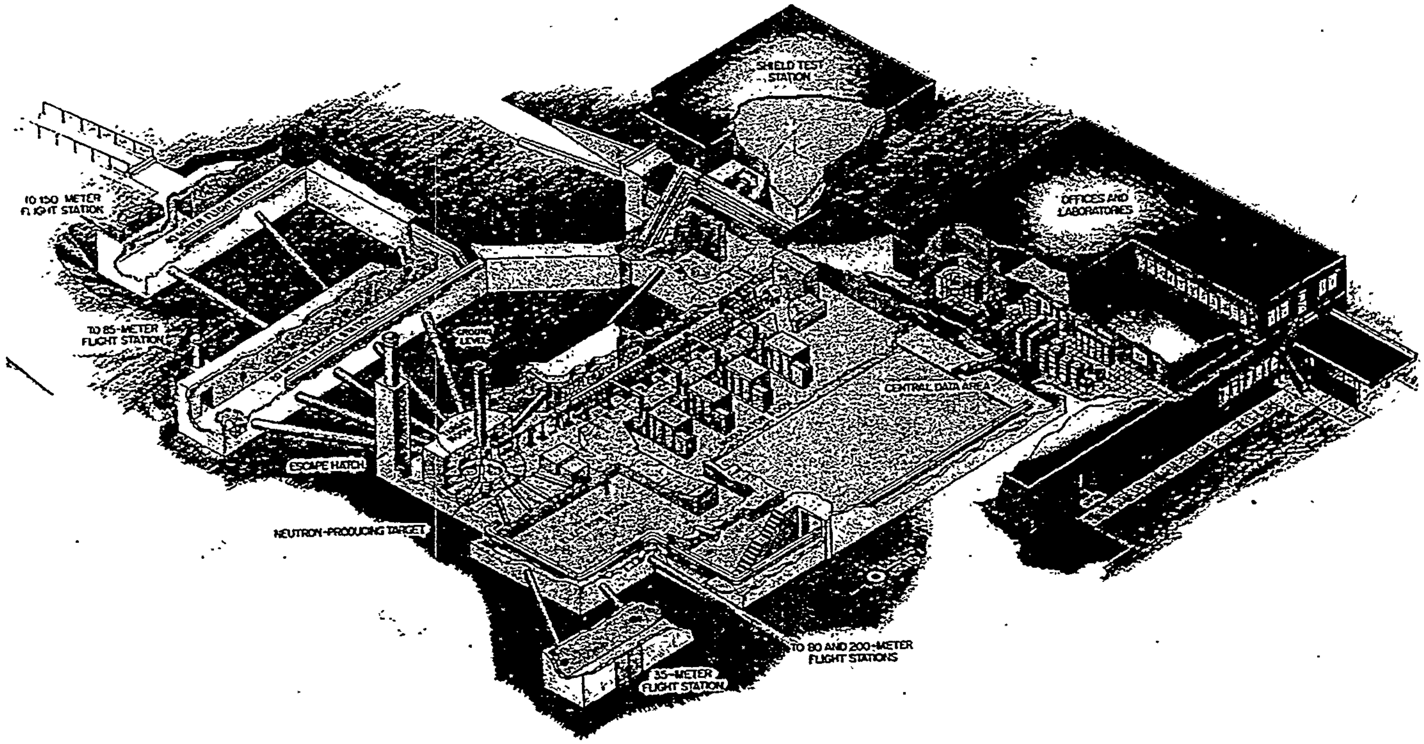

Collaborators

Klaus Guber
Bob Spencer
Ron Winters
Jack Harvey
S. Raman
Tommy Rauscher
Yuri Gledenov
Jozef Andrzejewski
John Becker
Dan Bardayan
Jeff Blackmon
Nat Hill
Duane Larson
T.A. Lewis
Don Pierce
Michael Smith

ORNL, Physics
ORNL, CPED
Denison University
University of Basel
JINR, Dubna, Russia
LLNL
University of Lodz, Poland
Also at Yale University

The Need for (n,γ) Data at Lower Energies

- **Isotopes with small cross sections.**

  Because level density low, a few low-energy resonances can have large effect on rate.
  If reaction rate is small, not reset by small exposure from $^{22}\mathrm{Ne}(\alpha,n)^{25}\mathrm{Mg}$.
  Small cross sections have "lever arm" effect, so need to be known to high precision.

- **Isotopes where high precision needed.**

  ***s*-only isotopes.**
  Isotopes near branchings.
  Meteoric anomalies.

The Red Giant Stardust Model

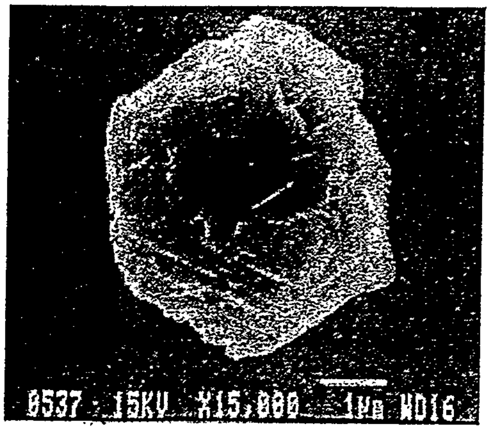

SiC grain from the Murchison meteorite.

- Microscopic grains of refractory materials (e.g. SiC) found in certain meteorites appear to be stardust.

  Carry nucleosynthesis signature of stars where they formed.

  Measured isotopic patterns for main and trace elements are very non-solar.

  Increase number and precision of calibration points for stellar models.

Need new neutron capture data with higher precision and to lower energies to use these stardust data to improve stellar models.

Possible *(n,n')* Experiments at ORELA

- Many nuclides in rare earth region have low lying excited states which would be populated in the stellar environment of the *s* process.

  ^{145}Nd(67), ^{147}Sm(50), ^{149}Sm(22), ^{151}Eu(22), ^{153}Eu(83), ^{155}Gd(60), ^{156}Gd(89), ^{157}Gd(54),^{158}Dy(99), ^{158}Gd(79), ^{159}Tb(58), ^{160}Dy(87), ^{161}Dy(26), ^{162}Dy(81), ^{163}Dy(73), ^{164}Dy(73), ^{165}Ho(95), ^{166}Er(80), ^{167}Er(79), ^{168}Er(80), ^{169}Tm(8.4), ^{170}Yb(84),...

- Neutron capture on these excited states would result in a reaction rate different from the terrestrially measured value.

- Can reliably calculate this effect if ground state capture, elastic, and inelastic cross sections are known. Missing link is inelastic/elastic ratio.

- Systematic study is needed to identify cases where there are significant differences between models, especially for *s*-only isotopes.

Effect of Capture on Excited States

- Example: Dy isotopes from Voss *et al.*
- Possible independent *s*-process thermometer.
- Need systematic study to identify discrepancies between theories, especially for *s*-only isotopes.

Stellar Enhancement Factors (SEF) for Dy Isotopes

Isotope	% Abundance	SEF_1	SEF_2	E_x
156	0.057	1.046	1.035	0.138
158	0.10	1.273	1.075	0.080
160	2.34	1.109	1.113	0.087
161	18.91	0.996	0.906	0.026
162	25.5	1.156	1.088	0.081
163	24.9	0.992	0.980	0.073
164	28.2	1.174	1.107	0.073

Summary: *s*-process Data Needs

- (*n*,γ) data needed at lower energies.
  Many old and new cross sections don't go to energies low enough for new stellar models.
- (*n*,γ) data needed to higher precision.
  For *s*-only calibration points.
  Near branchings.
  For meteoric anomalies.
- (*n*,γ) data needed for radioactive branch points.
- Data needed on neutron source reactions.
- Data needed for capture on excited states.

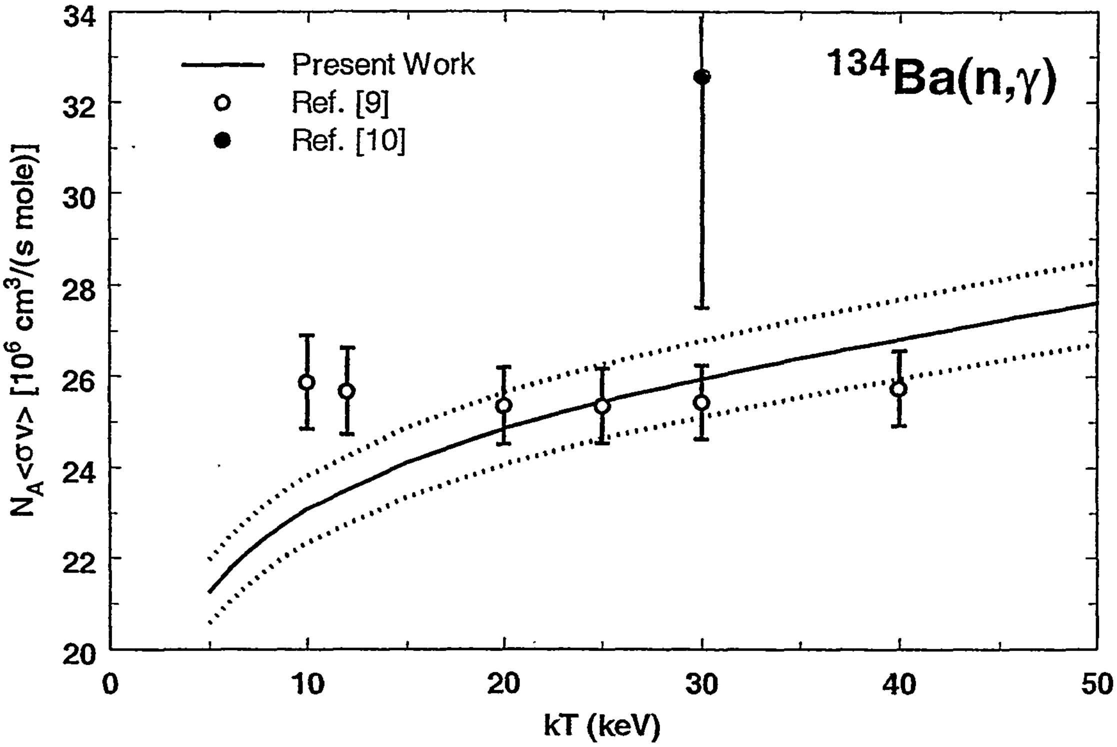

Problems with the *p*-process

- Parametric Studies => $T_9 \sim 1\text{-}3$, $t \sim 1$ sec, $\bar{\rho} \sim 10^6$ g/cm^3.
- Stellar models:
  O/Ne layers of pre-SN stars.
  Type-II SN explosions (II, II-L, II-p).
  Type-I SN explosions(Ia or Ic).
  X-ray bursters.
- Largest nuclear physics uncertainty: rates for (γ,α) and (α,p) reactions.
  1) Very difficult or impossible to measure.
  2) Poorly constrained by theory.

A series of (n,α) measurements could reduce these uncertainties considerably.

The Need for (n,α) Data

(n,α) Measurements

Improved Nuclear Models

Better (γ,α), (α,p) Reaction Rates

Tighter Constraints on p-process Environment

Better Understanding of Supernovae, Novae, Meteoric Anomalies, ...

The Oak Ridge Electron Linear Accelerator (ORELA) Facility

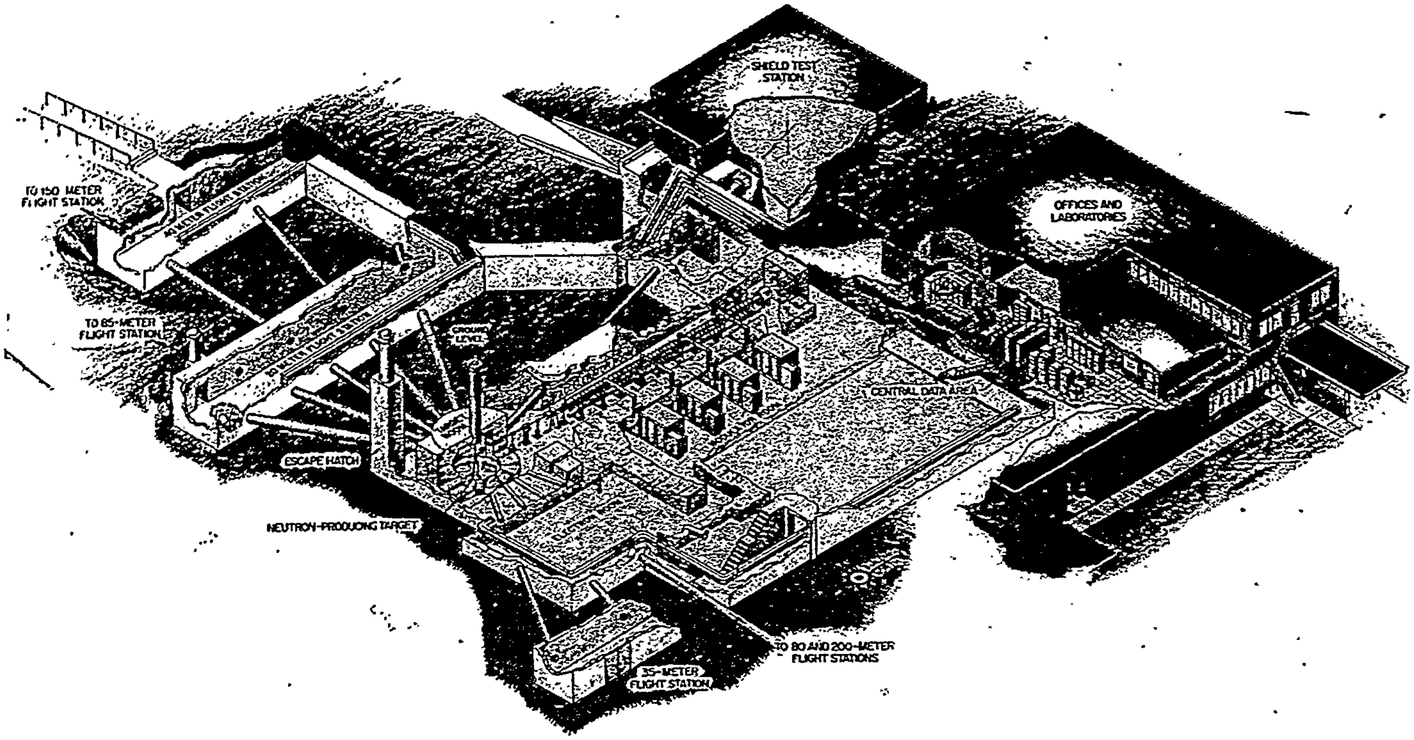

- **High flux (10^{14} n/sec) => gram-sized samples.**
- **Excellent resolution (Δt=4-30 ns) => good S/N.**
- **Simultaneous measurements => (n,γ), (n,α), (n,n'), and σ_{total} experiments at the same time on different beam lines.**
- **"White" neutron spectrum => E_n ~ 0.01 eV - 80 MeV.**
- **E_n via time-of-flight.**
- **Systems well understood => precise data.**

Neutron Capture and Total Cross Section Experiments at ORELA

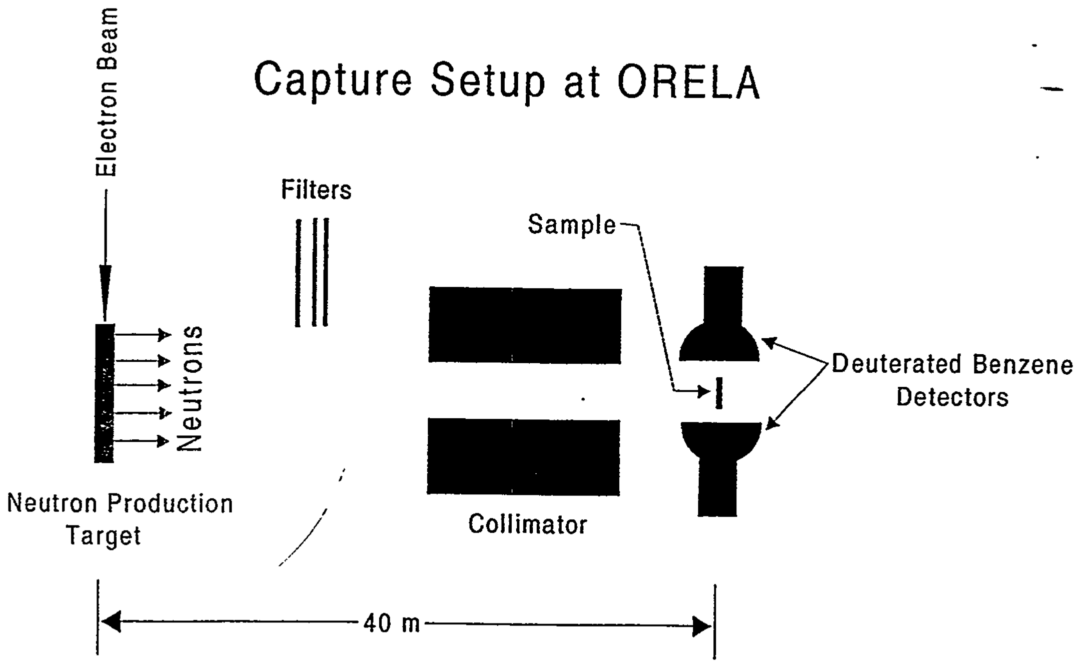
Capture Setup at ORELA

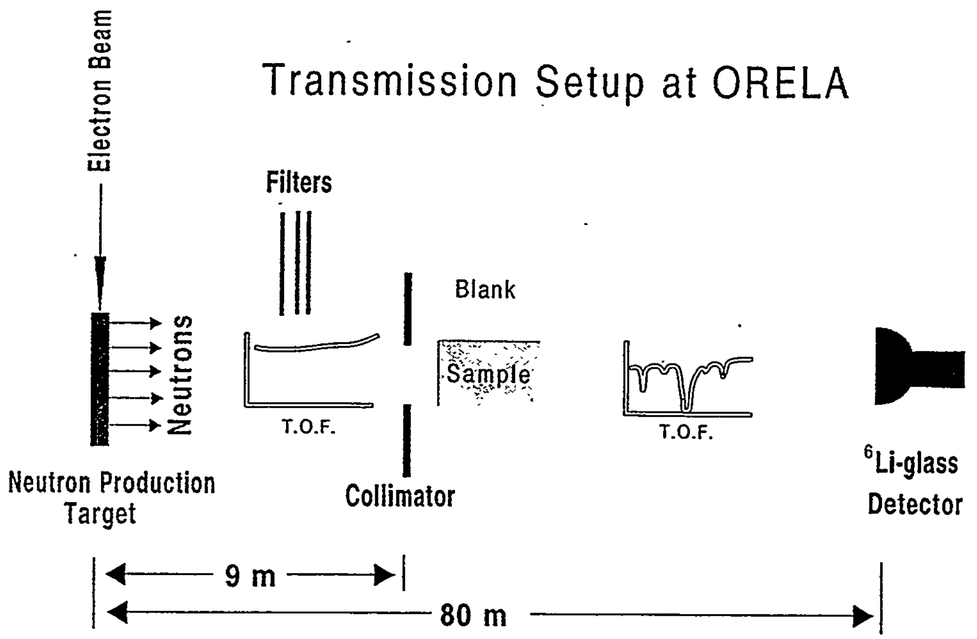
Transmission Setup at ORELA

^{137}Ba Capture and Transmission Data from Our ORELA Experiment

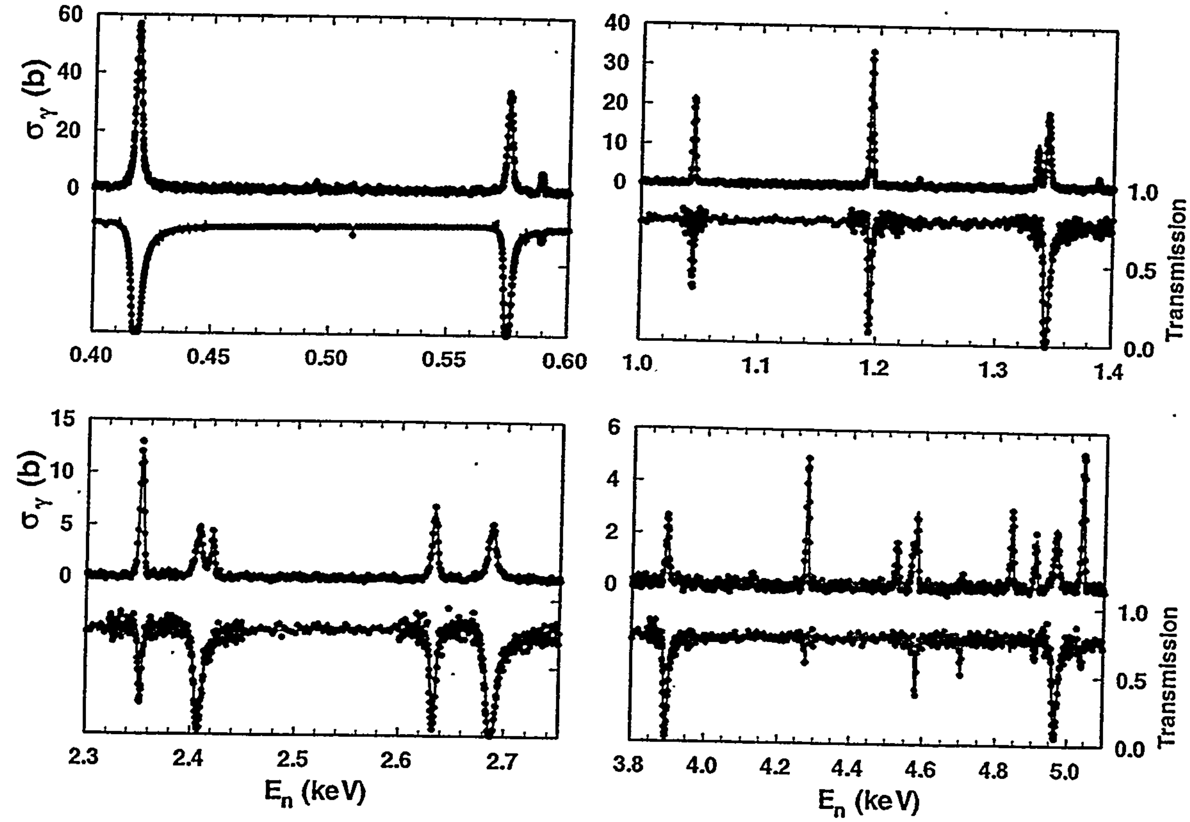

BA137CTA Sept. 30, 1997 8:11:25 AM

- Used Sammy to determine E, Γ_γ, Γ_n for 143 resonances between 100 eV and 20 keV (as well as several *l* and J^π assignments).

BaF_2 Detector at ORELA

- Setup consists of 12 optical isolated detectors with hexagonal shapes (140mm x 86.6mm)
- The detector covers nearly 90% of the solid angle. ΔE/E is 7.6% for the 6.13 MeV γ-ray line with an efficiency of ~30%
- Approx. 20 times smaller sample.

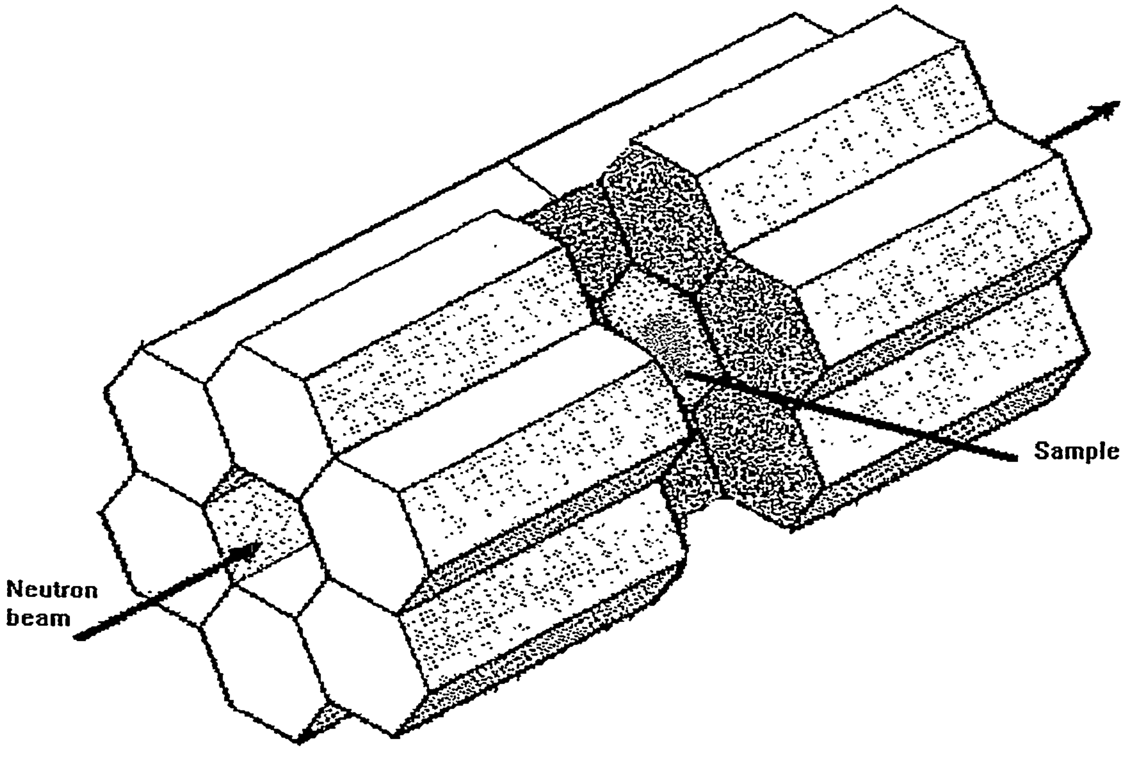

BaF_2 (n,γ) Data from ORELA

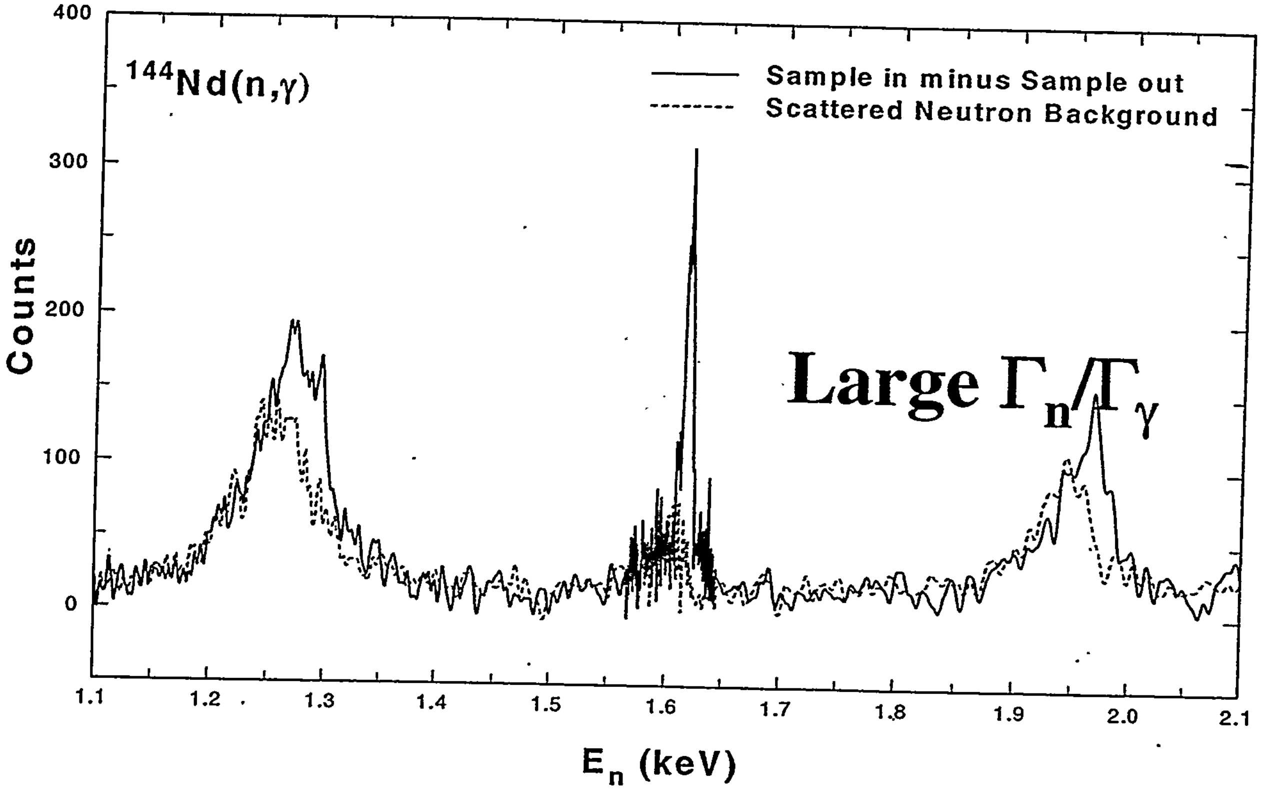

Large Γ_n/Γ_γ

- By using a scattering sample the effect of sample scattered neutrons can be simulated (dashed line). Together with the good TOF and pulse-height resolution the data can be corrected. This background is only sizable for resonances with large scattering to capture ratio.
- Could be further improved with better detector design.

BaF$_2$ (n,γ) Data from ORELA

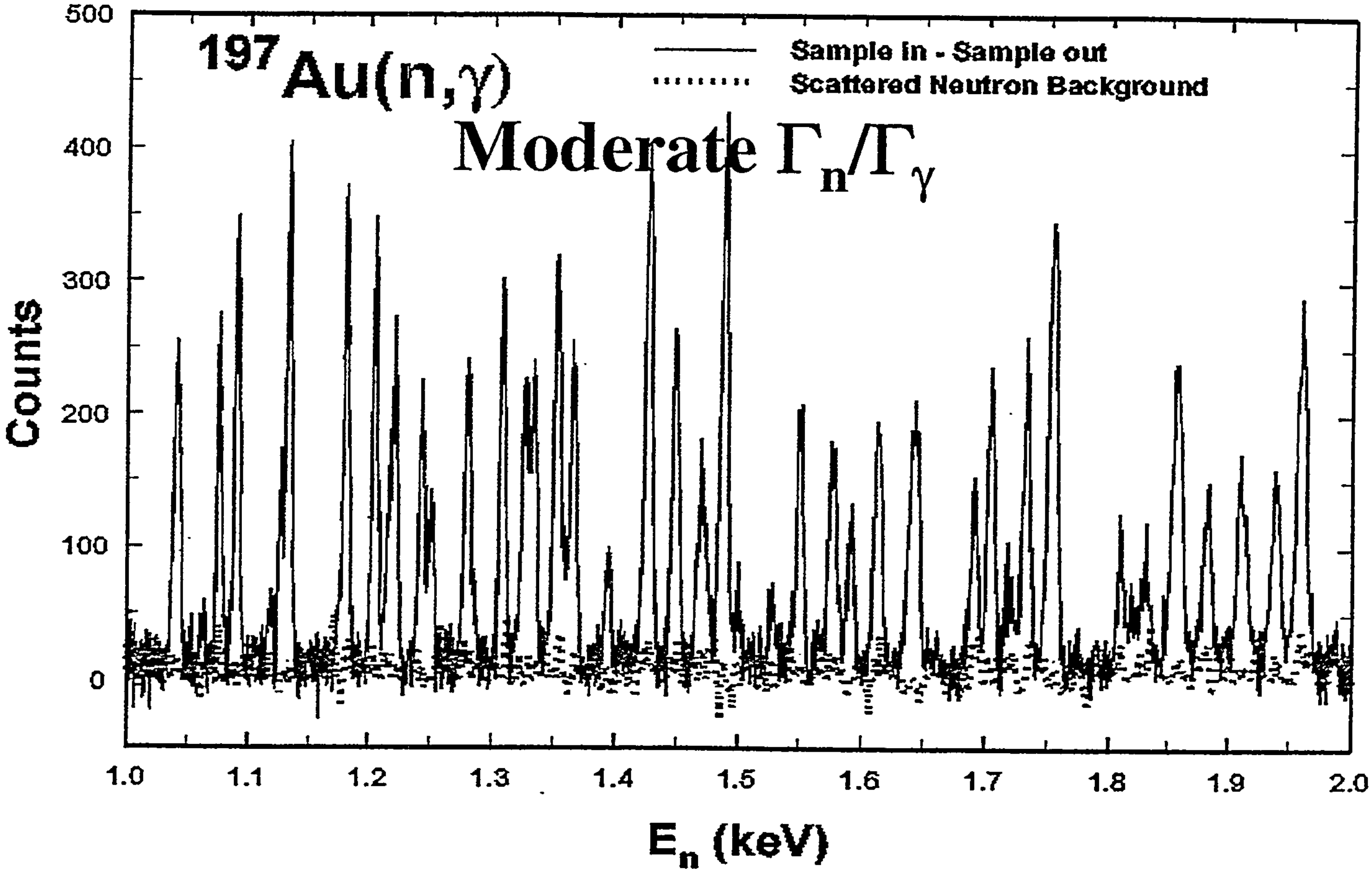

Proof-of-principle experiment completed. Needs work to become "production" facility.

(*n*,α) Experiments at ORELA

Setup for (n,α) Experiments at ORELA

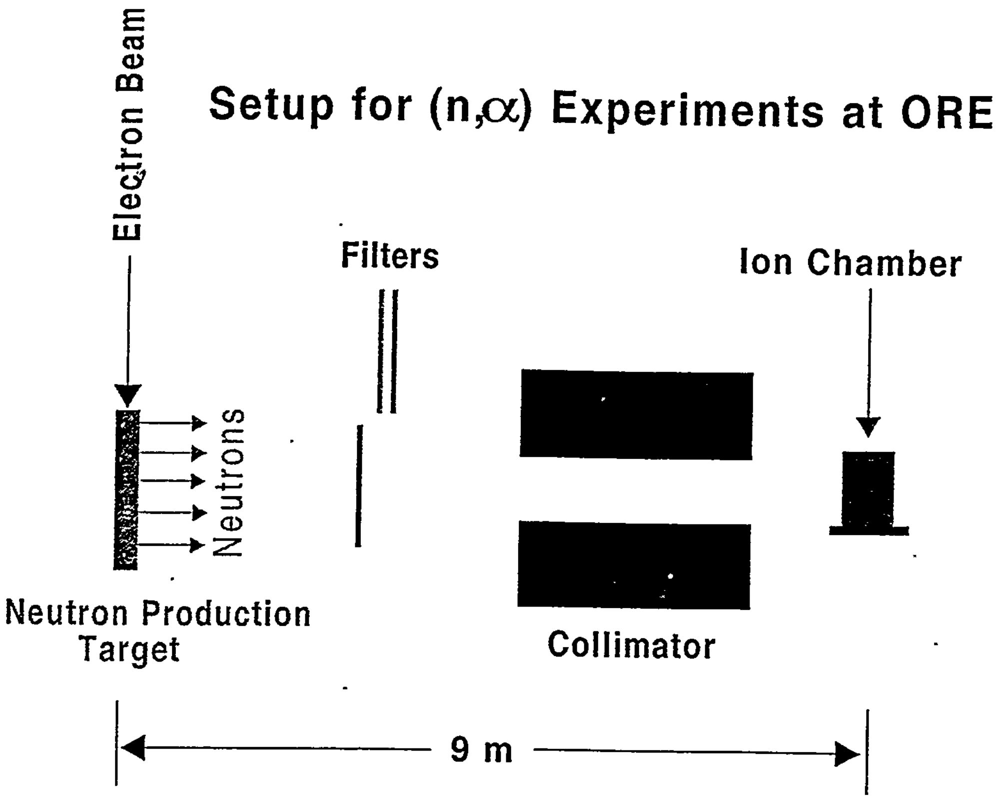

Compensated Ionization Chamber

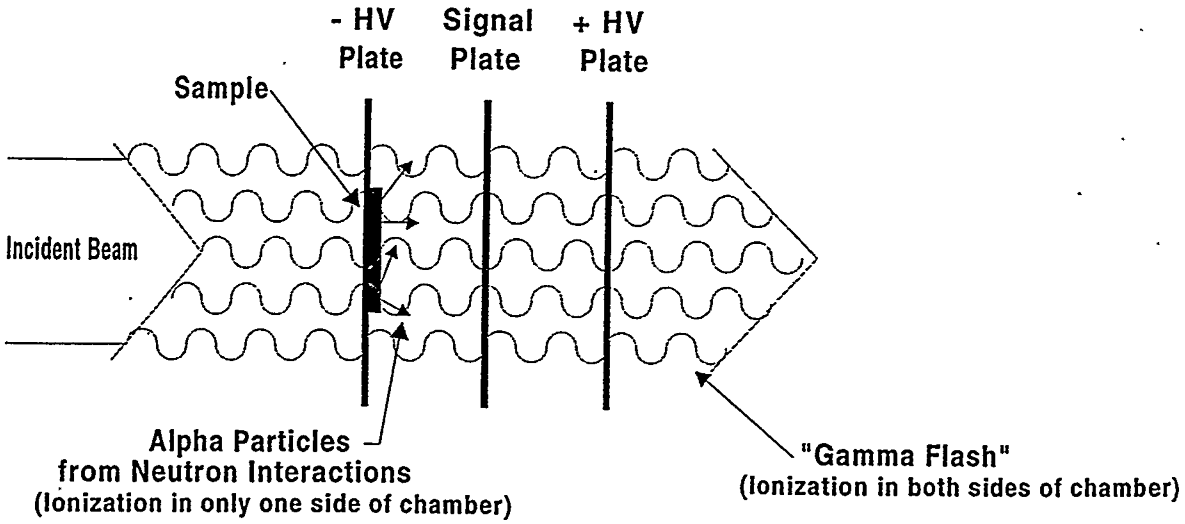

New ^{147}Sm(n,α) Data from ORELA

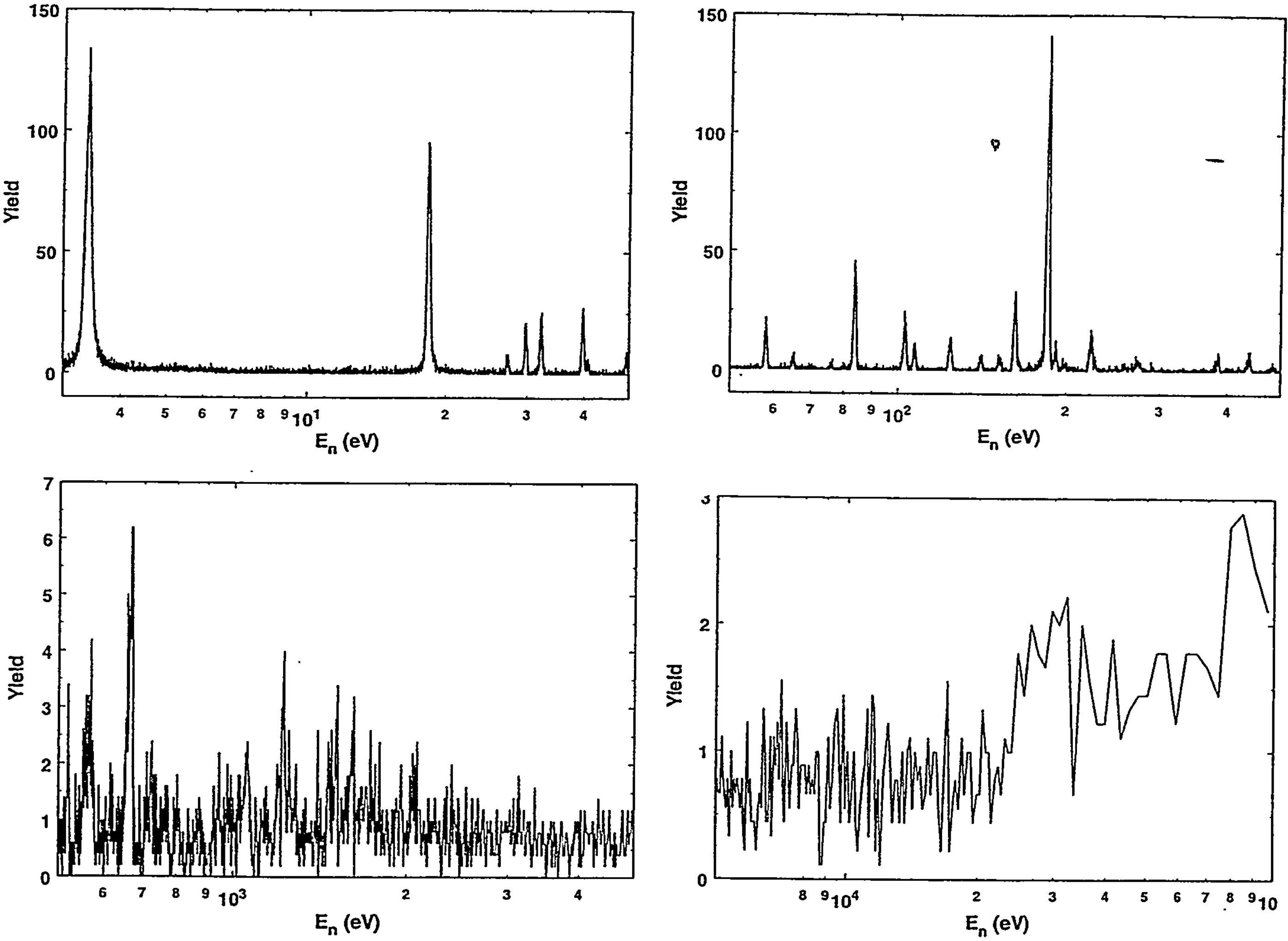

Demonstrates proof-of-principle of large CIC (also data on ^{59}Ni (n,α)).

Many more (n,α) measurements possible across wide mass range.

(*n,n'*) Experiments at ORELA

Setup for (*n,n'*) Experiments

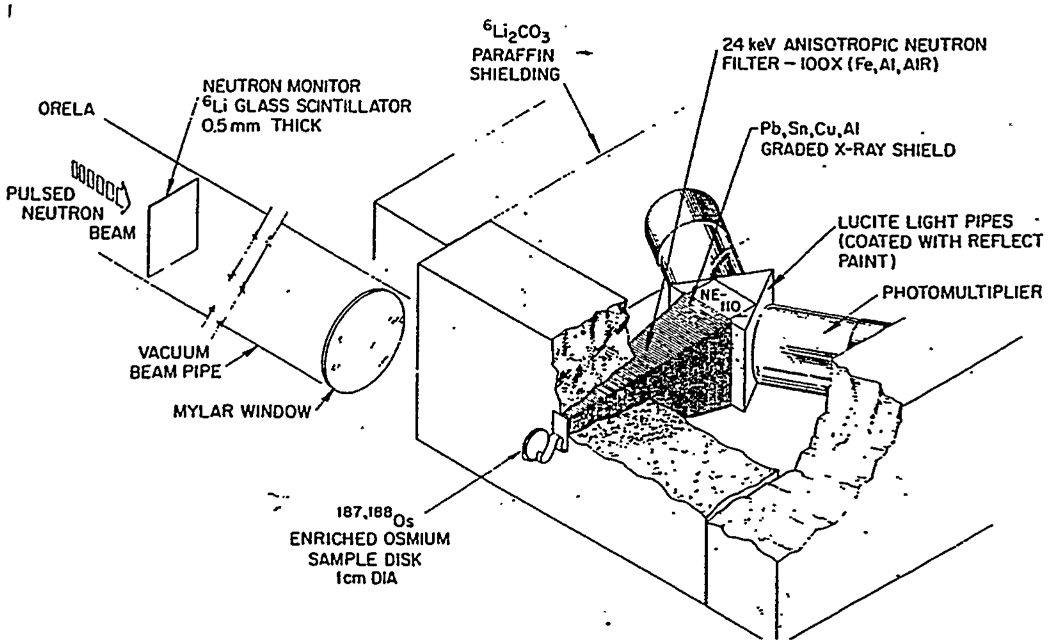

Experimental Result

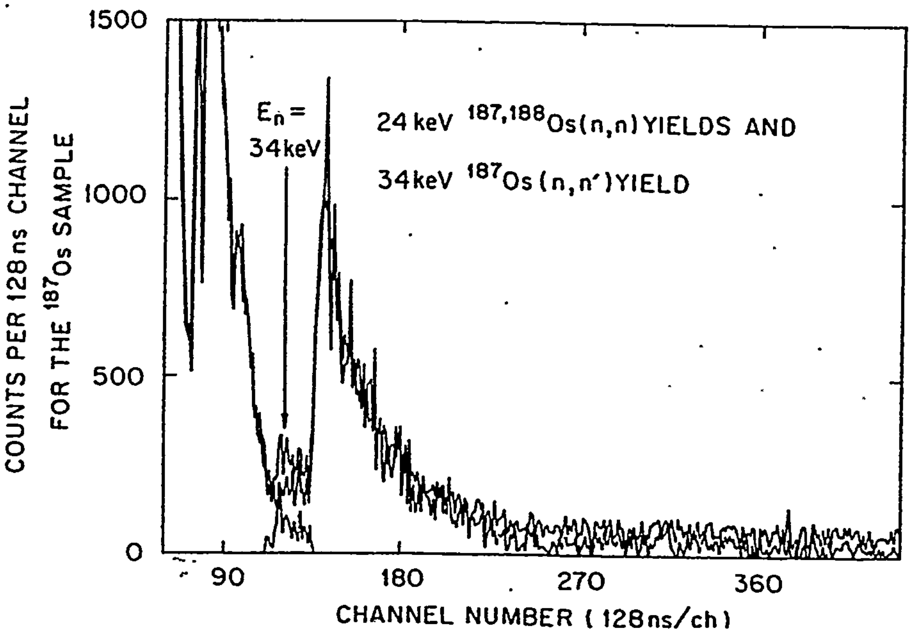

(*n*,*n'*) Experiments at ORELA

AlternativeSetup for (*n*,*n'*) Experiments

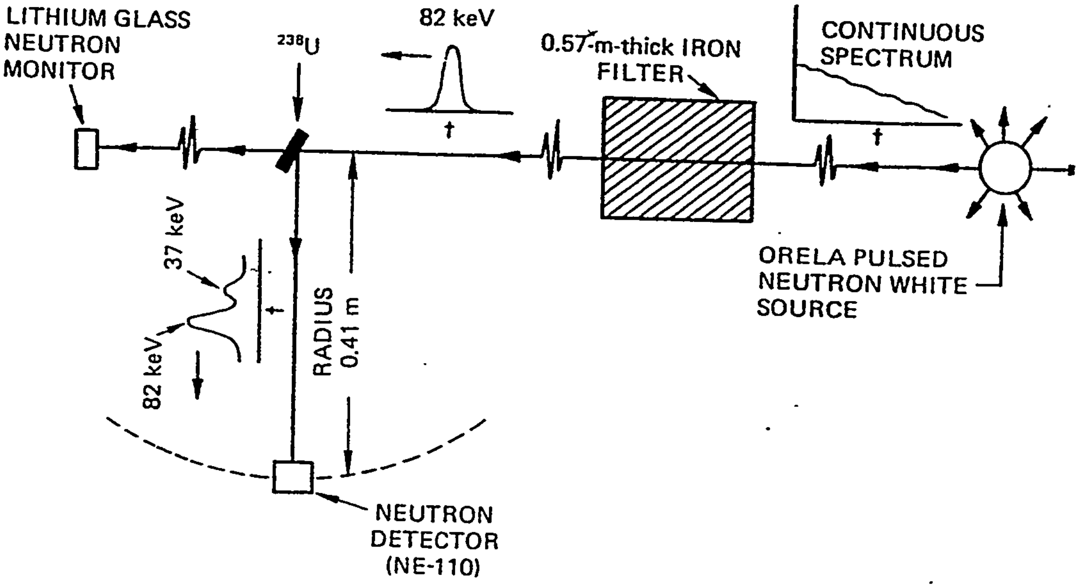

Experimental Result

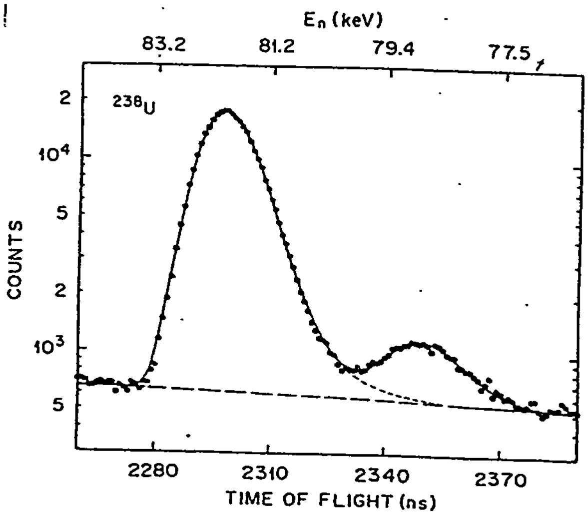

ORELA Facility (Continued)

- Operates on a "Full Cost Recovery" Basis.
- Operation:

FY96	1,214 hrs.
FY97	1,140 hrs.
FY98	1,482 hrs.

- Reliable.
  92% Availability Factor.
  Operates at or Above Original Acceptance Specs.
- Current Programs In:
  Criticality Safety (non-Division Program)
  RIB Production of Neutron-Rich Species.
  Nuclear Astrophysics.
- Long History of Nuclear Astrophysics Contributions.
  (n,γ) Measurements on Over 180 Isotopes
  Verified Classical *s*-process Concept.

Near Term Experiments at ORELA Possible With Increased Beam Time and Manpower

- **^{208}Pb(n,γ).**
  Termination of *s* process.
  Neutron sensitivity background.
  Large difference between previous data.
  Requires 4-6 weeks of beam, σ_t not needed.
- **(n,γ) and σ_t for isotopes of S, Si, Ca, and Ti.**
  Require excellent time-of-flight resolution.
  Large differences between *s*-process model predictions and meteoric anomalies, probably due to "chemical" or "galactic" evolution effects.
  ***s*-process production of rare isotopes.**
  Some overlap in interest with other ORELA users.
  Small cross sections => 3-4 weeks each.
- **(n,γ) and σ_t for isotopes of Te, Dy,...**
  Important *s*-process calibration points which may have sizable effects due to unmeasured low energy resonances.

Possible Near Term Experiments at ORELA (Continued)

- **^{64,67}Zn, ^{143}Nd, ^{149}Sm and other (*n*,α) experiments.**
  Approx. 30 measurements possible.
  Need data across a range of masses to improve models.
  Require at least 3-4 weeks of beam time each.
  Probably better if run at higher power.
- **(*n*,*n'*) experiments on Dy and isotopes of other rare earth elements.**
  Needed for "Stellar Enhancement Factors".
  Need systematic study of theory to identify discrepancies, especially for *s*-only isotopes.
  Potential thermometers.
  Impact on *r* process calculations?
  Could run at same time as other experiments if another beam line developed.

Possible Near Term Experiments at ORELA (Continued)

- (n,γ) and σ_t for ^{102}Pd and other isotopes of Pd. One of very few *p*-isotopes for which a fairly high enrichment (77.89%) sample is available. Complicated *s*-process branching at ^{107}Pd and ^{108}Ag.
  ^{106}Pd data needed for π-violation studies.
  Long chain of Pd isotopes could be valuable for calibrating statistical model calculations.

Possible Near Term Experiments at ORELA (Continued)

- **^{25}Mg transmission and scattering.**

  Determine J^π values of resonances in ^{26}Mg to constrain ^{22}Ne(α,*n*)^{25}Mg neutron source reaction.
  Expensive (k$ 25) sample needed.
  Need to reincarnate scattering setup.

- **^{13}C(α,*n*)^{16}O and ^{22}Ne(α,*n*)^{25}Mg via inverse.**

  May be possible with expanded version of compensated ion chamber.
  Direct measurements reached their limit?

Possible Near Term Experiments at ORELA: Some Points to remember

- Priority depends on available beam time.
  One typical (n,γ) and σ_t experiment pair requires minimum of 2 weeks of beam.
  Two experiments back-to-back requires minimum of 3 weeks of beam.
- Could run (n,γ), σ_t, (n,α), and (n,n') experiments at same time.
  Requires more than current manpower.
- Can sometimes piggyback on other programs.
  (n,γ) and σ_t setups in most demand by others.
  Could develop duplicate setups on other beam lines.
  Likely new users won't require both beam lines.

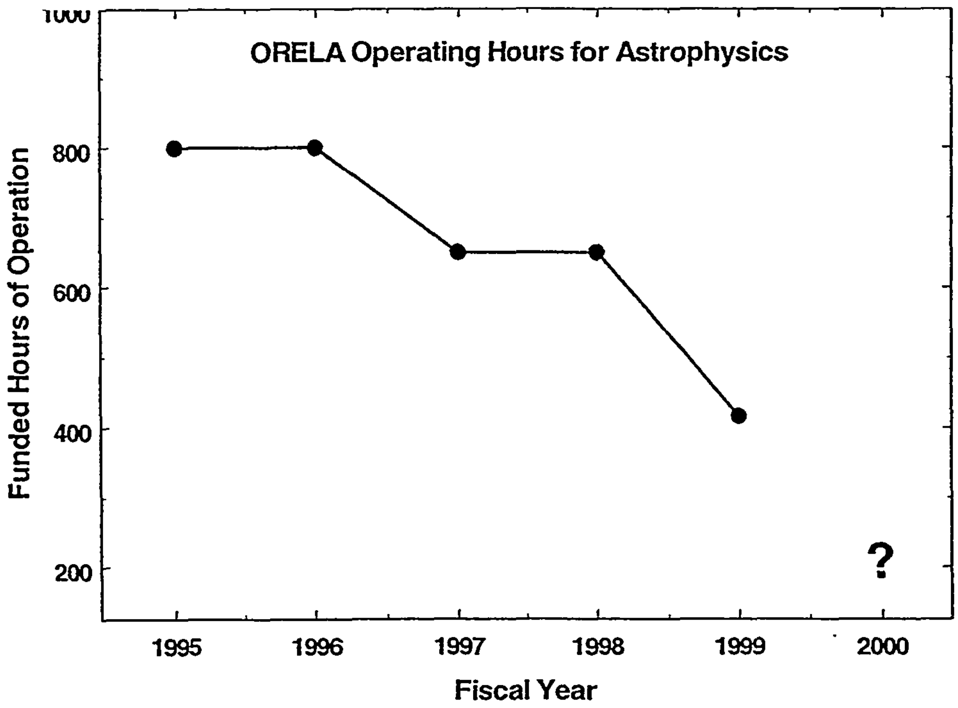

Planned Near Term Experiments at ORELA

- **FY2000**

  ^{195}Pt(n,γ) and σ_t.

    Needed for analysis of ^{192}Pt(n,γ) data.
    ^{192,194,196}Pt measured.
    Heaviest *s*-only isotope with no data.
    Termination of *s* process (Strong Component?).

  ^{64,67}Zn or ^{143}Nd or ^{149}Sm(n,α).

    Have Zn samples. Have material for others.
    Heavier A show larger deviations between models. Probably won't complete one.

- **FY2001**

  ^{86}Sr(n,γ) and σ_t.

    Normalization for meteoric anomalies.
    ***s*-only calibration point in complicated region.**

- **FY2002**

  ^{87}Sr(n,γ) and σ_t.

Plans for Measurements at Los Alamos

R.S. Rundberg, M.M. Fowler, R.C. Haight, G.G. Miller,
P.D. Palmer, E.H. Seabury, J.L. Ullmann, J.B. Wilhelmy,
P. E. Koehler, F. Kappeler

Los Alamos National Laboratory

The facilities at the Los Alamos Neutron Science Center (LANSCE) allow the measurement of neutron capture cross sections over the neutron energy range (1 to 100 keV) for submilligram target masses. A new Radioactive Species Isotope Separator (RSIS) will enable the separation of such quantities of unstable isotopes. Plans for measurements will be discussed.

Plans for Neutron Capture Measurements on Radioactive Samples at Los Alamos

Robert S. Rundberg, J.L. Ullmann, J.B. Wilhelmy, M.M. Fowler, R.C. Haight, E. Seabury, M. Dragowsky, G.G. Miller, P. D. Palmer
Los Alamos National Laboratory

F. Kaeppeler, R. Reifarth, M. Heil, K. Wisshak, F Voss
Forschungszentrum Karlsruhe, Germany

P. Koehler
Oak Ridge National Laboratory

Workshop on the Origin of the Heavy Elements: Astrophysical models and Experimental Challenges 3-4 September 1999, Santa Fe

Unique capabilities at Los Alamos

- Experience in handling and fabricating radioactive targets (CST Division)
  - Radioactive Species Isotope Separator
- Intense source of eV/keV neutrons
  - Manual Lujan Jr. Neutron Scattering Center
  - 1 mg targets
- Detectors for experiment
  - DANCE under design/development

S-Process Nucleosynthesis

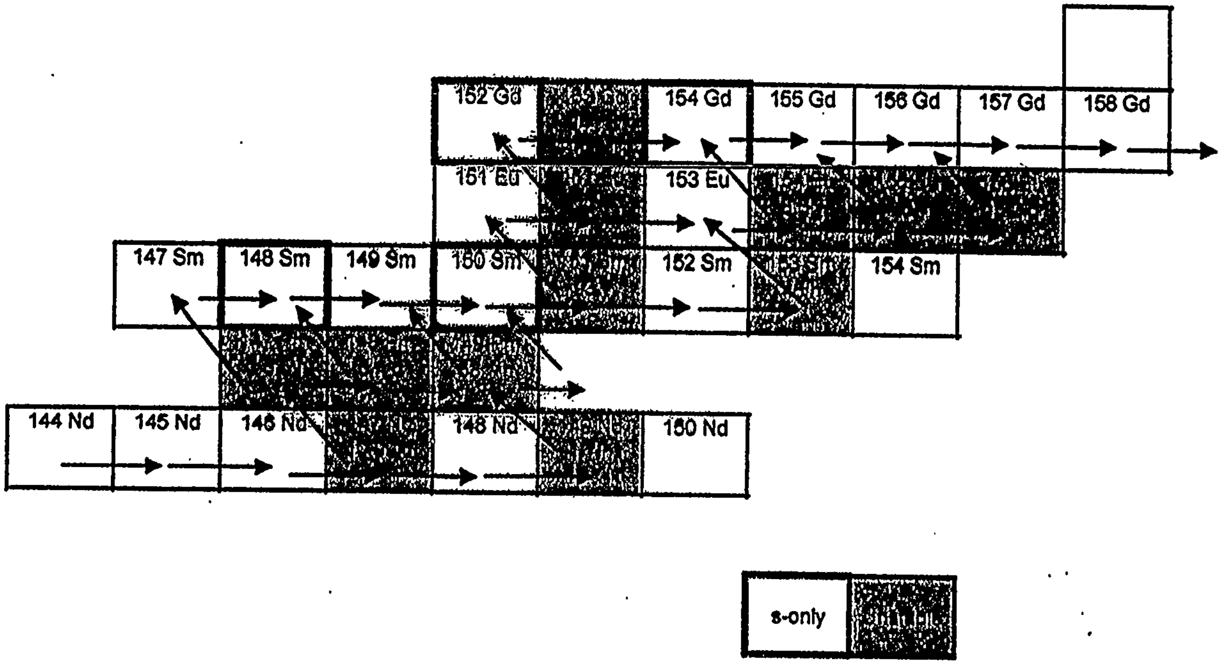

- The mass of nuclei is increased by neutron capture
- The z of nuclei is increased by β decay
- Competition between β decay and capture depends on the capture cross section, β decay rate and neutron flux
- Very few cross sections on unstable nuclei have been measured

Thulium S-process Branching

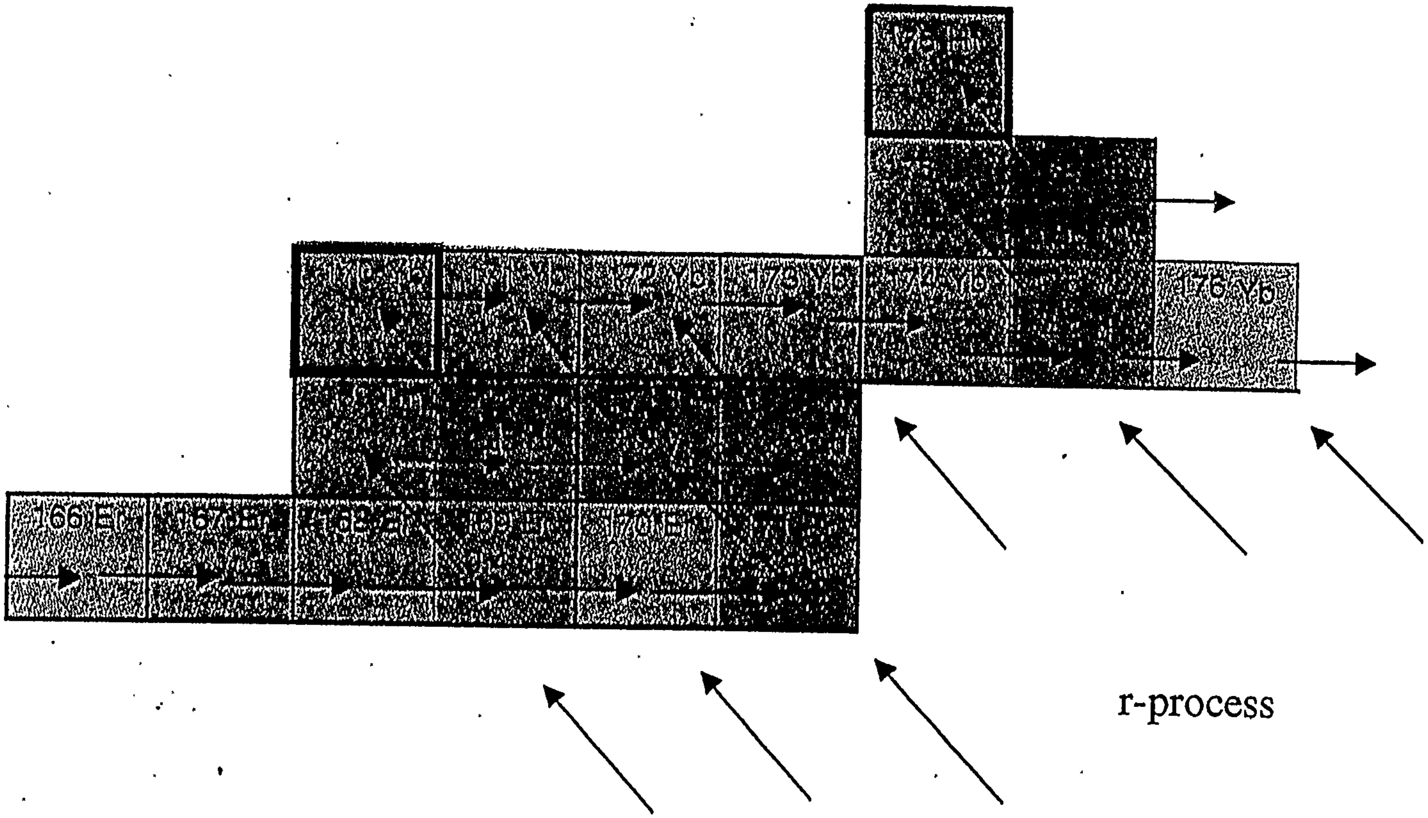

s-process

r-process

Radioactive and rare isotopes for which neutron capture cross sections are needed.

S-Process branching nuclei								
Isotope	Half-life		Rad-Chem	Koehler-Kappeler		G. Mathews	Wilhelmy	Comment
				Priority	Feasible?			
63 Ni	100	y		3	X			
79 Se	1.00E+04	y		1	X	X	X	
85 Kr	10.7	y		1	X	X	X	
86 Rb	18.8	d		1				
88 Y	106.6	d	X	4				
89 Sr	50.5	d		2				
90 Sr	28.8	y		2	X			
93 Zr	1.00E+06	y	R			X	X	Measured ORNL - rad chem
95 Zr	64	d	R	1			X	Rad-chem
94 Nb	2.00E+04	y		2	X			
95 Nb	3.50E+01	d		2				
99 Tc	2.00E+05	y				X	X	measured once ORNL
106 Ru	367	d		2	X			
107 Pd	1.00E+06	y				X	X	
119 Sn	Stable					X	X	250 day isomer
134 Cs	2	y		1			X	
135 Cs	3.00E+06	y		2	X		X	Measured at Karlsruhe
137 Cs	30.17	y		2	(X)			
141 Ce	32	d				X	X	
147 Nd	11	d		1				
147 Pm	2.6	y		1	X		X	
151 Sm	90	y				X	X	
152 Eu	13	y	R	1			X	
154 Eu	8.5	y	R	1				
155 Eu	5	y	R	1	X		X	
153 Gd	241	d		1	X	X	X	
160 Tb	72.1	d		1				
161 Tb	6.9	d		2				
163 Ho	33	y		1	X (x-ray)		X	
166 Ho	1200	y		2				
169 Er	9.4	d		1	X	X		
170 Tm	128	d	R	1	X (?)	X	X	
171 Tm	1.92	y	R	1	X			
175 Yb	4.19	d		2	(X)			
176 Lu	3.60E+10	y					X	
181 Hf	42.4	d		2				
182 Hf	9.00E+06	y		2	X			
179 Ta	1.70E+00	y		1	X			
185 W	75	d		1	X		X	
186 Re	1.00E+05	y		1		X	X	
191 Os	15.4	d		1	X			
192 Ir	74	d	R	1			X	
193 Pt	50	y		1	X (x-ray)	X	X	
198 Au	2.69	d		2				
203 Hg	46.8	d		1				
204 Tl	3.77	y		1	X	X		
205 Pb	1.00E+07	y					X	
210m Bi	3.00E+06	y		2	X			
210g Bi	5.01	d		2	X			

How to Measure with Radioactive Targets

- High Neutron Brightness
  (minimize target)
- Small Duty Factor
  (minimize background)
- Measure Q Value
  (calorimetry)
- Measure Multiplicity
  (high granularity)

Radioactive Species Isotope Separator - RSIS

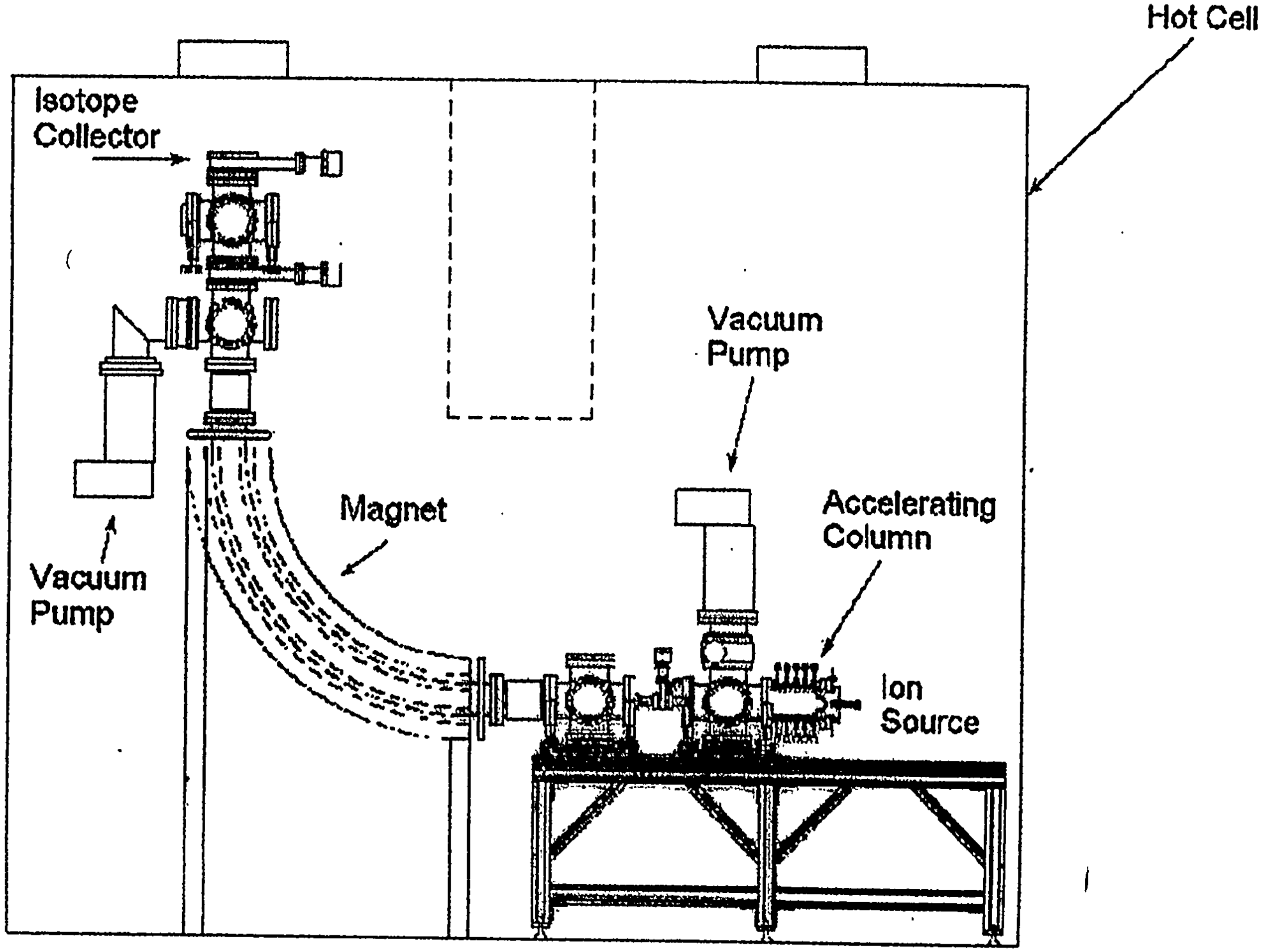

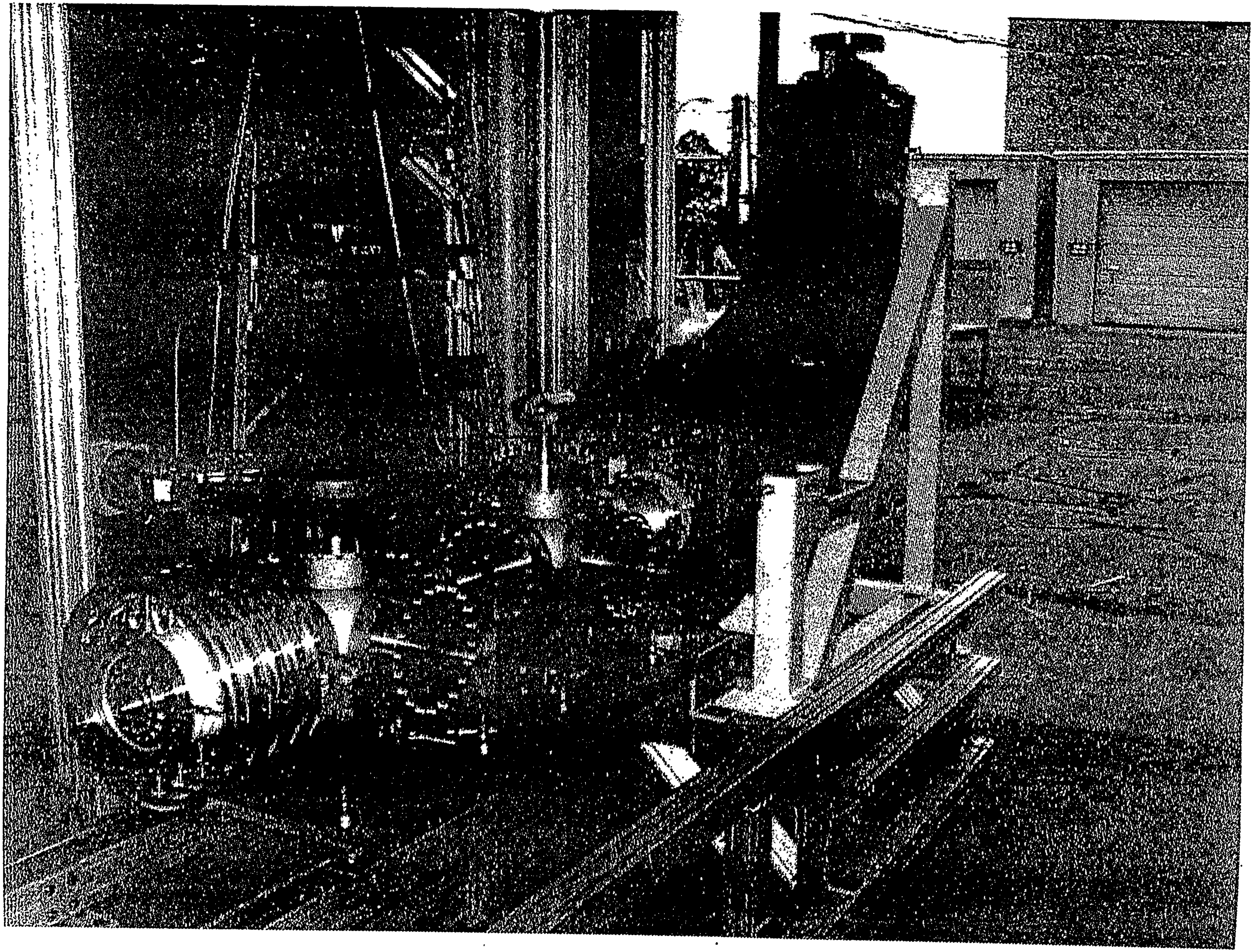

Neutron Capture Systematics

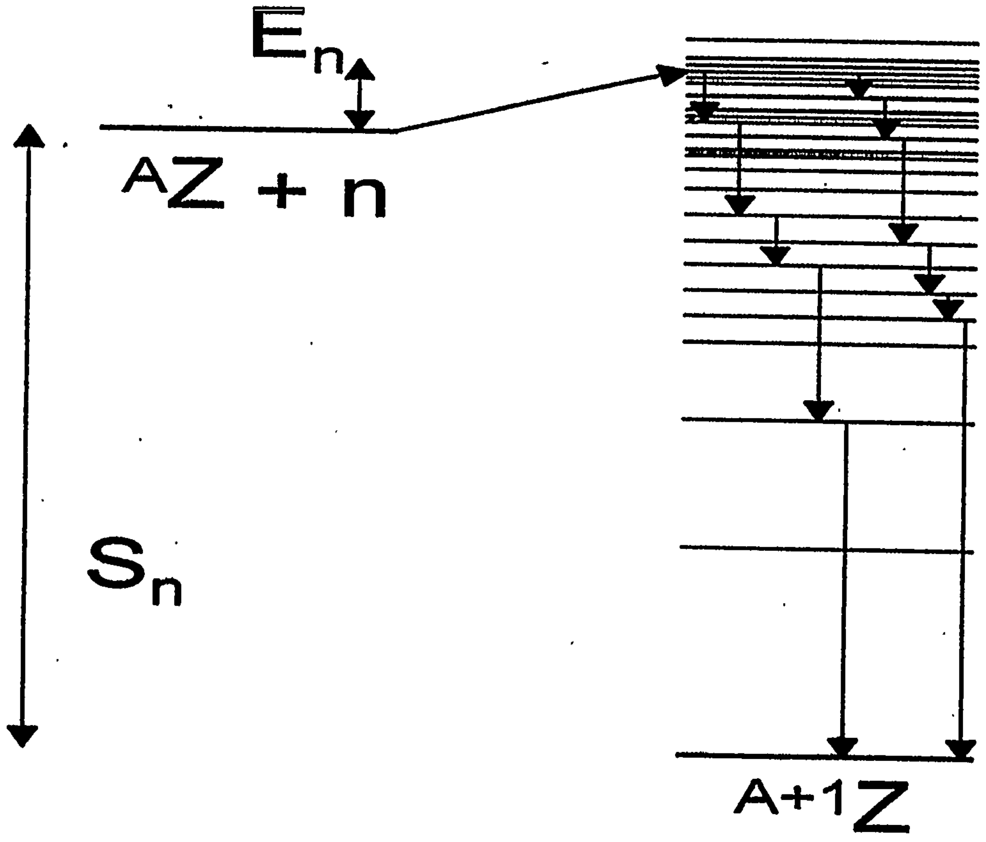

Detector for Advanced Neutron Capture Experiments (DANCE)

- DANCE is collaboration between LANSCE, CST, ORNL, LLNL and Karlsruhe,
- Radioactive Targets
  - Large background rate due to activity in the target and scattered neutrons
- Design Considerations
  - Fast Decay time
  - Highly segmented
    - 132, 162 or 192 element Soccer ball
  - Low neutron capture cross section

Material	Density g/cc	Decay Time ns	Wavelength nm	Photons/MeV
BaF_2	4.88	0.6, 630	180-310	1,800; 10,000
$Bi_4Ge_3O_{12}$	7.13	60, 300	480	700; 7,600
NaI(Tl)	3.67	230	415	38,000
CsI(Tl)	4.51	1000	540	59,000
CsI(pure)	4.51	8	315	2,300
CeF_3	6.16	3,27	300,340	200; 4,300
C_6D_6	0.954	2.8	425	10,000

Capture Cross Sections at 10 keV

Ba	0.15 b
F	0.01 b
Cs	1.0 b
I	1.0 b

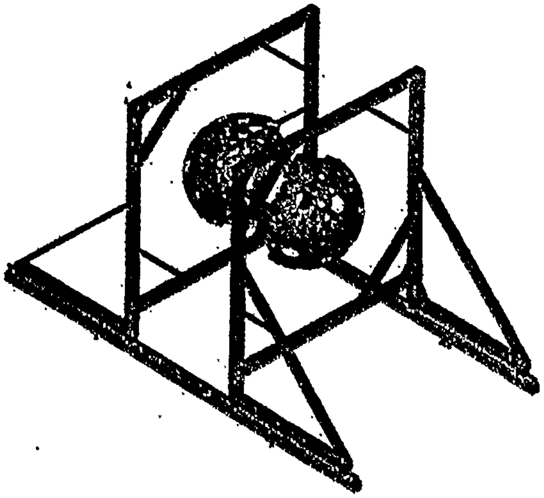

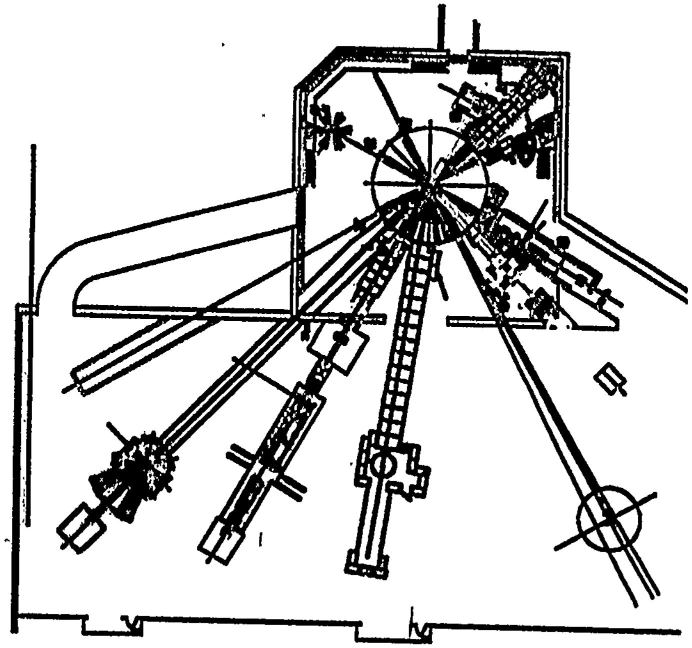

Scintillator Properties

Material	Density	Decay Time	Wavelength	Photons/MeV
	g/cc	ns	nm	
BaF_2	4.88	0.6, 630	180-310	1,800; 10,000
$Bi_4Ge_3O_{12}$	7.13	60, 300	480	700; 7,500
NaI(Tl)	3.67	230	415	38,000
CsI(Tl)	4.51	1000	540	59,000
CsI(pure)	4.51	8	315	2,300
CeF_3	6.16	3,27	300,340	200; 4,300
C_6D_6	0.954	2.8	425	10,000

Barium Fluoride Array

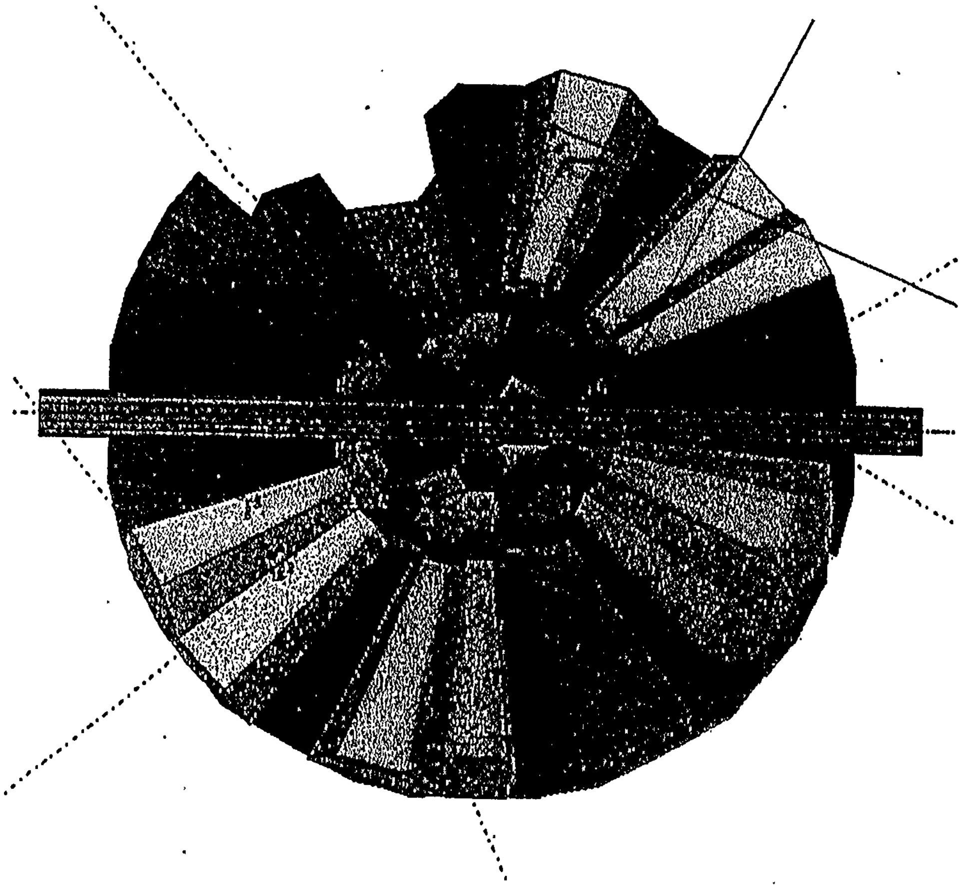

- Four Different Shapes of crystals
- Inner radius = 17 cm
- Outer radius = 32 cm
- 2.5 cm beam pipe through center

Monte Carlo Simulation
- M. Heil
- R. Reifarth
- F. Kaeppeler

Forschungzentrum
Karlsruhe

Device for Advanced Neutron Capture Experiments, DANCE

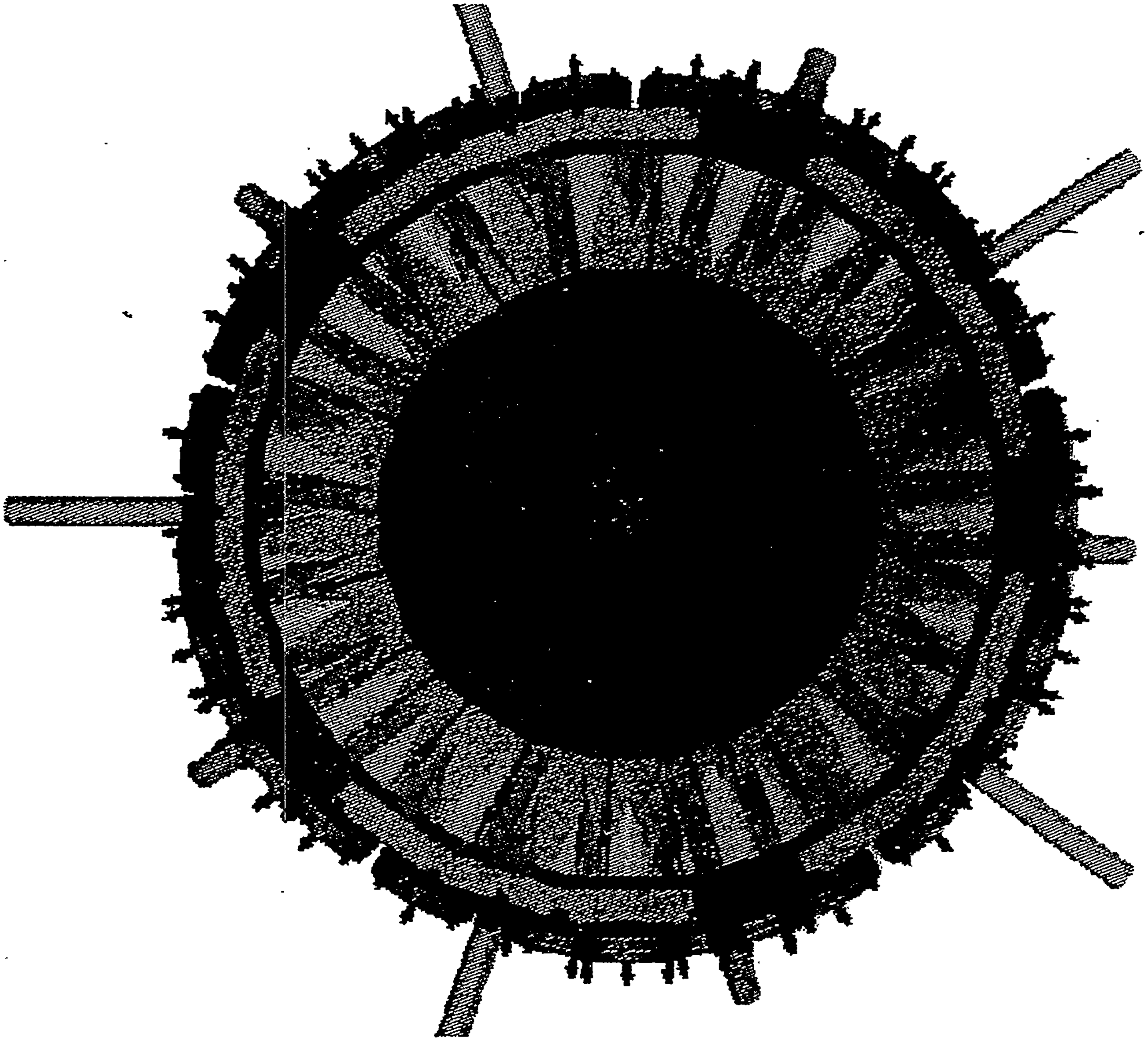

162 element Barium fluoride detector array

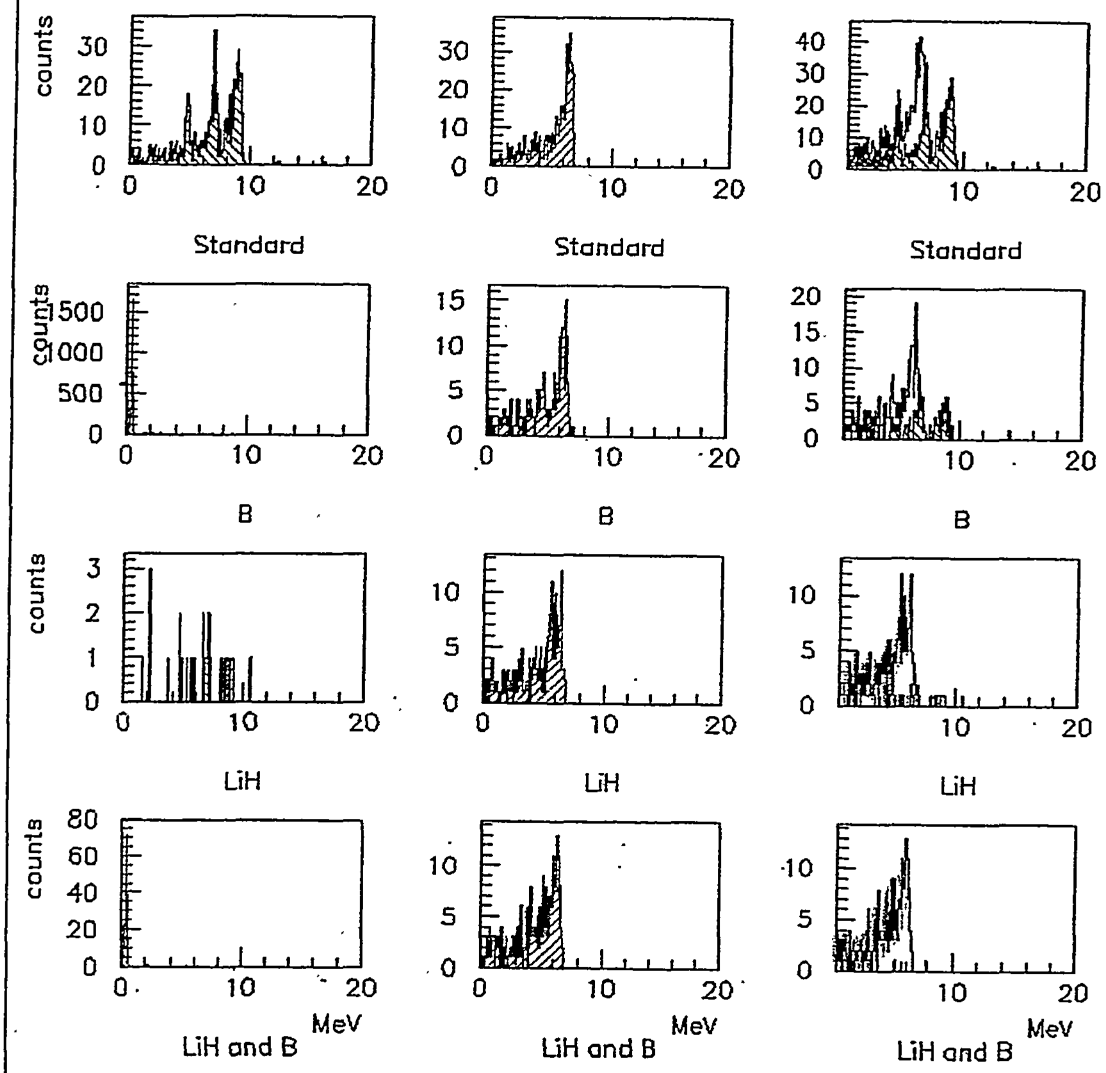

Figure 34: Comparison of setups 1, 8, 16 and 19 in the neutron energy range from 10-100 keV. First column shows the response to neutrons scattered from the gold sample, the middle column the response to neutron capture in the gold sample and the right column the sum of these two processes compared to the background (shaded area). Case 1 (1st row) is the standard setup, in case 8 (2nd row) the gaps between the crystals are filled with ^{10}B, in case 16 (3rd row) a moderator/absorber of ^{6}LiH around the beam pipe was used and in case 19 (4th row) both, the ^{10}B between the crystals and the moderator/absorber of ^{6}LiH were combined.

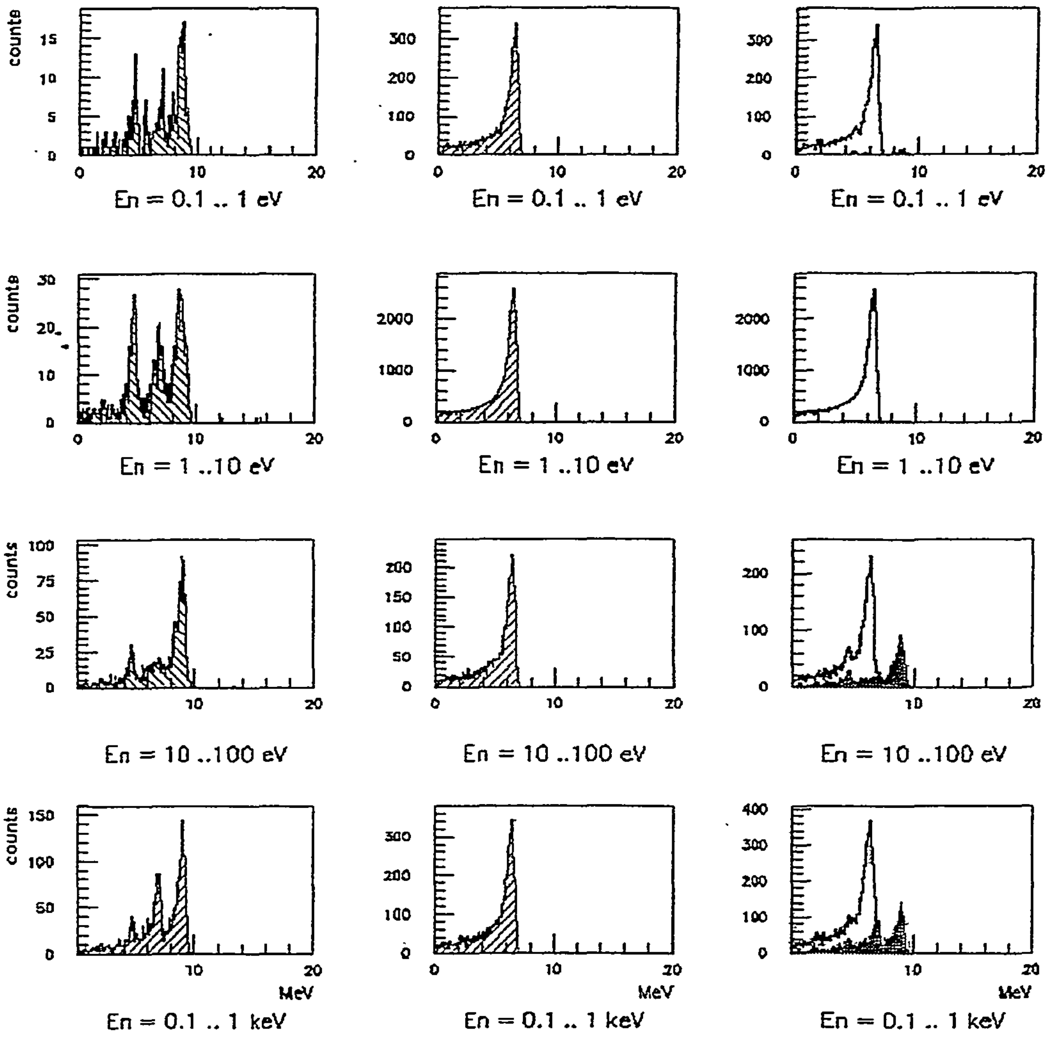

Figure 28: Energy projection of TOF spectra for scattered and captured neutrons and for various TOF cuts. The background from capture of scattered neutrons in BaF_2 (1st column), the (n,γ) events on gold (2nd column) and the expected signal (3rd column) are compared for neutron energy intervals below 1 keV.

Proposed Flight Path 14 Configuration

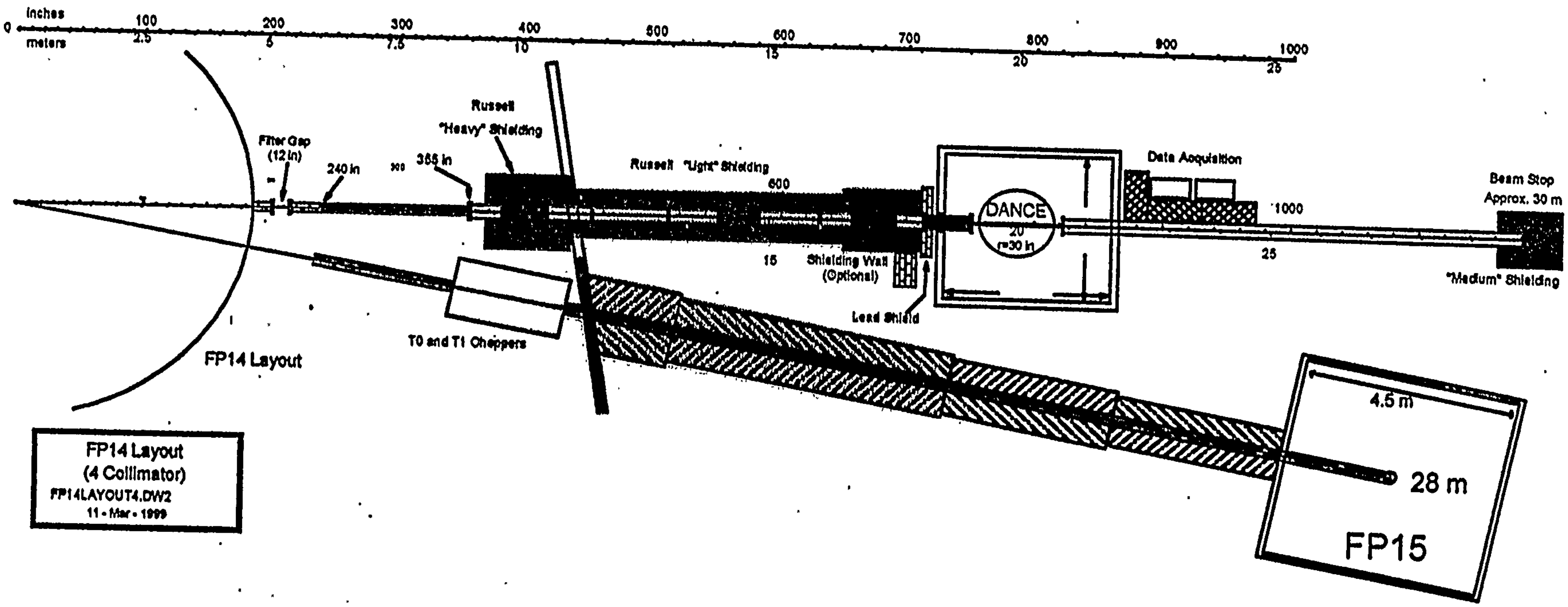

MLNSC/ORELA Comparison

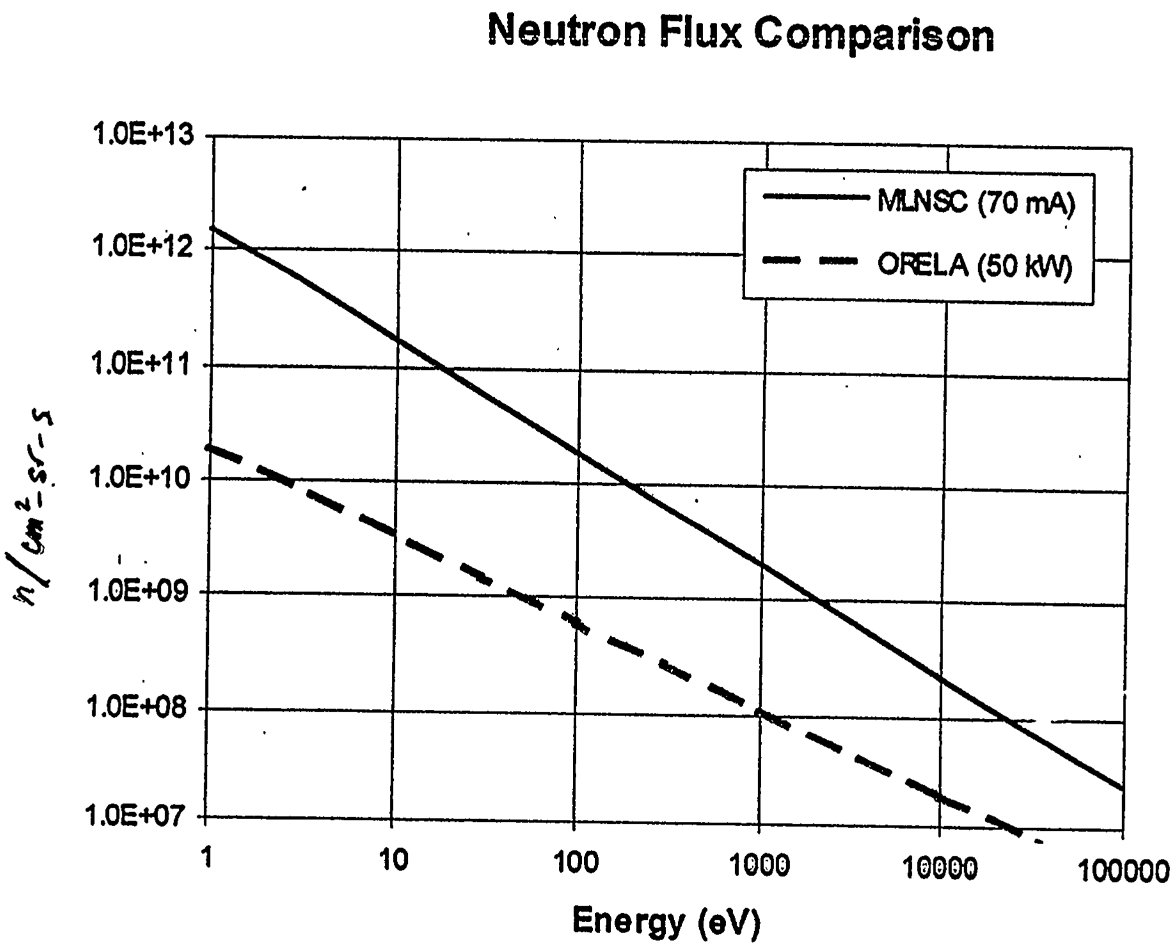

Calculated Energy Resolution at 20 meters

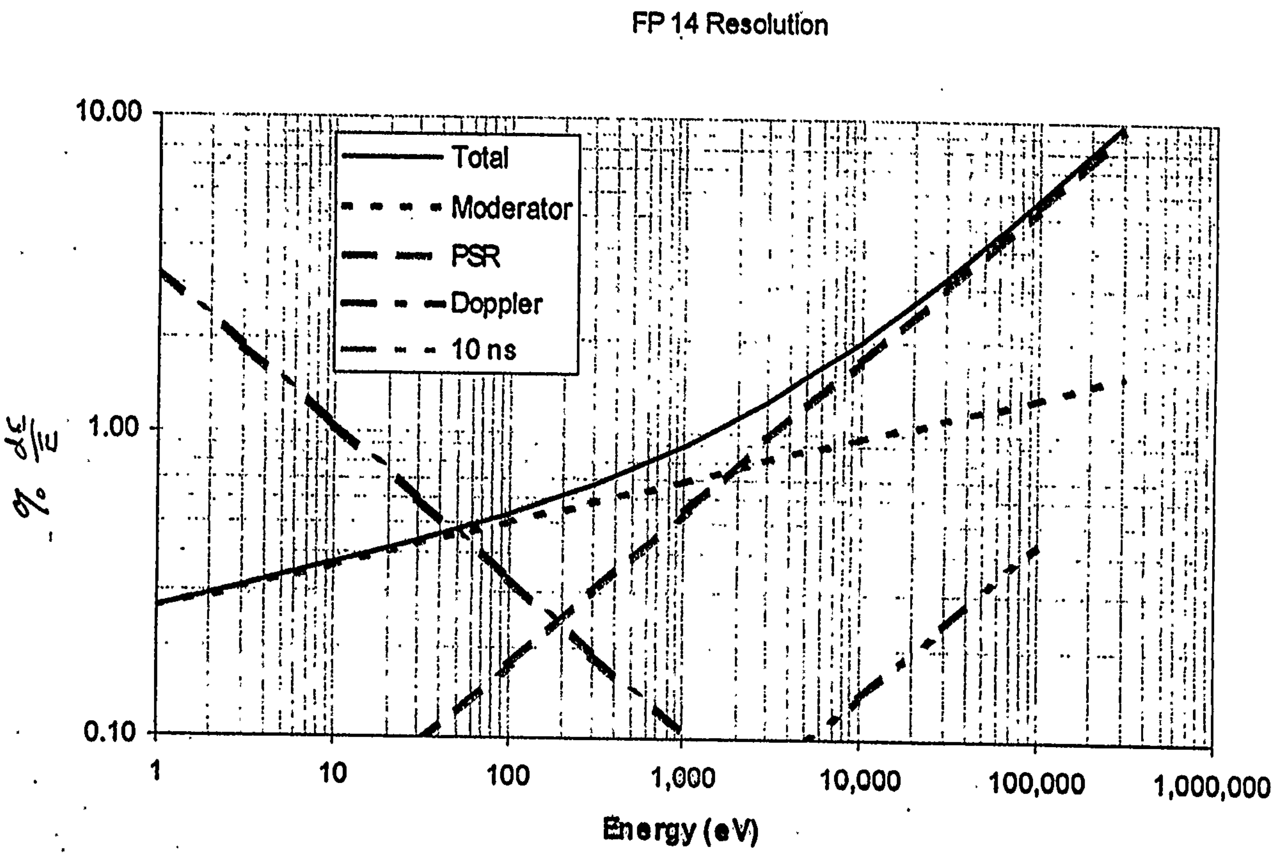

Reactions on Unstable Nuclei

- ^{169}Tm
  - Stable Tm was chosen for an initial test
  - 1 mg sample
  - Data agrees with previous data and with calculation

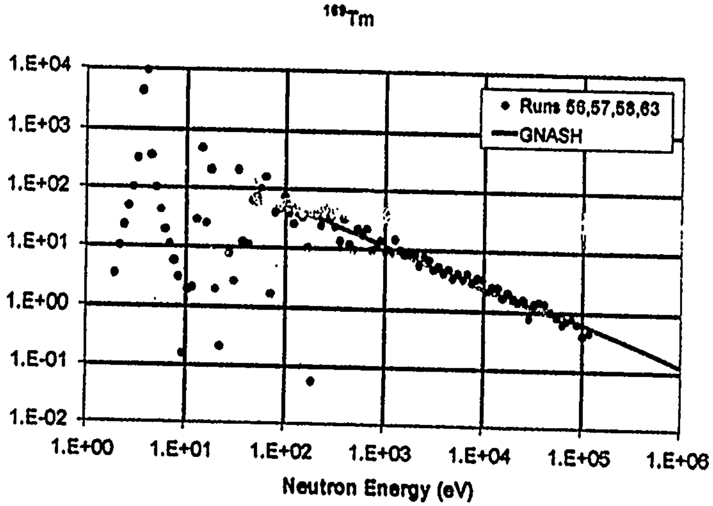

- ^{171}Tm
  - $\tau_{1/2} \sim 1.9$ year
  - Sample prepared by reactor irradiation of ^{170}Er and chemically separated
  - 1 mg (1 Ci) sample
  - Above 1 keV measurements and calculations diverge.

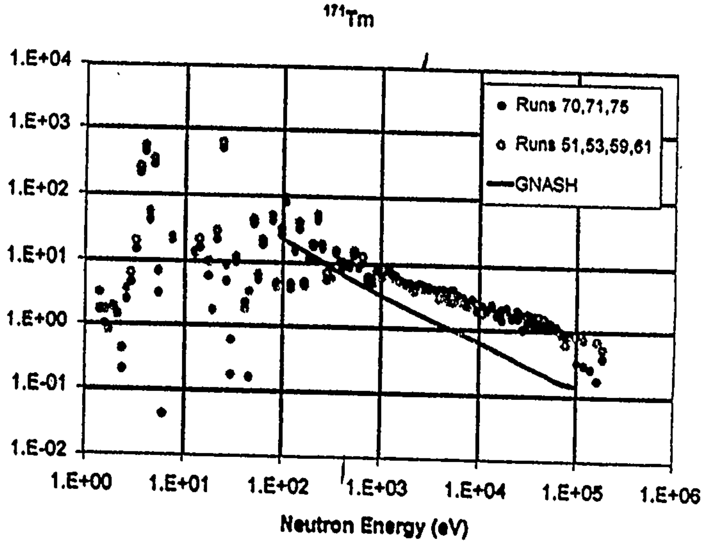

Experiment to Theory Ratios for (n,γ) Reactions on Stable ^{169}Tm and Radioactive ^{171}Tm